

---

Doctoral Dissertations

Student Theses and Dissertations

---

Fall 2013

## Polybenzoxazine aerogels: synthesis, characterization, conversion to porous carbons, and energetic composites

Shruti Mahadik-Khanolkar

Follow this and additional works at: [https://scholarsmine.mst.edu/doctoral\\_dissertations](https://scholarsmine.mst.edu/doctoral_dissertations)

 Part of the [Chemistry Commons](#)

Department: Chemistry

---

### Recommended Citation

Mahadik-Khanolkar, Shruti, "Polybenzoxazine aerogels: synthesis, characterization, conversion to porous carbons, and energetic composites" (2013). *Doctoral Dissertations*. 1821.

[https://scholarsmine.mst.edu/doctoral\\_dissertations/1821](https://scholarsmine.mst.edu/doctoral_dissertations/1821)

This thesis is brought to you by Scholars' Mine, a service of the Missouri S&T Library and Learning Resources. This work is protected by U. S. Copyright Law. Unauthorized use including reproduction for redistribution requires the permission of the copyright holder. For more information, please contact [scholarsmine@mst.edu](mailto:scholarsmine@mst.edu).



POLYBENZOXAZINE AEROGELS: SYNTHESIS, CHARACTERIZATION,  
CONVERSION TO POROUS CARBONS, AND ENERGETIC COMPOSITES

by

SHRUTI MAHADIK-KHANOLKAR

A DISSERTATION

Presented to the Faculty of the Graduate School of the  
MISSOURI UNIVERSITY OF SCIENCE AND TECHNOLOGY

In Partial Fulfillment of the Requirements for the Degree

DOCTOR OF PHILOSOPHY

in

CHEMISTRY

2013

Approved by:

Dr. Nicholas Leventis, Advisor  
Dr. Chariklia Sotiriou-Leventis, Co-Advisor  
Dr. Manashi Nath  
Dr. Jeffrey G. Winiarz  
Dr. Lokeswarappa R. Dharani

© 2013

Shruti Mahadik-Khanolkar

All Rights Reserved

**DEDICATED TO**

**MY BELOVED FATHER**

**Late Mr. SURYAKANT G. MAHADIK**

## **PUBLICATION DISSERTATION OPTION**

This dissertation consists of two articles that have been prepared for publications as follows:

Paper I found on pages 35-100 is intended to submit in *Chemistry of Materials*

Paper II found on pages 101-156 is intended to submit in *Chemistry of Materials*

## ABSTRACT

Aerogels are nanoporous, low-density bulk objects, consisting of three-dimensional assemblies of nanoparticle. Structured similarly, polymeric aerogels are emerging as a mechanically strong alternative to traditional silica aerogels, which are fragile. Amongst polymeric aerogels, those based on polybenzoxazine (PBO - a type of phenolic resin), are extremely robust and comprise an economic alternative to resorcinol-formaldehyde aerogels, also a class of phenolic resins, as the main source of carbon aerogels. The drawback of the PBO chemistry has been the long (days) processing time at high-temperatures ( $>130$  °C). Herewith, we have developed an energy- and time-efficient process to PBO aerogels by inducing acid-catalyzed gelation at room-temperature completed in a few hours. The new aerogels are compared directly with their conventional counterparts and are found equivalent or better in terms of mechanical strength, thermal insulation value, surface area and carbonization yield.

Hexahydrated iron chloride ( $\text{FeCl}_3 \cdot 6\text{H}_2\text{O}$ ) is a fairly strong Brønsted acid, which, based on the above, catalyzes formation interpenetrating networks of PBO and iron oxide nanoparticles (PBO-FeOx). Pyrolysis of that intimate mixture of a carbon source (PBO) and iron oxide undergoes smelting to highly porous ( $>90\%$  v/v) monolithic metallic iron aerogels. The porous network was loaded with oxidizers (e.g.,  $\text{LiClO}_4$ ) into a new class of energetic materials (thermites, explosives, pyrotechnics).

The PBO aerogels developed here comprise a wide-base platform for use as thermal insulators in civil and transportation applications (PBO aerogels themselves), electrodes for fuel cells, lithium ion batteries (nanoporous carbons), catalysts and energetic materials (PBO-FeOx).

## ACKNOWLEDGEMENTS

I would like to express my sincere gratitude to my advisor, Prof. Nicholas Leventis and Co-advisor Prof. Chariklia Sotiriou-Leventis for their continuous guidance, encouragement and support throughout my graduate studies at Missouri S & T. They have taught me to be systematic and persistent to excel in the field of research. Especially, the passion and enthusiasm of Prof. Leventis towards research, his eagerness to learn new things, and his critical thinking has always inspired me to go an extra mile in my work. I am fortunate to have them as my advisors.

I would like to thank my committee members, Dr. M. Nath, Dr. J. Winiarz, and Dr. L. R. Dharani for providing useful suggestions for my research. I thank the Department of Chemistry, Missouri S&T for providing financial assistance and resources. I am grateful to Mr. J. Counsil for his timely help with all the instruments and key insights in my projects. I would also like to thank Dr. E. Bohannan, Dr. A. Choudhury, and C. Wisner for crucial characterizations of samples for my thesis work.

I highly appreciate the help, guidance, and emotional support of my lab colleagues (Abhishek, Chakri, Dhuru, and Anand). Our brainstorming discussions helped me to nurture my research aptitude. I also want to extend my gratitude to all my friends for their moral support during tough as well as good times. Most importantly, I would like to thank my father (baba) Late Mr. S. G. Mahadik. I would not have pursued my goals without his belief and support. I am forever grateful to my mother (aai) Mrs. S. Mahadik and my sister (tai) Mrs. A. Sawant for their unconditional love and support. I am lucky to have found my soul mate, Mr. A. Khanolkar in Rolla. His love, understanding and constant motivation has given me strength to complete my Ph.D.



## TABLE OF CONTENTS

	Page
PUBLICATION DISSERTATION OPTION .....	iv
ABSTRACT.....	v
ACKNOWLEDGEMENTS.....	vi
LIST OF ILLUSTRATIONS.....	xi
LIST OF SCHEMES.....	xv
LIST OF TABLES.....	xvi
 SECTION	
1. INTRODUCTION .....	1
1.1. AEROGELS.....	1
1.2. THE SOL-GEL SYNTHESIS OF SILICA AEROGELS.....	3
1.3. SURFACE MODIFICATION OF SILICA AEROGELS WITH POLYMERS (X-LINKING).....	6
1.4. ORGANIC AEROGELS DERIVED FROM PHENOLIC CHEMISTRY .....	8
1.4.1. Resorcinol Formaldehyde Aerogels.....	8
1.4.2. Base Catalyzed and Acid Catalyzed Gelation of Resorcinol Formaldehyde .....	8
1.4.3. The Effect of Synthetic Parameters on the Morphology of RF Aerogels.....	12
1.4.4. Polybenzoxazine Chemistry.....	14
1.4.5. Porous Polybenzoxazines.....	18
1.5. CARBON AEROGELS .....	21
1.6. POROUS METALS FROM AEROGELS .....	27

## PAPER

I. POLYBENZOXAZINE AEROGELS I: HIGH-YIELD ROOM-TEMPERATURE ACID-CATALYZED SYNTHESIS OF ROBUST MONOLITHS, OXIDATIVE AROMATIZATION AND CONVERSION TO MICROPOROUS CARBONS .....	35
Abstract .....	35
1. INTRODUCTION .....	36
2. RESULTS AND DISCUSSION .....	39
2.1. Materials Synthesis .....	39
2.2. Chemical Transformation along Processing .....	42
2.3. PBO Aerogel Characterization .....	51
2.3.a. General material properties .....	51
2.3.b. The porous structure .....	53
2.3.c. The skeletal framework and interparticle connectivity .....	55
2.4. Carbonization .....	58
3. CONCLUSION .....	63
4. EXPERIMENTAL .....	64
4.1. Materials .....	64
4.2. Synthesis of the Benzoxazine Monomer (BO Monomer).....	64
4.3. Preparation of Polybenzoxazine (PBO) Aerogels.....	65
4.3.a Via heat-induced polymerization at 130 °C .....	65
4.3.b. Via acid-catalyzed polymerization at room temperature .....	66
4.4. Carbonization of PBO Aerogels .....	67
4.5. Methods.....	67
SUPPORTING INFORMATION.....	70

ACKNOWLEDGEMENTS.....	70
REFERENCES .....	74
FIGURES.....	77
SUPPORTING INFORMATION.....	89
REFERENCES .....	100
II. POLYBENZOXAZINE AEROGELS II: INTERPENETRATING NETWORKS WITH IRON OXIDE AND THE CARBOTHERMAL SYNTHESIS OF HIGHLY POROUS MONOLITHIC PURE IRON(0) AEROGELS AS ENERGETIC MATERIALS .....	101
Abstract.....	101
1. INTRODUCTION .....	102
2. RESULTS AND DISCUSSION.....	106
2.1. Synthetic Procedures and Material Properties along Processing.....	106
2.2. Detailed Physiochemical Characterization along Processing.....	113
2.2.a. The PBO-FeOx interpenetrating network.....	113
2.2.a.1. The gelation process and macroscopic characterization .....	114
2.2.a.2. Cross-particle chemical interaction.....	120
2.2.b. The Carbothermal conversion of PBO-FeOx to Fe(0).....	124
2.3. From Explosives to Thermites by Tuning the Porosity of Iron(0) Aerogels .....	127
3. CONCLUSION.....	129
4. EXPERIMENTAL SECTION .....	130
4.1. Materials .....	130
4.2. Preparation of Polybenzoxazine-iron Oxide Interpenetrating Networks (PBO-FeOx Aerogels).....	130
4.3. Conversion of PBO-FeOx Aerogels into Nanoporous Iron(0) Aerogels.....	131

4.4. Methods and Procedures .....	132
SUPPORTING INFORMATION .....	135
ACKNOWLEDGEMENTS .....	135
REFERENCES .....	136
FIGURES .....	141
SUPPORTING INFORMATION .....	149
SECTION	
2. CONCLUSIONS.....	157
BIBLIOGRAPHY.....	158
VITA.....	169

## LIST OF ILLUSTRATIONS

Figure	Page
1.1 Nanofabrication from top-down versus bottom-up assembly.....	2
1.2 The typical nanostructure of a silica aerogel on left and its macroscopic appearance on right .....	3
1.3 Preparation of silica aerogels via the sol-gel process. ....	4
1.4 Schematic representations of different processing conditions of silica sol .....	5
1.5 A thin polymer layer is formed conformally on the skeletal silica nanoparticles .....	7
1.6 <sup>13</sup> C NMR of resorcinol-formaldehyde mixtures in 1:2 mol ratio in CD <sub>3</sub> CN A: 15 min after mixing, using (HCl) catalyst, at RT B: 15 min after mixing, without any catalyst, at RT and C: 75 min after mixing, with base (ET <sub>3</sub> N) catalyst, at 80 °C.....	11
1.7 SEM of RF aerogels prepared with A: base-catalysis (0.07 g/cc) and B: acid-catalysis (0.175 g/cc).....	12
1.8 TEM of RF (10% w/w) aerogels prepared with base catalyst (Na <sub>2</sub> CO <sub>3</sub> ) at both A. low catalyst (R/C = 300) and B. high catalyst (R/C = 50) concentration .....	13
1.9 Chemical structure of 3,4-dihydro-6-methoxy-3-methyl- 2H,4H-benzo[e]1,3-benzoxazine (left) and corresponding crystal structure (right) showing semi chair conformation .....	15
1.10 Polybenzoxazine foams obtained with glass microballoons and silica fibers (left) and with azocarbonamide foaming agent (right).....	18
1.11 Morphological changes in the self-assembled nanostructures and mesoporous polybenzoxazines with different polybenzoxazine contents.....	20
1.12 Schematic representations showing a) the concept of template synthesis b) microporous, c) mesoporous, and d) macroporous carbon materials and e) carbon nanotubes were synthesized using zeolite, mesoporous silica opal, and an anodic aluminum oxide (AAO) membranes as templates, respectively. ....	22
1.13 SEM images of carbon aerogels obtained through a) Na <sub>2</sub> CO <sub>3</sub> catalyst (R/C = 300, 5% w/w); b) low catalyst (R/C = 1500, 30% w/w); c) acid catalyst (65% aq. Nitric acid, R/C = 30, 15% w/w); d) prepared from Ocellus (type of bacteria).....	23

1.14 Nitrogen sorption isotherms (left) and pore size distribution from DFT method (right) of carbon aerogels derived from tannin-formaldehyde at different pH value .....	25
1.15 Thermo-gravimetric analysis (TGA) of polybenzoxazine and RF aerogels.....	26
1.16 Formation of macroporous metals by gold nano-crystal-catalyzed electroless deposition.....	28
1.17 Scanning Electron micrograph (SEM) of A: Silver sponge monolith prepared at 520 °C B: Maghemite ( $\gamma$ -Fe <sub>2</sub> O <sub>3</sub> ) sponge prepared at 600 °C using the dextran templating method. ....	29
1.18 Pictorial representation and scanning electron micrographs (SEM) of A: a sintered NiO-ZnO pellet B: formation of macroporous ceramic (NiO) through selective leaching of a two-phase composite (leaching of ZnO) C: reduction to a porous metal (NiO reduction to Ni) D: decoration with conformal coating (La <sub>4</sub> Ni <sub>3</sub> O <sub>10</sub> ) and subsequent reaction (shown a Ni <sub>0.7</sub> Zn <sub>0.3</sub> O pellet decorated with lanthanum acetate, followed by decomposition and heating) E: hierarchically porous Ni obtained via leaching of Ni <sub>1-x</sub> Zn <sub>x</sub> O with 4M NaOH to remove ZnO .....	30
1.19 Photograph of iron foam next to an original pellet of Fe-BTA (Fe- bistetrazolamine) complex (left) TEM of Fe foam (0.011 – 0.040 g cm <sup>-3</sup> ) (right) and selected area diffraction pattern (inset).....	31
1.20 TEM (left) and EFTEM images (right) of iron (III) oxide aerogel/nanometric Al composite. ....	32

## PAPER I

1. Differential scanning calorimetry (DSC) in air at 10 °C min <sup>-1</sup> of representative PBO aerogel samples as shown .....	77
2. Optical photographs and the corresponding SEMs of representative HCl-catalyzed PBO aerogel monoliths at all stages of processing. Note that as-prepared samples pyrolyzed directly at 800 °C under inert atmosphere (Ar) do not yield nanoporous monoliths. (The carbonization yield was also low: 27% w/w versus 61% w/w from the air-cured samples– see Table 4.) .....	78
3. <sup>1</sup> H NMR of the BO monomer in DMF-d <sub>7</sub> and of two representative sols, also in DMF-d <sub>7</sub> , with the formulations shown at their respective gelation points (in parentheses). Acid-catalyzed PBO-A-15-RT gelled at room temperature, while the heat-polymerized PBO-H-40-130 gelled at 130 °C. “S” denotes solvent .....	79

4. Liquid  $^{13}\text{C}$  NMR spectra of the BO monomer in the APT and the normal mode (bottom, and second from bottom, respectively) in DMF- $d_7$  (marked with asterisks) containing chromium(III) tris(acetylacetonate). Peak assignments were based on integrated intensity and the APT spectrum. Solid-state CPMAS  $^{13}\text{C}$  NMR spectra of the aerogels samples as shown are cited above. (All samples shown were prepared with the same weight percent of BO monomer in the sol: -xx-:10.) ..... 80
5. Infrared (FTIR) spectra of the BO monomer and of representative aerogel samples as shown. (All samples shown were prepared with the same weight percent of BO monomer in sol: -xx-:10.) ..... 81
6. Representative porosimetry (top) and pore size distribution data of cured (200 °C/air), density-matched A- and H- PBO samples as shown (PBO-A-12-200,  $\rho_b=0.483\text{ g cm}^{-3}$ ; PBO-H-20-200,  $\rho_b=0.447\text{ g cm}^{-3}$ )  
Left: N<sub>2</sub> sorption data; Right: Hg-intrusion data. .... 82
7. Scanning electron microscopy (SEM) at two different magnifications of heat- and acid-polymerized PBO aerogels at different sol concentrations (-xx-) as shown. Dashed circles indicate the smallest particles identifiable ..... 83
8. A. Total thermal conductivity data ( $\lambda$ ) as a function of bulk density ( $\rho_b$ ) of PBO aerogels.  
B. Log-Log plot of the thermal conductivity through the solid framework ( $\lambda_s$ ) versus bulk density of PBO aerogels as shown ..... 84
9. Thermogravimetric analysis (5 °C min<sup>-1</sup>) under high purity nitrogen of bulk density-matched PBO aerogels samples as shown.  
(For  $\rho_b$  values see Table 3.) ..... 85
10. Elemental analysis data and evolution of IR spectra of PBO aerogels at progressively higher pyrolysis temperatures (5 h under high-purity Ar) ..... 86
11. Scanning electron microscopy (SEM) at two different magnifications of carbon aerogels originating from heat- and acid-polymerized PBO aerogels at different sol concentrations (-xx-) as shown ..... 87
12. N<sub>2</sub>-sorption porosimetry of C-aerogels originating from low-concentration sols (top, -xx-=5) and high-concentration sols (bottom, -xx-=20). Left: isotherms, Right: pore size distributions of micropores from the low-pressure ( $P/P_o \ll 0.1$ ) part of the isotherms, and of mesopores from the high partial pressure branch of the desorption isotherms ( $P/P_o \sim 1$ ). (Note, the C-H-5-800 isotherms do not show significant N<sub>2</sub> adsorption at low pressures and the samples lack micropores.) ..... 88

## PAPER II

1. Thermogravimetric analysis of samples as shown in air.(Heating rate: 10 °C min<sup>-1</sup>)  
Percent residual weights at 800 °C (% w/w): FeOx: 83.8; PBO-FeOx-200: 65.2;  
PBO-FeOx: 62.5; PBO-Fe<sup>3+</sup>-200: 24.8; PBO-A-7-200 (previous article): 0.0;  
Fe(0)/C: 138.6; Fe(0): 143.5 .....141
2. A-C: Scanning electron microscopy (SEM) at two different magnifications of  
FeOx-200 (A); PBO-Fe<sup>3+</sup>-200 (B); PBO-FeOx-200 (C). Scanning transmission  
electron microscopy (STEM- bright field) of PBO-FeOx-200 .....142
3. (A) Rheology of a PBO-FeOx sol at 80 °C (multifrequency oscillation mode;  
for clarity, only one frequency (1 rad s<sup>-1</sup>) is shown). (B) Referring to (A),  
plot of the statistical function as a function of time at all four frequencies  
employed. (C) DMA at 80 °C (multifrequency oscillation mode) of the same  
PBO-FeOx sample, right after gelation. Data shown at all frequencies  
employed (see Experimental). Arrow shows the effect of increasing frequency  
on the elastic modulus (G'). (D) Referring to (C), plot of the statistical function  
as a function of time at all five frequencies employed. (E) Variation of the pH  
during gelation (80 °C) of the two sols as shown. The first two dashed vertical  
lines mark the rheological gelation points (t<sub>g-rheom</sub>) of the two sols; the third one  
marks tDMA of the PBO-FeOx gel (see Table 2).....143
4. Infrared (FTIR) spectra of PBO-FeOx aerogels and controls as-prepared and after  
curing at 200 °C in air. The spectrum of an as-prepared HCl-catalyzed PBO  
aerogel (PBO-A-RT) is included for comparison. Arrow points to the lattice  
vibration of Fe<sub>3</sub>O<sub>4</sub> .....144
5. Mössbauer spectra (black solid lines) of the samples as shown. Spectra include  
the fitting spectra at scale (see Table 4) according to the index shown on top.....145
6. X-ray diffraction (XRD) data for interpenetrating networks and controls along  
processing as shown. Relevant line spectra are shown at the bottom .....146
7. SEM data, some at two different magnifications along processing of samples as  
shown. ....147
8. A) An exploding Fe(0)/LiClO<sub>4</sub> sample (iron(0):LiClO<sub>4</sub>=1:0.395 mol/mol) ignited  
with a burner (see also Movie S.1 in Supporting Information). (B) A Fe(0)-  
1200/LiClO<sub>4</sub> sample behaving as a thermite (see Movie S.2). Inset: Photograph  
on a millimeter paper of a Fe(0)-1200/LiClO<sub>4</sub> sample before ignition (left) and  
another one after testing (right). As shown, the latter remained monolithic. ....148



## LIST OF SCHEMES

Scheme	Page
1. Mechanism of base catalyzed gelation of RF .....	9
2. Mechanism of acid catalyzed gelation of RF .....	10
3. General reaction pathway for the synthesis of benzoxazine monomers .....	14
4. Proposed mechanism of ring opening of benzoxazine via phenolic or oligomeric impurities in heat induced polymerization .....	16
5. Proposed reaction pathway for ring opening reaction of benzoxazine .....	17
6. Synthesis of pa-OH, pa-PCL, pa-PCL/PBZZ and schematic representation of the generation of nanoporous PBZZ films from phase-separated polymers .....	19
7. Reaction of resorcinol and furfural catalyzed with NaOH in ethanol .....	24
 PAPER I	
1. Synthesis of Benzoxazine (BO) Monomer and the Generally Accepted Mode of Polymerization .....	37
2. Synthesis of PBO aerogels, carbonization and graphitization .....	41
3. Mechanism of acid-catalyzed polymerization of the BO monomer (for clarity, only half of the bisphenol A moiety is shown; arrow shows site for additional crosslinking).....	48
4. Proposed mechanism for the oxidative aromatization of the PBO network (for clarity, only half of the bisphenol A moiety is shown) .....	52
 PAPER II	
1. Synthesis of nanoporous iron .....	107
2. Chemical processes forming the interpenetrating networks .....	108
3. Proposed growth mechanism of PBO-FeOx interpenetrating networks.....	119

## LIST OF TABLES

Table	Page
<b>PAPER I</b>	
1. Representative elemental analysis data for PBO and corresponding carbon aerogels in comparison with the BO monomer.....	43
2. Experimental (recited from Table 1) versus calculated CHNO weight percent of plausible oxidized forms (Hox-I and Hox-II) of the generally accepted PBO structure (see Scheme 1) and of the polymer obtained by acid-catalysis (Aox-I and Aox-II).....	50
3. Properties of PBO-A-xx-200 and PBO-H-xx-200 polybenzoxazine aerogels .....	72
4. Properties of nanoporous carbons derived from PBO-A-xx-200 and PBO-H-xx-200 aerogels .....	73
<b>PAPER II</b>	
1. Material properties of PBO-FeOx interpenetrating networks and controls .....	113
2. Rheological and dynamic mechanical analysis data at 80 °C, of sols as indicated ...	115
3. Small angle x-ray scattering (SAXS) data of aerogels as shown.....	117
4. Mössbauer spectroscopy data for samples as shown .....	122

# 1. INTRODUCTION

## 1.1 AEROGELS

Nanotechnology is the field of science which involves manipulation of materials at atomic or molecular scale to achieve assemblies, structures, and devices with critical dimensions of nanometer range. Materials, after reduction to nanoscale, exhibit novel and significantly improved properties as compared to, bulk because of high surface area to volume ratios. This unique characteristic makes nanotechnology a hot field in science, business, and news today.

Generally, two approaches are involved in the synthesis of nanoscale structures: a) a 'top-down' approach, where larger entities are broken down to nano objects, and b) a 'bottom-up' approach, in which molecular components are assembled together to get more complex assemblies (as shown in Figure 1.1).<sup>1</sup> Lithography, ball milling (mechanical attrition) and reactive-ion etching are examples of top down approaches. Today, lithography is widely used for fabrication of computer chips. However, the top-down approach generally requires expensive techniques (laser ablation, E-beam lithography) and is time consuming.

The bottom-up method involves self-assembly of small molecules, which is easier to achieve. In that approach, growth of particles can be controlled by simple means. Quantum dot formation during epitaxial growth, and nanoparticles synthesis with colloidal dispersions, are few notable examples of the bottom-up approach.

Out of all nanostructured materials, aerogels are well known for their thermal insulation properties.<sup>2</sup> They are defined as quasi-stable, low density, three-dimensional assemblies of nanoparticles.<sup>3</sup> Aerogels possess an attractive collection of useful

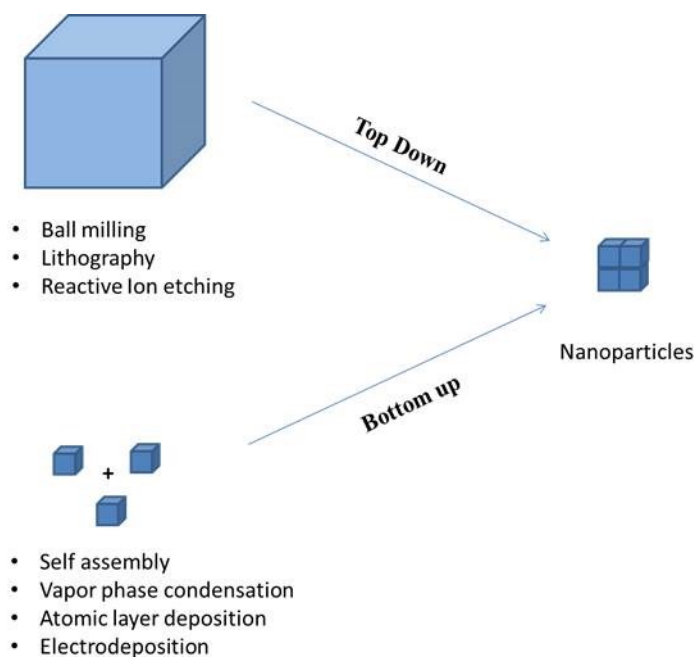


Figure 1.1 Nanofabrication from top-down versus bottom-up assembly

properties, such as high surface area, low thermal conductivity, high acoustic attenuation and low dielectric constants.<sup>4</sup> They were first invented by S. Kistler in the 1930s, whereas he prepared silica aerogels by acidic condensation of aqueous sodium silicate. Silica wet-gels obtained through that process were exchanged with copious amount of ethanol, followed by supercritical fluid extraction to remove the pore-filling solvent. The resultant dry gels did not shrink and retained their original shape.<sup>5</sup> Along with silica, Kistler also synthesized metal oxide and some other organic aerogels derived from cellulose, nitrocellulose, gelatin, agar or egg albumin.<sup>6</sup> Silica aerogels are the most common and well-studied materials in this class. Kistler perceived the potential industrial applications of silica aerogels and eventually commercialized them, through Monsanto Chemical Company. They utilized silica aerogels as thixotropic agents in cosmetics and toothpastes. Development of an inexpensive synthetic procedure for ‘fumed’ silica

(acting as a replacement of silica aerogels) seized the potential market of silica aerogels. Thirty years later, Teichner's group introduced an improved synthetic procedure for silica aerogels by introducing the sol-gel method with alkoxy silane. They used organic solvents in the synthesis, eliminating the time consuming washing steps to form aerogels.<sup>7</sup> The alkoxy silane method triggered research interest in silica aerogels followed by non-silicate inorganic oxides, natural and synthetic organic polymers, carbon, metal and ceramic materials.<sup>8</sup>

## 1.2 SOL-GEL SYNTHESIS OF SILICA AEROGELS

Silica aerogels consist of hierarchical structure of primary and secondary particles (see electron micrograph in Figure 1.2). The 3D-gel network is formed when secondary particles lead to tertiary aggregates. The shape and size of the pores are major contributing factors to the physical properties of silica aerogels.<sup>9</sup> In order to improve these physical properties, fine tuning of nano-porous structure is important. This can be done by understanding the chemistry of gelation which determines the size of primary particles and their assembly.

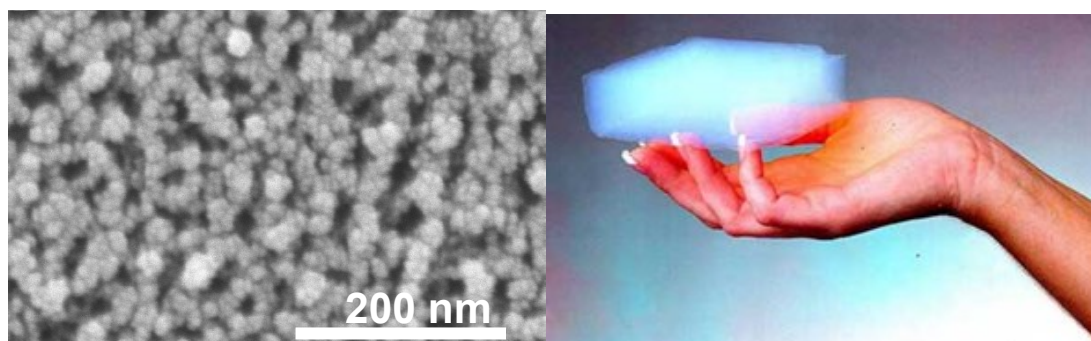


Figure 1.2 The typical nanostructure of a silica aerogel on left and its macroscopic appearance on right.<sup>10</sup>

Silica aerogels are prepared with sol-gel chemistry, where precursors are mixed together to form nanoparticles by hydrolysis. After the percolation threshold is reached, colloidal suspension of primary particles is formed, which is referred as a sol. Reactive primary particles in the sol undergo condensation reaction upon collision and connect with each other in the form of fractal aggregates referred to as secondary particles. Eventually, secondary particles agglomerate to yield three dimensional networks (wet-gel) with high porosity. Figure 1.3 shows the sol-gel synthesis of silica aerogels.

Typically, tetramethylorthosilicate ( $\text{Si}(\text{OCH}_3)_4$ , abbreviated as TMOS) or tetraethylorthosilicate ( $\text{Si}(\text{OC}_2\text{H}_5)_4$ , abbreviated as TEOS) are used for the synthesis of silica aerogels. Those precursors are dissolved in their respective alcohol, which acts as a co-solvent for the silane and water, which is added for hydrolysis.

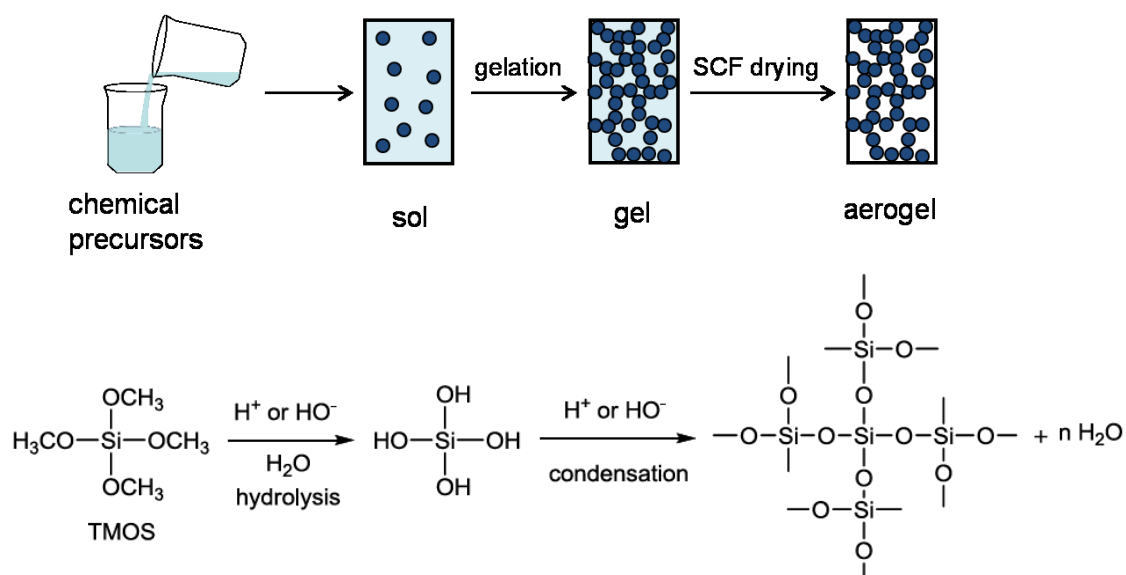


Figure 1.3 Preparation of silica aerogels via the sol-gel process

The first step involved in this process is either an acid- or a base-catalyzed hydrolysis of the alkoxy silane to form silanols, which undergo a condensation reaction *in situ* to form Si-O-Si linkages. The formation of 3D network in silica aerogels follows a sequential order of primary particles, secondary particles and higher aggregates (as shown in Figure 1.3).<sup>11</sup>

The resultant solvent-filled wet-gels are exchanged with alcohol to remove water from the network before drying. Depending upon the drying process, two different types of products are achieved: (a) by evaporation of the entrapped solvent at atmospheric pressure and temperature to form a xerogel, in which extensive takes place leading to a collapsed structure; or, (b) by exchanging the pore filling solvent with supercritical fluid (such as CO<sub>2</sub>) to form an aerogel, in which volume and porous structure of wet gel are retained (as shown in Figure 1.4).

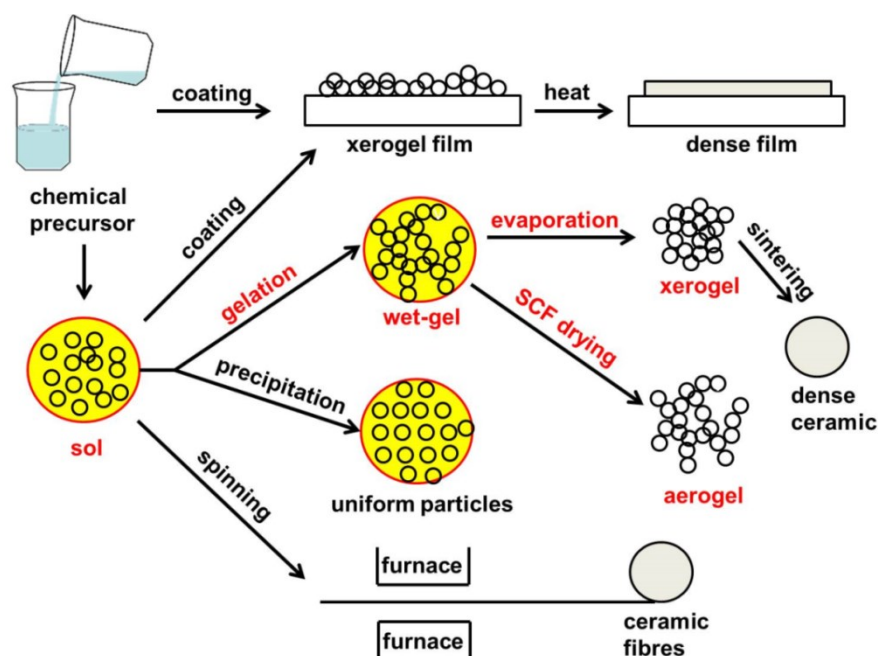


Figure 1.4 Schematic representations of different processing conditions of silica sol

In practice, supercritical drying involves use of an autoclave to replace the gelation solvent with liquid CO<sub>2</sub>, which is then converted to SCF and vented off isothermally (critical point of CO<sub>2</sub>: 31.1 °C at 1072 psi).<sup>12</sup> Figure 1.4 shows a schematic representation of different types of porous networks obtained with drying conditions.

### **1.3 SURFACE MODIFICATION OF SILICA AEROGELS WITH POLYMERS (X-LINKING)**

Intense research efforts in the field of aerogels have led to the development stage, and for the last few decades, more studies are focused on their applications and commercialization. Aerogels have found use in thermal and acoustic insulation,<sup>13</sup> dielectrics,<sup>14</sup> catalyst supports,<sup>15</sup> and as hosts for functional guests in chemical, electronic, and optical applications. Silica aerogels are also used in specialized environments, such as Cerenkov radiation detectors in certain nuclear reactors, aboard spacecraft as collectors for cosmic particles (NASA's Stardust program),<sup>17</sup> and for thermal insulation in planetary vehicles on Mars. Extreme fragility due to narrow interparticle necks is the major limitation in commercialization of silica aerogels.<sup>18</sup>

Leventis *et al.* have resolved the fragility issue by crosslinking aerogels with organic polymers.<sup>20</sup> In that process, silica nanoparticles bearing hydroxyl group on the surface were reacted with isocyanate using polyisocyanates (commercially available N3300A). Polyurethane tethers generated after the reaction, bridges (crosslinked) silica nanoparticles chemically, and reinforces interparticle necks. Conformal coating of polymer is formed on the entire skeletal framework and open pores are retained (Figure 1.5). The resulting materials have been referred to as polymer-crosslinked aerogels (X-aerogels). X-linking increases the flexural strength of an aerogel by 300 times for a nominal increase in density by only a factor of 3.



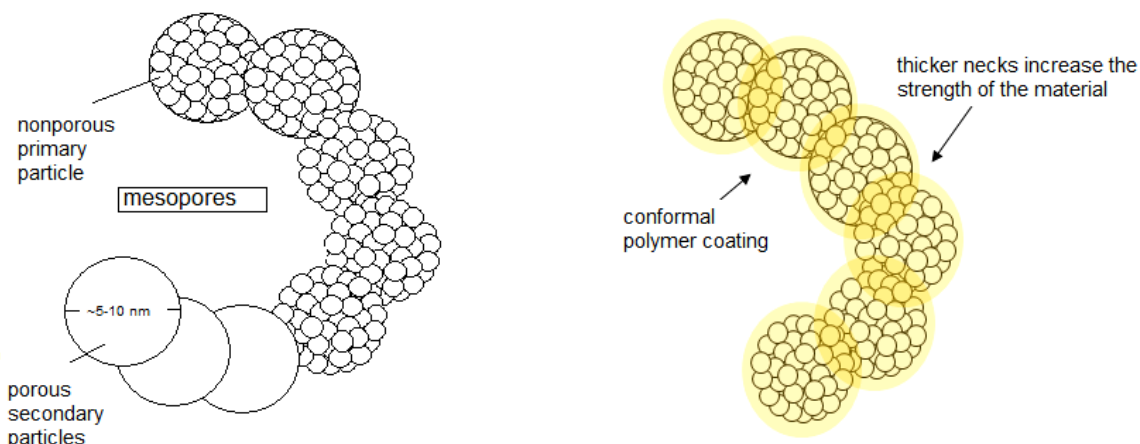


Figure 1.5 A thin polymer layer is formed conformally on the skeletal silica nanoparticles

If other functional groups (apart from hydroxyls) are brought on the surface of silica nanoparticles, then different chemistry can be resorted to form polymer bridges between the particles. This can be achieved by a careful choice of molecular precursors; for silica aerogels. Amine modified silica precursor ((3-Aminopropyl)triethoxy silane: APTES) undergoes hydrolysis at slower rate than Tetramethyl orthosilicate: TMOS, and the surface of silica particles is decorated with  $\text{-NH}_2$  group from APTES.<sup>21</sup> Epoxy resin,<sup>22</sup> polyurea<sup>19</sup> or polystyrene<sup>19</sup> are other alternatives for X-linking in these  $\text{-NH}_2$  group modified aerogels.

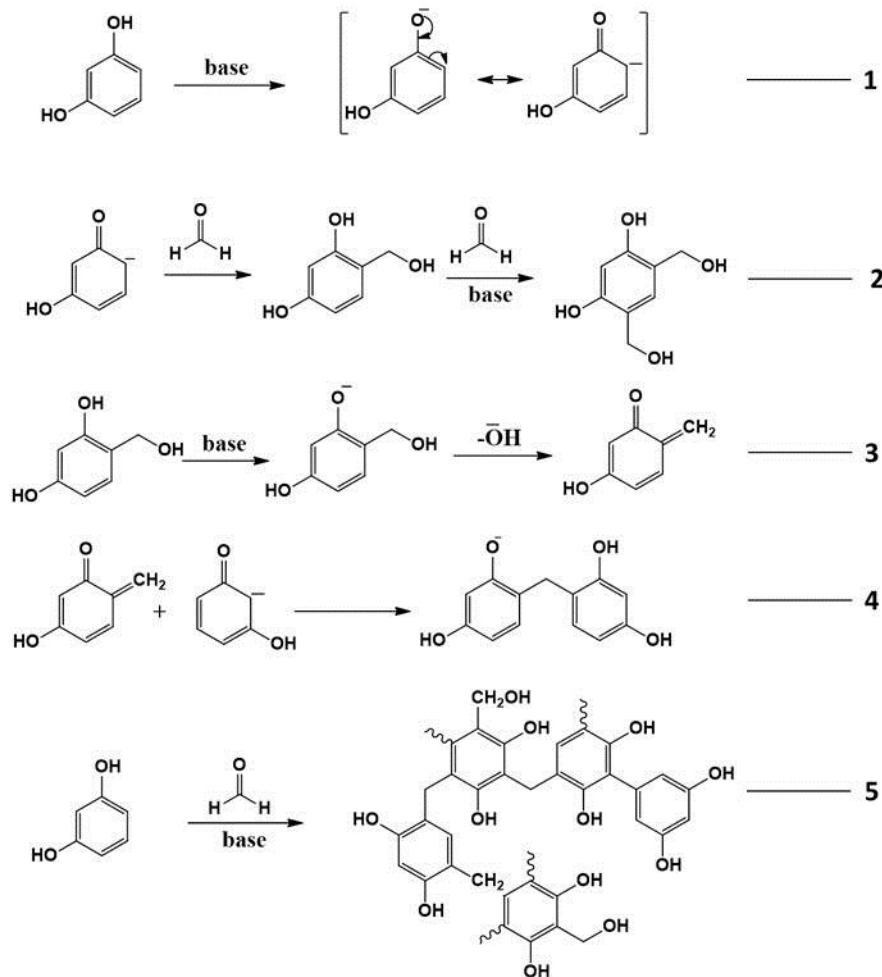
X-aerogels are exceptionally strong in comparison not only with their non-crosslinked counterparts (native aerogels), but also with other materials that are usually considered strong, such as steel, Kevlar and silicon carbide.<sup>20</sup> Since, mechanical strength of X-aerogels is due to the conformal coating of polymers, it would be worth looking into polymer-based aerogels. This lead our group to concentrate on purely organic aerogels derived from different polymers.

## 1.4 ORGANIC AEROGELS DERIVED FROM PHENOLIC CHEMISTRY

**1.4.1 Resorcinol Formaldehyde Aerogels.** Although organic aerogels were reported along with their inorganic counterparts (e.g.; silica) by Kistler in the 1930's,<sup>5b</sup> most development in the next few decades concentrated on silica aerogels. Almost 60 years later, Pekala reinvented organic aerogels in the form resorcinol-formaldehyde (RF) resins.<sup>23a</sup> Those aerogels were introduced as carbon aerogel precursors and for quite some time they were synonymous to organic aerogels. Along the way, it was discovered that RF aerogels have properties equivalent to silica aerogels in terms of surface area ( $> 400 \text{ m}^2 \text{ g}^{-1}$ ), porosity ( $> 80\%$ ) and thermal conductivity ( $0.012 \text{ W m}^{-1} \text{ K}^{-1}$  at  $0.16 \text{ g cm}^{-3}$ )<sup>23b</sup> and they were considered as replacement of silica aerogels.

Following the success of the RF aerogels, other organic aerogels based on phenolic chemistry started appearing such as phenol-formaldehyde, melamine-formaldehyde, cresol-formaldehyde, phenol-furfural.<sup>24</sup> Each of those materials has its own advantages, for example melamine-formaldehyde aerogels are transparent,<sup>24a</sup> cresol-formaldehyde aerogels yield low density carbon aerogels,<sup>24b</sup> and phenol-furfural are prepared in an organic solvent (1-propanol) eliminating washing steps.<sup>24c</sup> Pekala's method was based on polycondensation of resorcinol with formaldehyde in basic aqueous environment ( $\text{Na}_2\text{CO}_3$ ) with water as a solvent. That method has been time consuming (7 days at  $85 \text{ }^\circ\text{C}$ ). With the limitations of the aqueous base-catalyzed route becoming evident, attention started shifting to acid catalyzed processes.<sup>25</sup>

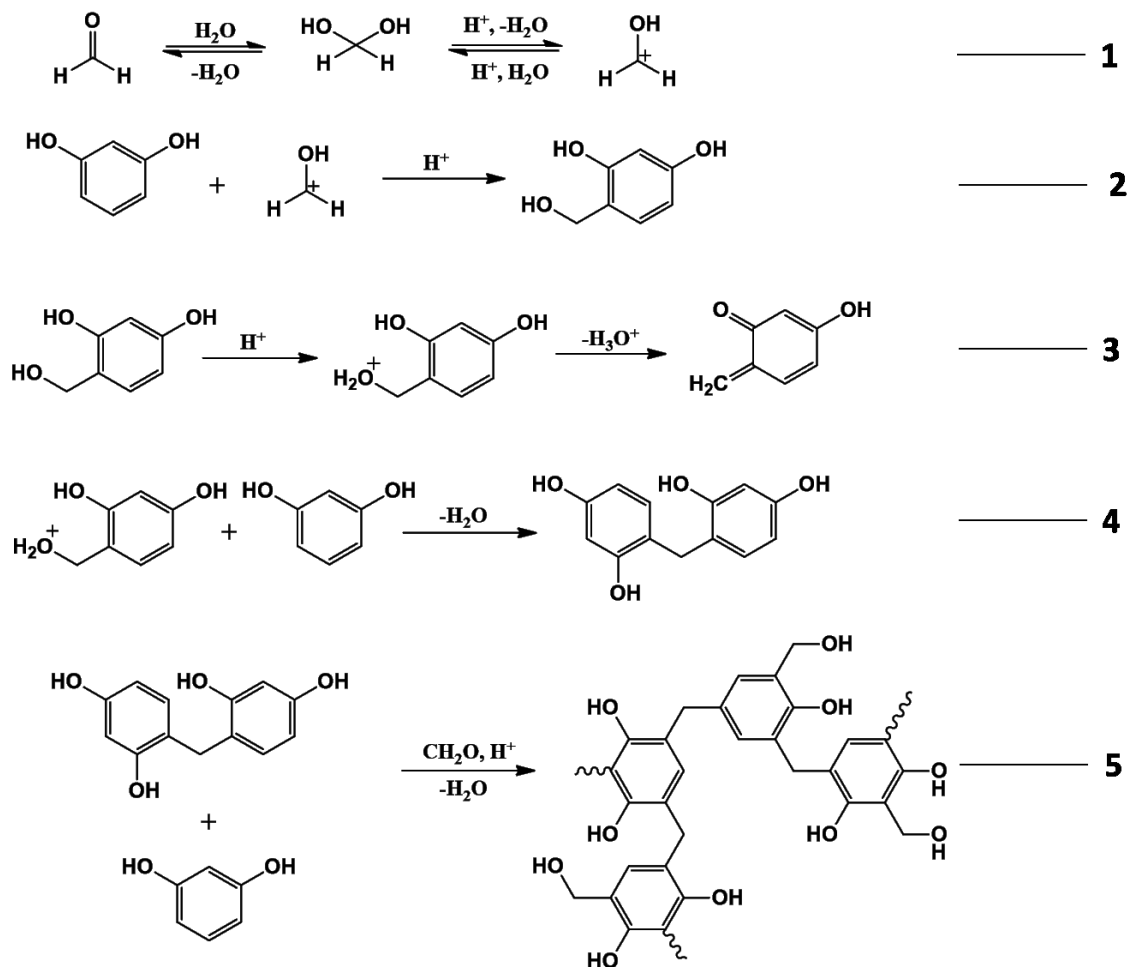
**1.4.2 Base Catalyzed and Acid Catalyzed Gelation of Resorcinol Formaldehyde.** As shown in Scheme 1<sup>26a</sup> in the case of base catalyzed gelation, the resorcinol anion is formed by deprotonation (Scheme 1).

Scheme 1 Mechanism of base catalyzed gelation of RF<sup>26a</sup>

As shown in Scheme 2,<sup>26b</sup> in case of acid catalyzed polymerization, the reaction proceeds via protonation of formaldehyde (step 1), resulting in enhanced electrophilicity of formaldehyde. Protonated formaldehyde is attacked by resorcinol to yield hydroxymethylated product (step 2). In the acidic reaction, *o*-quinone methide formation is easier due to protonation of the hydroxymethylated group (step 3). Methylene bridges are formed at faster rates either through reaction with *o*-quinone methide intermediate

similar to the base-catalyzed mechanism or through direct attack by resorcinol's  $\pi$ -cloud on the protonated hydroxymethylated resorcinol (step 4).

Scheme 2 Mechanism of acid-catalyzed gelation of RF<sup>26b</sup>



The most efficient acid catalyzed gelation (10 min at 80 °C) of RF aerogels was obtained with hydrochloric acid as catalyst in acetonitrile sols.<sup>26b</sup>

For comparison purposes both the acid and base catalyzed gelation processes were monitored with  $^{13}\text{C}$  NMR (Figure 1.6). In the case of the acid-catalyzed reaction, the peak at 29.5 ppm ( $-\text{CH}_2-$  linkages) is due to the condensation product of hydroxymethylated resorcinol with resorcinol. That peak was absent in base catalyzed reaction even after 45 min at 80 °C. In the case of base-catalyzed reaction, a small-intensity resonance appears at around 66 ppm, which is attributed to aromatic  $\text{C}-\text{O}-\text{CH}_2-\text{OH}$ .<sup>27</sup> That observation had led to the conclusion that acid (HCl) causes a more

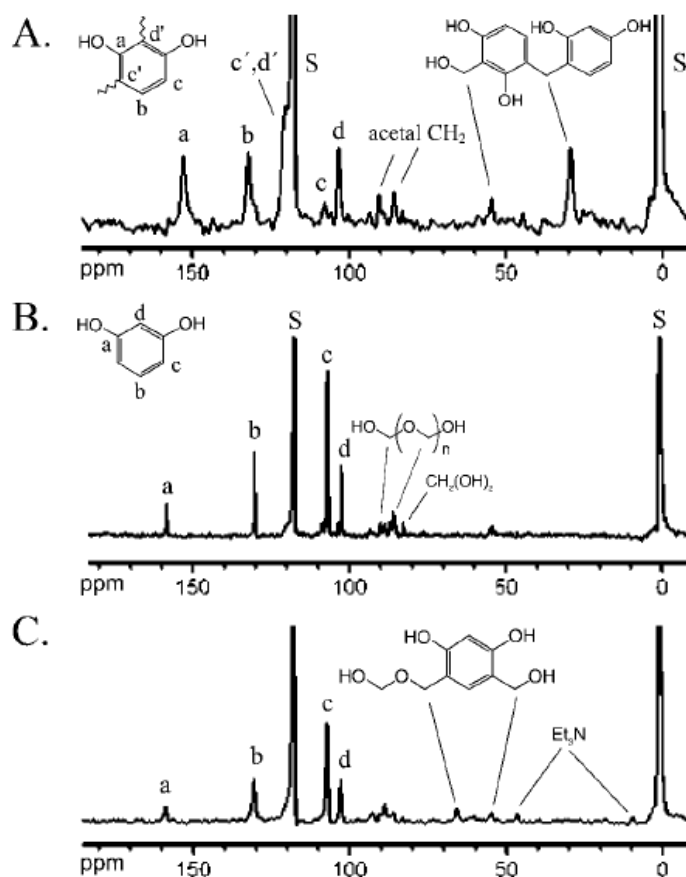


Figure 1.6  $^{13}\text{C}$  NMR of resorcinol-formaldehyde mixtures in 1:2 mol ratio in  $\text{CD}_3\text{CN}$  A: 15 min after mixing, using acid (HCl) catalyst, at RT B: 15 min after mixing, without any catalyst, at RT and C: 75 min after mixing, with base ( $\text{Et}_3\text{N}$ ) catalyst, at 80 °C.<sup>26b</sup>

efficient polymerization than base ( $\text{Et}_3\text{N}$ ). Many other reports also describe acid catalyzed synthesis of RF aerogels,<sup>28</sup> but the vast literature on the base-catalyzed RF process overshadowed the acid-catalyzed route. Recently, Peikolainen group synthesized 5-methylresorcinol-based aerogels in acetonitrile with an organic acid.<sup>29</sup> Organic acid not only catalyzed the reaction, but also got incorporated in the polymer network. That eliminated solvent exchange steps, as there were no unreacted products. Aerogels obtained through acid catalysis are chemically indistinguishable from the base catalyzed ones, but their particle formation and aggregation mechanism differs significantly due to the difference in their growth mechanism.<sup>27</sup> Figure 1.7 depicts the morphological difference between conventional base catalyzed and acid catalyzed RF aerogels.

#### 1.4.3 The Effect of Synthetic Parameters on the Morphology of RF Aerogels.

RF aerogels synthesized via base catalysis have been investigated intensely in terms of the effect of the catalyst and monomer concentration, pH of the solution and solvent effect on their properties.<sup>5c,28b,30</sup> Thus it was found that the resorcinol to catalyst

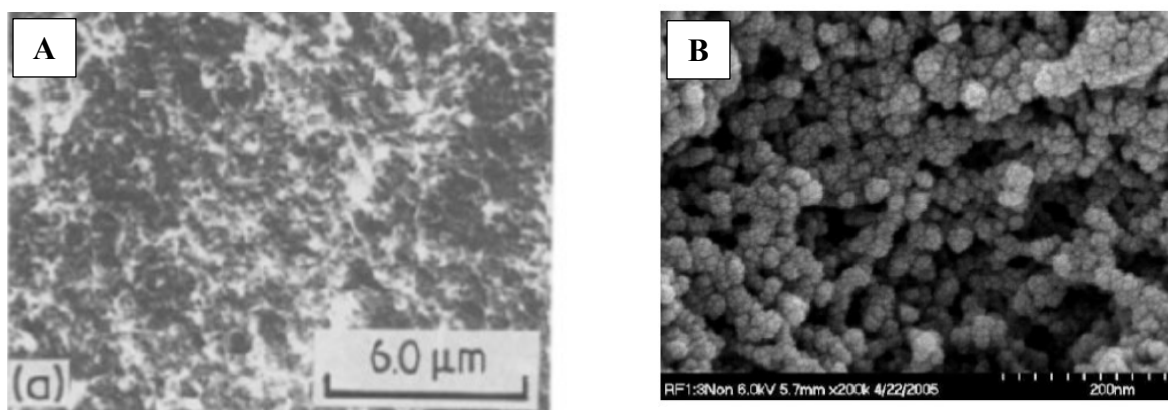


Figure 1.7 SEM of RF aerogels prepared with A: base catalysis ( $0.079 \text{ g/cc}$ )<sup>23a</sup> and B: acid catalysis ( $0.175 \text{ g/cc}$ ).<sup>26b</sup>

ratio (R/C) is the major contributing factor in determining the morphology of the RF aerogels, which affects their surface area, mechanical properties and thermal conductivity.<sup>31</sup>

Aerogels prepared with high concentration of catalyst (e.g., R/C = 50) consist of smaller particles in the range of 3-5 nm connected with wider necks, whereas the ones with low catalyst concentration (R/C = 200) form larger particles (11-14 nm) and they are referred to as colloidal RF aerogels (Figure 1.8).<sup>32</sup> Along with the catalyst ratio, chemical identity of the catalyst ( $K_2CO_3$ ,  $KHCO_3$ , and  $NaHCO_3$ ) has also been responsible for the particle size.<sup>30</sup> The development of cross-linking in RF aerogels, has not only provided mechanical strength, but has also increased the char yield (% mass left after pyrolysis).

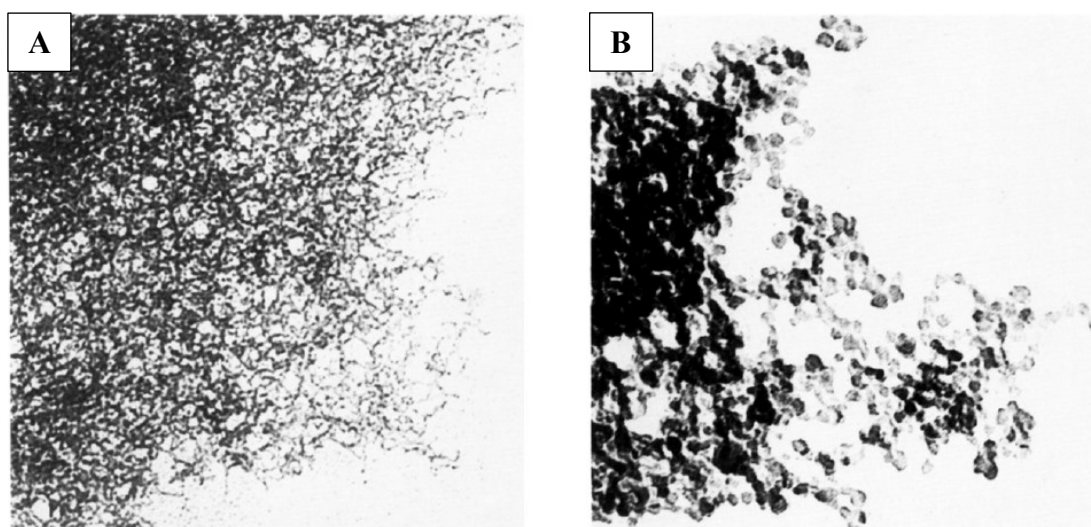


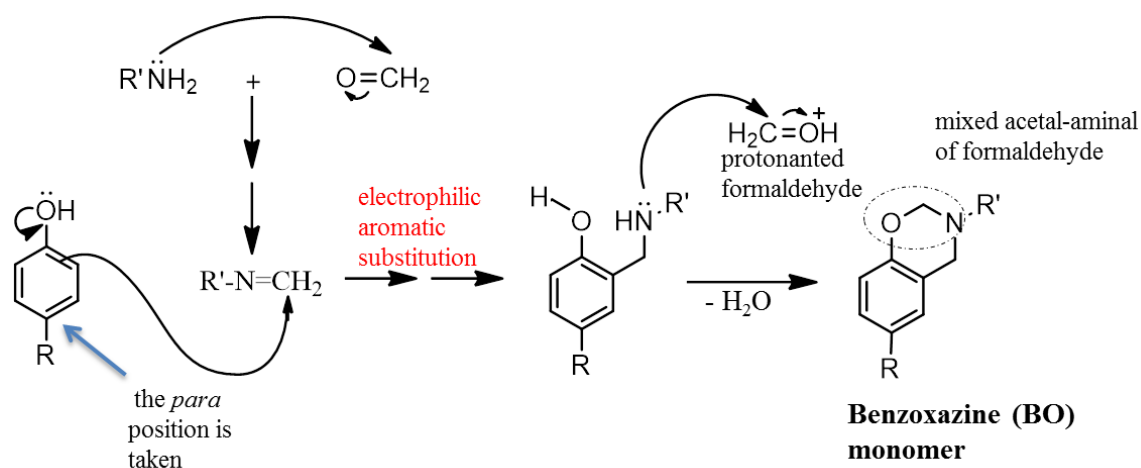
Figure 1.8 TEM of RF (10% w/w) aerogels prepared with base catalyst ( $Na_2CO_3$ ) at both A. low catalyst (R/C = 300) and B. high catalyst (R/C = 50) concentration.<sup>32</sup>

Overall, the phenolic chemistry is well known for its cost-effective raw materials. In order to improve the properties of phenolic aerogels further without increasing the cost

of processing, one should resort to more cross-linked structures within the same class. Thus, in the quest of such materials, a new class of phenolic aerogels is emerged in the last few years, which is based on polybenzoxazines.

**1.4.4 Polybenzoxazine Chemistry.** Benzoxazines were first synthesized by Cope and Holy in 1940s.<sup>33</sup> Burke *et al.* developed several small molecular weight benzoxazines and contributed towards the fundamental understanding of benzoxazine chemistry.<sup>34</sup> Schreiber and Higginbottom independently reported use of benzoxazine oligomers in coatings.<sup>35</sup> Though benzoxazine monomer has been invented in 1940's, detailed studies on the properties of polymer derived from benzoxazine were reported recently by Ishida and Ning.<sup>36</sup> Benzoxazine monomers (BO monomer) are obtained from the condensation reaction of phenolic derivatives, amine and formaldehyde via a Mannich reaction (Scheme 3)<sup>33,34</sup> X-Ray crystallography shows that the benzoxazine ring prefers a distorted semi-chair conformation (Figure 1.9).

Scheme 3 General reaction pathway for the synthesis of benzoxazine monomers<sup>33,34</sup>





Therefore, ring-opening under certain conditions relieves strain.<sup>37</sup> The strong basicity of the N and O atoms makes ring-opening favorable via a cationic mechanism.<sup>38</sup> Reiss et al. described reaction kinetics for the oligomer formation with monofunctional benzoxazine.<sup>39</sup>

To facilitate synthesis, Ishida introduced a solventless synthetic method of the preparation of benzoxazine monomers, whereas all the reactants (phenol, paraformaldehyde and amine) are mixed together and heated at 85-140 °C.<sup>40</sup> That method generates small amount of dimer, some oligomers and leaves some unreacted phenol as impurity which acts as initiator for polymerization after heating above 150 °C. The generally accepted mechanism for the ring opening reaction by phenol or oligomers of benzoxazine is given in Scheme 4.

It is found that the benzoxazine ring reacts preferentially with the *ortho* positions of free phenolic compounds to form a dimer with a Mannich base bridge structure. The polymer obtained by the heat induced route is cost effective in terms of materials, but requires longer times and high temperatures.



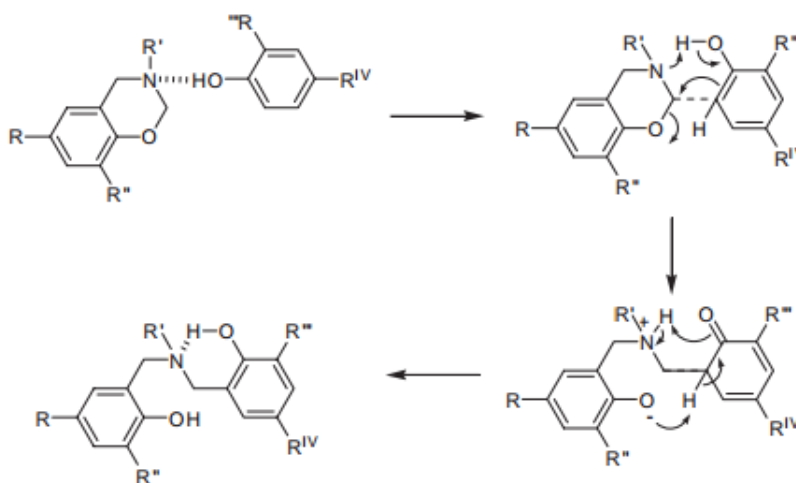
Figure 1.9 Chemical structure of 3,4-dihydro-6-methoxy-3-methyl-2H,4H-benzo[e]1,3-benzoxazine (left) and corresponding crystal structure (right) showing semi chair conformation.<sup>37</sup>

Catalyst-assisted polymerization routes are therefore studied in order to reduce polymerization temperature and to accelerate the reaction rate.<sup>38,41</sup> Mechanistic studies of cationic polymerization suggest that, in the presence of Lewis acids or nucleophilic catalysts, (such as metal halides, triflic acid) ring opening of benzoxazine takes place faster giving N,O-acetal kind of linkages. Those acetal linkages decompose upon heating and rearrange into a true phenolic Mannich type bridge structure.<sup>38,42</sup>

Along those lines, Sebastián and co-workers proposed a reaction pathway for catalyst-assisted ring opening polymerization of benzoxazines on the basis of <sup>1</sup>H NMR.<sup>42b,42c</sup> Their study shows that, the catalyst should have an active cationic part for ring opening, and a good leaving anionic part to complete polymerization.

However, due to the complexity in the <sup>1</sup>H NMR spectra in the aromatic region, none of their reports specify a particular pathway but instead they claim that all of the possible reactions happen simultaneously and eventually lead to a structure similar to that

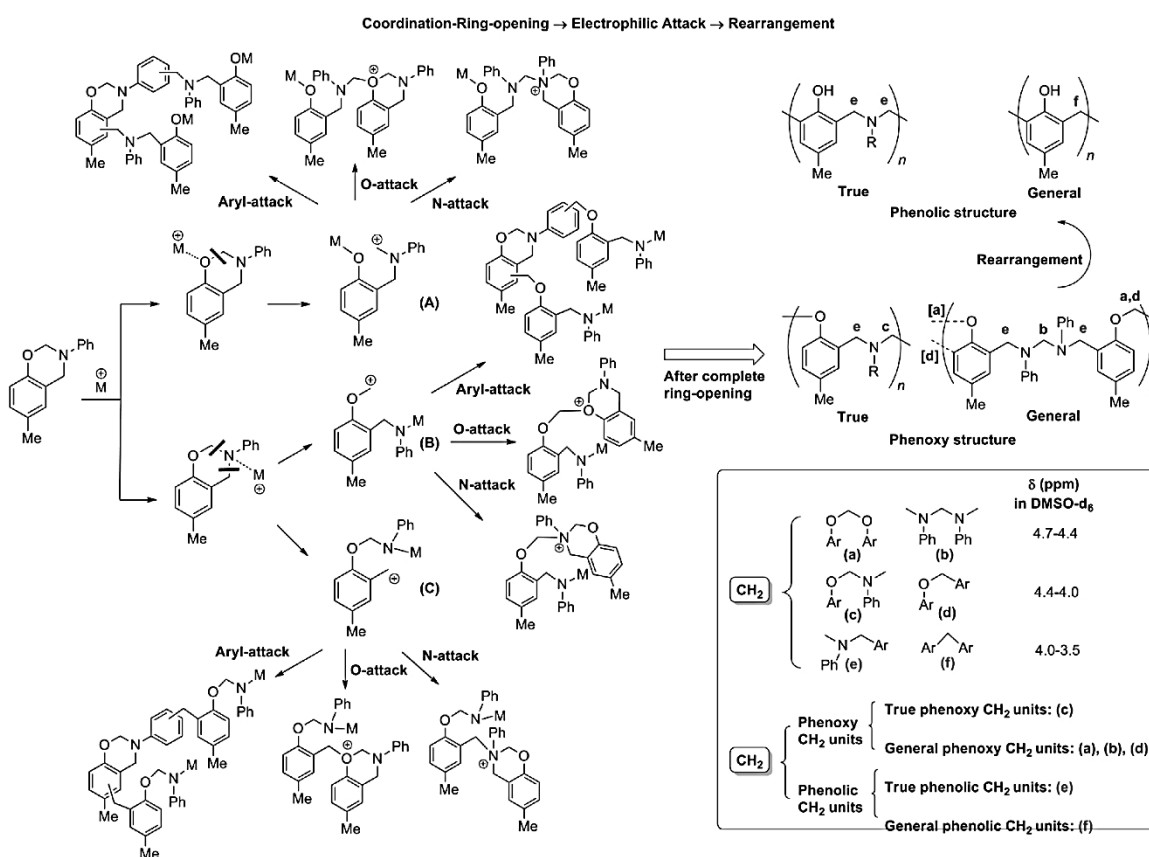
Scheme 4 Proposed mechanism of ring opening of benzoxazine via phenolic or oligomeric impurities in heat induced polymerization



of heat-induced polymerization. Scheme 5 summarizes Sebastian's reaction pathways for ring opening and polymerization of benzoxazine with active catalyst.

Polybenzoxazines (PBO) are suitable for replacement of traditional phenolic resins. They possess unique properties such as good thermal, chemical, and mechanical properties, flame retardancy, low water retention, high char yield, near zero shrinkage upon polymerization, and high glass transition temperature ( $T_g$ ). All those properties make them comparable to other high performance polymers.<sup>44</sup> In addition, PBOs gained

Scheme 5 Proposed reaction pathway for ring opening reaction of benzoxazine<sup>42b,42c</sup>



immense interest because of their provided flexibility in molecular design, and their cost effective raw materials. Part of current research concentrates on porous polybenzoxazines.<sup>43</sup>

**1.4.5. Porous Polybenzoxazines.** The first effort in that regard was made by Kumar and co-workers in 2008 for the synthesis of PBO foams with the help of glass microballoons. Incorporation of silica fibers in those foams increased shock absorbing properties as well as the thermal and thermoxidative properties.<sup>43a,43b</sup> Later in 2009, Lorjai et al. proposed a cost effective way to make polybenzoxazine foam with the use of azocarbonamide (AZD) as a foaming agent instead of expensive glass microballoons. AZD decomposes at the curing temperature of polybenzoxazine and generates pores in the network.<sup>43c</sup> PBO foams derived from AZD show better compressive strength than foams with microballoons.<sup>43c</sup> Figure 1.10 compares microscopic properties of benzoxazine foams obtained through both routes. Chang and co-workers synthesized porous polybenzoxazines using a templating method with poly( $\epsilon$ -caprolactone) (PCL) as a labile constituent.

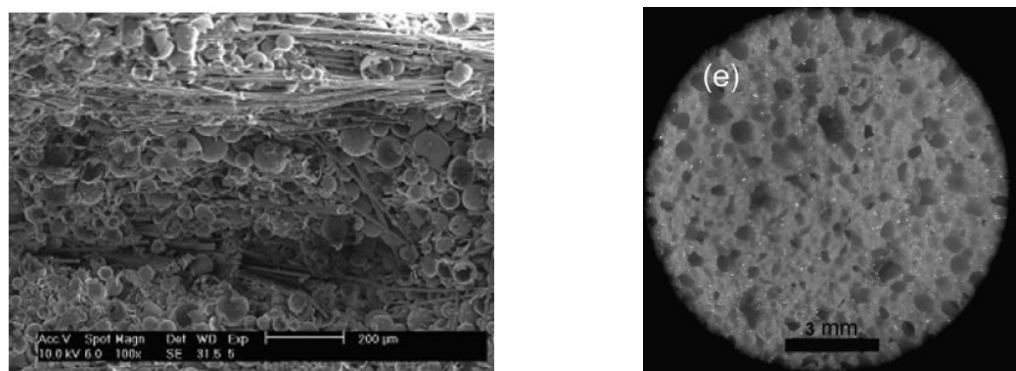
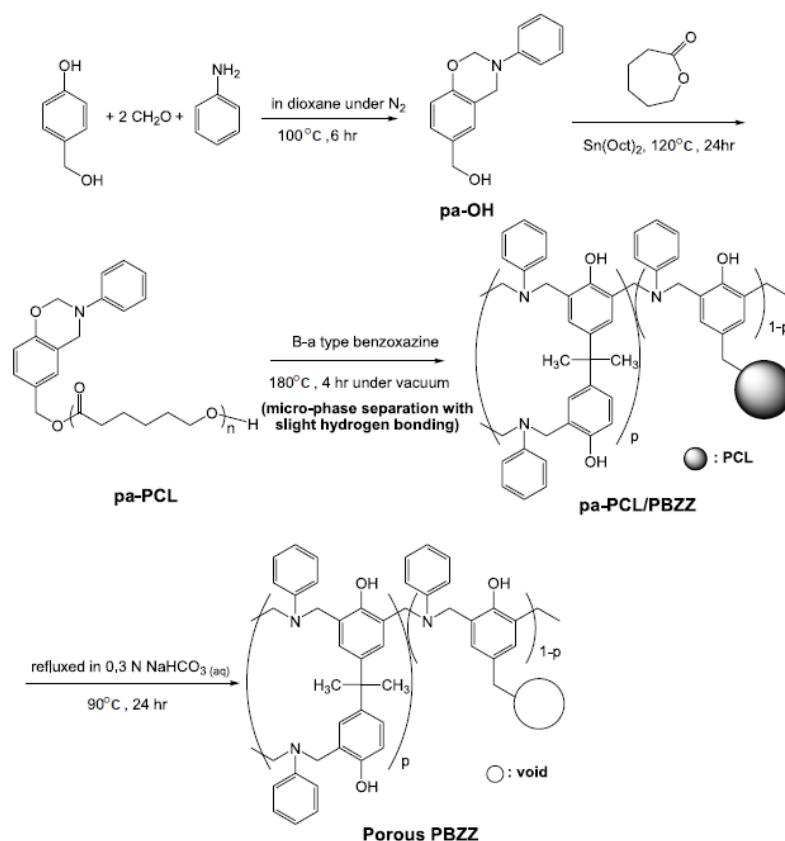


Figure 1.10 Polybenzoxazine foams obtained with glass microballoons and silica fibers (left)<sup>44b</sup> and with azocarbonamide foaming agent (right).<sup>44c</sup>

For this, 4-Hydroxybenzyl alcohol-based benzoxazine was modified with PCL; the resulting product was referred to as pa-PCL. Uniform dispersion of PCL was then achieved via copolymerization of pa-PCL with B-a type (Ishida's Bisphenol A and aniline based) benzoxazine. Uniformly distributed pores are generated by elimination of PCL with  $\text{NaHCO}_3$  hydrolysis, (Scheme 6).<sup>43d</sup> Zheng *et al.* prepared short-range-ordered (Figure 1.11) and Lorjai and co-workers further extended their porous polybenzoxazine into PBO aerogels, and studied their conversion to porous carbons.<sup>43h</sup> PBO aerogels via the heat-induced polymerization method were found to be more thermally stable than the bulk polymer.<sup>45</sup>

Scheme 6 Synthesis of pa-OH, pa-PCL, pa-PCL/PBZZ and schematic representation of the generation of nanoporous PBZZ films from phase-separated polymers<sup>44d</sup>



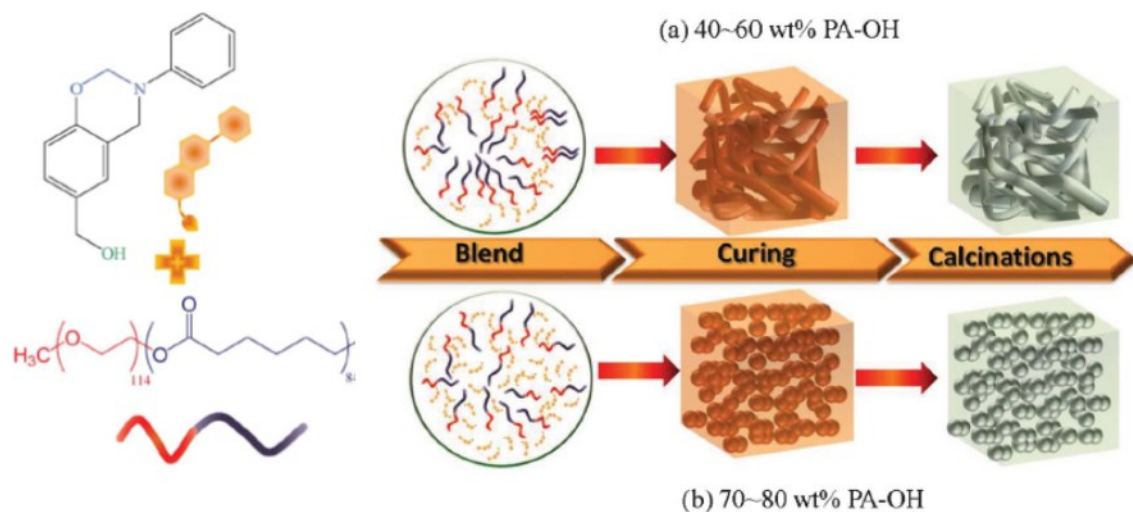


Figure 1.11 Morphological changes in the self-assembled nanostructures and mesoporous polybenzoxazines with different polybenzoxazine contents.<sup>43f</sup>

BO monomer prepared via the Ishida's solventless synthetic method was very effective for the synthesis of PBO aerogels as described by Lorjai. However, long gelation times and high temperatures (1-4 days, 130 °C, respectively) were major disadvantages of that method.

As reviewed above, ring opening of benzoxazine is faster when cationic initiators or Lewis acids are used. Inspired by those reports, we have explored acid catalyzed gelation of PBO aerogels in the first part of the thesis. Acid catalyzed polymerization reduced the gelation time from several days to a couple of hours, and the process was carried out at room temperature. Chemically, they are found to be somewhat different from conventional heat-induced aerogels, and possess better properties in terms of surface area and thermal stability. The polybenzoxazine aerogels surface resembles the

extracellular matrix in bone, hence they were evaluated for the biocompatibility by Rubenstein and co-workers.<sup>46</sup>

## 1.5 CARBON AEROGELS

Carbon aerogels have been pursued for their good electrical conductivity and thermal stability combined with high surface area, and porosity. They are generally derived from thermal treatment (pyrolysis) of different organic aerogels in inert atmosphere.<sup>47</sup> Porous carbons are used for separations,<sup>48</sup> hydrogen storage,<sup>49</sup> CO<sub>2</sub> adsorption,<sup>50</sup> catalyst supports,<sup>51</sup> and as electrodes for lithium ion batteries and supercapacitors.<sup>52</sup> Knox and co-workers developed templated synthesis of porous carbons with uniform distribution of pores.<sup>53</sup> Since then, many inorganic templates have been used for that purpose, such as mesoporous silica, zeolites, clays, silica sols, gels and opals and metal organic frameworks.<sup>54</sup> Figure 1.12 depicts a brief review of the templated synthesis of porous carbons. In addition to the extra cost, one of the major disadvantages of templated synthesis is the extra step needed to remove the template. To avoid that time-consuming process, direct pyrolytic conversion of organic aerogels has proved to be an effective route to nanoporous carbon aerogels.

However, it is difficult to obtain uniformly distributed pores through pyrolytic conversion of organic aerogels. Most of the time, mixtures of micro, meso, and macropores are obtained. However, that in fact is an advantage, as it is more often than not desirable to have multiscale porosities rather than orderly distribution of pores.<sup>55</sup> One can tune the structural properties of RF derived carbon aerogels by varying catalyst-to-resorcinol ratio or the monomer concentration (R+F).<sup>28b, 28c, 28d, 28e, 29</sup> Figure 1.13 shows the carbon aerogel morphology obtained by using different catalysts.

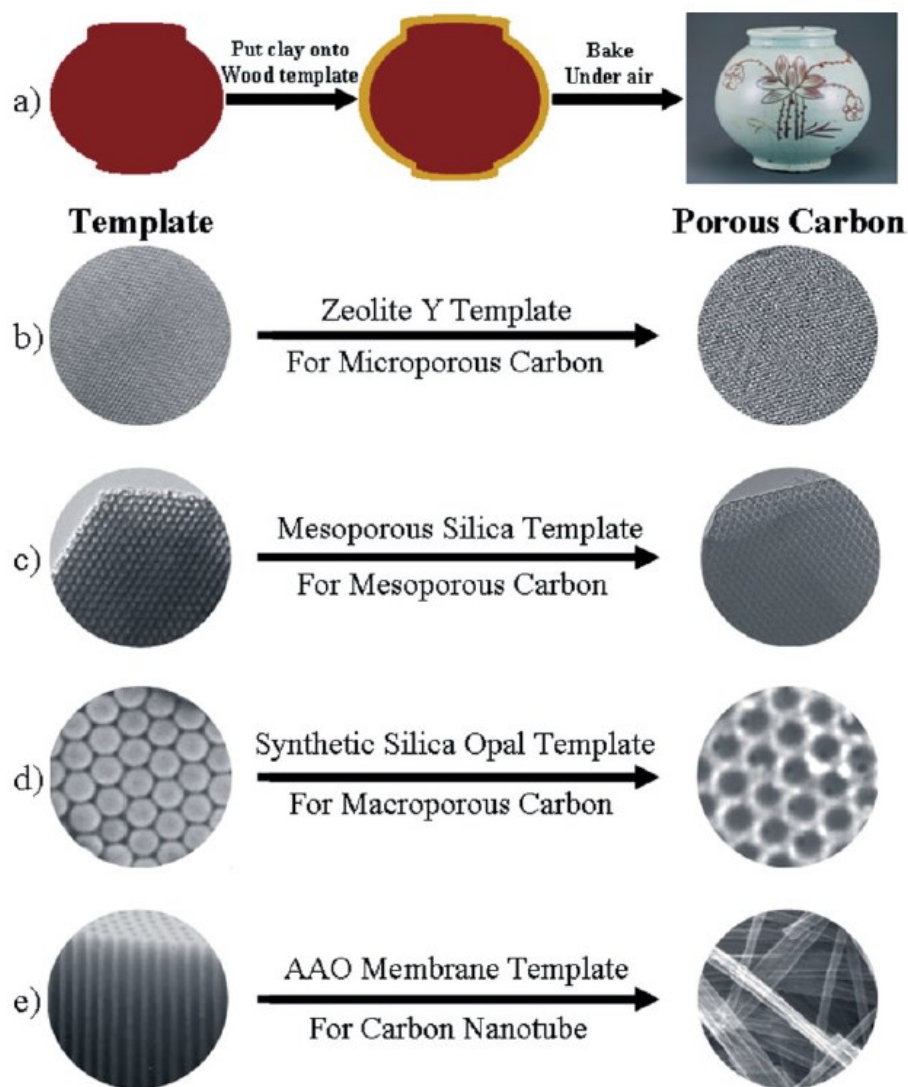


Figure 1.12 Schematic representation showing a) the concept of templated synthesis b) microporous, c) mesoporous and d) macroporous carbon materials and e) carbon nanotubes were synthesized using zeolite, mesoporous silica, a synthetic silica opal, and an anodic aluminum oxide (AAO) membranes as templates, respectively.<sup>47</sup>

dissolves in the solvent while washing and results in permanent swelling of X-linked

Apart from RF, other phenolic aerogels have also been explored extensively to reduce the cost of manufacturing for carbon aerogels. Li and co-workers evaluated a cresol mixture (*m*-cresol, phenol, *o*-cresol and *p*-cresol) for low density carbon aerogels. Isomers of



cresol react in different way, for example, a linear polymer is obtained through reaction of *o*- and *p*-cresol with formaldehyde and X-linked structure is obtained when phenol and *m*-cresol reacts with formaldehyde. Linear polymer thus obtained structure and decreasing bulk density further.<sup>57</sup>

Carbon aerogels doped with nitrogen (2.80 % w/w) are obtained with phenolic resole and methylated melamine.<sup>58</sup> Resorcinol furfural derived carbons had smaller particles (in the range of 20-30 nm) and possess higher surface area (698-753 m<sup>2</sup> g<sup>-1</sup>) than RF derived carbon aerogels. Scheme 7 shows the polymerization of resorcinol and furfural in the presence of base catalyst.<sup>59</sup>

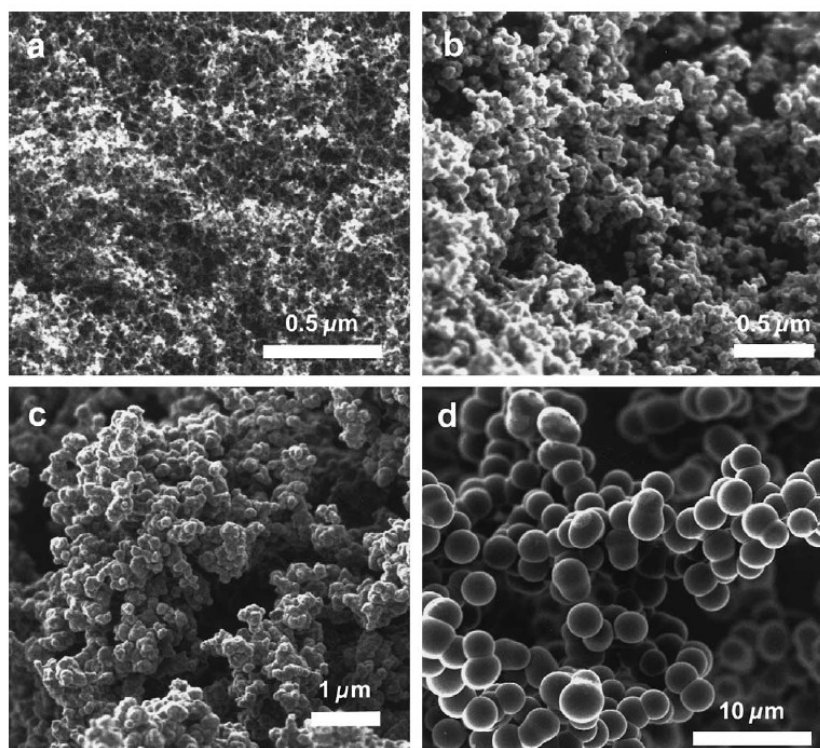
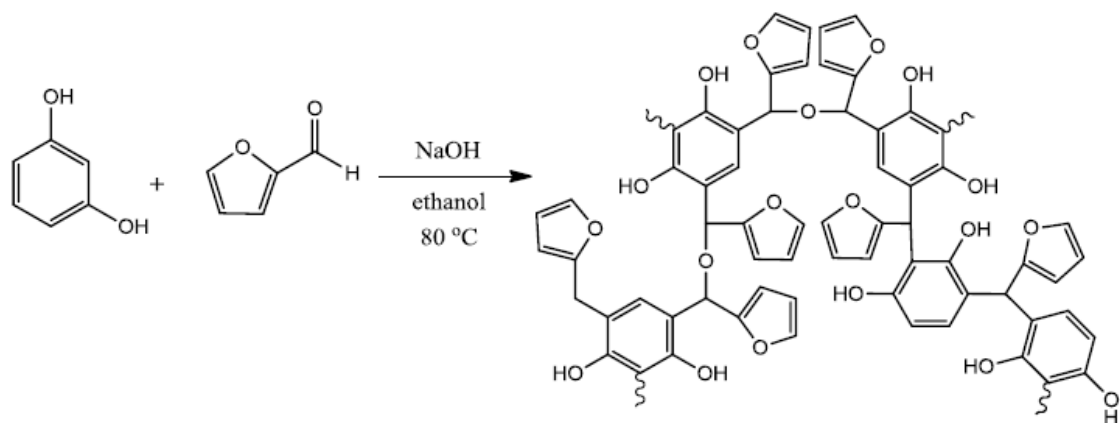


Figure 1.13 SEM images of carbon aerogels obtained through: a) Na<sub>2</sub>CO<sub>3</sub> catalyst (R/C = 300, 5% w/w); b) low catalyst (R/C=1500, 30% w/w); c) acid catalyst (65% aq. Nitric acid, R/C = 30, 15% w/w); d) prepared from Ocellus (type of bacteria).<sup>56</sup>

Fu *et al.* developed a phenol-furfural route to carbon aerogels via a two-step process. The first step involved formation of a pre-polymer with the reaction of phenol and furfural in the presence of NaOH. Later, HCl is added to cause gelation of the precursor. Organic aerogels thus obtained had higher yield in terms of polymerization and carbonization, but more shrinkage encountered due to the increased crosslinking density.<sup>60</sup>

Recent reports have involved use of naturally occurring chemicals such as tannin and lignin as replacement of resorcinol. The cost of carbon aerogels obtained through those materials was reduced by 5 times.<sup>61</sup> Tannin-derived carbon aerogels in different pHs showed porosities ranging from 85-95%. The mesopore fraction in those materials can be tuned by changing the pH of the sol. Surface areas as high as 715 m<sup>2</sup> g<sup>-1</sup> were reported through that route for carbon aerogels. Figure 1.14 shows nitrogen sorption isotherms and pore size distributions of carbon aerogels.<sup>61</sup>

Scheme 7 Reaction of resorcinol and furfural catalyzed with NaOH in ethanol<sup>60</sup>



Apart from phenolic resins, many other polymers such as polyurethanes,<sup>62</sup> aromatic polyureas,<sup>63</sup> polyacrylate, polyacrylonitrile,<sup>64</sup> and polyimides<sup>65</sup> have been used to prepare carbon aerogels. Biesmans et al. developed polyurethane-based macroporous carbons, using oligomeric alcohols. Polyurethane network obtained is collapsed during pyrolysis resulting in macroporosity, with surface area of  $77 \text{ m}^2 \text{ g}^{-1}$ .<sup>62</sup> Polyacrylonitrile is the high yield carbonizable polymer and primary industrial source to produce graphite fiber. Dao *et al.* have used polyacrylonitrile carbon aerogel for electro-polymerization of aniline and further utilized them as supercapacitors.<sup>64a</sup> Leventis et al. introduced water-based emulsion-gelation of polyacrylonitrile and demonstrated graphitic aerogels by heat treatment of carbon aerogels.<sup>64b</sup> In other recent work, PAN fibers were introduced in the organic networks (Resorcinol-formaldehyde, RF) and were pyrolyzed in situ to obtain sturdy yet flexible network of carbon aerogels.<sup>64c</sup> In spite of all these efforts to reduce the cost of carbon aerogels, RF aerogels are still the primary commercial source of carbon aerogels.

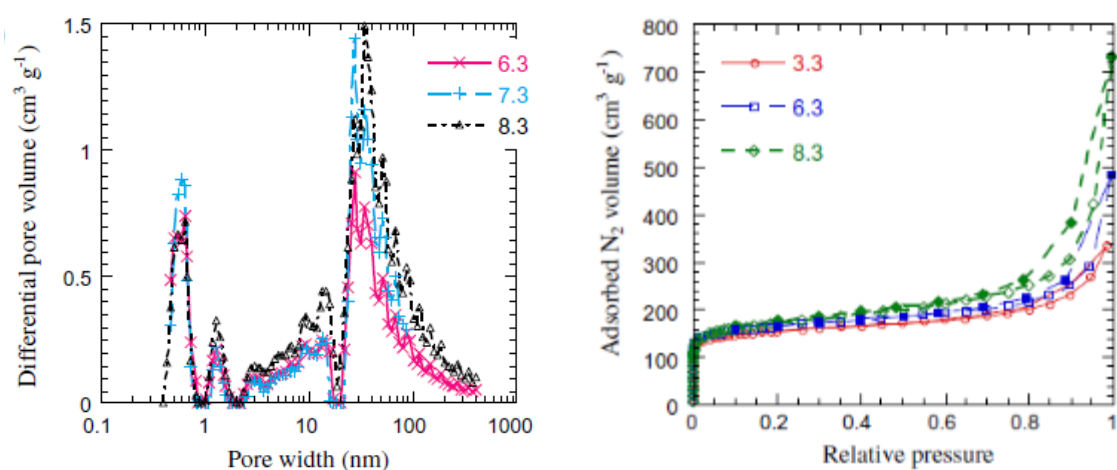


Figure 1.14 Nitrogen sorption isotherms (left) and pore size distribution from DFT method (right) of carbon aerogels derived from tannin-formaldehyde at different pH value.<sup>61</sup>

On the other hand, as a new class of phenolic resins, polybenzoxazines give high char yields than RF and utilize cheaper raw material e.g. bisphenol-A (\$ 36/g, Acros Organics catalogue no. AC15824-5000) than resorcinol (\$ 68/g, Acros Organics catalogue no. AC13229-0050). Figure 1.15 shows the thermo-gravimetric analysis of polybenzoxazine aerogel showing the high yield conversion to carbon upon pyrolysis. Clearly, they are good candidates for replacing traditional RF aerogels for the production of porous carbons. In addition, PBO derived carbon aerogels are evaluated for CO<sub>2</sub> absorption,<sup>44c</sup> supercapacitors,<sup>44h</sup> and as catalyst supports.<sup>52,66</sup>

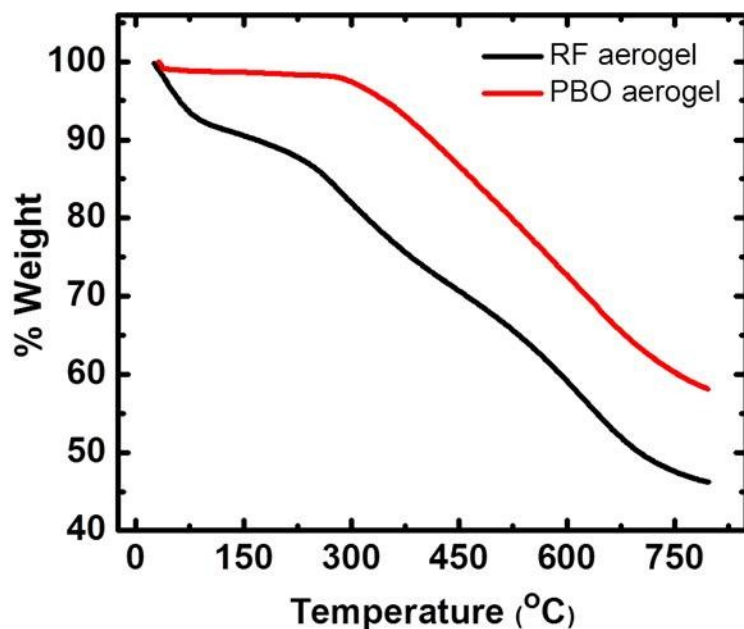


Figure 1.15 Thermo-gravimetric analysis (TGA) of polybenzoxazine and RF aerogels.

In the first part of thesis, it has demonstrated that acid-catalyzed polybenzoxazine aerogels can be converted to porous carbons with yet higher char yield (51% w/w vs 57% w/w) than reported in the literature.<sup>45</sup> Surface areas obtained for all carbon aerogels

derived from acid-catalyzed PBO aerogels are comparable to RF-derived carbon aerogels. Cheaper raw materials, time efficient synthesis, higher char yields and sturdiness of the resultant carbons are the main advantage of acid catalyzed PBO aerogels. All these properties renders PBO aerogels potential candidates for replacing conventional RF aerogels commercially in carbon aerogels production.

## 1.6 POROUS METALS FROM AEROGELS

Typically, porous metals result from using templating,<sup>67</sup> chemical vapor deposition (CVD),<sup>68</sup> alloying-dealloying,<sup>69</sup> and combustion-synthesis methods.<sup>70</sup> In particular, colloidal crystal templating is the most commonly used method for the formation of ordered macroporous metals: metals are deposited on a template (e.g., silica, polystyrene, latex, surfactant assemblies) either by precipitation, filtration or electroless plating.<sup>67</sup> Subsequently, the template is removed either by heat treatment (in case of polystyrene) or with 2% HF solution treatment.

Plating fits well with electroless processes, which are inexpensive and amenable to industrial production of macroporous metals.<sup>67a, 71</sup> Figure 1.16 shows formation of macroporous gold by electroless deposition using colloidal silica as the templating agent, which later was removed with HF.<sup>67a</sup> In another approach, Mann *et al.* used dextran as a sacrificial template for the fabrication of silver and gold sponges. For that, a dextran solution was mixed with a concentrated metal ion precursor solution to form a gel (or a paste), which was subjected to heat treatment (500-900 °C) that causing reduction and eventually formation of a metal sponge.<sup>70</sup>

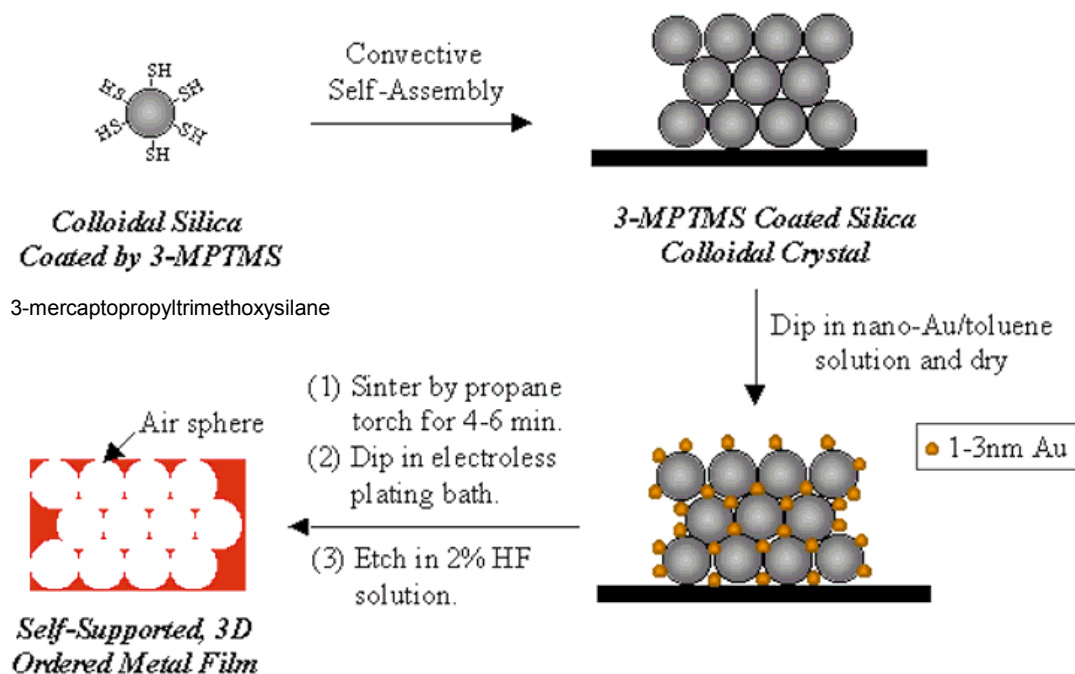


Figure 1.16 Formation of macroporous metals by gold nanocrystal-catalyzed electroless deposition.<sup>67a</sup>

Mann's method is inexpensive, facile, environmentally benign and easy to scale up. The same group also demonstrated fabrication of a magnetic foam with iron oxide nanoparticles and dextran solution.<sup>70</sup> Figure 1.17 shows representative scanning electron micrographs of silver and maghemite ( $\gamma\text{-Fe}_2\text{O}_3$ ) sponges.<sup>70</sup>

Mesoporous metals are mainly obtained via electrochemically driven dealloying of binary alloys, and they are pursued because of their high yield strengths relative to their macroporous counterparts.<sup>69</sup> Along the same line of reasoning, selective leaching of one phase from biphasic composites leads to macroporous metals, or metal-oxides.<sup>72a</sup> Figure 1.18 shows a schematic representation for the synthesis of porous metals and ceramics.

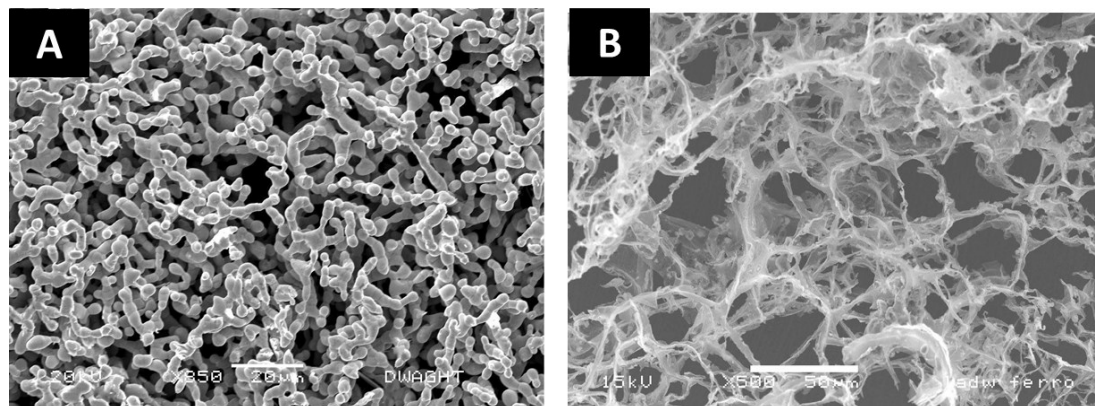


Figure 1.17 Scanning Electron micrograph (SEM) of A: Silver sponge monolith prepared at 520 °C B: Maghemite ( $\gamma\text{-Fe}_2\text{O}_3$ ) sponge prepared at 600 °C using the dextran templating method.<sup>70</sup>

More recently, high surface area, porous noble metals were reported from the reduction of metal precursors with  $\text{NaBH}_4$  or hydrazine, at room temperature.<sup>73</sup> Also, rapid combustion of metal complexes with energetic ligand such as bistetrazolamine (BTA) in inert atmosphere produced low density ( $0.011 \text{ g cm}^{-3}$ ) monolithic metal foam (Fe, Cu, Co and Ag).<sup>74</sup> Figure 1.19 shows an optical photograph and a TEM image of an iron foam, produced by rapid combustion of metal complexes with energetic ligands.<sup>74</sup> On the same basis, Yang *et al.* introduced a sol-gel auto-combustion method to overcome safety issues associated with combustion of energetic ligands.<sup>75</sup>

In the field of nanoporous foams classified as aerogels, there are quite a few reports on non-supported porous monolithic metals. Armor *et al.* synthesized the first metallic copper aerogels from cupric acetate and water followed by hypercritical removal of the pore-filling solvent (methanol at 270 °C).<sup>76</sup> That method was extended to metallic gold and Cu/Pd alloys.<sup>76</sup>

More recently, platinum, gold, and silver aerogels were synthesized via destabilization of colloidal solutions of the metal,<sup>77</sup> and copper nanowire aerogels were made via freeze-drying of copper nanowire solutions.<sup>78</sup> Gold, silver, palladium, platinum, copper, nickel, bismuth and some mixed alloys are pursued mainly for their applications in catalysis,<sup>69</sup> fuel cells,<sup>79</sup> electrodes for ultrasensitive quartz crystal microbalance,<sup>80</sup> sensors,<sup>81</sup> actuators,<sup>82</sup> and antibacterial biofiltration membranes.<sup>73</sup>

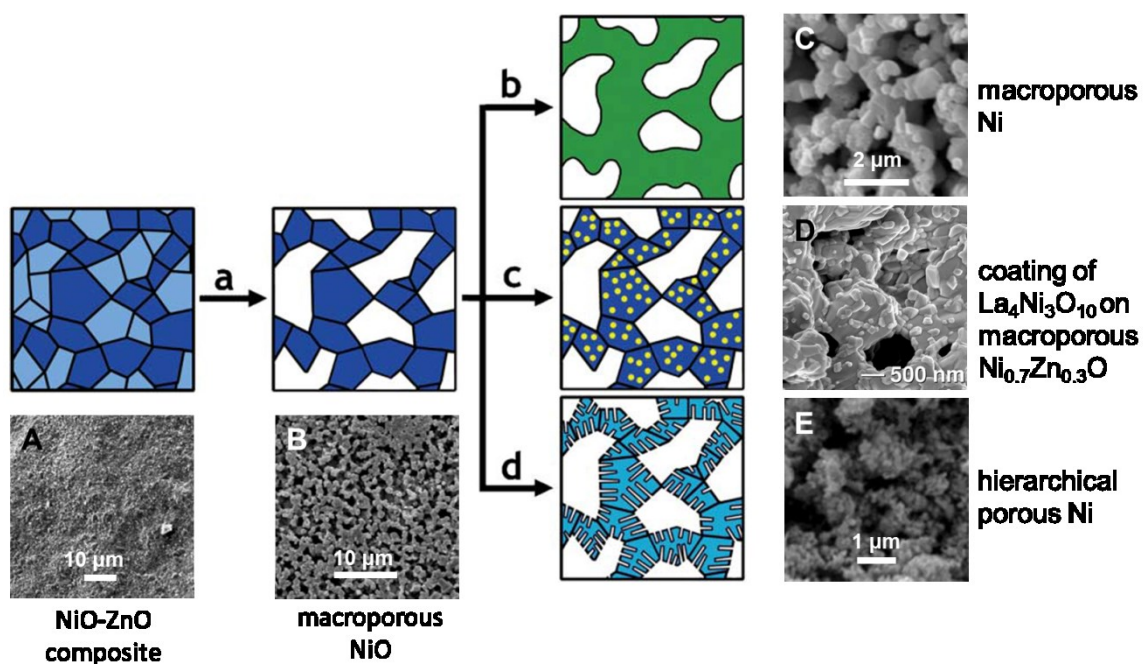


Figure 1.18 Pictorial representation<sup>72a</sup> and scanning electron micrographs (SEM) of A: a sintered NiO-ZnO pellet<sup>72b</sup> B: formation of macroporous ceramic (NiO) through selective leaching of a two-phase composite (leaching of ZnO)<sup>72b</sup> C: reduction to a porous metal (NiO reduction to Ni)<sup>72b</sup> D: decoration with conformal coating (La<sub>4</sub>Ni<sub>3</sub>O<sub>10</sub>) and subsequent reaction (shown a Ni<sub>0.7</sub>Zn<sub>0.3</sub>O pellet decorated with lanthanum acetate, followed by decomposition and heating)<sup>72c</sup> E: hierarchically porous Ni obtained via leaching of Ni<sub>1-x</sub>Zn<sub>x</sub>O with 4M NaOH to remove ZnO.<sup>72d</sup>



Fuel in energetic materials (EMs) is a major potential application of several porous pyrophoric metals such as iron, copper, magnesium, zirconium, and nickel.<sup>83</sup> Those metals, in combination with oxidizers, undergo solid-state redox reactions with rapid energy release. Typical oxidizers are metal oxides in nanoparticulate form for better contact with the fuel. In that regard, aerogels are gaining increase interest as a means for the synthesis of metal oxides nanoparticles.

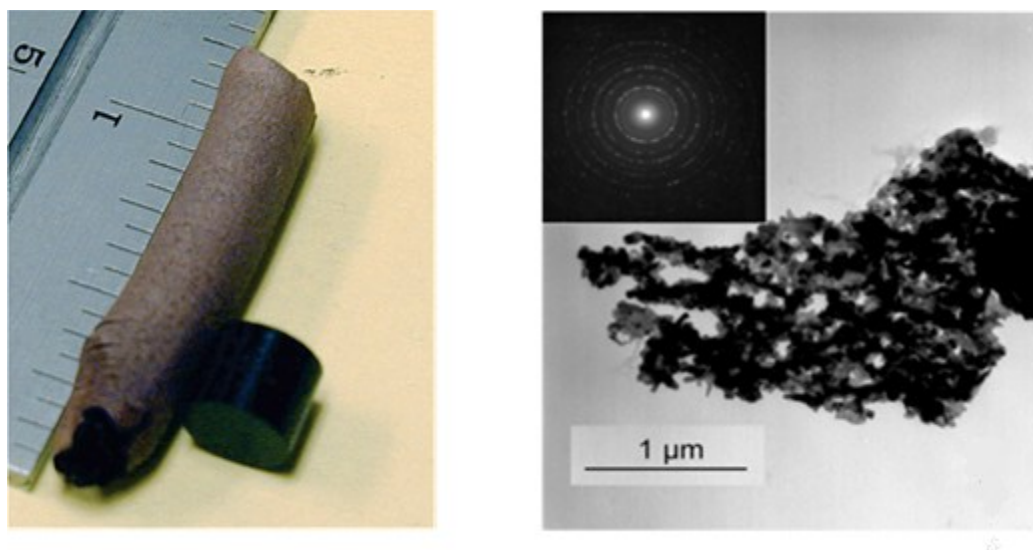


Figure 1.19 Photograph of iron foam next to an original pellet of Fe-BTA (Fe-bistetrazolamine) complex (left) TEM of Fe foam ( $0.011 - 0.040 \text{ g cm}^{-3}$ ) (right) and selected area diffraction pattern (inset).<sup>74</sup>

Conventionally, EMs are prepared by grinding together the dry fine powders of the two reactants (oxidizer and oxophilic metal), which can be extremely hazardous.<sup>84</sup> It is thus recognized that the sol-gel approach not only avoids the hazard of mixing, but also facilitates homogenous dispersion of the two phases through ultrafine particle formation

*insitu*. The first energetic nanocomposite in aerogel form was prepared by Tillotson and co-workers, by suspending aluminum nanoparticles (or microparticles) in iron oxide sols just about to undergo gelation. Homogenous mixing of aluminum and iron oxide was confirmed with elemental filtered transmission electron microscopy (EFTEM) as shown in Figure 1.20.<sup>84</sup>

Kim *et al.* also emphasized the importance of homogenous mixing of two phases in order to achieve rapid energy release.<sup>85</sup> In that regard, porosity, surface area and homogenous distribution, all have strong impact on the combustion rate. Large surface area due to small particles and high porosity in the mesoporous range result in efficient dispersion of two components that, in turn, increase contact and improve the reaction rate.<sup>86</sup>

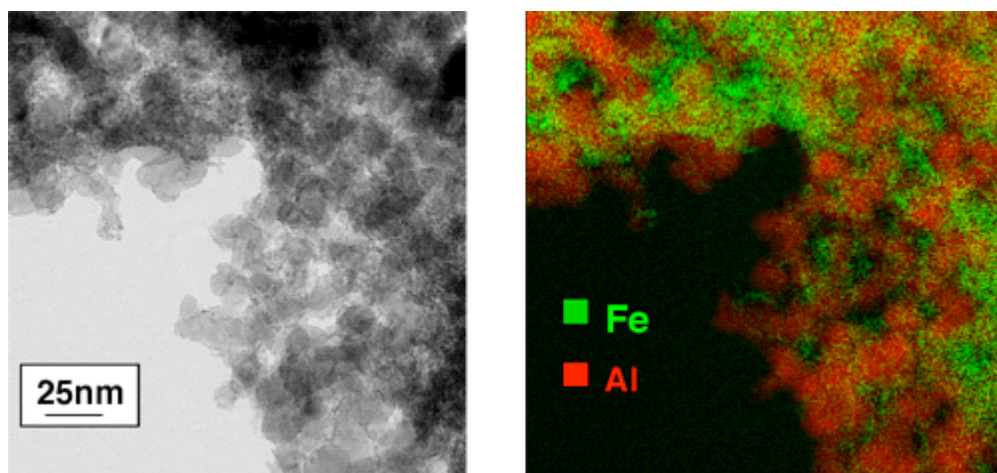


Figure 1.20 TEM (left) and EFTEM images (right) of iron (III) oxide aerogel/nanometric Al composite.<sup>84</sup>

Another interesting class of energetic materials involves pyrophoric metals, which are used as aircraft decoy flares.<sup>83</sup> Nanoparticles of metallic iron get oxidized immediately upon exposure to air and release tremendous amount of energy within a fraction of a second. In such efforts to make pyrophoric materials, Merzbacher *et al.* deposited iron on the pores of resorcinol-formaldehyde (RF) aerogels and their carbon derivatives by passing iron pentacarbonyl ( $\text{Fe}(\text{CO})_5$ ) vapors.<sup>87</sup> That method has been simplified by Gash and co-workers via impregnation of iron dopant liquid (or any other metal dopant) into the pores of carbon aerogels.<sup>88</sup> Another approach involved reduction of iron oxide network in a hydrogen atmosphere yielding sub-micron sized iron particles, which were not immediately pyrophoric (because of passivation layer of iron oxide) but upon heating undergo oxidation readily.<sup>89</sup> In a different approach, Leventis *et al.* reported synthesis of metal nanostructures via co-gelation of RF and metal oxide networks. Pyrolysis of such interpenetrating networks resulted in smelting of the metal oxides, yielding metal aerogels supported on carbon.<sup>90</sup> That process was improved by polymer coating (X-linking) of the interpenetrating network. The polymer melts at relatively low temperature (400 °C) and causes collapse of the network that further enhances homogenous mixing of nanoparticles, and results in much lower smelting temperature.<sup>91</sup>

Apart from inorganic metal oxides, various organic aerogels have been also utilized as energetic nanocomposites, but those are out of the scope of our work and are not discussed here.<sup>92</sup> Sol-gel derived materials are generally processed at room temperature, and possess high surface area, which allows them to adsorb water and other contaminants from their environment. Small amount of impurities act as energy traps and

retard the combustion wave speed. Fabrication of pure metallic materials without hampering their aerogel properties is a challenge for the sol-gel method.

Here we have introduced polybenzoxazine-iron oxide (PBO-FeOx) interpenetrating networks similar to the RF-FeOx aerogels.<sup>91a</sup> Hydrated metal chloride salts gelling through the epoxide route are Brønsted acids and can catalyze polymerization of benzoxazine. Upon pyrolysis, hybrid networks of polybenzoxazine and iron oxide gave highly crystalline, porous monolithic iron with more than 98% yield at 93% porosity. The high porosity of the iron framework facilitates infiltration of oxidizers (e.g., LiClO<sub>4</sub> or KClO<sub>4</sub>), and results in energetic composites (explosives, thermites).

## PAPER

**I. POLYBENZOXAZINE AEROGELS I: HIGH-YIELD ROOM-TEMPERATURE ACID-CATALYZED SYNTHESIS OF ROBUST MONOLITHS, OXIDATIVE AROMATIZATION AND CONVERSION TO MICROPOROUS CARBONS**

Shruti Mahadik-Khanolkar, Suraj Donthula, Chariklia Sotiriou-Leventis\* and Nicholas Leventis\*

Department of Chemistry, Missouri University of Science and Technology, Rolla, MO 65409, U.S.A. E-mail: [leventis@mst.edu](mailto:leventis@mst.edu); [cslevent@mst.edu](mailto:cslevent@mst.edu)

Prepared for Publication as an Article in *Chemistry of Materials*

**Abstract.** We describe a new room-temperature HCl-catalyzed method for the synthesis of polybenzoxazine (PBO) aerogels from bisphenol A, formaldehyde and aniline that cuts the typical multi-day high-temperature ( $\geq 130$  °C) route to a few hours. The new materials are studied comparatively to those from heat-induced polymerization, and both types are evaluated as precursors of carbon (C-) aerogels. In addition to the *ortho*-phenolic position of bisphenol A, the HCl-catalyzed process engages the *para*-position of the aniline moieties leading to a higher degree of crosslinking. Thereby, the resulting aerogels consist of smaller particles with higher mesoporosity, higher surface areas (up to  $72 \text{ m}^2 \text{ g}^{-1}$ ) and lower thermal conductivities (down to  $0.071 \text{ W m}^{-1} \text{ K}^{-1}$ ) than their thermally-polymerized counterparts (corresponding best values:  $64 \text{ m}^2 \text{ g}^{-1}$ , and  $0.091 \text{ W m}^{-1} \text{ K}^{-1}$ , respectively). It is also reported that the carbonization efficiency (up to 61% w/w), the nanomorphology and the pore structure of the resulting C-aerogels depend *critically* on a prior curing step of as-prepared PBO aerogels at 200 °C in air. According to spectroscopic evidence and CHN analysis, that operation oxidizes the  $-\text{CH}_2-$  bridges along the polymeric backbone and fuses aromatic rings in analogy to transformations during carbonization processing of polyacrylonitrile. C-aerogels from cured PBO

aerogels are microscopically similar to their respective parent aerogels, however, they have greatly enhanced surface areas, which, for C-aerogels from HCl-catalyzed PBOs, can be as high as  $520 \text{ m}^2 \text{ g}^{-1}$  with up to 83% of that attributed to newly created micropores. The acid-catalyzed route is used in the next article for the synthesis of iron oxide/PBO interpenetrating networks as precursors of iron(0) aerogels.

**Keywords:** polybenzoxazine, aerogels, acid catalysis, energy efficient, room temperature

## 1. INTRODUCTION

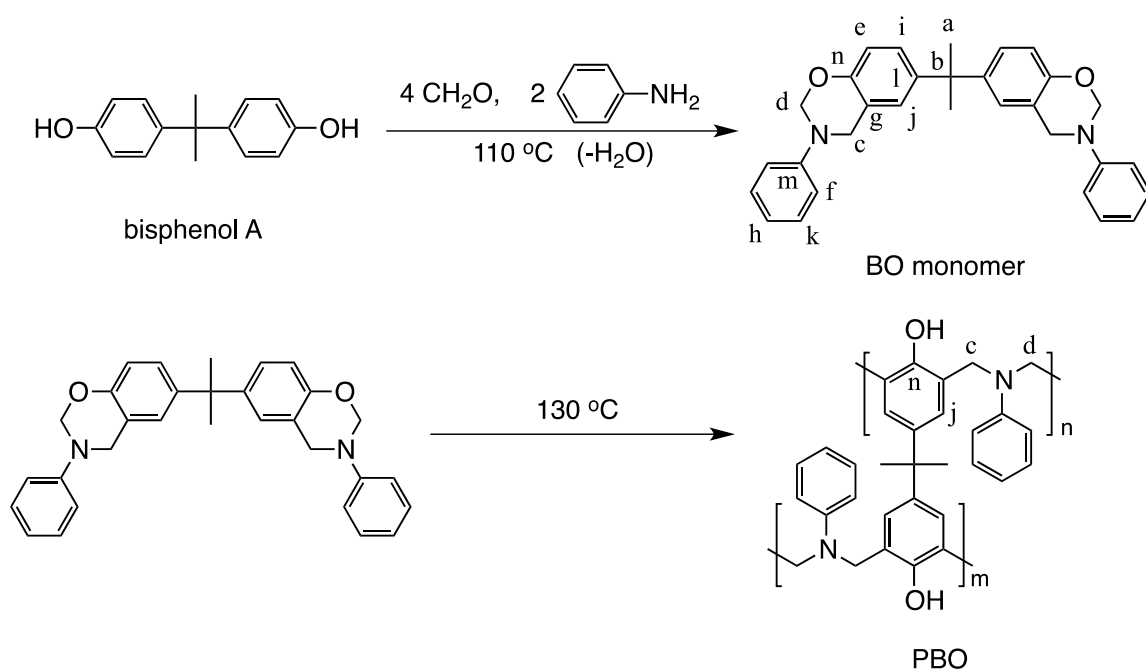
Polybenzoxazines (PBOs) are phenolic resins that owing to their high mechanical strength, innate flame retardancy, low water retention and relatively high char yields, have been raised to a polymeric class of their own.<sup>1</sup> From an engineering perspective, near-zero shrinkage upon polymerization and exceptional thermal properties in terms of high glass transition and decomposition temperatures, render PBOs inexpensive alternatives to engineering plastics like polyimides.<sup>2</sup>

Although benzoxazines were first reported in the 1940s,<sup>3</sup> systematic development of PBOs begun with Ning and Ishida's work in the mid-1990s.<sup>4</sup> PBOs are typically prepared via thermally induced ring-opening polymerization of suitable benzoxazine (BO) monomers, whose benchmark has been Ishida's condensation product of bisphenol A, aniline and formaldehyde (Scheme 1).<sup>4,5,6</sup>

With an eye on porous carbons, macroporous polybenzoxazines have been described by Ninan using templating with glass microballons,<sup>7</sup> and by Lorjai *et al.* using azodicarbonamide as a foaming agent.<sup>8</sup> Nanoporous PBOs via microphase separation were first reported by Chang *et al.*<sup>9</sup> using a co-polymer from Ishida's BO-monomer (Scheme 1) and benzoxazine-terminated poly( $\epsilon$ -caprolactone) (PCL) that was removed

from the co-polymer at the end hydrolytically. Mesoporous PBOs were obtained via reaction-induced phase separation applied in two modes. First, Chu *et al.*, using blends of a block co-polymer (PEO-*b*-PCL) with 4-hydroxybenzyl alcohol-based polybenzoxazines, demonstrated that formation of the latter forces phase-separation of PEO-*b*-PCL into cylindrical nanostructures that remain dispersed in PBO via strong intermolecular hydrogen bonding through their PEO segments;<sup>10</sup> polybenzoxazines obtained after mild pyrolytic removal of PEO-*b*-PCL included significant microporosity, while the tubular mesopores were reminiscent of silicas templated with similar block co-polymers employed as surfactants.<sup>11</sup> In a second approach, Lorjai *et al.*, using sol-gel processing of Ishida's BO monomer in xylene at 130 °C for 96 h, obtained wet-gels that were dried into PBO aerogels.<sup>12</sup>

Scheme 1. Synthesis of Benzoxazine (BO) Monomer and the Generally Accepted Mode of Polymerization



Based on the above, the aerogel route to nanoporous PBOs is perhaps the most straightforward. Thus, motivated by the intrinsic properties of PBOs, at first we became interested in Lorjai's PBO aerogels for their potential application as tissue engineering scaffolds, and demonstrated their biocompatibility.<sup>13</sup> Meanwhile, we also noted that, reportedly, PBO aerogels can be pyrolyzed to mesoporous carbons with yields higher than those of the bulk polymer (e.g., 51% w/w versus 27% w/w, respectively).<sup>12b</sup> In other words, PBO aerogels are emerging as a viable alternative to resorcinol-formaldehyde (RF) aerogels, which have been the main carbon aerogel precursors.<sup>14</sup> While both PBOs and RF are phenolic resins, the advantage of the PBO-route to carbons is the replacement of expensive resorcinol with inexpensive bisphenol A. On the down side, the high-temperature processing of PBOs may be more energy intensive.<sup>15</sup>

The range of potential applications of PBO aerogels warrant a more focused investigation targeted specifically on their time- and energy-efficient synthesis. In that regard, it has been also shown, mostly through studies at elevated temperatures, that polymerization of benzoxazines can be assisted with both strong and weak carboxylic acids, phenols (thereby benzoxazine ring opening is an autocatalytic process),<sup>16</sup> as well as cationic initiators, for example Lewis acids such as  $\text{PCl}_5$ ,  $\text{PCl}_3$ ,  $\text{TiCl}_4$ ,  $\text{AlCl}_3$ ,<sup>17</sup> and anhydrous metal ions (e.g.,  $\text{FeCl}_3$  and lithium salts).<sup>18</sup> With that background, here we explore the gelation of Ishida's BO monomer (Scheme 1) using concentrated aqueous HCl as an acid catalyst. The new process is time- and energy-efficient. The resulting aerogels are chemically similar, yet distinguishably different from and more robust than those obtained via heat-induced polymerization (Scheme 1). It is further established that oxidative aromatization (200 °C/air) is essential for the high-yield (56-61%) conversion



of PBO aerogels into multiscale (micro, meso, macroporous) carbon aerogels. The latter explains adequately Lorjai's observation regarding the higher carbonization efficiency of PBO-aerogels versus the bulk polymer, as mentioned above. Those findings are employed directly in the next article of this issue, whereas a gelling solution of  $[\text{Fe}(\text{H}_2\text{O})_6]^{3+}$ , a fairly strong Brønsted acid itself, catalyzes low-temperature co-gelation of Ishida's BO monomer into an interpenetrating network of PBO and iron oxide nanoparticles; the PBO network serves the dual purpose of a robust structure-directing nanoscopic scaffold, and of the reagent for the carbothermal conversion of the iron oxide network into pure iron(0) aerogels.

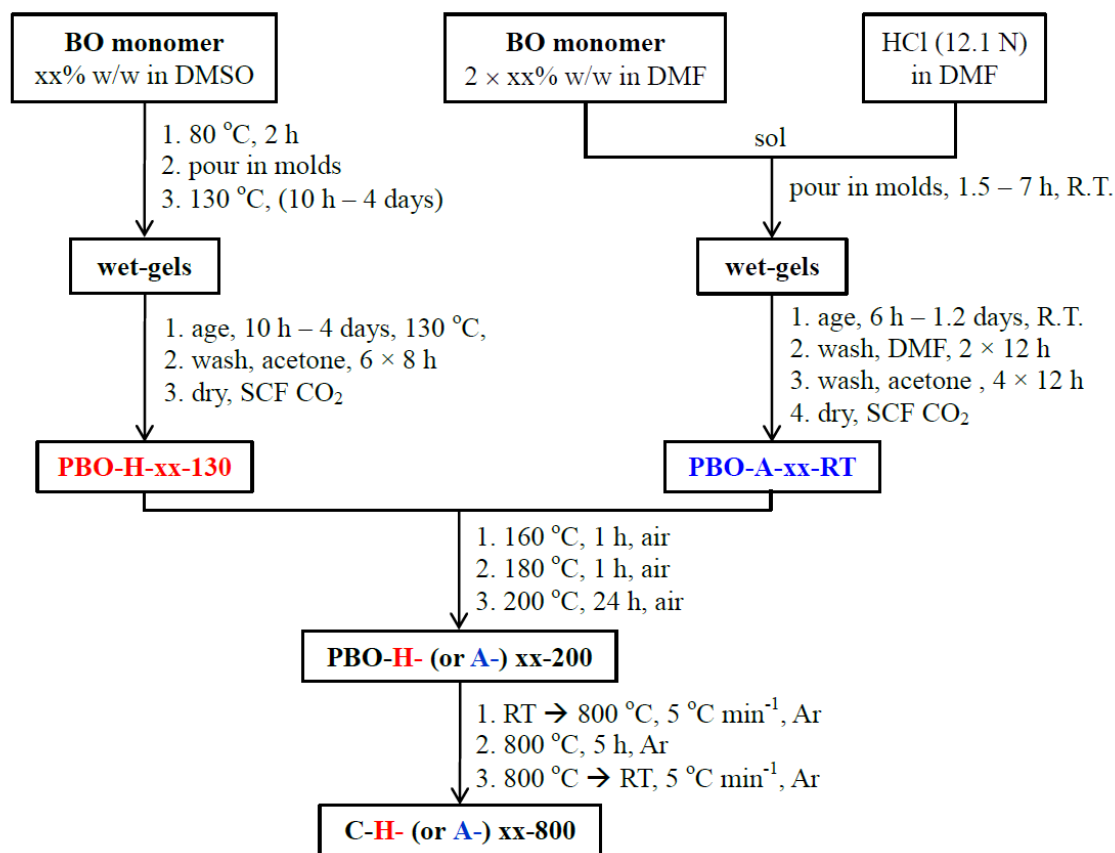
## 2. RESULTS AND DISCUSSION

**2.1 Materials Synthesis.** The BO monomer (Scheme 1) was synthesized using Ishida's solventless method (see Experimental section).<sup>5b</sup> Scheme 2 compares the PBO aerogel synthesis via the typical thermally-induced polymerization of the BO monomer at 130 °C (Scheme 1), with the new HCl-catalyzed process of this report. (For details refer to the Experimental section.) The striking difference of the two routes is that the HCl-catalyzed process induces gelation at room temperature in a few hours, in contrast to the thermal process that requires on average a few days. The heat-induced (**H-**) method works equally well in DMF and DMSO, however gels obtained via the acid-catalyzed (**A-**) route were sturdier from DMF sols, thus we opted for that solvent. **H**-gels were aged for periods equal to their gelation times, **A**-gels for periods equal to 4× their gelation times. Gelation solvents were exchanged with acetone and wet-gels were dried into aerogels with liquid CO<sub>2</sub>, taken out at the end as a supercritical fluid (SCF). Typically, PBOs obtained via heat-induced polymerization have been step-cured without any particular

precautions (i.e., in air) at temperatures up to 200 °C.<sup>4,12a,19</sup> For direct comparison, HCl-catalyzed aerogels were treated similarly. Subsequently, cured samples by either route were pyrolyzed at 800 °C under flowing Ar. Samples processed up to 200 °C are referred to as PBOs and the sample names, **PBO-H-(or A)-xx-temperature**, describe the gelation process (**H-**: heat; **A-**: acid catalysis), the weight percent of the BO monomer in the sol (**-xx-**) and the process temperature. (All formulations including molar concentrations and gelation times are provided in Table S.1 of the Supporting Information.) According to this convention, as-prepared **H**-samples are denoted as **PBO-H-xx-130**, and as-prepared **A**-samples as **PBO-A-xx-RT** (RT: room temperature). **-xx-** was varied from 5 to 40%; outside that range gels were either too soft to handle, or the BO monomer could not be dissolved completely. All carbon aerogels are referred to as **C-**; the **H-**, **A-** and **-xx-** descriptors are used again to show their origin. For consistency, the process temperature (800 °C) is also included in the sample names.

Both as-prepared **H-** and **A-** aerogels look and feel very similar: brown, monolithic, and sturdy. Step-curing of **H**-samples is presumed to complete the polymerization process.<sup>4,12a,20</sup> Indeed, based on differential scanning calorimetry (DSC, Figure 1) a similar claim could be also made for the **A**-samples. However, it is noted that the exotherms of the two materials are distinctly different, implying a significant chemical differentiation between the **H-** and **A-** process. Furthermore, taking as-prepared **PBO-A-xx-RT** samples directly into the carbonization furnace under Ar, i.e., by circumventing the curing process in air, causes severe deformation and the resulting materials look like blown foams (Figure 2).

Scheme 2. Synthesis of PBO aerogels, carbonization and graphitization

**Heat-Induced Route****Acid (HCl)-Catalyzed Route**

Microscopically, **PBO-A-20-RT** are particulate and nanoporous, **PBO-A-xx-200** retain that microstructure albeit some particle coalescence and fusion seems to have occurred, and that appearance is retained by the **C-A-xx-800** samples. On the other hand, **PBO-A-xx-RT** samples taken directly to 800 °C under Ar are no longer particulate or nanoporous (Figure 2). Clearly, curing by heat-treatment at 200 °C in air is necessary in order to fix the microstructure. However, curing does more than just completing polymerization; that could have happened equally well by heating under Ar. Oxygen must play an important role. This is investigated in detail below.

**2.2 Chemical Transformations along Processing.** Gelation was followed with  $^1\text{H}$  NMR. The resulting aerogels were characterized before and after curing with solid-state CPMAS  $^{13}\text{C}$  NMR, FTIR, CHN elemental analysis and energy dispersive spectroscopy (EDS).

Figure 3 compares the  $^1\text{H}$  NMR spectrum of the BO monomer with those of the **H**- and **A**-sols at their respective gel points. Peak assignment for the BO monomer (following the notation in Scheme 1), is based on integration and  $J$ -coupling analysis. The  $H_a$  resonance splits into two peaks in the **H**-sol, and into at least three peaks in the **A**-sol indicating more diverse pathways. The  $H_d$  resonance from the mixed acetal-aminal of formaldehyde decreases in size and the peak-intensity of the  $H_c$  protons increases, consistent with the conventional mechanism of polymerization (Scheme 1). (The fact that  $H_d$ , albeit decreased in intensity, is split into multiple peaks suggests the presence of oligomers with the benzoxazine ring still closed.) The intensity of  $H_e$  protons in the *ortho*-position of phenolic  $O$  has been diminished in both **H**- and **A**-sols as expected from Scheme 1. Most importantly, however, the intensity of the  $H_h$  protons has been also decreased drastically in the **A**-sol, therefore the acid-catalyzed process engages the *para*-position of the aniline moiety.

Elemental analysis results for the BO monomer and representative PBO and carbon aerogels are summarized in Table 1. (For the primary data set for those as well as for additional samples refer to Table S.2.A of the Supporting Information.) According to the accepted polymerization mechanism of Scheme 1, the CHN weight percent of the PBO aerogels should be equal to that of the BO monomer. This is hardly the case for any **H**-sample. An increased oxygen content is observed both in as-prepared **PBO-H-xx-130**

(8-10 % w/w versus 6.92% w/w calculated for the BO monomer), and in **PBO-H-xx-200** (14-15% w/w), signifying a significant departure from the idealized polymer structure of Scheme 1.

On the other hand, as-prepared HCl-catalyzed **PBO-A-xx-RT** show an oxygen content closer to that in the BO monomer, but they also contain chlorine, presumably as

Table 1. Representative elemental analysis data for PBO and corresponding carbon aerogels in comparison with the BO monomer

Sample	% C <sup>a</sup>	% H <sup>a</sup>	% N <sup>a</sup>	% O	% Cl
<b>BO monomer</b>					
Calculated	80.49	6.54	6.06	6.92	<sup>b</sup>
Found	81.46 ± 0.38	6.44 ± 0.05	5.73 ± 0.05	6.38 ± 0.38 <sup>c</sup>	<sup>b</sup>
<b>via acid-catalyzed gelation</b>					
<b>PBO-A-10-RT</b>	76.54 ± 0.16	5.24 ± 0.25	6.25 ± 0.10	5.59 <sup>d</sup>	6.38 <sup>d</sup>
<b>PBO-A-10-200</b>	69.40 ± 0.28	4.26 ± 0.15	5.60 ± 0.04	15.52 <sup>d</sup>	5.22 <sup>d</sup>
<b>C-A-10-800</b>	87.72 ± 0.33	0.60 ± 0.23	4.76 ± 0.11	6.77 <sup>d</sup>	0.14 <sup>d</sup>
<b>via heat-induced gelation</b>					
<b>PBO-A-20-RT</b>	71.82 ± 0.33	5.85 ± 0.83	5.83 ± 0.11	9.45 <sup>d</sup>	7.05 <sup>d</sup>
<b>PBO-A-20-200</b>	70.86 ± 0.13	3.78 ± 0.12	5.60 ± 0.03	17.67 <sup>d</sup>	2.09 <sup>d</sup>
<b>C-A-20-800</b>	87.23 ± 0.67	0.78 ± 0.28	5.55 ± 0.33	5.55 <sup>d</sup>	0.89 <sup>d</sup>
<b>via heat-induced gelation</b>					
<b>PBO-H-10-130</b>	79.45 ± 0.38	4.49 ± 0.27	6.25 ± 0.04	9.81 ± 0.61 <sup>c</sup>	<sup>b</sup>
<b>PBO-H-10-200</b>	75.75 ± 0.08	4.39 ± 0.09	5.52 ± 0.09	14.34 ± 0.17 <sup>c</sup>	<sup>b</sup>
<b>C-H-10-800</b>	88.74 ± 0.31	0.92 ± 0.04	4.40 ± 0.12	5.94 ± 0.38 <sup>c</sup>	<sup>b</sup>
<b>via heat-induced gelation</b>					
<b>PBO-H-20-130</b>	79.43 ± 0.09	6.41 ± 0.17	6.23 ± 0.07	7.93 ± 0.32 <sup>c</sup>	<sup>b</sup>
<b>PBO-H-20-200</b>	75.12 ± 0.09	4.84 ± 0.11	5.06 ± 0.08	14.98 ± 0.14 <sup>c</sup>	<sup>b</sup>
<b>C-H-20-800</b>	88.56 ± 0.24	1.07 ± 0.02	4.30 ± 0.08	6.07 ± 0.15 <sup>c</sup>	<sup>b</sup>

<sup>a</sup> Obtained from CHN analysis. Average of three samples. <sup>b</sup> Sample contains no chlorine. <sup>c</sup> From the difference 100-CHN. <sup>d</sup> The residual %weight of the CHN analysis was allocated to %O and %Cl based on energy dispersive spectroscopic (EDS) analysis as outlined in Table S.2.A of the Supporting Information.

the hydrochloride salt of the amine groups on the polymer backbone. Upon step-curing, the amount of chlorine in **PBO-A-xx-200** generally decreases, but at the same time the oxygen content increases dramatically (up to ~18% w/w). Clearly, step-curing causes oxidation in all cases. Furthermore, importantly, corresponding carbonized samples (also included in Table 1) retain some oxygen (6-7% w/w) and practically all the nitrogen of the parent polymer.

The liquid  $^{13}\text{C}$  NMR spectrum of the BO monomer is compared in Figure 4 with the solid-state  $^{13}\text{C}$  NMR spectra of as-prepared **H-** and **A-**aerogels, and of samples after curing at 200 °C. Peak assignment for the BO monomer (following the notation of Scheme 1) was based on the APT spectrum shown at the bottom of Figure 4. As-prepared **PBO-A-xx-RT** lack any resonance in the 80 ppm region indicating that (a) *all* benzoxazine rings have reacted (i.e., all  $C_d\text{-O}$  bonds have been broken); and, (b) the polymer includes no phenoxy bonding arrangements (i.e., no  $\text{-CH}_2\text{-O-Ph-}$ ). **PBO-A-xx-RT** also show an atypically broad resonance in the 40-60 ppm region ( $C_c$ ) indicating a multitude of bonding environments for the  $\text{-N-CH}_2\text{-}$  carbons, hence the simple polymeric structure of Scheme 1 is no longer valid, in agreement with conclusions reached from  $^1\text{H}$  NMR above. On the other hand, as-prepared **PBO-H-xx-130** retain a weak signal in the 80 ppm region, which could be attributed to unreacted benzoxazine. However, the conspicuously weak signal from  $C_c$  (40-60 ppm), together with the complete lack of any resonance from either  $C_d$  or  $C_c$  type of carbons in any step-cured sample (either **PBO-H-xx-200** or **PBO-A-xx-200**), and the significant oxygen uptake from **PBO-H-xx-130**, **PBO-H-xx-200** and **PBO-A-xx-200** (Table 1) suggests that aliphatic carbons have been

involved in oxidation processes, which, in the case of **PBO-H-xx-130** must have started as early as during gelation and aging.

The  $^{13}\text{C}$  NMR region above 100 ppm is harder to analyze. Based on the evolution of the  $^{13}\text{C}$  NMR spectrum of the BO monomer during gelation (not shown), peak assignment with a higher degree of confidence can be made only for as-prepared **PBO-A-xx-RT** (as shown). The main observations can be summarized as follows: (a) the spectra of as-prepared **PBO-H-xx-130** and **PBO-A-xx-RT** are quite different, implying different pathways for the **H-** and **A-** processes; (b) the spectrum of **PBO-A-xx-RT** and **PBO-A-xx-200** are also quite different from one another, suggesting that aliphatic carbons in the 40-60 ppm range have found their way into newly formed carbonyls, or aromatic systems; on the other hand, (c) **PBO-H-xx-130** and **PBO-H-xx-200** are very similar, all peak positions remain the same, some intensities, however, vary, thus supporting that oxidative processes already start during aging at 130 °C; and, (d) **PBO-H-xx-200** and **PBO-A-xx-200** are also generally similar in terms of peak positions, but they differ in some peak intensities, particularly above 140 ppm, e.g., e.g., at 164, 156/154 ppm and 148 ppm. Conceivably some of those resonances could still be coming from the conventional polymer structure of Scheme 1, or alternatively from newly-formed aromatic rings via oxidation of that conventional structure. In that regard, it is noted that the 140-165 ppm region is where newly-formed pyridine carbons show up after aromatization of polyacrylonitrile (also by heating - at 230 °C in air) on its way to carbonization and graphitization.<sup>21</sup> Finally, it is noted that both **PBO-A-xx-200** and **PBO-H-xx-200** show a broad low-intensity resonance around 190-195 ppm (see magnified inset in Figure 4).

Further insight into the chemistry of gelation and curing is obtained with FTIR (Figure 5). All samples show broad phenolic O-H stretches. In addition, the strong asymmetric/symmetric Ph-O-C stretches of the BO monomer at  $1230\text{ cm}^{-1}$  and  $1030\text{ cm}^{-1}$ , as well as of the cyclic acetal at  $944\text{ cm}^{-1}$ ,<sup>17,22</sup> have been replaced with a new, common for all samples, absorption at  $1266\text{ cm}^{-1}$  attributed to the C-O stretching of phenols.<sup>22, 23</sup> The weak/medium absorption pattern of the BO monomer at  $908/824\text{ cm}^{-1}$  is attributed to out-of-plane (OOP) C-H bending of the 1,2,4-trisubstituted aromatic ring of bisphenol A; that pattern is lost from all samples after reaction. The strong absorptions of the BO monomer at  $752\text{ cm}^{-1}$  and  $692\text{ cm}^{-1}$  are again C-H OOP bending vibrations from the dangling aniline.<sup>24</sup> Those absorptions are present in as-prepared **PBO-H-xx-130**, but become *very* weak after curing at  $200\text{ }^{\circ}\text{C}$  (in the **PBO-H-xx-200** aerogels). Those aniline absorptions are *already completely absent* in room-temperature **PBO-A-xx-RT**, whereas an additional key difference from *all H*-materials is the prominent strong absorption at  $824\text{ cm}^{-1}$ , which, having lost its weak satellite at  $908\text{ cm}^{-1}$ , is attributed to C-H OOP bending from a *para*-substituted aromatic ring.<sup>23</sup> That absorption partly survives the curing process, and is visible, albeit much weaker, in all **PBO-A-xx-200**. Clearly, the aniline moiety is involved with the polymerization and curing process in both kinds of materials, **H**- and **A**-, but by different modes: in the **A**-process, aniline undergoes early substitution in its *para*-position (during gelation), consistent with the reaction of the  $H_h$  protons observed in  $^1\text{H}$  NMR (Figure 3); in the **H**-process, aniline also reacts during the polymerization process, but mostly during curing. Most importantly, reaction of aniline during curing in both H- and A- processes yields products with no clear substitution



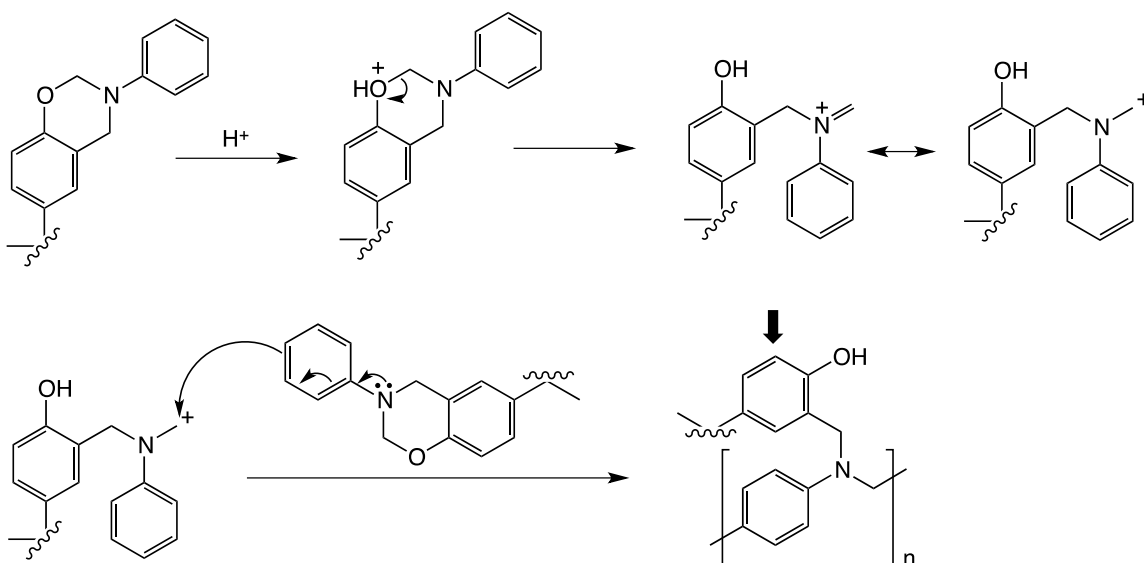
pattern in the OOP bending region (900-690  $\text{cm}^{-1}$ ), consistent with ring-fusion aromatization (see below).

About other absorptions, the band at 1111  $\text{cm}^{-1}$  is attributed to C-N stretching of the Mannich bridges, and is noted that it becomes extremely weak in all 200 °C-cured samples. The absorption at 1183  $\text{cm}^{-1}$  is attributed to the Ar-C-Ar stretching in the bisphenol A moiety,<sup>25a</sup> and survives processing as expected. The weak absorptions at 1363  $\text{cm}^{-1}$  and 1388  $\text{cm}^{-1}$  are in the range of in-plane C-H bending.<sup>25b</sup> The 1500-1800  $\text{cm}^{-1}$  region is dominated by C=C stretches and more difficult to interpret. Notably though, shoulders in the 1700-1750  $\text{cm}^{-1}$  region of all heat-treated samples (pointed with arrows) could be attributed to C=O stretches of carbonyls formed by oxidation, consistent with the higher O content of all those materials. Finally, regarding the C-H stretching region, the below 3000  $\text{cm}^{-1}$  absorption pattern, attributed to C(sp<sup>3</sup>)-H stretches, is simplified dramatically in the 200 °C-cured samples (more so in **PBO-A-10-200** than in **PBO-H-10-200**), in accord with the decrease in intensity of the 1111  $\text{cm}^{-1}$  band, implying that Mannich bridges have reacted (with O<sub>2</sub> – see below); the above 3000  $\text{cm}^{-1}$  absorption pattern, attributed to C(sp<sup>2</sup>)-H stretches, also becomes extremely weak after curing, implying that aromatic Hs are also lost, presumably to aromatization (see below).

Considering the above together, the structure of **PBO-A-xx-RT** departs significantly from the conventional polymer structure of Scheme 1, which, therefore, needs to be modified in order to account for polymerization through *para*-coupling of aniline. This is reconciled based on the generally accepted mode of the benzoxazine ring opening into an iminium ion (Scheme 3),<sup>26</sup> which, in a low-activation environment (room temperature), undergoes electrophilic aromatic substitution at the activated *para*-position

of the aniline moiety, rather than at the sterically hindered *ortho*-position of bisphenol A.<sup>18b</sup> According to <sup>1</sup>H NMR, the *ortho*-position of phenol (pointed with an arrow in Scheme 3) is also engaged eventually by iminium electrophiles, resulting in a more tightly crosslinked polymer, whereas each repeat unit has six points of attachment versus four in the heat-induced process.

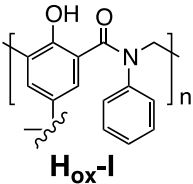
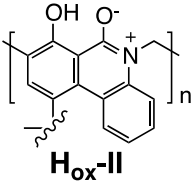
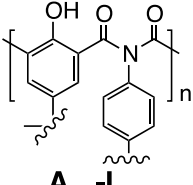
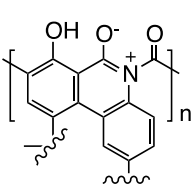
Scheme 3. Mechanism of acid-catalyzed polymerization of the BO monomer (for clarity, only half of the bisphenol A moiety is shown; arrow shows site for additional crosslinking)



**PBO-H-xx-130/200** aerogels produced via thermally-induced polymerization and curing show no evidence for *para*-substituted aniline, nevertheless in view of the increased weight percent of oxygen in both the **-130** and the **-200** materials (Table 1), the idealized PBO structure of Scheme 1 is in need of revision. Plausible oxidized forms (**H<sub>ox</sub>-I**, **H<sub>ox</sub>-II**, **A<sub>ox</sub>-I** and **A<sub>ox</sub>-II**) for both types of aerogels (**H-** and **A-**) are shown in

Table 2. Prone to oxidation are the  $-\text{CH}_2-$  groups along the polymer backbone (structures **H<sub>ox</sub>-I** and **A<sub>ox</sub>-I**), consistent with the reduction-in-size and/or disappearance of the bridging  $-\text{CH}_2-$ s from the solid-state  $^{13}\text{C}$  NMR spectra. Additional oxidation is driven by aromatization and results in ring fusion as outlined in Scheme 4 following well-established oxygen/superoxide/hydroperoxyl radical chemistry<sup>27</sup> (see structures **H<sub>ox</sub>-II** and **A<sub>ox</sub>-II**). Aromatization accounts for fixation of nitrogen into a rigid polymeric backbone, which is almost a requirement for nitrogen to survive pyrolysis at 800 °C (Table 1). The calculated CHNO weight percent of structures **H<sub>ox</sub>-I** and **H<sub>ox</sub>-II** are closer to the experimental data from **PBO-H-xx-200**, albeit  $^{13}\text{C}$  NMR, which indicates no residual  $-\text{CH}_2-$  carbons. On the other hand, the calculated CHNO values for **A<sub>ox</sub>-I** and **A<sub>ox</sub>-II** match closer with the experimental ones from **PBO-A-xx-200** (note in particular the high percent level of oxygen). Furthermore, as described by equation 4 of Scheme 4, phenolic  $-\text{OH}$  is expected to be more acidic than  $+\text{N}=\text{C}-\text{OH}$  (phenolic  $-\text{O}-$  is delocalized through the phenyl ring, while the  $+\text{N}=\text{C}-\text{O}- \leftrightarrow \text{N}-\text{C}=\text{O}$  resonance destroys aromaticity), therefore we expect proton-transfer tautomerization through the six-membered ring transition state, as shown. The simulated  $^{13}\text{C}$  NMR spectrum of tautomer **Aox-II-T** (Scheme 4 eq 4) shows resonances for the  $\text{C}_n/\text{C}_o/\text{C}_j$  carbons at 165/158/148 ppm, respectively, that is very close to the downfield pattern observed experimentally (164/156/148 ppm - Figure 4). In addition, the carbonyl carbon  $\text{C}_d$  is expected roughly at 200 ppm, again close to the experimentally observed broad resonance at 193 ppm (common to both A- and H- cured samples - Figure 4).

Table 2. Experimental (recited from Table 1) versus calculated CHNO weight percent of plausible oxidized forms (**H<sub>ox</sub>-I** and **H<sub>ox</sub>-II**) of the generally accepted PBO structure (see Scheme 1) and of the polymer obtained by acid-catalysis (**A<sub>ox</sub>-I** and **A<sub>ox</sub>-II**)

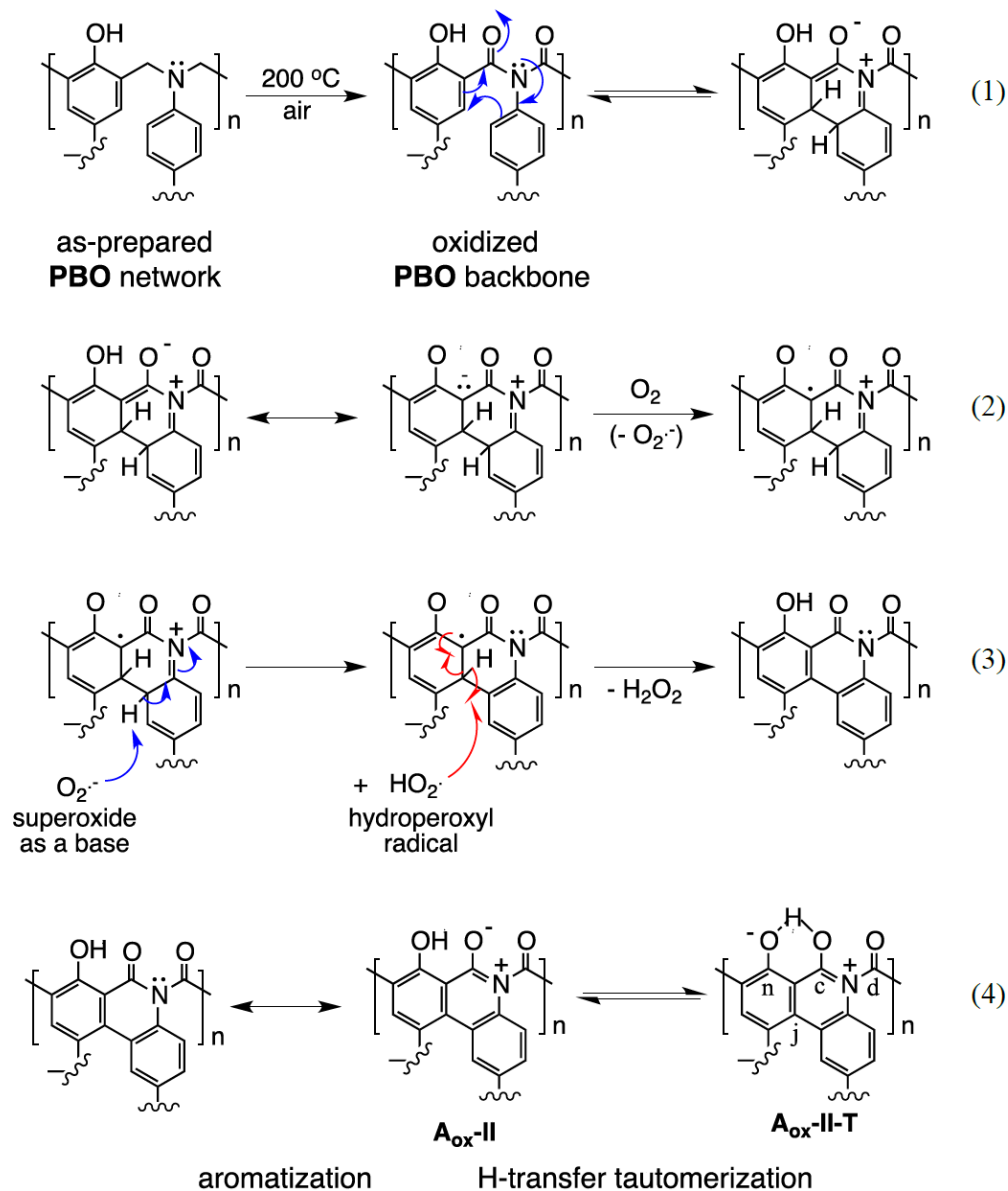
Polymer	% C	% H	% N	% O
<b>PBO-H-10-200</b>	75.75	4.39	5.52	14.34
<b>PBO-H-20-200</b>	75.12	4.84	5.06	14.98
<b>PBO-A-10-200</b>	69.40	4.26	5.60	15.52
<b>PBO-A-20-200</b>	70.86	3.78	5.60	17.67
<b>Idealized PBO</b>	80.5	6.54	6.10	6.92
 <b>H<sub>ox</sub>-I</b>	75.9	5.31	5.71	13.1
 <b>H<sub>ox</sub>-II</b>	76.5	4.53	5.76	13.2
 <b>A<sub>ox</sub>-I</b>	72.1	3.87	5.43	18.6
 <b>A<sub>ox</sub>-II</b>	72.7	3.13	5.47	18.8

**2.3 PBO Aerogel Characterization.** This section discusses the porous structure, the skeletal framework and the interparticle connectivity of step-cured PBO aerogels **PBO-H-xx-200** and **PBO-A-xx-200**. Key materials properties are given in Table 3.

*2.3a General material properties.* All **-200** samples have shrunk significantly relative to their molds (Table 3). Shrinkage is extremely reproducible. Some shrinkage is noted during aging, but mostly upon gelation solvent exchange to acetone and upon step-curing (see Figure 2). No shrinkage was observed during drying. Despite the fact that polybenzoxazines as polymeric materials are not expected to shrink on processing,<sup>4,5a,28</sup> shrinkage observed during *aerogel* processing should not be considered surprising,<sup>29</sup> as oftentimes shrinkage of 3D nanostructures has a nanoscopic rather than a molecular origin, whereas skeletal nanoparticles partially penetrate into the empty fractal space of one another.<sup>30</sup> Overall, in both **A**- and **H**-aerogels, shrinkage first increases with the [BO monomer], reaches a maximum at **-xx-** ~ 15-20 and then decreases. **A**- aerogels shrink slightly more (up to 37% in linear dimensions) than their **H**- counterparts (up to 33%), and without going into excessive speculation, that could be attributed to the tighter molecular structure of the former due to their higher degree of crosslinking.

Bulk densities,  $\rho_b$ , increase monotonically, albeit not linearly, with the BO monomer concentration in the sol. Importantly, it is also noted that at the same BO monomer concentrations in the sol (i.e., same **-xx-** in the sample names), heat-polymerized **H**-aerogels are significantly less dense (30-50%) than their **A**-counterparts. The differential shrinkage may partly explain that effect, however, the main contributing factor is a significant mass loss in the **H**-samples during post-aging washing. Mass balance based on the relative weight of the BO monomer and of the resulting

Scheme 4. Proposed mechanism for the oxidative aromatization of the PBO network (for clarity, only half of the bisphenol A moiety is shown)



**PBO-H-xx-200** shows only a  $60 \pm 1\%$  w/w mass recovery for  $5 \leq \text{xx} \leq 20$ , versus a 92-95% for the corresponding acid-catalyzed **PBO-A-xx-200** samples. Clearly, the HCl-

catalyzed room temperature gelation process is not only shorter, but also more mass-efficient. Further data analysis, and a fair comparison of **A**- and **H**-aerogels is based on **A**- and **H**- sample pairs with approximately equal bulk densities. For quick reference, such pairs are denoted with asterisks in Table 2.

The skeletal densities,  $\rho_s$ , of **PBO-A-xx-200** aerogels are invariant of **-xx-**. On the other hand, except **PBO-H-5-200**, the skeletal densities of all other **PBO-H-xx-200** ( $10 \leq \text{xx} \leq 40$ ) are markedly lower than those of the **PBO-A-xx-200** aerogels and decrease as the bulk density increases. Such behavior has been observed in other systems before,<sup>31</sup> and has been attributed to closed pores on the skeletal framework. The percent volume fraction of the closed pores on the skeletal framework,  $V_{CP}$ , can be calculated via  $V_{CP} = 100 \times (\rho_{PBO} - \rho_s) / \rho_{PBO}$ , whereas  $\rho_{PBO}$  is the intrinsic density of the PBO polymer. Taking the highest skeletal density, that of **PBO-H-5-200** ( $1.317 \text{ g cm}^{-3}$ , Table 3) as equal to  $\rho_{PBO}$ , it is calculated that  $V_{CP}$  varies from 3.0% to 8.3% v/v. The closed porosity of the skeletal framework is not included in calculations of the open porosity,  $\Pi$ , via  $\Pi = 100 \times (\rho_s - \rho_b) / \rho_s$ . In that regard, the  $\Pi$  values of density-matched **A**- and **H**-aerogels are extremely close to one another (Table 3).

*2.3b The porous structure.* That was investigated with  $\text{N}_2$ -sorption and Hg intrusion porosimetry. All data are shown in Figures S.1 and S.2 of the Supporting Information and results are also summarized in Table 3. Representative data with density-matched **PBO-A-12-200** and **PBO-H-20-200** are shown in Figure 6.  $\text{N}_2$ -sorption isotherms show no signs of microporosity, generally rising above  $P/P_0 = 0.8-0.9$ , thus pointing to mostly macroporous materials. By the same token, **A**-aerogels show narrow hysteresis loops that become wider and reach short saturation plateaus as the bulk density

increases, signifying increasing mesoporosity. Similar signs of mesoporosity are shown only by higher-density **H**-aerogels (e.g., **PBO-H-20-200** - see Figure 6), yet the volume of N<sub>2</sub> adsorbed by **H**-aerogels is throughout much lower than that adsorbed by **A**-aerogels. Surface areas,  $\sigma$ , via the Brunauer-Emmett-Teller (BET) method are about double or higher in the **PBO-A-xx-200** materials than their  $\rho_b$ -matched **PBO-H-xx-200** counterparts (Table 3).

A more quantitative evaluation of the porous structure was obtained via pore volume and average pore diameter analysis (Table 3). Total pore volumes calculated via  $V_{\text{Total}}=(1/\rho_b)-(1/\rho_s)$  account for the entire open porosity of the samples, which, as discussed above, is practically equal among  $\rho_b$ -matched **A**- and **H**-samples. As  $\rho_b$  increases, those  $V_{\text{Total}}$  values come closer to  $V_{1.7-300 \text{ nm}}$  (BJH cumulative pore volume), yet even at the point of the closest numerical proximity, the ratio  $V_{1.7-300 \text{ nm}}:V_{\text{Total}}$  is equal to 0.5 and only to 0.1 for the highest density **PBO-A-20-200** and **PBO-H-40-200**, respectively. Similarly, pore sizes calculated via the  $4 \times V/\sigma$  method using either  $V=V_{\text{Total}}$ , or the single (max) point of volume adsorbed on the isotherm, diverge significantly for lower-density aerogels; they get closer in higher-density **PBO-A-xx-200**, but remain widely apart in **PBO-H-xx-200**. An independent evaluation of the average pore sizes using Hg intrusion porosimetry yields values that generally match well with the pore sizes calculated via the  $4 \times V_{\text{Total}}/\sigma$  method. That correlation is stronger either when average pore diameters are >300 nm, or when materials include significant mesoporosity (i.e., when  $V_{\text{Total}}$  and  $V_{1.7-300 \text{ nm}}$  converge).

Overall, both **A**- and **H**-aerogels include meso and macropores. The former have higher volumes attributed to pore sizes below 300 nm than the latter. Within those two



size regimes (i.e., above and below 300 nm) both macropore and mesopore size distributions of **A**-aerogels as a group are shifted to lower diameters than their **H**-counterparts (Figure 6 and Figures S.1 and S.2 in the Supporting Information).

*2.3c The skeletal framework and interparticle connectivity.* The skeletal framework was probed with SEM and particle size analysis via N<sub>2</sub>-sorption and small angle x-ray scattering (SAXS). Those data point to a major structural change as a function of  $\rho_b$ , which was confirmed through an evaluation of the relative interparticle connectivity of **A**- and **H**-aerogels in a top-down fashion from solid thermal conduction data. All those findings are used together in the formulation of the growth mechanism.

Microscopically, both **H**- and **A**- aerogels consist of particles. SEM images at two different magnifications for all 5 ≤ **xx** ≤ 20 samples are compared in Figure 7. No organization, as for example into strings-of-beads or fibers, is noticeable at any length scale. Particles simply aggregate into larger, apparently random clusters. An important observation, however, is that the apparent particle size in **PBO-H-xx-200** increases with density (i.e., as **xx** moves from 5 to 20), while in **PBO-A-xx-200** the trend is exactly the opposite. (The smallest identifiable particles in Figure 7 are denoted with dashed circles for quick reference.) The same trends are obtained from particle size calculations using skeletal density and gas sorption data (via particle diameter,  $d = 6/\rho_s\sigma$ , see Table 3). The agreement between those values and the particle sizes in SEM is remarkable. However, particle sizes measured with SAXS (Figure S.3) show somewhat different trends. At first approximation, primary particle diameters for **PBO-A-xx-200** are generally in good overall agreement with the  $6/\rho_s\sigma$  data (see Table 3) signifying that the particles in circles (Figure 7) correspond closely to the fundamental building blocks of the network. Upon

closer examination though, the  $6/\rho_s\sigma$  values seem invariant with  $\rho_b$ , while the SAXS particle sizes show a downward trend and a noticeable drop when **-xx-** goes from 10 to 12. Thus, while initially (for **-xx-<10**) the  $6/\rho_s\sigma$  values are somewhat smaller than the SAXS particle sizes, eventually there is a crossover point whereas the  $6/\rho_s\sigma$  values become larger than the latter (and, at the end, the two values become 70 nm versus 52 nm, respectively, for **PBO-A-20-200**). On the other hand, the SAXS primary particles of **PBO-H-xx-200** are overall larger than those of the **A**-samples, and also trend downwards as **-xx-** increases. Again, a size-crossover is observed whereas  $6/\rho_s\sigma$  values become larger than the SAXS sizes when **-xx-** goes from 10 to 15, but most importantly, above that crossover point particle diameters calculated via  $d = 6/\rho_s\sigma$  (and observed with SEM) and those found via SAXS diverge a lot (e.g., 244 nm versus 96 nm, respectively, for **PBO-H-40-200**). Thus, it is concluded that the true primary particles of **PBO-H-xx-200** are embedded inside a thick yet conformal polymer layer of different density that results into the larger, almost featureless spheres observed in SEM when **-xx- $\geq$ 15**.

At first glance, the curious common crossover at  $10 \leq \text{-xx-} \leq 15$ , whereas particle diameters calculated via  $d = 6/\rho_s\sigma$  become larger than the primary particle sizes found via SAXS, could be dismissed as an artifact, however, it turns out that it represents a true structural change common in both materials. That is inferred via a top-down evaluation of the interparticle connectivity (number of contacts and contact area per unit volume) from thermal conductivity data (Figure 8). The total thermal conductivity ( $\lambda$ , calculated from thermal diffusivity data as described in the Experimental section) varies with  $\rho_b$  in a similar fashion for the two materials (see Figure 8A – all numerical data are provided in Table S.4 in the Supporting Information.) Overall, at all  $\rho_b$  **A**-aerogels are much better

thermal insulators than their **H**-counterparts, a fact attributed intuitively to their smaller pore and particle sizes that both contribute towards higher thermal resistance. On the other hand, it is noted that  $\lambda$  has three additive components, a radiative heat conduction component  $\lambda_{\text{irr}}$ , the heat conduction through the pore filling gas  $\lambda_{\text{g}}$ , and the heat conduction through the solid network  $\lambda_{\text{s}}$ .<sup>32</sup>  $\lambda_{\text{irr}}$  was eliminated experimentally,  $\lambda_{\text{g}}$  was calculated using the Knudsen equation (refer to Table S.4) and the resulting  $\lambda_{\text{s}}$  is plotted versus  $\rho_{\text{b}}$  in Figure 8B. In porous materials, including several aerogels,  $\lambda_{\text{s}}$  has been modeled according to:<sup>33</sup>  $\lambda_{\text{s}}=C\exp[\rho_{\text{b}}\times\alpha]$ , whereas  $C$  depends on the interparticle connectivity and  $\alpha$  on the way matter fills space. According to Figure 8B that relationship is not valid over the entire  $\rho_{\text{b}}$ -range of either **A**- or **H**-aerogels, with a clear common discontinuity between 0.2 and 0.4 g cm<sup>-3</sup>, i.e., exactly in the range where the crossover of particle sizes calculated via  $d = 6/\rho_{\text{s}}\sigma$  and SAXS takes place. Since in the case of **PBO-H-xx-200**, that crossover was attributed to embedding of skeletal primary particles within polymer of different density, it is suggested that the same structural evolution, albeit to a lesser extent, takes place in **PBO-A-xx-200**. Therefore, in order to remain internally consistent conceptually, below the discontinuity points in Figure 8B  $\lambda_{\text{s}}$  is controlled by the interplay of increasing number of particles and decreasing particle size; above those points,  $\lambda_{\text{s}}$  is controlled by the growing size of interparticle necks as more polymer accumulates on the network.

The morphostructural variation between **H**- and **A**- aerogels can be reconciled based on the molecular structures of the **H**- and **A**- polymers. Clearly, the acid-catalyzed reaction is much faster and more efficient, consuming quickly all the BO monomer (it is reminded, the material recovery in **A**-aerogels is > 90% w/w). More crosslinked, hence

more insoluble **A**-polymer phase-separates earlier than **H**-polymer into smaller particles. In the **H**- reaction, the fact that despite extensive aging at elevated temperatures the material balance is generally low (typically around 60%), signifies that a large amount of oligomers (as those observed with  $^1\text{H}$  NMR right after gelation– Figure 3) is *always* present in the pore-filling solution of the newly formed gel. Oligomers keep on reacting with surface functional groups on the newly formed skeletal network, and build up a layer that increases the apparent (SEM) particle size, prevents the probing gas ( $\text{N}_2$ ) from reaching the small crevices between primary particles (hence, the SEM and the gas-sorption diameters agree) and creates closed porosity. Correlating trends in apparent and SAXS particle-sizes with thermal conductivity data suggest that a similar process takes place in **A**-samples, but to a much lesser extent: remaining oligomers at the gel-point (supported by Figure 3) do accumulate on the framework, but their amount is low and not enough to erase the fine registration of the primary particles in SEM.

In summary, the accelerated rate of the acid-catalyzed reaction, together with the additional possibilities for crosslinking become responsible for efficient use of the monomer, smaller more numerous particles, hence finer structures with mesoporosity and higher surface areas.

**2.4 Carbonization.** Thermogravimetric analysis (TGA) under inert atmosphere (Figure 9) shows that all **PBO-A-(or H-)xx-200** aerogels are equally resistant to heat, starting losing mass at around 270 °C. The 10% mass-loss point is also common for all materials at around 350 °C. Heated up to 900 °C, both kinds of aerogels leave significant amounts of residue. However, since TGA traces have not leveled off at that point yet (probably because of heat transfer reasons – after all, aerogels are good thermal

insulators) the terminal 900 °C-values are inaccurate and cannot be referred to as carbonization yields. Thus, it is noted (Figure 10) that in order to remove the C-H and O-H stretching absorptions (albeit the latter not completely) it is necessary to carry out pyrolysis at over 600 °C. Preparative pyrolysis was conducted under flowing high-purity Ar at 800 °C. Carbonization yields are provided in Table 4 and were found somewhat higher for C-A-xx-800 (56-61% w/w) than for C-H-xx-800 samples (50-55% w/w). The C-content in those aerogels was found increased relative to their parent -200 samples to 88-89% w/w (Figure 10; data in Tables 1 and S.2.B), the amount of H decreased to below 1% w/w, O and particularly N, however, remained with the samples as described above. The resistance of N and of H-bonded O (up to at least 600 °C - see FTIR spectra in Figure 10) is consistent with oxidative curing and aromatized structures Aox-II and Hox-II (refer to Table 2 and Scheme 4).

**C-A-(or H-)-xx-800** carbon aerogels are sturdy and electrically conducting. Under quasi-static compression, **C-H-20-800** ( $0.450 \text{ g cm}^{-3}$ ) behave as linearly elastic materials, failing at about 2.5% strain. The Young's modulus ( $\sim 1.12 \text{ GPa}$ ) is much higher than those of  $\rho_b$ -matched **PBO-A-** or **PBO-H-**aerogels ( $\sim 400 \text{ MPa}$ ). (Representative mechanical characterization data under quasi-static compression are shown in Figure S.4 of the Supporting Information.) The electrical conductivity of the same sample was measured equal to  $0.0043 \text{ mho cm}^{-1}$ . By comparison, at similar densities ( $0.480 \text{ g cm}^{-3}$ ) porous carbons derived from benzoxazine foams of the same BO monomer have a compressive modulus of  $829 \text{ MPa}$  and electrical conductivity of  $0.005 \text{ mho cm}^{-1}$ .<sup>8</sup> It is noteworthy that the electrical conductivity of PBO-derived carbon aerogels is found consistently much lower than what has been reported for RF aerogels at similar densities

(2.5 mho cm<sup>-1</sup> at 0.47 g cm<sup>-3</sup>), or polyacrylonitrile aerogels (up to 140 mho cm<sup>-1</sup>, albeit at somewhat higher densities – about 0.7 g cm<sup>-3</sup>).<sup>21a</sup> It is difficult to speculate on those discrepancies in the electrical conductivities among those materials. They may be related to molecular-level defects associated with the retention of high levels of *N* and *O*, or they may be related to the relative particle sizes and interparticle contacts. A correlation of the electrical with the thermal conductivity and with the elastic modulus over the  $\rho_b$ -range of the C-aerogels might be instructive.

In terms of materials properties, **C-A-(or H)-xx-800** shrink an additional 20-29% relative to their parent PBO aerogels (e.g., see Figure 2), to a total shrinkage of 40-53% from the molds (Table 4). A combination of factors (parent aerogel density, shrinkage, mass loss during pyrolysis) work synergistically to yield more dense **C-A-** aerogels (0.13-0.90 g cm<sup>-3</sup>) than their **C-H-** counterparts (0.09-0.45 g cm<sup>-3</sup>). Skeletal densities,  $\rho_s$ , of **C-A-xx-800** aerogels are also somewhat higher (1.81-1.90 g cm<sup>-3</sup>) than those of the **C-H-xx-800** aerogels (1.66-1.86 g cm<sup>-3</sup>), but all values are either within or close to the range expected for amorphous carbon (1.8-2.0 g cm<sup>-3</sup>).<sup>34</sup> Unlike the parent **PBO-H-xx-200**, skeletal densities of **C-H-xx-800** no longer show a dependence on  $\rho_b$ , signifying absence of closed porosity. Porosities,  $\Pi$ , calculated from the  $\rho_b$  and  $\rho_s$  data, vary inversely with  $\rho_b$  as expected.  $\Pi$  values of  $\rho_b$ -matched **C-A-** and **C-H-** samples (indicated with asterisks in Table 4) are practically identical.

Microscopically, the skeletal framework of carbon aerogels (Figure 11) follows closely the trends set by the parent PBOs (compare with Figure 7). Larger particles in the parent PBOs result in larger particles in the carbons. However, overall there is a sense

that particles have undergone a surface melting-like fusion (sintering), which is evident in both higher-density **C-H-20-800** and **C-A-20-800** aerogels.

Figure 12 shows the N<sub>2</sub>-sorption isotherms and pore size distributions of carbon aerogels derived from **H-** or **A-** PBO aerogels at low and high monomer concentrations (-**xx**- equal to 5 and 20, respectively). Just a cursory comparison with the N<sub>2</sub>-sorption data of the parent PBO aerogels shown in Figure 6 reveals some similarities, but also one major difference. First, a property inherited from the parent **PBO-H-** and **PBO-A-** aerogels is that at high relative pressures ( $P/P_0 \sim 1$ ), **C-H-**aerogels adsorb much less N<sub>2</sub> than **C-A-**aerogels. Also, similarly to the parent PBOs, the isotherms of **C-A-xx-800** reach narrow saturation plateaus and show hysteresis loops at all densities, signifying mesoporosity. In contrast, the isotherms of the **C-H-**aerogels show that those are mostly macroporous materials at all densities. Pore size distributions by the BJH method (shown in Figure 12) support those conclusions. On the other hand, at low relative pressures all **C-A-xx-800** aerogels show a rapid rise of the volume of N<sub>2</sub> adsorbed at  $P/P_0 \ll 0.1$ , indicating microporosity (pore sizes  $< 2$  nm). This is confirmed by pore size distribution analysis using the Horvath-Kawazoe method on N<sub>2</sub>-sorption data under low-pressure dosing, and assuming cylindrical pore geometry (Figure 12). (It is noted that oftentimes the best fit yields multiple, closely-spaced pore sizes - case of **C-A-20-800**). (Average pore diameter data for meso- and micropores are included in Table 4.)

Surface area analysis with the BET method followed by *t*-plot analysis with the Harkins and Jura method shows that 74-82% of the greatly-increased total surface area of *all* **C-A-**aerogels relative to their parent PBOs, is attributed to the micropores (Table 4). In fact, the remaining BET surface areas are very similar to the BET surface areas of the

parent **PBO-A**-aerogels (for example, consider **C-A-5-800** (Table 4);  $\sigma = 516 \text{ m}^2 \text{ g}^{-1}$ ; micropore area =  $427 \text{ m}^2 \text{ g}^{-1}$ ; therefore, meso+macropore area =  $89 \text{ m}^2 \text{ g}^{-1}$ ; meanwhile for **PBO-A-5-200** (Table 3),  $\sigma = 72.2 \text{ m}^2 \text{ g}^{-1}$ ). Similar observations are made for all **C-H-xx-800** when  $xx > 5$  (the **C-H-5-800** isotherm does not indicate microporosity). Again, for  $xx > 5$ , 69-81% of the BET surface area is assigned to micropores, and the remainders are very close to the BET surface areas of the parent **PBO-H**-aerogels. Overall, it can be stated that carbonization leaves the mesopore surface area almost intact and creates new surface area within micropores.

A quantitative evaluation of the relative contribution of the various pore sizes in the total porosity comes from a detailed pore volume analysis. Results are include in Table 4. All low-density samples ( $xx=5$ ) are mostly macroporous, as only a very small fraction (1.4-4.0%) of the total pore volume ( $V_{\text{Total}}$ ) is associated with pore sizes less than 300 nm. As the bulk density increases, carbons from acid-catalyzed PBOs (namely, **C-A-15-800** and **C-A-20-800**) become mostly meso/microporous, whereas 75-85% of  $V_{\text{Total}}$  is allocated to pores with sizes less than 300 nm. For those samples, the pore volume of less-than-300 nm pores is allocated more to meso than to micropores (in a 2.5-5 ratio), however, it is emphasized that the micropore surface area *always* far exceeds the mesopore area, as discussed above. Using the same criteria, **C-H-xx-800** samples remain macroporous even at higher densities (refer to **C-H-15-800** and **C-H-20-800**): the pore volume assigned to pore sizes less than 300 nm is always less than 10% of  $V_{\text{Total}}$ . The case of **C-H-20-800** is noteworthy as the micropore volume exceeds that of the mesopores (0.15 versus  $0.06 \text{ cm}^3 \text{ g}^{-1}$ , respectively).



At last, a most important observation is that all micropore volumes vary within a narrow range, 0.09-0.15 cm<sup>3</sup> g<sup>-1</sup>, and are practically invariant of the carbon aerogel origin (A- or H-), density or morphology. In other words, the ability to yield micropores does not depend on the micromorphology or the pore structure of the precursor PBO aerogels; therefore, the ability to create microporosity is an inherent property of the polymer. Considering this together with the results of direct pyrolysis (i.e., without the curing step in air – Figure 2) leads to the conclusion that the ability to yield micropores is not the result of an inherent molecular rigidity of crosslinked benzoxazines (in the context of intrinsically microporous polymers<sup>35</sup>), but rather the result of additional rigidity imposed by oxidative curing, which apparently prevents the molecular network from collapsing during carbonization.

### 3. CONCLUSION

Robust, monolithic PBO aerogels have been synthesized over a wide density range via a new time-efficient HCl-catalyzed room-temperature route from Ishida's benzoxazine monomer derived from bisphenol A, aniline and formaldehyde. The acid-catalyzed process imposes additional crosslinking that results into smaller skeletal particles, with increased surface areas and reduced thermal conductivity. Irrespective of route (i.e., heat-induced polymerization, or the new acid-catalyzed process) both the carbonization efficiency and the nanomorphology of the resulting carbon aerogels depend *critically* on a curing step (200 °C in air) that oxidizes, aromatizes and rigidizes the polymeric backbone. That finding explains well the curious observation reported by Lorjai *et al.*, namely that polybenzoxazine aerogels have higher char yields than the bulk material (see Introduction):<sup>12b</sup> clearly, because of their open porosity, PBO aerogels can

be oxidized more thoroughly. All PBO-derived carbon aerogels are extremely robust multiscale nanoporous materials, with porosities that span from the micro to the meso to the macroscopic size regime. The relative volume ratio of the micro, meso and macropores can be adjusted via the bulk density of the material. The greatly enhanced surface areas of those carbon aerogels are mostly (up to 83%) assigned to the newly formed micropores, which are the result of additional rigidity imposed by oxidative curing. As they do not require any sacrificial etching, to our knowledge, acid-catalyzed PBO aerogels comprise the most economic route to microporous carbon aerogels to date.

#### **4. EXPERIMENTAL**

**4.1 Materials.** Dimethyl sulfoxide (DMSO), paraformaldehyde (96%), aniline, and 4,4'-isopropylidenediphenol (bisphenol A) were obtained from Acros Organics. Concentrated aqueous HCl (12.1 N) was purchased from Fisher. *N,N*-dimethylformamide (DMF) and diethyl ether were purchased from Aldrich Chemical Company. Deuterated DMSO (DMSO- $d_6$ ),  $CDCl_3$ , acetone- $d_6$  and DMF (DMF- $d_7$ ) were obtained from Cambridge Isotope Laboratories Inc. All reagents and solvents were used as received unless noted otherwise.

**4.2 Synthesis of the Benzoxazine Monomer (BO Monomer).** Bisphenol A, aniline (distilled), and paraformaldehyde were mixed in a 1:2:4 mol ratio in a round bottom flask and placed in a preheated oil bath (110 °C). The mixture was stirred for 1 h. The resulting yellow viscous liquid was dissolved in diethyl ether, and extracted 3× with an aqueous NaOH solution (3M) and 3× with deionized water. The ether layer was dried over anhydrous sodium sulfate and the solvent was removed with a rotary evaporator. The white solid was vacuum-dried at room temperature overnight. Yield (~ 60%). For

NMR, the white solid was re-dissolved in hexane and filtered. Hexane was then removed and the sample was dried in a vacuum oven overnight.  $^1\text{H}$  NMR (400 MHz,  $\text{CDCl}_3$ )  $\delta$  (ppm) 7.39-7.27 (m, 4H,  $\text{H}_k$ ), 7.21-7.14 (m, 4H,  $\text{H}_f$ ), 7.04 (dd,  $J_{ie}$  = 8.6 Hz,  $J_{ij}$  = 2.4 Hz, 2H,  $\text{H}_i$ ), 6.99 (t,  $J_{hk}$  = 7.3 Hz, 2H,  $\text{H}_h$ ), 6.93 (d,  $J_{ij}$  = 2.4 Hz, 2H,  $\text{H}_j$ ), 6.80 (d,  $J_{ei}$  = 8.6 Hz, 2H,  $\text{H}_e$ ), 5.39 (s, 4H,  $\text{H}_d$ ), 4.64 (s, 4H,  $\text{H}_c$ ), 1.66 (s, 6H,  $\text{H}_a$ );  $^1\text{H}$  NMR (400 MHz,  $\text{DMF-d}_7$ )  $\delta$  (ppm) 7.26-7.18 (m, 4H,  $\text{H}_k$ ), 7.18-7.12 (m, 4H,  $\text{H}_f$ ), 7.09 (d,  $J_{ij}$  = 2.3 Hz, 2H,  $\text{H}_j$ ), 6.94 (dd,  $J_{ie}$  = 8.5 Hz,  $J_{ij}$  = 2.3 Hz, 2H,  $\text{H}_i$ ), 6.84 (tt,  $J_{hk}$  = 7.2 Hz,  $J_{hf}$  = 1.1 Hz, 2H,  $\text{H}_h$ ), 6.66 (d,  $J_{ei}$  = 8.5 Hz, 2H,  $\text{H}_e$ ), 5.41 (s, 4H,  $\text{H}_d$ ), 4.62 (s, 4H,  $\text{H}_c$ ), 1.66 (s, 6H,  $\text{H}_a$ );  $^{13}\text{C}$  NMR (100 MHz, acetone- $\text{d}_6$ )  $\delta$  (ppm) 153.0 (s, 2C,  $\text{C}_n$ ), 149.3 (s, 2C,  $\text{C}_m$ ), 143.8 (s, 2C,  $\text{C}_l$ ), 129.9 (s, 4C,  $\text{C}_k$ ), 127.0 (s, 2C,  $\text{C}_j$ ), 125.7 (s, 2C,  $\text{C}_i$ ), 121.5 (s, 2C,  $\text{C}_g$ ), 121.3 (s, 2C,  $\text{C}_h$ ), 118.5 (s, 2C,  $\text{C}_f$ ), 116.8 (s, 2C,  $\text{C}_e$ ), 79.5 (s, 2C,  $\text{C}_d$ ) 50.8 (s, 2C,  $\text{C}_c$ ), 42.3 (s, 1C,  $\text{C}_b$ ), 31.4 (s, 2C,  $\text{C}_a$ );  $^{13}\text{C}$  NMR (100 MHz,  $\text{DMF-d}_7$ )  $\delta$  (ppm) 152.5 (s, 2C,  $\text{C}_n$ ), 148.7 (s, 2C,  $\text{C}_m$ ), 143.2 (s, 2C,  $\text{C}_l$ ), 129.4 (s, 4C,  $\text{C}_k$ ), 126.5 (s, 2C,  $\text{C}_j$ ), 125.3 (s, 2C,  $\text{C}_i$ ), 121.0 (s, 2C,  $\text{C}_g$ ), 120.8 (s, 2C,  $\text{C}_h$ ), 117.7 (s, 2C,  $\text{C}_f$ ), 116.2 (s, 2C,  $\text{C}_e$ ), 79.0 (s, 2C,  $\text{C}_d$ ) 50.0 (s, 2C,  $\text{C}_c$ ), 41.8 (s, 1C,  $\text{C}_b$ ), 30.9 (s, 2C,  $\text{C}_a$ ); HRMS Calcd for  $\text{C}_{31}\text{H}_{31}\text{O}_2\text{N}_2^+$ : 463.23800; Found: 463.23613; Elemental analysis Calcd for  $\text{C}_{31}\text{H}_{30}\text{O}_2\text{N}_2$ : C, 80.49; H, 6.54; N, 6.06; O, 6.92; Found: C, 81.46; H, 6.44; N, 5.73; O, 6.38.

**4.3 Preparation of Polybenzoxazine (PBO) Aerogels.** Formulations and gelation times for all aerogels are provided in Table S.1 of the Supporting Information. This section provides experimental details.

*4.3.a Via heat-induced polymerization at 130 °C.* In a typical procedure, BO monomer (e.g., 5 g, 0.011 mol) was dissolved in DMSO (20 g) by heating at 80 °C for approximately 2 h under  $\text{N}_2$ . The viscous yellow liquid was poured in glass molds (30 mL

Fisherbrand Class B Amber Glass Threaded Vials, 2.12 cm inner diameter, Fisher part No. 03-339-23E), which were sealed with their screw caps and kept at 130 °C in a convection oven. The gelation time varied depending on the concentration of the monomer. Higher concentration sols (e.g., 40% w/w BO monomer) gelled in approximately 12 h, while the lowest concentration sol (5% w/w BO monomer) required 3-4 days. Gels were aged in their molds at 130 °C for periods equal to their gelation time (i.e., 40 % w/w gels were aged for 12 h at 130 °C). At the end of that period glass molds were broken, wet-gels were removed and the pore-filling solvent (DMSO) was exchanged with acetone by washing 6×, 8 h each time. Finally, wet-gels were dried in an autoclave with liquid CO<sub>2</sub> taken out at the end as a supercritical fluid (SCF). The resulting aerogels are referred to as **PBO-H-xx-temperature**, where **H** stands for heat, **xx** for the weight percent of BO monomer in the sol (varied from 5 to 40), and **temperature** refers to the processing temperature. Thus, samples as-received after drying are referred to as **PBO-H-xx-130**.

*4.3.b Via acid-catalyzed polymerization at room temperature.* For example, 20% w/w concentration sols were obtained by mixing two solutions, one containing BO monomer (5 g, 0.011 mol) dissolved in 10 g (10.6 mL) DMF, with another one containing aqueous HCl (12.1 N, 1.04 g, 0.944 mL, 0.011 mol HCl) and DMF (9.9 g, 10.5 mL). The resulting sol was stirred at room temperature for 10 min and was poured in molds (either scintillation vials from Sigma-Aldrich, catalogue no. Z376825, inner diameter: 1.41 cm; or, Norm-Ject syringes (20 mL), purchased from Fisher Scientific, part no. 1481732, inner diameter: 2 cm - the top part of the syringes was cut off with a razor blade, and was covered with multiple layers of Parafilm<sup>TM</sup>). The gelation time again

varied depending on the concentration of the monomer. Higher concentration sols (e.g., 20% w/w BO monomer) gelled in 90 min from mixing, while the lowest concentration sol (5% w/w BO monomer) required 5 h. All gels were aged in their molds for a period of 4× their gelation time. Subsequently, wet-gels were removed from their molds, washed with DMF (2×, 12 h each time) and acetone (4×, 12 h each time), and dried with CO<sub>2</sub> taken out as a SCF. The resulting aerogels are referred to as **PBO-A-xx-RT**, where **A** stands for acid, **xx** for the weight percent of the BO monomer in the sol, and was varied from 5 to 20.

All PBO aerogels obtained via either route were step-cured in air at 160 °C (1 h), 180 °C (1 h) and 200 °C (24 h) using a conventional convection oven. Terminal samples after heating at 200 °C are referred to as **PBO-H-xx-200** or **PBO-A-xx-200**.

**4.4 Carbonization of PBO Aerogels.** All **PBO-H-xx-200** and **PBO-A-xx-200** were pyrolyzed in a tube furnace under flowing Ar (250-300 mL min<sup>-1</sup>) at 800 °C for 5 h. The furnace temperature was increase at 5 °C min<sup>-1</sup>, and to avoid cracking, cooling was also controlled at 5 °C min<sup>-1</sup>. Carbon aerogels are referred to as **C-H-xx-800** or **C-A-xx-800**.

**4.5 Methods.** SCF drying was conducted in an autoclave (SPI-DRY Jumbo Supercritical Point Dryer, SPI Supplies, Inc. West Chester, PA). Bulk densities ( $\rho_b$ ) were calculated from the weight and the physical dimensions of the samples. Skeletal densities ( $\rho_s$ ) were determined with helium pycnometry using a Micromeritics AccuPyc II 1340 instrument. Porosities ( $II$ ) as percent of empty space were determined from the  $\rho_b$  and  $\rho_s$  values via  $II=100\times[(\rho_s-\rho_b)/\rho_s]$ .

*Chemical Characterization.* CHN elemental analysis was conducted with Perkin-Elmer Model 2400 CHN Elemental Analyzer, calibrated with acetanilide purchased from the National Bureau of Standards. Elemental analysis via energy-dispersive x-ray spectroscopy (EDS) was conducted on a Hitachi Model S-4700 field-emission microscope equipped with an EDAX energy dispersive X-Ray unit and an Apollo SDD detector. Infrared (IR) spectra were obtained in KBr pellets using a Nicolet-FTIR Model 750 spectrometer. Liquid  $^1\text{H}$  NMR as well as liquid  $^{13}\text{C}$  NMR and APT (Attached Proton Test) spectra of the BO monomer were obtained with a 400 MHz Varian Unity Inova NMR instrument (100 MHz carbon frequency). For  $^{13}\text{C}$  NMR, chromium(III) trisacetylacetonate ( $\text{Cr}(\text{acac})_3$ , 5 mg) was added as a spin relaxation agent in combination with an 8 s relaxation delay. Solid-state  $^{13}\text{C}$  NMR spectra were obtained with samples ground into fine powders on a Bruker Avance 300 spectrometer with a carbon frequency of 75.475 MHz, using magic-angle spinning (at 7 kHz) with broadband proton suppression and the CPMAS TOSS pulse sequence for spin sideband suppression.

*Skeletal framework analysis.* Scanning electron microscopy (SEM) was conducted with Au-coated samples on a Hitachi Model S-4700 field-emission microscope. Small angle x-ray scattering (SAXS) was conducted with a PANalytical X'Pert Pro multipurpose diffractometer (MPD) configured for SAXS, using Cu  $K\alpha$  radiation ( $\lambda = 1.54 \text{ \AA}$ ) and a  $1/32^\circ$  SAXS slit and a  $1/16^\circ$  anti-scatter slit on the incident beam side, and 0.1 mm anti-scatter slit and Ni 0.125 mm automatic beam attenuator on the diffracted beam side. Samples were placed in circular holders between thin Mylar<sup>TM</sup> sheets and scattering intensities were measured with a point detector in transmission geometry by 2 Theta scans ranging from  $-0.1$  up to  $5^\circ$ . All scattering data were reported

in arbitrary units as a function of  $Q$ , the momentum transferred during a scattering event. Data analysis was conducted using the Beaucage Unified Model<sup>36</sup> applied with the *Irena SAS* tool for modeling and analysis of small angle scattering within the commercial *Igor Pro* application (scientific graphing, image processing, and data analysis software from Wave Metrics, Portland, OR).

*Porosimetry.* Surface area, and pore size distributions for smaller pores were determined with N<sub>2</sub> sorption porosimetry using a Micromeritics ASAP 2020 surface area and porosity analyzer equipped with low pressure transducer (0.1 Torr) for micropore analysis. Samples for porosimetry and skeletal density determination were outgassed for 24 h, at 80 °C, under vacuum, before analysis. Average pore diameters were determined with the  $4 \times V / \sigma$  method, where  $V$  is the pore volume per gram of sample and  $\sigma$ , the surface area determined by the Brunauer-Emmett-Teller (BET) method.  $V$  can be taken either as the single highest volume of N<sub>2</sub> adsorbed along the adsorption isotherm, or can be calculated from the relationship  $V = V_{\text{Total}} = (1/\rho_b) - (1/\rho_s)$ . Materials lack macroporosity when the two average pore diameters calculated with the two different  $V$  values coincide. The average pore diameters for macroporous samples were probed with Hg-intrusion porosimetry using a Micromeritics Autopore IV instrument, Model 9500.

*Mechanical characterization.* Quasi-static compression was conducted on an Instron Model 4469 universal testing machine frame, following the testing procedures and specimen length-to-diameter ratio (2.0 cm/1.0 cm) that was specified in ASTM D1621-04a (“Standard Test Method for Compressive Properties of Rigid Cellular foam”)

*Thermal analysis.* Thermogravimetric analysis (TGA) was conducted under N<sub>2</sub> or air with a TA Instruments Model TGA Q50 thermogravimetric analyzer, using a heating

rate of 5 °C min<sup>-1</sup>. Differential scanning calorimetry (DSC) was conducted with a TA Instruments apparatus Model TA-DSC 2010 at a heating rate of 10 °C min<sup>-1</sup>. Samples were subjected to two heating scans and one cooling scan from 25 °C to 300 °C. Thermal conductivities,  $\lambda$ , were calculated at 23 °C via  $\lambda = R \times c_p \times \rho_b$ . The thermal diffusivities,  $R$ , was determined with a Netzsch NanoFlash Model LFA 447 flash diffusivity instrument using disk samples ~1 cm in diameter, 2-3 mm thick (the thickness of each sample was measured with 0.01mm resolution and was entered as required by the data analysis software). The heat capacity of polybenzoxazine, ( $c_p = 1.384 \text{ J g}^{-1} \text{ K}^{-1}$ ) was taken from the literature.<sup>37</sup> The radiative contribution to  $\lambda$ ,  $\lambda_{\text{irr}}$ , was eliminated by first sputter-coating the samples with Au, followed by spray-coating with carbon black. The gaseous contribution to  $\lambda$ ,  $\lambda_g$ , was calculated using Knudsen's equation (see Table S.4 in the Supporting Information). The solid conduction component of  $\lambda$ ,  $\lambda_s$ , was then calculated from  $\lambda_s = \lambda - \lambda_g$ .

**SUPPORTING INFORMATION.** Aerogel formulations and gelation times (Table S.1). Elemental analysis data of PBO aerogels, carbon aerogels and aerogels during carbonization (Table S.2). Complete N<sub>2</sub>-sorption primary data of PBO aerogels (Figure S.1). Complete Hg-intrusion primary data of PBO aerogels (Figure S.2). SAXS data (Figure S.3 and Table S.3). Thermal conductivity data (Table S.4). Mechanical characterization data (Figure S.4). This information is available free of charge via the Internet at <http://pubs.acs.org>.

**ACKNOWLEDGEMENTS.** This project was supported by the Army Research Office under Award Numbers W911NF-10-1-0476 and W911NF-12-2-0029. The project was initiated with funding from the National Science Foundation (NSF-DMR-0907291). We



also thank the Materials Research Center of MS&T for support with materials characterization, and Dr. Wei Wycoff of the University of Missouri Columbia for her assistance with solid state NMR.

Table 3. Properties of **PBO-A-xx-200** and **PBO-H-xx-200** polybenzoxazine aerogels

Sample <sup>a</sup>	Linear shrinkage [%] <sup>b, c</sup>	Bulk density $\rho_b$ [g cm <sup>-3</sup> ] <sup>b</sup>	Skeletal density $\rho_s$ [g cm <sup>-3</sup> ] <sup>d</sup>	Porosity $\Pi$ [% v/v]	BET Surface area, $\sigma$ [m <sup>2</sup> g <sup>-1</sup> ]	Pore volume (cm <sup>3</sup> g <sup>-1</sup> )		Average pore diameter [nm]			particle diameter [nm] <sup>h</sup>
						$V_{\text{Total}}$ <sup>e</sup>	$V_{1.7-300\text{nm}}$ <sup>f</sup>	via $4V/\sigma$		from Hg-intrusion <sup>g</sup>	
								V: single max point adsorption	$V=V_{\text{Total}}$		
<b>PBO-A-5-200</b> *	26.24 ± 0.20	0.109 ± 0.006	1.314 ± 0.007	917	72.2	8.41	0.18	11	466	393	64 (95.4)
<b>PBO-A-7-200</b> **	30.85 ± 0.21	0.224 ± 0.018	1.305 ± 0.005	82.8	60.7	3.69	0.15	11	244	185	76 (91.8)
<b>PBO-A-10-200</b>	36.17 ± 0.60	0.373 ± 0.019	1.320 ± 0.006	71.7	65.6	1.92	0.19	13	117	90	70 (82.0)
<b>PBO-A-12-200</b> ***	34.43 ± 0.05	0.483 ± 0.051	1.321 ± 0.004	63.4	60.1	1.31	0.19	13	87	80	76 (58.8)
<b>PBO-A-15-200</b>	35.46 ± 0.05	0.560 ± 0.024	1.319 ± 0.002	57.5	69.8	1.03	0.39	23	59	41	65 (64.4)
<b>PBO-A-20-200</b> ****	32.15 ± 0.17	0.670 ± 0.030	1.333 ± 0.002	49.7	64.6	0.74	0.37	23	46	46	70 (52.0)
<b>PBO-H-5-200</b>	28.84 ± 1.16	0.075 ± 0.013	1.317 ± 0.007	94.3	63.9	12.57	0.15	11	787	748	70 (117)
<b>PBO-H-10-200</b> *	23.39 ± 0.49	0.112 ± 0.015	1.261 ± 0.005	91.1	46.9	8.13	0.15	13	694	606	102 (112)
<b>PBO-H-15-200</b> **	28.38 ± 0.66	0.232 ± 0.021	1.275 ± 0.004	81.8	32.8	3.52	0.09	12	430	399	144 (105)
<b>PBO-H-20-200</b> ***	33.11 ± 1.68	0.447 ± 0.072	1.278 ± 0.005	65.0	25.5	1.45	0.04	13	227	146	184 (92.0)
<b>PBO-H-30-200</b> ****	29.60 ± 0.80	0.670 ± 0.051	1.245 ± 0.005	46.1	23.7	0.69	0.08	15	116	84	204 (83.8)
<b>PBO-H-40-200</b>	22.87 ± 0.75	0.732 ± 0.020	1.208 ± 0.002	39.4	20.3	0.59	0.06	13	106	63	244 (95.6)

<sup>a</sup> Asterisks match samples of approximately equal bulk densities. <sup>b</sup> Average of ten samples. <sup>c</sup> Shrinkage =  $100 \times (\text{mold diameter} - \text{sample diameter})/(\text{mold diameter})$ . <sup>d</sup> Single sample, average of 50 measurements. <sup>e</sup> Via  $V_{\text{Total}} = (1/\rho_b) - (1/\rho_s)$ . <sup>f</sup> BJH-desorption cumulative pore volume. <sup>g</sup> From the Log(differential intrusion) versus pore diameter plot. <sup>h</sup> Via  $d = 6/\rho_s\sigma$ ; for number in (parentheses), diameter was calculated from SAXS data (see Figure S.3 and Table S.3 in the Supporting Information).

Table 4. Properties of nanoporous carbons derived from **PBO-A-xx-200** and **PBO-H-xx-200** aerogels

Sample <sup>a</sup>	Carbonization yield [% w/w] <sup>b</sup>	Linear Shrinkage [%] <sup>b,c</sup>	Bulk density $\rho_b$ [g cm <sup>-3</sup> ] <sup>b</sup>	Skeletal density $\rho_s$ [g cm <sup>-3</sup> ] <sup>d</sup>	Porosity $\Pi$ [% v/v]	BET Surface area, $\sigma$ (micropore area) [m <sup>2</sup> g <sup>-1</sup> ]	Pore volume (cm <sup>3</sup> g <sup>-1</sup> )			Mesopore diameter [nm] <sup>h</sup>	Micropore diameter [Å] <sup>i</sup>
							$V_{\text{Total}}$ <sup>e</sup>	$V_{1.7-300 \text{ nm}}$ <sup>f</sup>	$V_{\text{micropore}}$ <sup>g</sup>		
<b>C-A-5-800</b> *	58 ± 1	20.0 ± 0.2 (41)	0.126 ± 0.012	1.894 ± 0.043	93	516 (427)	7.40	0.11	0.17	24.1 (14.2)	5.622
<b>C-A-10-800</b> **	58 ± 1	25.6 ± 0.5 (53)	0.469 ± 0.013	1.806 ± 0.019	74	510 (422)	1.58	0.19	0.13	34.9 (32.6)	5.728
<b>C-A-15-800</b>	56 ± 2	20.9 ± 0.3 (49)	0.724 ± 0.032	1.902 ± 0.005	62	524 (431)	0.85	0.54	0.11	39.0 (26.4)	5.570
<b>C-A-20-800</b>	61 ± 3	20.8 ± 0.2 (46)	0.886 ± 0.025	1.870 ± 0.003	53	348 (258)	0.59	0.36	0.14	26.0 (19.0)	5.943
<b>C-H-5-800</b>	53 ± 3	16.3 ± 0.5 (40)	0.090 ± 0.015	1.655 ± 0.055	94	61 (7)	10.50	0.14	0.01	65.3 (44.2)	7.698
<b>C-H-10-800</b> *	50 ± 3	21.6 ± 0.4 (40)	0.127 ± 0.019	1.799 ± 0.034	93	190 (132)	7.31	0.20	0.16	64.4 (43.7)	5.467
<b>C-H-15-800</b>	54 ± 3	28.3 ± 0.8 (49)	0.227 ± 0.008	1.863 ± 0.050	88	347 (265)	3.86	0.25	0.09	59.9 (77.3)	5.740
<b>C-H-20-800</b> **	55 ± 3	28.8 ± 0.4 (52)	0.450 ± 0.083	1.790 ± 0.014	75	372 (301)	1.66	0.06	0.15	21.1 (24.1)	5.610

<sup>a</sup> Asterisks match samples of approximately equal bulk densities. <sup>b</sup> Average of 5 samples. <sup>c</sup> Shrinkage relative to parent PBO aerogels =  $100 \times [1 - (\text{C-sample diameter} / \text{PBO-sample diameter})]$ . Values in (parentheses): total shrinkage relative to the original molds. <sup>d</sup> Single sample, average of 50 measurements. <sup>e</sup> Via  $V_{\text{Total}} = (1/\rho_b) - (1/\rho_s)$ . <sup>f</sup> BJH-desorption cumulative pore volume. <sup>g</sup> Cumulative volume of N<sub>2</sub> adsorbed at  $P/P_0 \leq 0.1$  using a low-pressure N<sub>2</sub> dosing routine. <sup>h</sup> Maxima of BJH-desorption plots. Values in (parentheses): widths at half maxima (nm). <sup>i</sup> Median pore width obtained with the Horvath-Kawazoe method applied to N<sub>2</sub>-sorption data under low-pressure dosing.

## REFERENCES

1. Ishida, H. "Overview and Historical Background of Polybenzoxazine Research," in *Handbook of Benzoxazine Resins*, Ishida, H.; Agag, T. Ed.s, Elsevier: New York, N.Y., 2011, Chapter 1, pp 3-81.
2. (a) Demir, K. D.; Kiskan, B.; Yagci, Y. *Macromolecules*, **2011**, *44*, 1801-1807. (b) Low, H. Y.; Ishida, H. *Polymer* **1999**, *40*, 4365-4376. (c) Takeichi, T.; Guo, Y.; Rimdusit, R. *Polymer* **2005**, *46*, 4909-4916. (d) Takeichi, T.; Agag, T.; Rachib, Z. *J. Polym. Sci., Part A: Polym. Chem.* **2001**, *39*, 2633-2641.
3. Holly, F. W.; Cope, A. C. *J. Am. Chem. Soc.* **1944**, *66*, 1875.
4. Ning, X.; Ishida, H. *J. Polym. Sci.: Part A: Polym. Chem.* **1994**, *32*, 1121-1129.
5. (a) Ning, X.; Ishida, H. *J. Polym. Sci.:Part A: Polym. Chem.* **1994**, *32*, 921-927 (b) Ishida H. U.S. Patent No. 5,543,516 (1996).
6. Santhosh Kumar K. S. "Polybenzoxazines and State-of-the-Art High-Temperature Polymers," in *Polybenzoxazines: Chemistry and Properties*, Santhosh Kumar, K. S.; Raghunadhan Nair, C. P. Ed.s, iSmithers Rapra Technology: Shrewsbury, Shropshire, 2010, Chapter 1.
7. Kumar, K. S. S.; Nair, C. P.; Ninan, K. N. *J. Appl. Polym. Sci.* **2008**, *108*, 1021-1028.
8. Lorjai, P.; Wongkasemjit, S.; Chaisuwan, T. *Mat. Sci. Eng. A* **2009**, *527*, 77-84.
9. Su, Y. C.; Chen, W. C.; Ou, K. L.; Chang, F. C. *Polymer* **2005**, *46*, 3758-3766.
10. Chu, W.-C.; Li, J.-G.; Kuo, S.-W. *RSC Adv.* **2013**, *3*, 6485-6498.
11. See for example: (a) Amatani, T.; Nakanishi, K.; Hirao, K.; Kodaira, T. *Chem. Mater.* **2005**, *17*, 2114-2119. (b) Leventis, N.; Mulik, S.; Wang, X.; Dass, A.; Patil, V. U.; Sotiriou-Leventis, C.; Lu, H.; Churu, G.; Capecelatro, A. *J. Non-Cryst. Solids* **2008**, *354*, 632-644.
12. (a) Lorjai, P.; Chaisuwan, T.; Wongkasemjit, S. *J. Sol-Gel Sci. Technol.* **2009**, *52*, 56-64. (b) Lorjai, P.; Wongkasemjit, S.; Chaisuwan, T.; Jamieson, A. M. *Polym. Degrad. Stabil.* **2011**, *96*, 708-718.
13. Rubenstein, D. A.; Lu, H.; Mahadik, S. S.; Leventis, N. Yin, W. *J. Biomat. Sci.-Polym. E* **2012**, *23*, 1171-1184.
14. (a) Pekala, R. W. *J. Mater. Sci.* **1989**, *24*, 3221-3227. (b) Pekala, R. W.; Alviso, C. T.; Kong, F. M.; Hulse, S. S. *J. Non-Cryst. Solids* **1992**, *145*, 90-98. (c) Al-Muhtaseb, S. A.; Ritter, J. A. *Adv. Mater.* **2003**, *15*, 101-114. (d) Mulik, S.; Sotiriou-Leventis, C.; Leventis, N. *Chem. Mater.* **2008**, *20*, 6985-6997.

15. This point can be debated both ways as the typical base-catalyzed RF synthesis is also an elevated-temperature, multi-day process. Our statement rather refers to the acid-catalyzed gelation of RF that is faster and takes place at lower temperatures: Mulik, S.; Sotiriou-Leventis, C.; Leventis, N. *Chem. Mater.* **2007**, *19*, 6138-6144.
16. Dunkens, J.; Ishida, H. *J. Polym. Sci.: Part A: Polym. Chem.* **1999**, *37*, 1913-1921.
17. (a) Wang, Y.-X.; Ishida, H. *Polymer* **1999**, *40*, 4563-4570. (b) Wang, Y.-X.; Ishida, H. *Macromolecules* **2000**, *33*, 2839-2847.
18. (a) Liu, C.; Shen, D.; Sebastián, R. M.; Marquet, J.; Schönfeld, R. *Macromolecules* **2011**, *44*, 4616-4622. (b) Ran, Q.-C.; Zhang, D.-X.; Zhu, R.-Q.; Gu, Y. *Polymer* **2012**, *53*, 4119-4127. (c) Liu, C.; Shen, D.; Sebastián, R. M.; Marquet, J.; Schönfeld, R. *Polymer* **2013**, *54*, 2873-2878.
19. (a) Takeichi, T.; Kano, T.; Agag, T. *Polymer* **2005**, *46*, 12172-12180. (b) Andronescu, C.; Gârea, S. A.; Deleanu, C.; Lovu, H. *Thermochim. Acta* **2012**, *530*, 42-51.
20. Velez-Herrera, P.; Doyama, K.; Abe, H.; Ishida, H. *Macromolecules* **2008**, *41*, 9704-9714.
21. (a) Sadekar, A. G.; Mahadik, S. S.; Bang, A. N.; Larimore, Z. J.; Wisner, C. A.; Bertino, M. F.; Kalkan, A. K.; Mang, J. T.; Sotiriou-Leventis, C.; Leventis, N. *Chem. Mater.* **2012**, *24*, 26-47. (b) Rahaman, M. S. A.; Ismail, A. F.; Mustafa, A. *Polym. Degrad. Stab.* **2007**, *92*, 1421-1432. (c) Usami, T.; Itoh, T.; Ohtani, H.; Tsuge, S. *Macromolecules* **1990**, *23*, 2460-2465. (d) Morgan, P. *Carbon Fibers and Their Composites*; CRC Press: Boca Raton, FL, 2005.
22. Ishida, H.; Sanders, D. P. *Macromolecules* **2000**, *33*, 8149-8137.
23. Silverstein, R. M.; Webster, F. X. *Spectrometric Identification of Organic Compounds*, 6<sup>th</sup> ed., John Wiley & Sons, New York, N.Y., 1999, Chapter 3, pp 71-143.
24. Huang, R.; Carson, S. O.; Silva, J.; Aga, T.; Ishida, H.; Maia, J. M. *Polymer*, **2013**, *54*, 1880-1886.
25. (a) Liu, Y.; Zhao, S.; Zhang, H.; Wang, M.; Run, M. *Thermochim. Acta.* **2012**, *549*, 42-48. (b) Dunkers, J.; Ishida, H. *Spectrochim. Acta.* **1995**, *51A*, 855-867.
26. (a) Reiss, G.; Schwob, J. M.; Guth, G.; Roche, M.; Lande, B. *Advances in Polymer Synthesis*; Culbertson, B. M., McGrath, J. E., Eds., Plenum: New York, 1986. pp 27-30 (b) Chutayothin, P.; Ishida, H. *Macromolecules*, **2010**, *43*, 4562-4575.

27. Sawyer, D. T.; Valentine, J. S. *Acc. Chem. Res.* **1981**, *14*, 393-400. (b) Wilshire, J.; Sawyer, D. T. *Acc. Chem. Res.* **1979**, *12*, 105-110. (c) Collins, C. M.; Sotiriou-Leventis, C.; Canalias, M. T.; Leventis, N. *Electrochimica Acta* **2000**, *45*, 2049-2059. Collins, C. M.; Leventis, N.; Sotiriou-Leventis, C. *Electrochimica Acta* **2001**, *47*, 567-576.
28. (a) Ghosh, N. N.; Kiskn B.; Yagci, Y. *Prog. Polym. Sci.* **2007**, *32*, 1344-1391. (b) Ishida, H.; Allen, D. J. *Polymer*, 1996, *37*, 4487-4495.
29. Chaisuwan, T. "Porous Materials from Polybenzoxazine," in *Handbook of Benzoxazine Resins*, Ishida, H.; Agag, T. Ed.s, Elsevier: New York, N.Y., 2011, Chapter 26, pp 457-468.
30. Mohite, D. P.; Mahadik-Khanolkar, S.; Luo, H.; Lu, H.; Sotiriou-Leventis, C.; Leventis, N. *Soft Matter* **2013**, *9*, 1531-1539.
31. Mohite, D. P.; Larimore, Z. J.; Lu, H.; Mang, J. T.; Sotiriou-Leventis, C.; Leventis, N. *Chem. Mater.* **2012**, *24*, 3434-3448.
32. Weigold, L.; Mohite, D. P.; Mahadik-Khanolkar, S.; Leventis, N.; Reichenauer, G. *J. Non-Cryst. Solids* **2013**, *368*, 105-111.
33. (a) Lu, X.; Caps, R.; Fricke, J.; Alviso, C. T.; Pekala, R. W. *J. Non-Cryst. Solids* **1995**, *188*, 226-234. (b) Lu, X.; Nilsson, O.; Fricke, J.; Pekala, R. W. *J. Appl. Phys.* **1993**, *73*, 581-584. (c) Chidambareswarapattar, C.; McCarver, P. M.; Luo, H.; Lu, H.; Sotiriou-Leventis, C.; Leventis, N. *Chem. Mater.* **2013**, *25*, 3205-3224.
34. McKenzie, D. R.; Muller, D.; Pailthorpe, B. A. *Phys. Rev. Lett.* **1991**, *67*, 773-776.
35. (a) McKeown, N. B.; Budd, P. M.; Msayib, K. J.; Ghanem, B. S.; Kingston, H. J.; Tattershall, C. E.; Makhseed, S.; Reynolds, K. J.; Fritsch, D. *Chem. Eur. J.* **2005**, *11*, 2610-2620. (b) Mckeown, N. B.; Budd, P. M. *Macromolecules* **2010**, *43*, 5163-5176. (c) Jiang, S.; Jones, J. T. A.; Hasell, T.; Blythe, C. E.; Adams, D. J.; Trewin, A.; Cooper, A. I. *Nature Commun.* **2011**, *2*, 207 DOI: 10.1038/ncomms1207.
36. (a) Beaucage, G. *J. Appl. Cryst.* **1995**, *28*, 717-728. (b) Beaucage, G. *J. Appl. Cryst.* **1996**, *29*, 134-146.
37. Ishida, H.; Rimdusit, S. *J. Therm. Anal. Calorim.* **1999**, *58*, 497-507.

## FIGURES

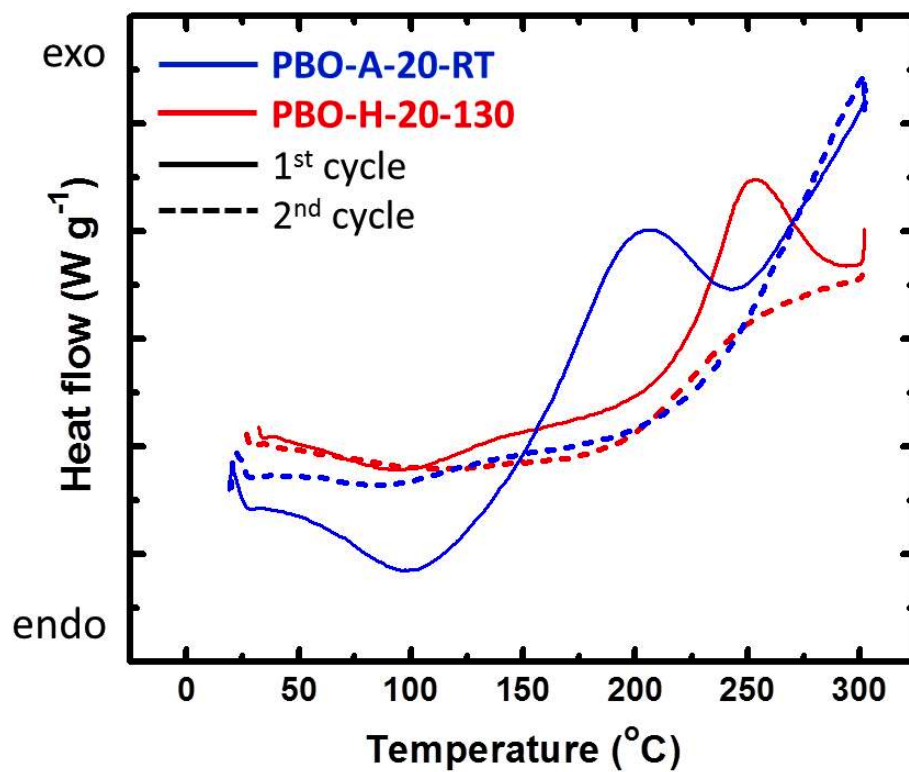


Figure 1 Differential scanning calorimetry (DSC) in air at 10 °C min<sup>-1</sup> of representative PBO aerogel samples as shown.

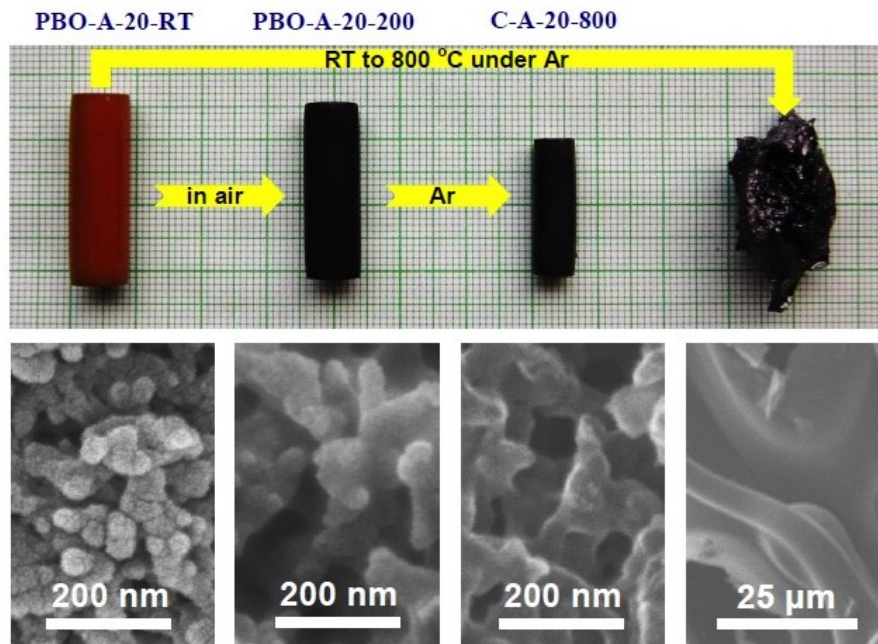


Figure 2 Optical photographs and the corresponding SEMs of representative HCl-catalyzed PBO aerogel monoliths at all stages of processing. Note that as-prepared samples pyrolyzed directly at 800 °C under inert atmosphere (Ar) do not yield nanoporous monoliths. (The carbonization yield was also low: 27% w/w versus 61% w/w from the air-cured samples – see Table 4.)



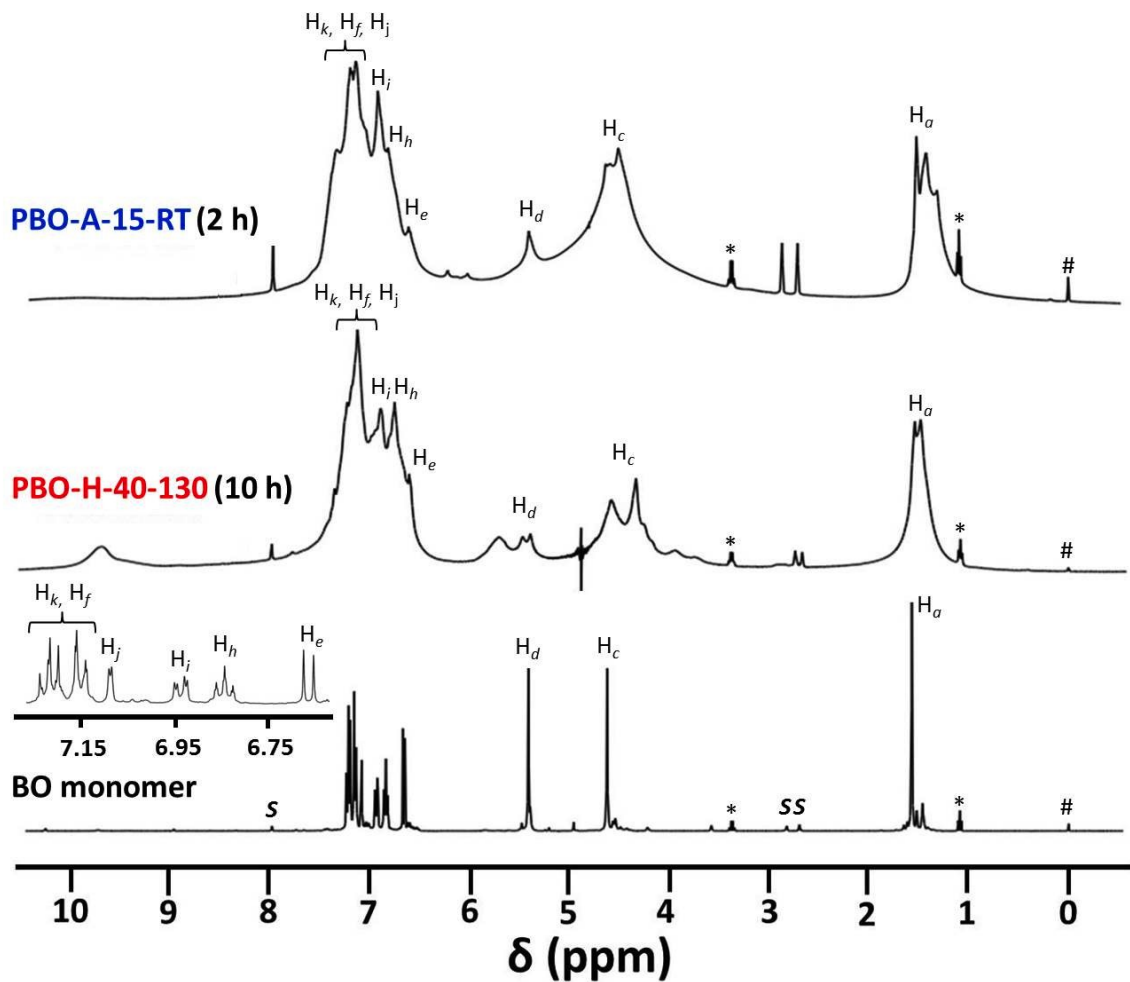


Figure 3  $^1\text{H}$  NMR of the BO monomer in  $\text{DMF-d}_7$  and of two representative sols, also in  $\text{DMF-d}_7$ , with the formulations shown at their respective gelation points (in parentheses). Acid-catalyzed PBO-A-15-RT gelled at room temperature, while the heat-polymerized PBO-H-40-130 gelled at 130  $^\circ\text{C}$ . “S” denotes solvent.

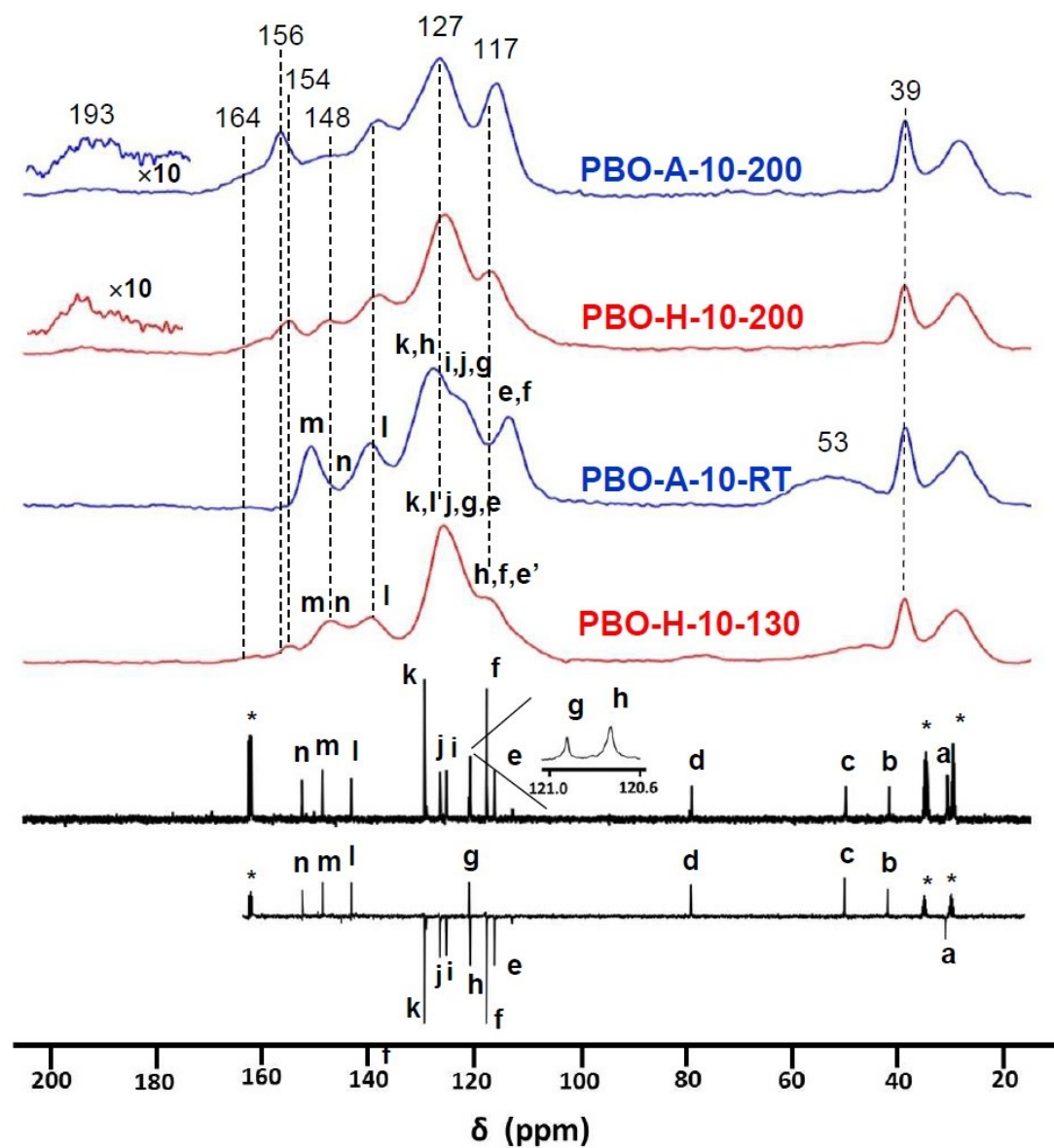


Figure 4 Liquid  $^{13}\text{C}$  NMR spectra of the BO monomer in the APT and the normal mode (bottom, and second from bottom, respectively) in DMF- $d_7$  (marked with asterisks) containing chromium(III) tris(acetylacetonate). Peak assignments were based on integrated intensity and the APT spectrum. Solid-state CPMAS  $^{13}\text{C}$  NMR spectra of the aerogels samples as shown are cited above. (All samples shown were prepared with the same weight percent of BO monomer in the sol: -xx-:10.)

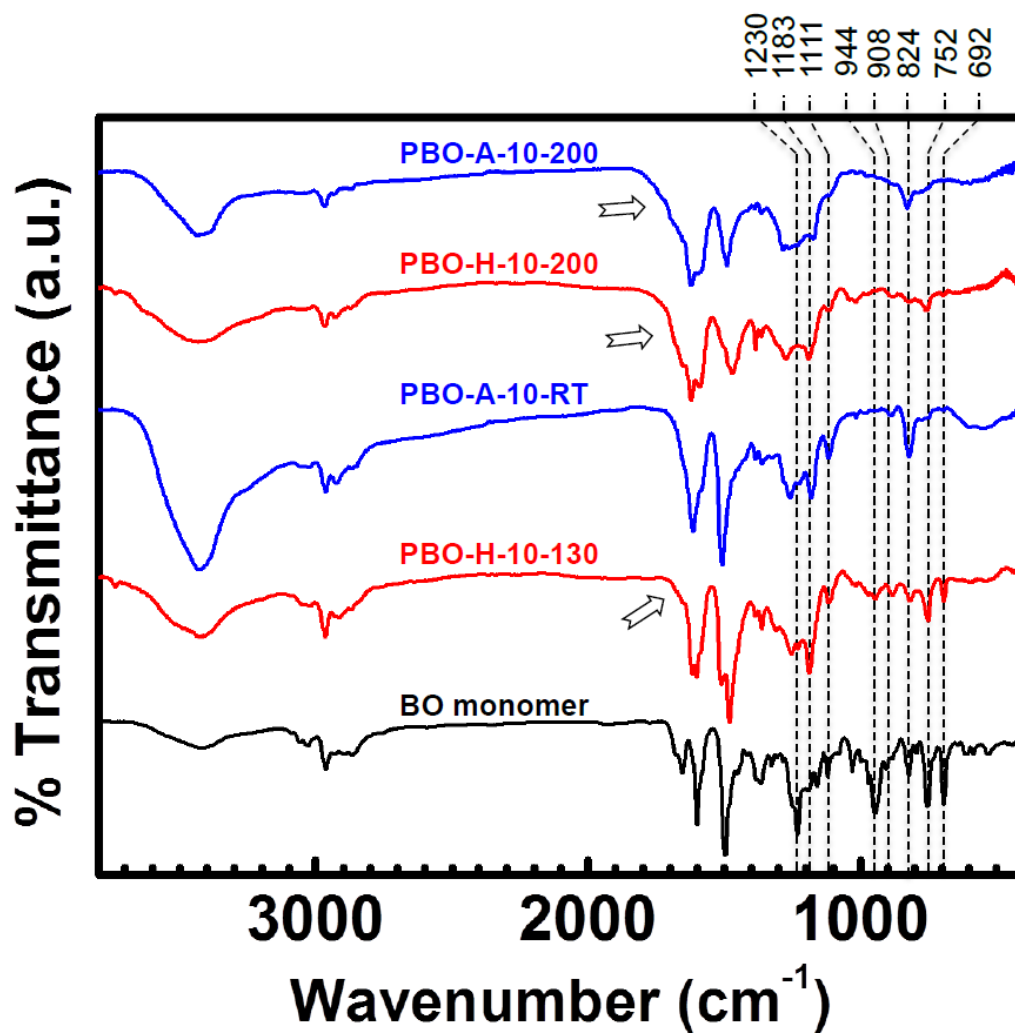


Figure 5 Infrared (FTIR) spectra of the BO monomer and of representative aerogel samples as shown. (All samples shown were prepared with the same weight percent of BO monomer in sol: -xx-:10.)

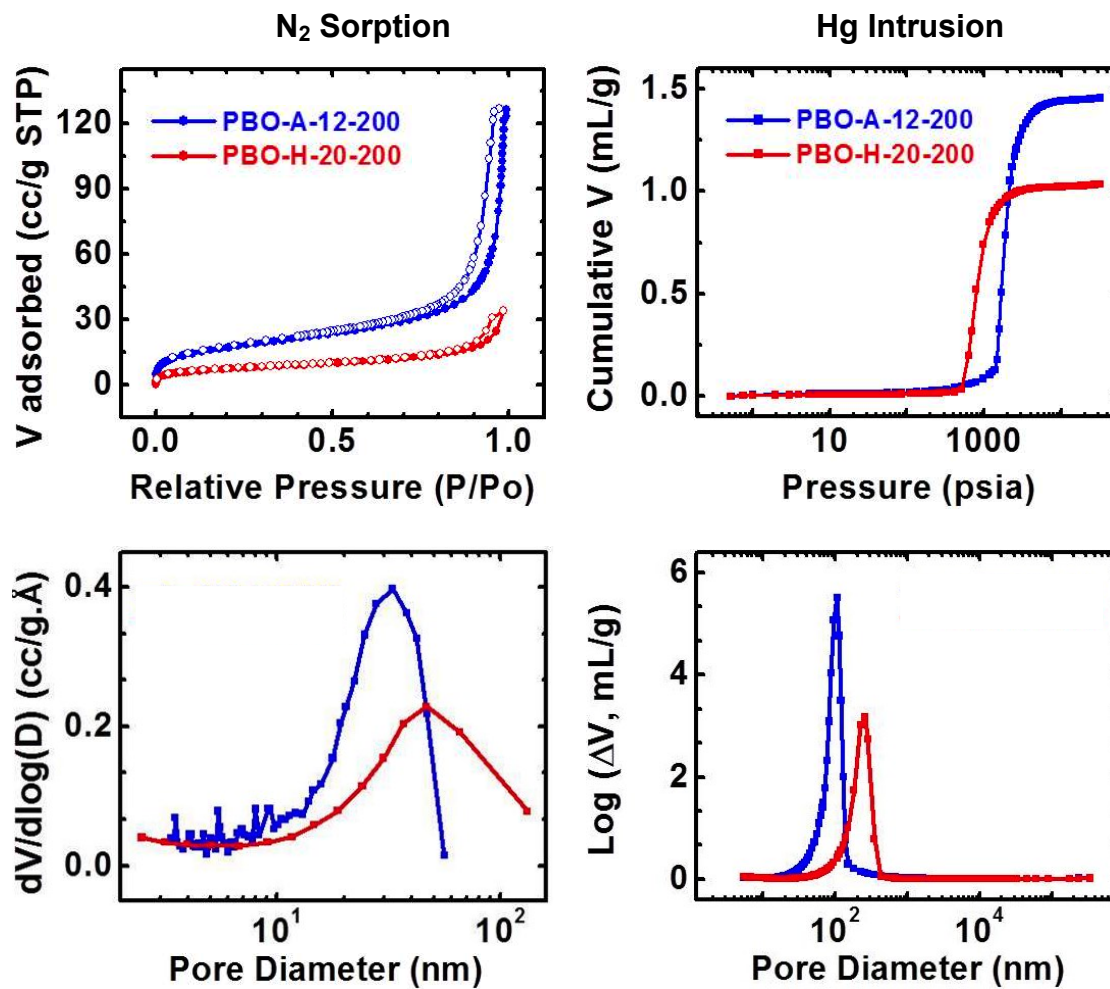


Figure 6 Representative porosimetry (top) and pore size distribution data of cured (200 °C/air), density-matched A- and H- PBO samples as shown (PBO-A-12-200,  $\rho_b=0.483$  g cm<sup>-3</sup>; PBO-H-20-200,  $\rho_b=0.447$  g cm<sup>-3</sup>). Left: N<sub>2</sub> sorption data; Right: Hg-intrusion data.

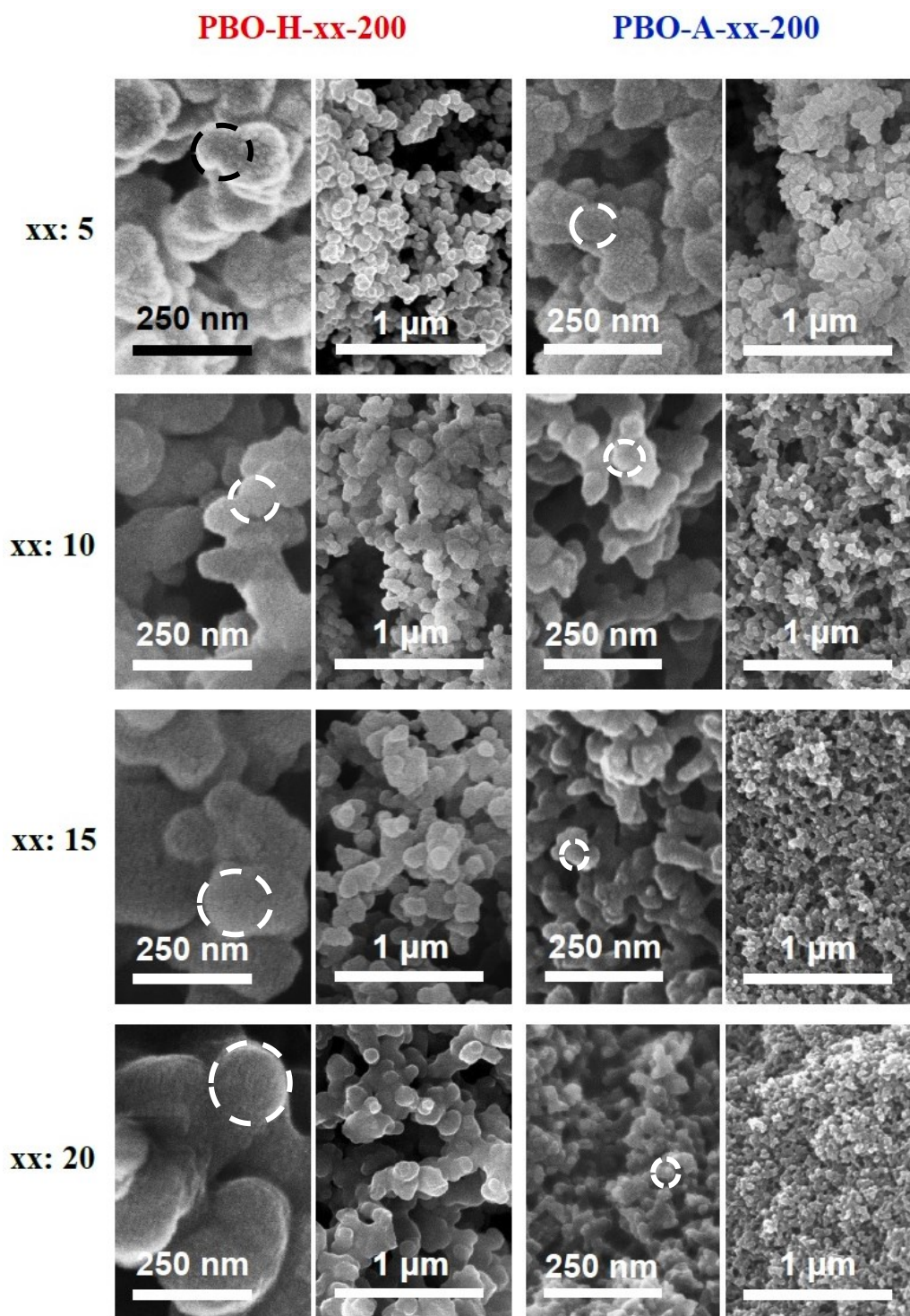


Figure 7 Scanning electron microscopy (SEM) at two different magnifications of heat- and acid-polymerized PBO aerogels at different sol concentrations (-xx-) as shown. Dashed circles indicate the smallest particles identifiable.

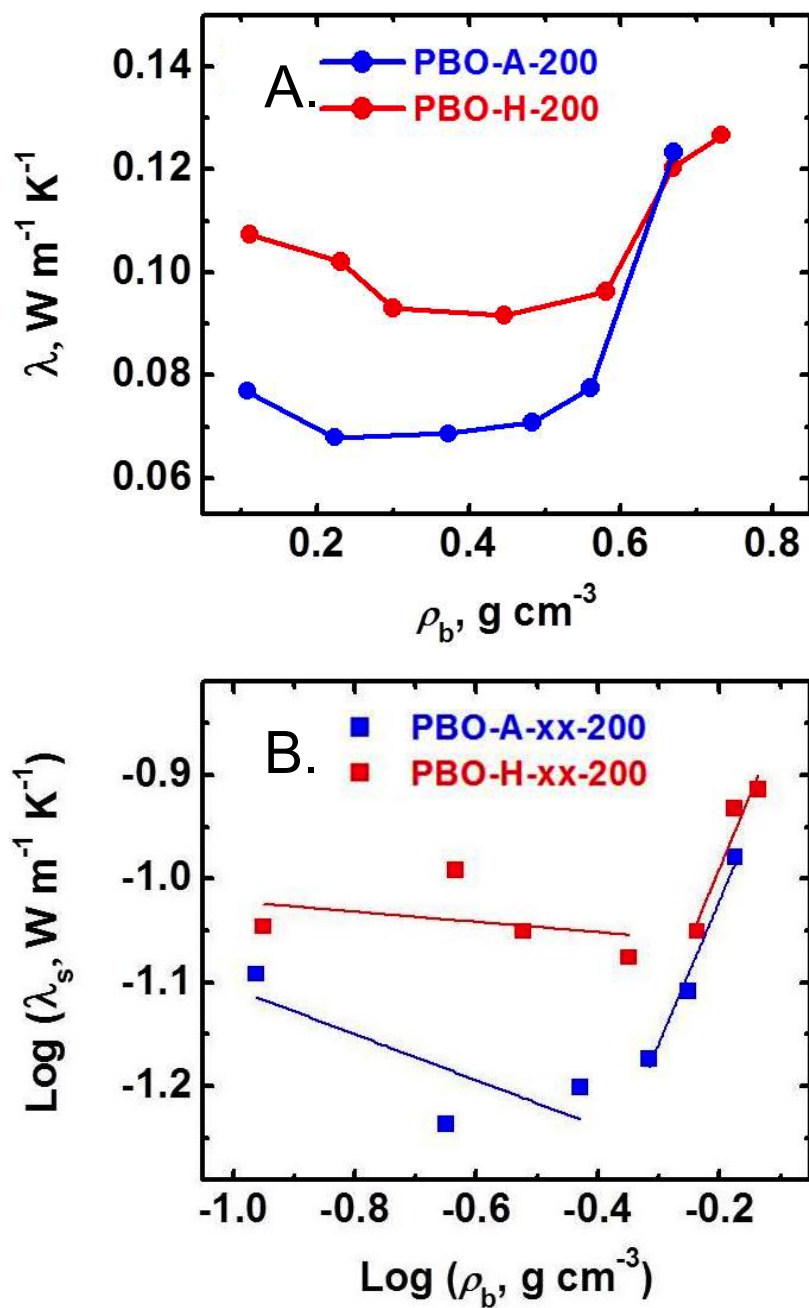


Figure 8 A. Total thermal conductivity data ( $\lambda$ ) as a function of bulk density ( $\rho_b$ ) of PBO aerogels. B. Log-Log plot of the thermal conductivity through the solid framework ( $\lambda_s$ ) versus bulk density of PBO aerogels as shown.

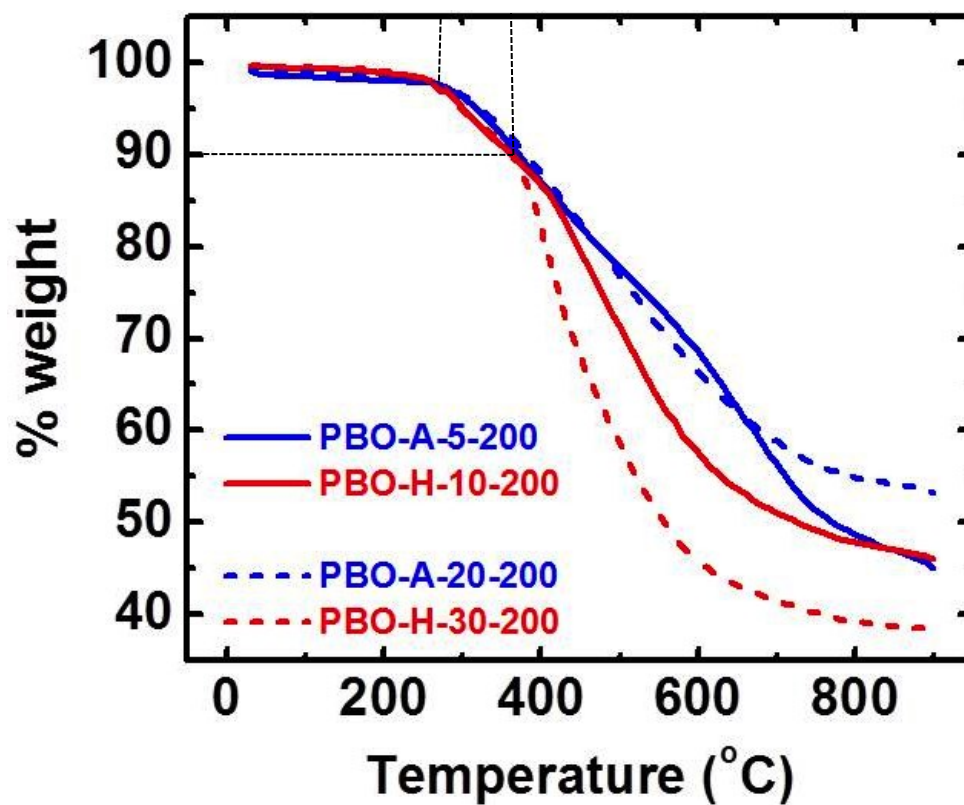


Figure 9 Thermogravimetric analysis ( $5\text{ }^{\circ}\text{C min}^{-1}$ ) under high purity nitrogen of bulk density-matched PBO aerogels samples as shown. (For  $\rho_b$  values see Table 3.)

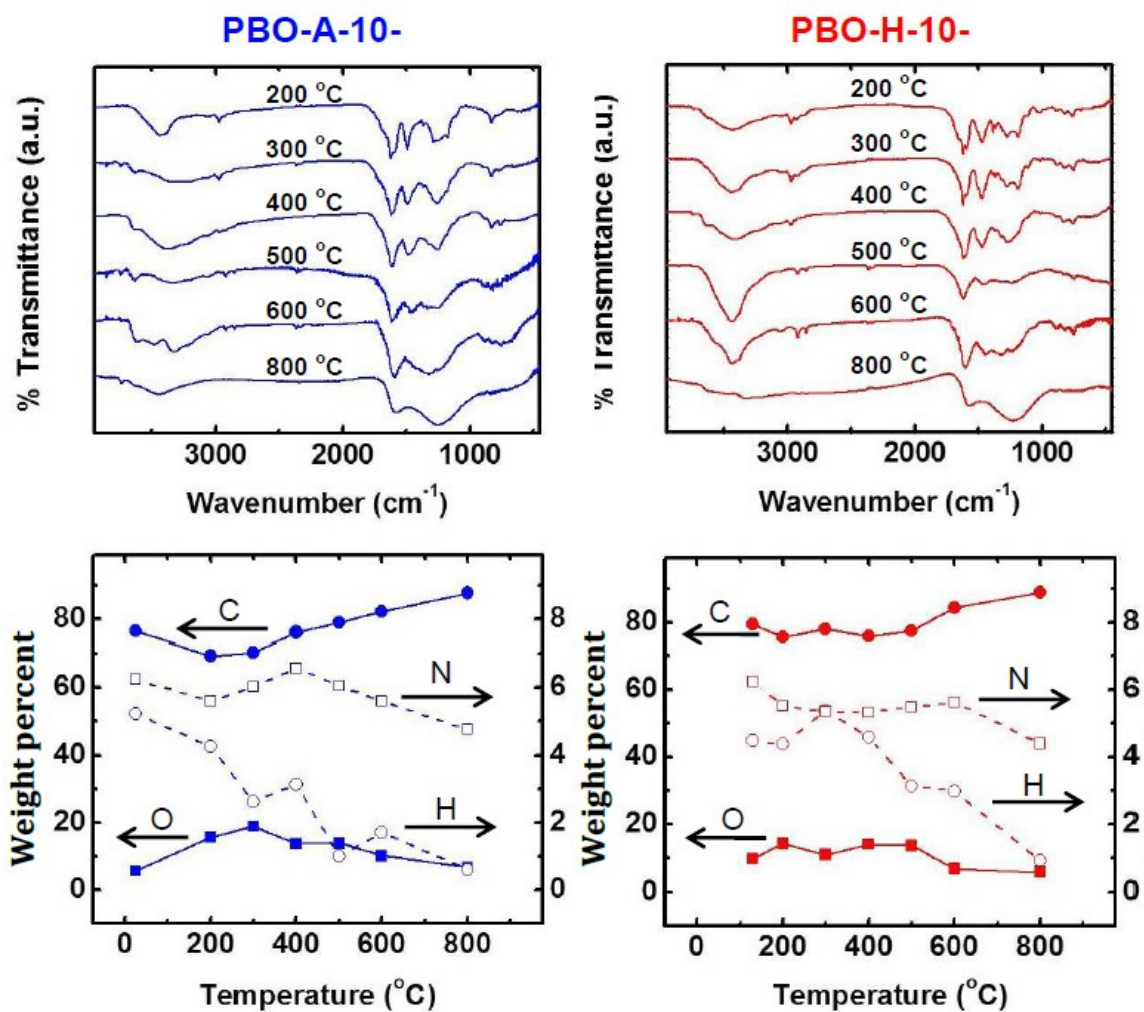


Figure 10 Elemental analysis data and evolution of IR spectra of PBO aerogels at progressively higher pyrolysis temperatures (5 h under high-purity Ar).



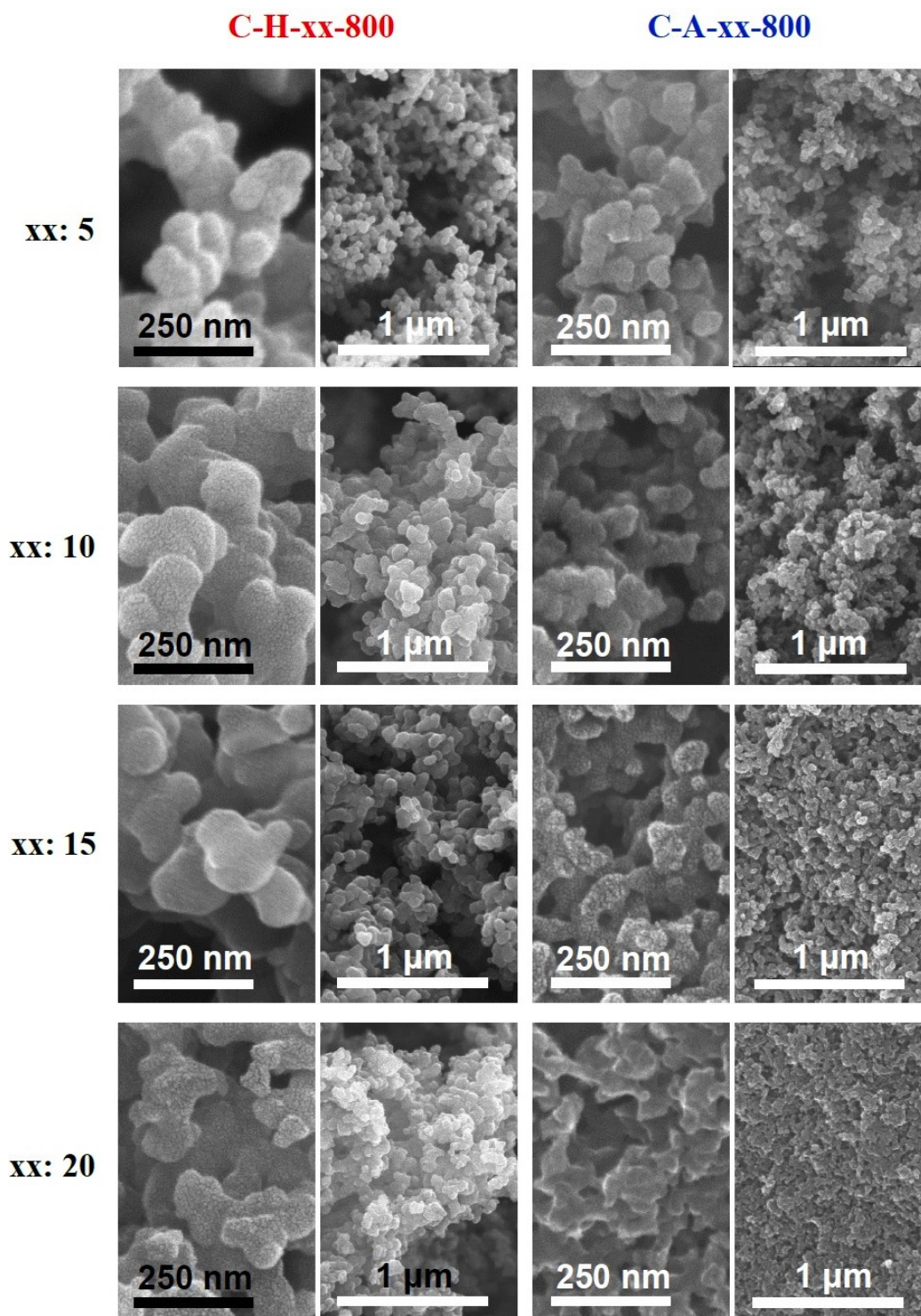


Figure 11 Scanning electron microscopy (SEM) at two different magnifications of carbon aerogels originating from heat- and acid-polymerized PBO aerogels at different sol concentrations (-xx-) as shown.

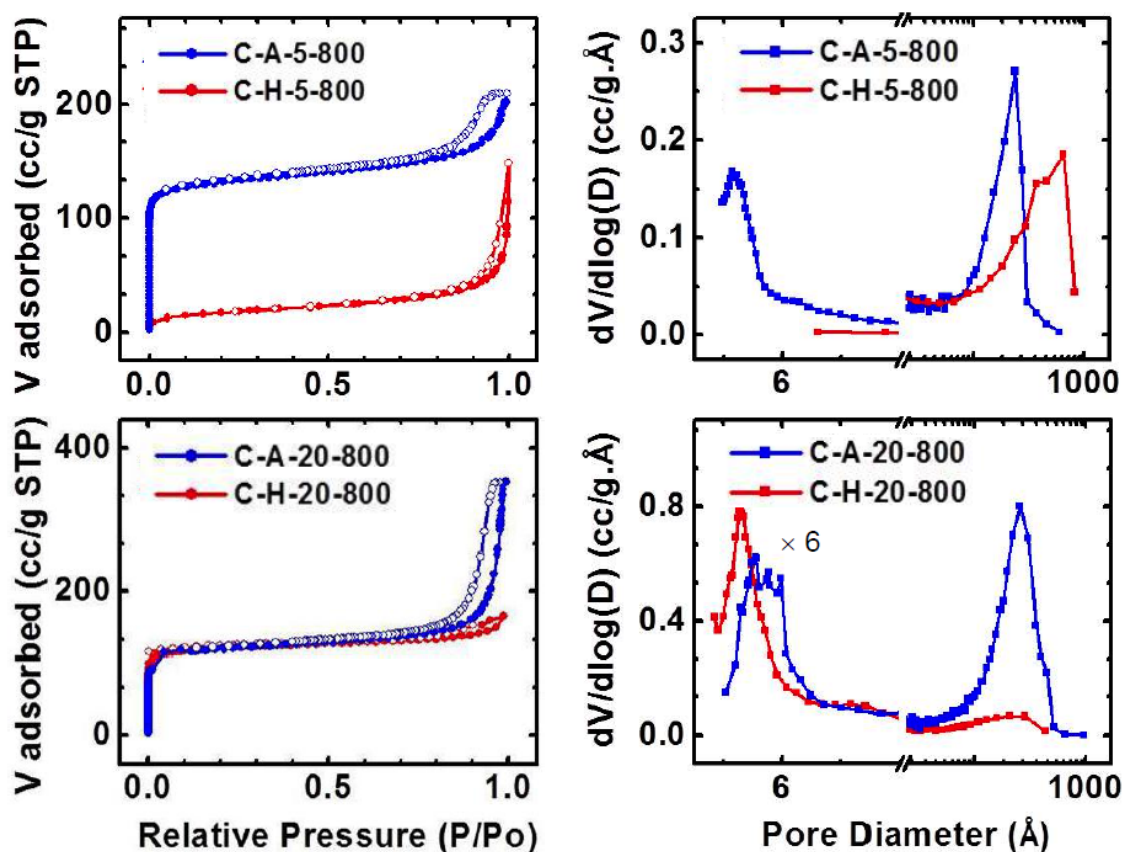


Figure 12  $N_2$ -sorption porosimetry of C-aerogels originating from low-concentration sols (top, -xx=5) and high-concentration sols (bottom, -xx=20). Left: isotherms, Right: pore size distributions of micropores from the low-pressure ( $P/P_0 \ll 0.1$ ) part of the isotherms, and of mesopores from the high partial pressure branch of the desorption isotherms ( $P/P_0 \sim 1$ ). (Note, the **C-H-5-800** isotherms do not show significant  $N_2$  adsorption at low pressures and the samples lack micropores.)

## SUPPORTING INFORMATION

Index

**Table S.1.** Formulation and apparent gelation times of PBO sols

**Table S.2.** Elemental analysis data obtained via CHN and EDS analysis

**Figure S.1.** N<sub>2</sub>-sorption porosimetry data for all PBO aerogels

**Figure S.2.** Hg-intrusion porosimetry data for all PBO aerogels

**Figure S.3.** Small angle x-ray scattering data (SAXS)

**Table S.3.** Results from small angle x-ray scattering (SAXS)

**Table S.4.** Thermal conductivity data

**Figure S.4.** Mechanical characterization data

**References**

Table S.1. Formulation and apparent gelation times of PBO sols

Part A. Acid-catalyzed route <sup>a</sup>

Formulation	BO monomer (g [mmol])	Aqueous HCl 12.1 N HCl (g [mL])	DMF (g [mL])	[BO monomer] (% w/w [M])	Apparent gelation time
PBO-A-5-RT	1.00 [2.16]	1.04 [0.94]	19.9 [21.08]	4.56 [0.09]	~ 7 h
PBO-A-7-RT	1.62 [3.50]	1.04 [0.94]	19.9 [21.08]	7.18 [0.14]	~ 5h 30 min
PBO-A-10-RT	2.22 [4.80]	1.04 [0.94]	19.9 [21.08]	9.59 [0.20]	~ 3 h 20 min
PBO-A-12-RT	2.85 [6.16]	1.04 [0.94]	19.9 [21.08]	11.98 [0.25]	~ 2h 30 min
PBO-A-15-RT	3.52 [7.61]	1.04 [0.94]	19.9 [21.08]	14.39 [0.30]	~ 2 h
PBO-A-20-RT	5.00 [10.81]	1.04 [0.94]	19.9 [21.08]	19.27 [0.41]	~ 1 h 30 min

Part B. Heat-induced polymerization <sup>a</sup>

Formulation	BO monomer (g [mol])	DMSO (g [mL])	[BO monomer] (% w/w [M])	Apparent gelation time
PBO-H-5-130	1.00 [2.16]	19 [17.27]	5.00 [0.12]	3 - 4 days
PBO-H-10-130	2.00 [4.32]	18 [16.36]	10.00 [0.24]	2.5 - 3 days
PBO-H-15-130	3.00 [6.49]	17 [15.45]	15.00 [0.36]	2 - 2.5 days
PBO-H-20-130	4.00 [8.65]	16 [14.55]	20.00 [0.48]	1.5 - 2 days
PBO-H-30-130	5.97 [12.90]	14 [12.73]	29.89 [0.73]	~ 1 day
PBO-H-40-130	10.00 [21.62]	15 [13.64]	40.00 [0.98]	10-12 h

<sup>a</sup> The calculation of [BO monomer] requires the BO monomer density =  $1.185 \pm 0.007 \text{ g cm}^{-3}$

Table S.2. Elemental analysis data obtained via CHN and EDS analysis

Part A. PBO aerogels as-prepared, after curing at 200 °C in air, and after carbonization at 800 °C under Ar

Sample	% C		% H		% N		% O		% Cl		True Values <sup>a</sup>				
	CHN	EDS	CHN	EDS	CHN	EDS	CHN	EDS	CHN	EDS	% C	% H	% N	% O <sup>b</sup>	% Cl <sup>b</sup>
<b>BO monomer</b>	80.49	<sup>c</sup>	6.54	<sup>d</sup>	6.06	<sup>c</sup>	6.92 <sup>e</sup>	<sup>c</sup>	<sup>f</sup>	<sup>c,f</sup>	80.49	6.54	6.06	6.92 <sup>e</sup>	<sup>f</sup>
<b>Materials via acid-catalyzed gelation</b>															
<b>PBO-A-5-RT</b>	79.25	79.84	5.89	<sup>d</sup>	6.45	6.93	<sup>g</sup>	8.92	<sup>g</sup>	4.38	79.25	5.89	6.45	5.64	2.77
<b>PBO-A-10-RT</b>	76.54	81.85	5.24	<sup>d</sup>	6.25	4.34	<sup>g</sup>	6.45	<sup>g</sup>	7.37	76.54	5.24	6.25	5.59	6.38
<b>PBO-A-20-RT</b>	71.82	82.94	5.85	<sup>d</sup>	5.83	7.08	<sup>g</sup>	5.71	<sup>g</sup>	4.26	71.82	5.85	5.83	9.45	7.05
<b>PBO-A-5-200</b>	70.16	79.31	3.55	<sup>d</sup>	5.69	6.54	<sup>g</sup>	12.24	<sup>g</sup>	1.91	70.16	3.55	5.69	17.82	2.78
<b>PBO-A-10-200</b>	69.40	78.79	4.26	<sup>d</sup>	5.60	5.09	<sup>g</sup>	12.06	<sup>g</sup>	4.06	69.40	4.26	5.60	15.52	5.22
<b>PBO-A-20-200</b>	70.86	77.74	3.78	<sup>d</sup>	5.60	6.39	<sup>g</sup>	14.19	<sup>g</sup>	1.68	70.86	3.78	5.60	17.67	2.09
<b>C-A-5-800</b>	82.23	92.93	1.58	<sup>d</sup>	3.48	4.68	<sup>g</sup>	2.35	<sup>g</sup>	0.04	82.23	1.58	3.48	12.49	0.21
<b>C-A-10-800</b>	87.72	87.77	0.60	<sup>d</sup>	4.76	7.03	<sup>g</sup>	5.09	<sup>g</sup>	0.11	87.72	0.60	4.76	6.77	0.14
<b>C-A-20-800</b>	87.23	91.45	0.78	<sup>d</sup>	5.55	4.73	<sup>g</sup>	3.29	<sup>g</sup>	0.53	87.23	0.78	5.55	5.55	0.89

Part A. (Continued)

Sample	% C		% H		% N		% O		% Cl		True Values <sup>a</sup>				
	CHN	EDS	CHN	EDS	CHN	EDS	CHN	EDS	CHN	EDS	% C	% H	% N	% O <sup>b</sup>	% Cl <sup>b</sup>
<b>BO monomer</b>	80.49	<sup>c</sup>	6.54	<sup>d</sup>	6.06	<sup>c</sup>	6.92 <sup>e</sup>	<sup>c</sup>	<sup>f</sup>	<sup>c,f</sup>	80.49	6.54	6.06	6.92 <sup>e</sup>	<sup>f</sup>
<b>Materials via heat-induced gelation</b>															
<b>PBO-H-10-130</b>	79.45	81.36	4.49	<sup>d</sup>	6.25	8.32	<sup>g</sup>	10.32	<sup>f</sup>	<sup>f</sup>	79.45	4.49	6.25	9.81	<sup>f</sup>
<b>PBO-H-20-130</b>	79.43	86.87	6.41	<sup>d</sup>	6.23	5.71	<sup>g</sup>	7.42	<sup>f</sup>	<sup>f</sup>	79.43	6.41	6.23	7.93	<sup>f</sup>
<b>PBO-H-40-130</b>	79.35	86.93	6.10	<sup>d</sup>	5.76	6.83	<sup>g</sup>	6.23	<sup>f</sup>	<sup>f</sup>	79.35	6.10	5.76	8.79	<sup>f</sup>
<b>PBO-H-10-200</b>	75.75	79.66	4.39	<sup>d</sup>	5.52	6.70	<sup>g</sup>	13.64	<sup>f</sup>	<sup>f</sup>	75.75	4.39	5.52	14.34	<sup>f</sup>
<b>PBO-H-20-200</b>	75.12	79.52	4.84	<sup>d</sup>	5.06	8.12	<sup>g</sup>	12.37	<sup>f</sup>	<sup>f</sup>	75.12	4.84	5.06	14.98	<sup>f</sup>
<b>PBO-H-40-200</b>	77.03	83.58	6.20	<sup>d</sup>	5.28	7.88	<sup>g</sup>	8.54	<sup>f</sup>	<sup>f</sup>	77.03	6.20	5.28	11.49	<sup>f</sup>
<b>C-H-5-800</b>	88.92	<sup>c</sup>	0.73	<sup>c</sup>	4.38	<sup>c</sup>	<sup>g</sup>	<sup>c</sup>	<sup>f</sup>	<sup>c,f</sup>	88.92	0.73	4.38	5.97	<sup>f</sup>
<b>C-H-10-800</b>	88.74	<sup>c</sup>	0.92	<sup>c</sup>	4.40	<sup>c</sup>	<sup>g</sup>	<sup>c</sup>	<sup>f</sup>	<sup>c,f</sup>	88.74	0.92	4.40	5.94	<sup>f</sup>
<b>C-H-20-800</b>	88.56	<sup>c</sup>	1.07	<sup>c</sup>	4.30	<sup>c</sup>	<sup>g</sup>	<sup>c</sup>	<sup>f</sup>	<sup>c,f</sup>	88.56	1.07	4.30	6.07	<sup>f</sup>

<sup>a</sup> True values for C, H, N are considered those obtained by CHN elemental analysis. <sup>b</sup> The residual %weight of the CHN analysis was allocated to %O and %Cl based on energy dispersive spectroscopic (EDS) analysis. Thus, %O + %Cl = 100-%CHN; this equation comprises a system with the weight percent ratio %O: %Cl, which is obtained from the EDS data, and allows calculation of the two values. <sup>c</sup> Not conducted. <sup>d</sup> Not available through EDS. <sup>e</sup> Value calculated from the difference: %O=100-%CHN. <sup>f</sup> Sample does not contain chlorine. <sup>g</sup> Not available through CHN analysis.

Part B. Elemental analysis of **PBO-A-10-temperature** and **PBO-H-10-temperature** after pyrolysis at the temperatures indicated by the sample names. (Note: **PBO-A-10-RT** and **PBO-H-10-130** are samples as-prepared; **-200** samples were heated (cured) in air; all other samples at temperatures  $\geq 300$  °C were heated in Ar. Footnotes as in Part A.)

Sample ID	% C		% H		% N		% O		% Cl		True Values <sup>a</sup>				
	CHN	EDS	CHN	EDS	CHN	EDS	CHN	EDS	CHN	EDS	% C	% H	% N	% O <sup>b</sup>	% Cl <sup>b</sup>
<b>BO monomer</b>	80.49	<sup>c</sup>	6.54	<sup>d</sup>	6.06	<sup>c</sup>	6.92 <sup>e</sup>	<sup>c</sup>	<sup>f</sup>	<sup>c,f</sup>	80.49	6.54	6.06	6.92 <sup>e</sup>	<sup>f</sup>
<b>Materials via acid-catalyzed gelation</b>															
<b>PBO-A-10-RT</b>	76.54	81.85	5.24	<sup>d</sup>	6.25	4.34	<sup>g</sup>	6.45	<sup>g</sup>	7.37	76.54	5.24	6.25	5.59	6.38
<b>PBO-A-10-200</b>	69.40	78.79	4.26	<sup>d</sup>	5.60	5.09	<sup>g</sup>	12.06	<sup>g</sup>	4.06	69.40	4.26	5.60	15.52	5.22
<b>PBO-A-10-300</b>	70.45	80.97	2.62	<sup>d</sup>	6.04	6.20	<sup>g</sup>	11.58	<sup>g</sup>	1.24	70.45	2.62	6.04	18.86	2.02
<b>PBO-A-10-400</b>	76.12	83.37	3.14	<sup>d</sup>	6.52	6.57	<sup>g</sup>	9.73	<sup>g</sup>	0.33	76.12	3.14	6.57	13.75	0.46
<b>PBO-A-10-500</b>	79.06	85.91	1.00	<sup>d</sup>	6.09	6.07	<sup>g</sup>	8.02	<sup>g</sup>	0.00	79.06	1.00	6.07	13.85	0.00
<b>PBO-A-10-600</b>	82.33	90.84	1.70	<sup>d</sup>	5.60	5.33	<sup>g</sup>	3.75	<sup>g</sup>	0.09	82.33	1.70	5.60	10.12	0.24
<b>C-A-10-800</b>	87.72	87.77	0.60	<sup>d</sup>	4.76	7.03	<sup>g</sup>	5.09	<sup>g</sup>	0.11	87.72	0.60	4.76	6.77	0.14
<b>Materials via heat-induced gelation</b>															
<b>PBO-H-10-130</b>	79.45	<sup>c</sup>	4.49	<sup>d</sup>	6.25	<sup>c</sup>	<sup>g</sup>	<sup>c</sup>	<sup>f</sup>	<sup>f</sup>	79.45	4.49	6.25	9.81	<sup>f</sup>
<b>PBO-H-10-200</b>	75.75	<sup>c</sup>	4.39	<sup>d</sup>	5.52	<sup>c</sup>	<sup>g</sup>	<sup>c</sup>	<sup>f</sup>	<sup>f</sup>	75.75	4.39	5.52	14.34	<sup>f</sup>
<b>PBO-H-10-300</b>	78.18	<sup>c</sup>	5.38	<sup>d</sup>	5.35	<sup>c</sup>	<sup>g</sup>	<sup>c</sup>	<sup>f</sup>	<sup>f</sup>	78.18	5.38	5.35	11.09	<sup>f</sup>
<b>PBO-H-10-400</b>	75.96	<sup>c</sup>	4.59	<sup>d</sup>	5.33	<sup>c</sup>	<sup>g</sup>	<sup>c</sup>	<sup>f</sup>	<sup>f</sup>	75.96	4.59	5.33	14.12	<sup>f</sup>
<b>PBO-H-10-500</b>	77.56	<sup>c</sup>	3.15	<sup>d</sup>	5.48	<sup>c</sup>	<sup>g</sup>	<sup>c</sup>	<sup>f</sup>	<sup>f</sup>	77.56	3.15	5.48	13.81	<sup>f</sup>
<b>PBO-H-10-600</b>	84.33	<sup>c</sup>	2.99	<sup>d</sup>	5.63	<sup>c</sup>	<sup>g</sup>	<sup>c</sup>	<sup>f</sup>	<sup>f</sup>	84.33	2.99	5.63	7.05	<sup>f</sup>
<b>C-H-10-800</b>	88.74	<sup>c</sup>	0.92	<sup>c</sup>	4.40	<sup>c</sup>	<sup>g</sup>	<sup>c</sup>	<sup>f</sup>	<sup>c,f</sup>	88.74	0.92	4.40	5.94	<sup>f</sup>

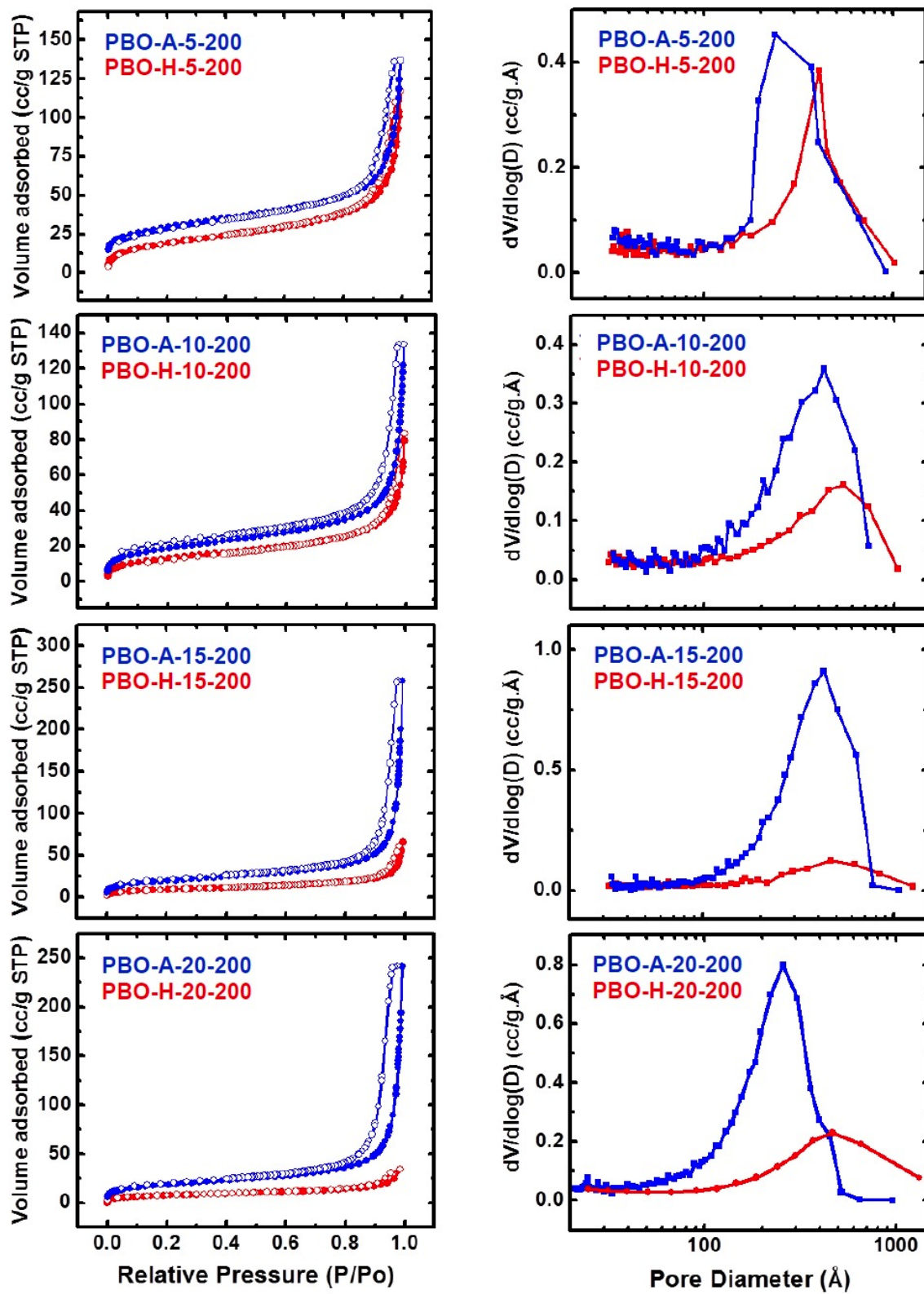


Figure S.1.  $N_2$ -sorption porosimetry data (isotherms and pore size distributions by the BJH method) for all **PBO-A-xx-200** and **PBO-H-xx-200** aerogels.



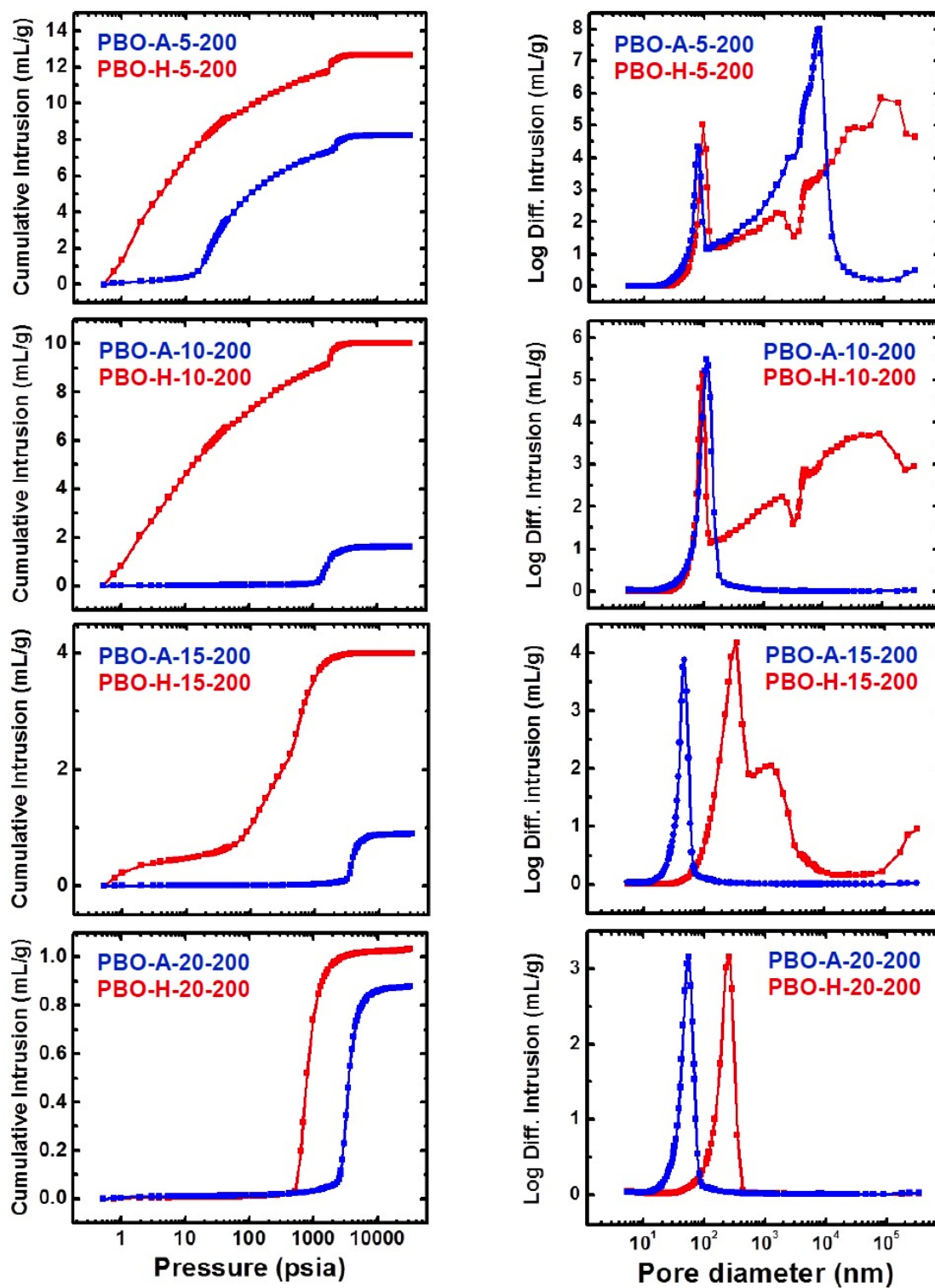


Figure S.2. Hg-intrusion porosimetry data (volume of Hg intruding and pore size distributions) for all PBO-A-xx-200 and PBO-H-xx-200 aerogels.

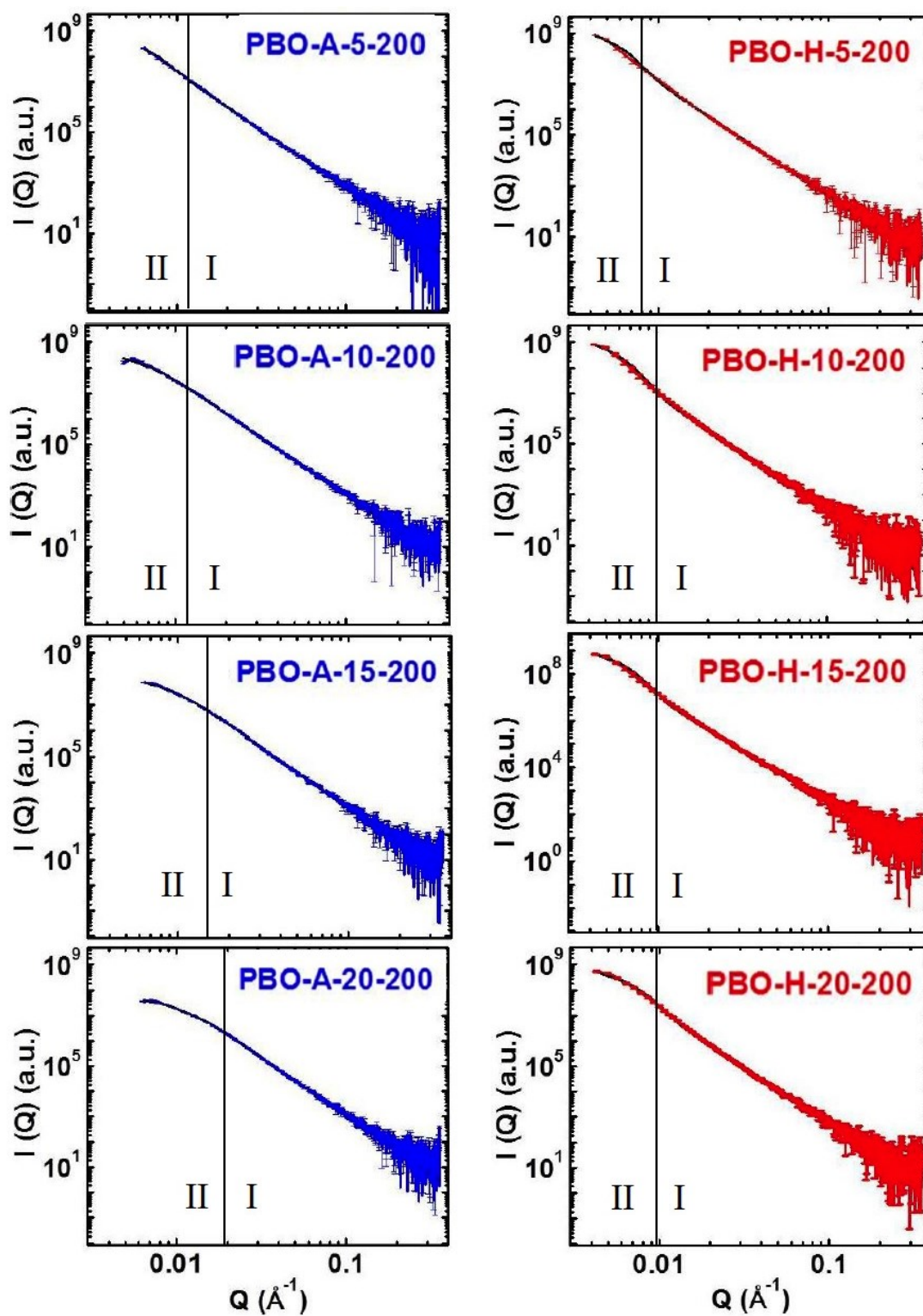


Figure S.3. Small angle x-ray scattering data (SAXS) for PBO aerogels as shown. Data were fitted to the Beaucage Unified Model [R-1]. Results are summarized in Table S.3. (Region I: high- $Q$  power low; Region II: Guinier knee).

Table S.3. Results from small angle x-ray scattering (SAXS) for PBO aerogels as shown.

sample	Primary Particles		
	high- $Q$ slope <sup>a</sup>	$R_G$ <sup>b</sup> (nm)	$R$ <sup>c</sup> (nm)
<b>PBO-A-5-200</b>	-4.58±0.00 <sub>6</sub>	36.7±0.8	47.7
<b>PBO-A-7-200</b>	-4.35±0.00 <sub>5</sub>	35.3±1.0	45.9
<b>PBO-A-10-200</b>	-4.57±0.00 <sub>5</sub>	31.9±1.4	41.5
<b>PBO-A-12-200</b>	-4.62±0.00 <sub>7</sub>	22.6±0.3	29.4
<b>PBO-A-15-200</b>	-4.62±0.00 <sub>5</sub>	24.8±0.4	32.2
<b>PBO-A-20-200</b>	-4.62±0.00 <sub>6</sub>	20.0±0.2	26.0
<b>PBO-H-5-200</b>	-4.46±0.00 <sub>0</sub>	44.8±0.7	58.3
<b>PBO-H-10-200</b>	-4.52±0.01 <sub>0</sub>	43.2±0.5	56.1
<b>PBO-H-15-200</b>	-4.38±0.00 <sub>6</sub>	40.5±0.5	52.6
<b>PBO-H-20-200</b>	-4.46±0.00 <sub>7</sub>	35.4±0.3	46.0
<b>PBO-H-30-200</b>	-4.42±0.00 <sub>7</sub>	32.3±0.2	41.9
<b>PBO-H-40-200</b>	-4.52±0.01	36.8±0.4	47.8

Referring to Figure S.3:

- <sup>a</sup> From power-law Region I. Slopes < -4.0, signifying primary particles with density-gradient boundaries.
- <sup>b</sup> Radius of gyration  $R_G$ , from Guinier Region II.
- <sup>c</sup> Primary particle radius =  $R_G/0.77$ .

Table S.4. Thermal conductivity data of all **PBO-A-xx-200** and **PBO-H-xx-200** aerogels of this study

sample	$\rho_b$ (g cm <sup>-3</sup> )	$c_p$ (J g <sup>-1</sup> K <sup>-1</sup> ) <sup>a</sup>	$R$ (mm <sup>2</sup> s <sup>-1</sup> ) <sup>b</sup>	$\lambda$ (W m <sup>-1</sup> K <sup>-1</sup> ) <sup>c</sup>	average pore diameter $\Phi$ (nm) <sup>d</sup>	$\lambda_g$ (W m <sup>-1</sup> K <sup>-1</sup> ) <sup>e</sup>	$\lambda_s$ (W m <sup>-1</sup> K <sup>-1</sup> ) <sup>f</sup>
<b>PBO-A-xx-200</b>							
<b>PBO-A-5-200</b>	0.109 ± 0.006	1.384	0.637 ± 0.031	0.096±0.007	466	0.015	0.081
<b>PBO-A-7-200</b>	0.224 ± 0.018	1.384	0.219 ± 0.019	0.068±0.008	244	0.010	0.058
<b>PBO-A-10-200</b>	0.373 ± 0.019	1.384	0.133 ± 0.002	0.069±0.004	117	0.005	0.063
<b>PBO-A-12-200</b>	0.483 ± 0.051	1.384	0.106 ± 0.001	0.071±0.008	87	0.004	0.067
<b>PBO-A-15-200</b>	0.560 ± 0.024	1.384	0.104 ± 0.004	0.080±0.005	59	0.003	0.078
<b>PBO-A-20-200</b>	0.670 ± 0.030	1.384	0.115 ± 0.015	0.106±0.014	46	0.002	0.105
<b>PBO-H-xx-200</b>							
<b>PBO-H-10-200</b>	0.112 ± 0.015	1.384	0.693 ± 0.082	0.107±0.016	694	0.017	0.090
<b>PBO-H-15-200</b>	0.232 ± 0.021	1.384	0.358 ± 0.011	0.115±0.011	430	0.013	0.102
<b>PBO-H-17.5-200</b>	0.300 ± 0.039	1.384	0.236 ± 0.019	0.098±0.015	214	0.009	0.089
<b>PBO-H-20-200</b>	0.447 ± 0.072	1.384	0.148 ± 0.004	0.091±0.014	227	0.008	0.084
<b>PBO-H-25-200</b>	0.580 ± 0.016	1.384	0.119 ± 0.003	0.096±0.004	231	0.006	0.089
<b>PBO-H-30-200</b>	0.670±0.051	1.384	0.130 ± 0.005	0.121±0.010	116	0.003	0.117
<b>PBO-H-40-200</b>	0.732±0.020	1.384	0.124±0.005	0.125±0.006	106	0.003	0.122

<sup>a</sup> Polybenzoxazine heat capacity [R-2]. <sup>b</sup> Thermal diffusivity, measured with a laser flash method (see Experimental section). <sup>c</sup> Via  $\lambda =$

$\rho_b \times c_p \times R$ . <sup>d</sup> Via  $\Phi = 4 \times V_{\text{Total}} / \sigma$  method using  $V_{\text{Total}} = (1/\rho_b) - (1/\rho_s)$ ; <sup>e</sup> From Knudsen's equation [R-3]:  $\lambda_{\varepsilon} = \frac{\lambda_{g,0} \Pi}{1 + 2\beta(l_g / \Phi)}$ , whereas  $\lambda_{g,0} = 0.02619$  W m<sup>-1</sup> K<sup>-1</sup> is the thermal conductivity of air at standard conditions,  $\Pi$  is the aerogel porosity in decimal notation,  $\beta$  is a parameter that accounts for the energy transfer between the pore-filling gas and the aerogel walls (for air  $\beta = 2$ ), and  $l_g$  is the mean free path of the gas molecules (for air at 1 bar pressure,  $l_g \approx 70$  nm). <sup>f</sup> Via  $\lambda_s = \lambda - \lambda_g$ .  $\Phi$  and  $\Pi$  values are taken from Table 2 of the main article.

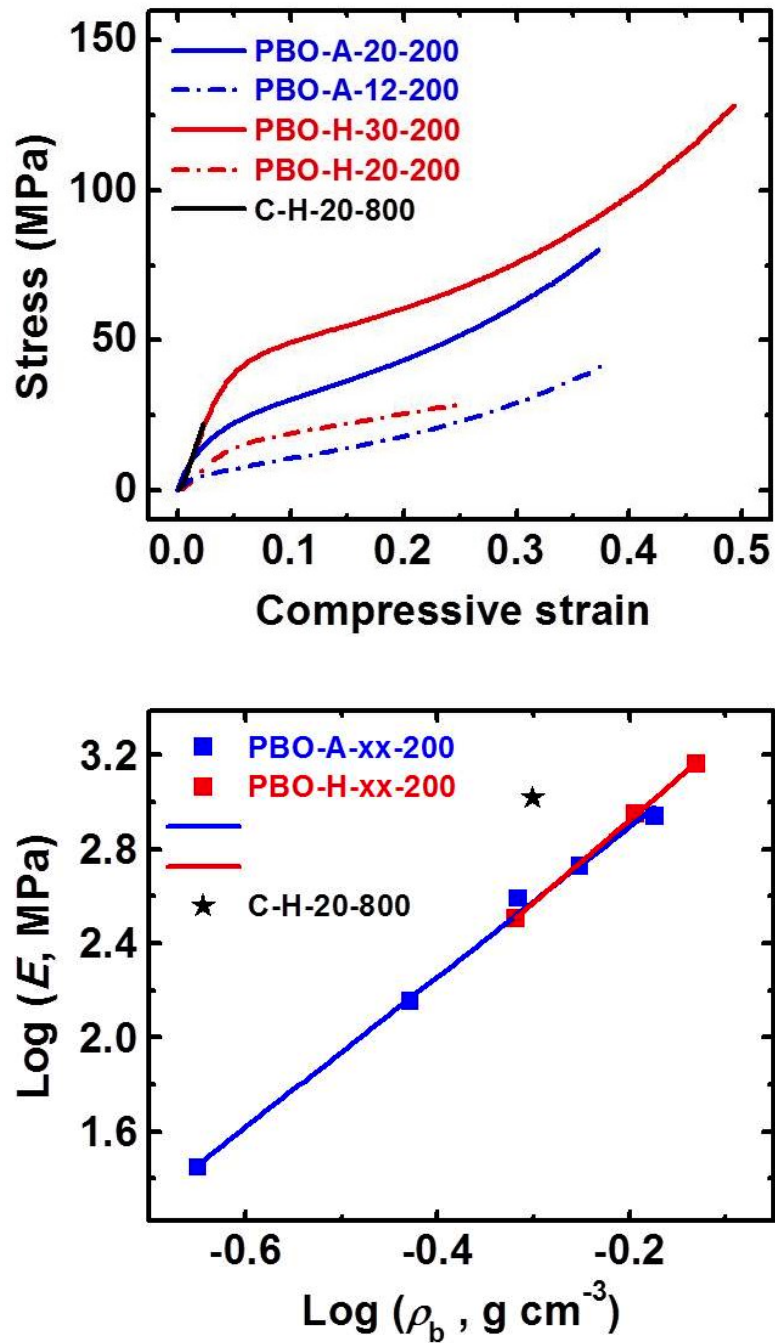


Figure S.4 Mechanical characterization data. Stress-strain curves for **PBO-A-xx-200** and **PBO-H-xx-200** under quasi-static compression. A carbonized sample, **C-H-20-800** (indicated with an asterisk), shows only a short elastic range, but its elastic modulus is much higher than same-density **H-** or **A-**aerogels.

**REFERENCES**

- R-1 (a) Beaucage, G. *J. Appl. Cryst.* **1995**, 28, 717-728.  
(b) Beaucage, G. *J. Appl. Cryst.* **1996**, 29, 134-146.
- R-2 Ishida, H.; Rimdusit, S. *J. Therm. Anal. Calorim.* **1999**, 58, 497-507.
- R-3. (a) Lu, X.; Arduini-Schuster, M. C.; Kuhn, J.; Nilsson, O.; Fricke, J.; Pekala, R. W. *Science* **1992**, 255, 971-972.  
(b) Reichenauer, G.; Heinemann, U.; Ebert, H.-P. *Colloids Surf. A* **2007**, 300, 204-210.

## II. POLYBENZOXAZINE AEROGELS II: INTERPENETRATING NETWORKS WITH IRON OXIDE AND THE CARBOTHERMAL SYNTHESIS OF HIGHLY POROUS MONOLITHIC PURE IRON(0) AEROGELS AS ENERGETIC MATERIALS

Shruti Mahadik-Khanolkar, Suraj Donthula, Abhishek Bang, Clarissa Wisner, Chariklia Sotiriou-Leventis\* and Nicholas Leventis\*

Department of Chemistry, Missouri University of Science and Technology, Rolla, MO 65409, U.S.A. E-mail: leventis@mst.edu; cslevent@mst.edu

**Abstract.** There is a specific need for nanoporous monolithic pyrophoric metals as energetic materials and catalysts. Adapting modern-day blast furnace methodology, namely direct reduction of highly porous iron oxide aerogels with H<sub>2</sub> or CO, yielded coarse powders. Turning to smelting reduction, we used the acid environment of gelling [Fe(H<sub>2</sub>O)<sub>6</sub>]<sup>3+</sup> sols to catalyze co-gelation of a second, extremely sturdy, carbonizable in high yield polybenzoxazine (PBO) network that plays the dual role of a reactive template. Formation of two independent gel networks was confirmed with rheology/dynamic mechanical analysis performed in tandem with the same sol and its gel, and results were correlated with data from microscopy (SEM, STEM) and small angle x-ray scattering (SAXS) for the elucidation of the exact topological association of the two components. By probing the chemical interaction of the two networks with infrared, Mössbauer, XRD and CHN analysis, we found out that iron(III) oxide undergoes pre-reduction to Fe<sub>3</sub>O<sub>4</sub> and participates in the oxidation of PBO, which is a prerequisite for robust carbons suitable as structure-directing templates. Subsequently, interconnected submicron-size Fe<sub>3</sub>O<sub>4</sub> nanoparticles undergo annealing at more than 800 °C below the melting point of the bulk oxide, and are reduced to iron(0) at 800 °C, presumably via a solid (C)/liquid (Fe<sub>3</sub>O<sub>4</sub>) process. Carbothermal reduction, oxidative removal of residual carbon (air) and re-reduction (H<sub>2</sub>) of α-Fe<sub>2</sub>O<sub>3</sub> formed in the previous step were all carried out as a single

process in a tube furnace by switching gases. The resulting pure iron(0) monoliths had a density of  $0.54 \pm 0.07 \text{ g cm}^{-3}$  and were 93% porous. Infiltration with  $\text{LiClO}_4$  and ignition led to a new type of explosive behavior due to rapid heating and expansion of gases filling nanoporous space; annealing at  $1200 \text{ }^\circ\text{C}$  reduced porosity to 66% and those materials behaved as thermites. Ignition in a bomb calorimeter released  $59 \pm 9 \text{ Kcal mol}^{-1}$  of iron(0) reacted and is associated with oxidation to FeO (theoretical:  $66.64 \text{ Kcal mol}^{-1}$ ).

**Keywords:** iron, aerogel, carbothermal, smelting, polybenzoxazine, energetic materials

## 1. INTRODUCTION

The acid-catalyzed gelation of polybenzoxazines (PBO) is a viable method for the synthesis of robust, carbonizable PBO aerogels (see previous article of this issue). A useful application of that process involves co-gelation of interpenetrating networks (IPN) of PBO with iron oxide ( $\text{FeOx}$ ), catalyzed by the acid environment of gelling  $[\text{Fe}(\text{H}_2\text{O})_6]^{3+}$  sols. PBO-FeOx IPNs serve as the point of departure for the carbothermal synthesis of sturdy highly porous (>90%) monolithic pure iron(0) aerogels for applications as energetic materials.

Porous metals are pursued mostly for applications in catalysis,<sup>1</sup> electrochemistry,<sup>2</sup> fuel cells,<sup>3</sup> sensors<sup>4</sup> actuators,<sup>5</sup> antibacterial biofiltration membranes,<sup>6</sup> and are typically prepared via templating,<sup>7</sup> chemical vapor deposition (CVD),<sup>8</sup> selective removal of one component from binary alloys,<sup>9</sup> reduction of metal salts with  $\text{NaBH}_4$  or hydrazine,<sup>10</sup> or by self-propagating rapid combustion synthesis using transition metal complexes with high-nitrogen containing ligands.<sup>11</sup>

Pyrophoric metals (e.g., Fe, Al, Mg, Zr, Cu, Ni) deserve special attention because of their high energy density and harmless combustion products (oxides). Applications as alternative fuels and energetic materials<sup>12</sup> involve solid-state reactions, which are



facilitated by intimate mixing of the pyrophoric metal with an oxidizer.<sup>13</sup> Mixing has been typically carried out by grinding fine powders, which can be extremely hazardous. Thus, it has been recognized that sol-gel synthesis not only bypasses grinding, but also creates nanoscopic-level dispersions of the two phases via *in situ* formation of ultrafine particles, and allows molding to shape from the beginning.<sup>14</sup> Among sol-gel materials, aerogels have the additional advantage of large surface areas for improved contact, hence higher reaction rates between solid reactants.<sup>15</sup>

The first aerogel-based energetic nanocomposites were reported by Tillotson *et al.*, by suspending aluminum particles (30 nm in diameter, synthesized independently via a dynamic gas condensation method) in iron(III) sols just about to undergo gelation.<sup>16</sup> However, based on the above, it is desirable to reverse the location of the fuel and the oxidizer by creating nanoporous pyrophoric metal aerogels that can be doped with an oxidizer at any stage of processing, in particular by post-gelation infiltration.

The most common metal aerogels have been based on precious elements (Pt, Au, Ag) and have been prepared via destabilization of colloidal solutions of the metals themselves.<sup>17</sup> Among non-precious metals, copper aerogels were first reported in the 1980s from gelation of cupric acetate and water followed by hypercritical removal of the pore-filling solvent (methanol, at 270 °C, >80 bar). That method was extended to metallic gold and Cu/Pd alloys.<sup>18</sup> Very recently, copper nanowire aerogels were demonstrated via freeze-drying of copper nanowire solutions.<sup>19</sup> In efforts to prepare pyrophoric iron aerogels, iron oxide aerogels have been reduced with H<sub>2</sub> yielding sub-micron sized iron particles.<sup>20</sup> As shown herewith, our attempts to duplicate the last approach yielded coarse powders, thus our attention shifted to reports on metal-doped carbon aerogels, which are

pursued mainly for catalytic applications. Among other methods,<sup>21</sup> such materials have been also obtained from pyrolysis of resorcinol-formaldehyde (RF) aerogels doped with metal ions (Fe, Co, Ni, Cu). Doping was carried out by coordination of metal ions to the polymer network by either replacing resorcinol with chelating 2,4-dihydrobenzoate,<sup>22</sup> or by anchoring metal ions to the RF network using cogelation with complexing agents.<sup>23</sup> The metal-doping level of the final carbon aerogels was low (<10% w/w), but curiously, the dopant was never the original salt, or even an oxide, but rather the metal itself.<sup>24</sup> Based on those reports, we inferred that metal ions are reduced carbothermally, in analogy to the smelting process that has been used in extractive metallurgy for millennia.<sup>25</sup>

In order to use smelting for the synthesis of purely metallic aerogels, the metal precursor concentration in RF aerogels should be increased to levels that would match stoichiometrically the amount of the resulting carbon. For this, we synthesized mixed metal oxide – RF aerogels, whose pyrolysis under Ar yielded metals (case of Co, Ni, Sn, Cu), carbides (case of Cr, Ti, Hf), or mixtures of metals and carbides (case of Fe).<sup>26</sup> The process efficiency was improved by coating the skeletal networks with polyurea in the X-aerogel fashion.<sup>27</sup> Melting of that polymer at relatively low temperatures (200-250 °C) caused local collapse of the network that enhanced contact between RF and metal oxide nanoparticles, and lowered the smelting temperatures by as much as 400 °C. Iron devoid of carbide could only be obtained by that method, which, however, is long and expensive for practical use.<sup>26</sup> In addition, that method always leaves behind a small weight percent of unreacted carbon. (For example, iron(0) aerogels contained a minimum of 5% w/w C.) For applications as energetic materials, even small amount of impurities can act as energy

traps and retard the speed of a combustion wave through the porous metal.<sup>28</sup> Moreover, combustion of carbon generates gases, which may be undesirable for applications in thermites. Residual carbon could not be removed from those materials without affecting their integrity: treatment of Fe(0)/C aerogels with either O<sub>2</sub>, H<sub>2</sub>O vapor or CO<sub>2</sub> turned monoliths into powders. Thus, it was concluded that the RF network could not hold the inorganic network well or long enough to promote metal particle interconnectivity for structural integrity.

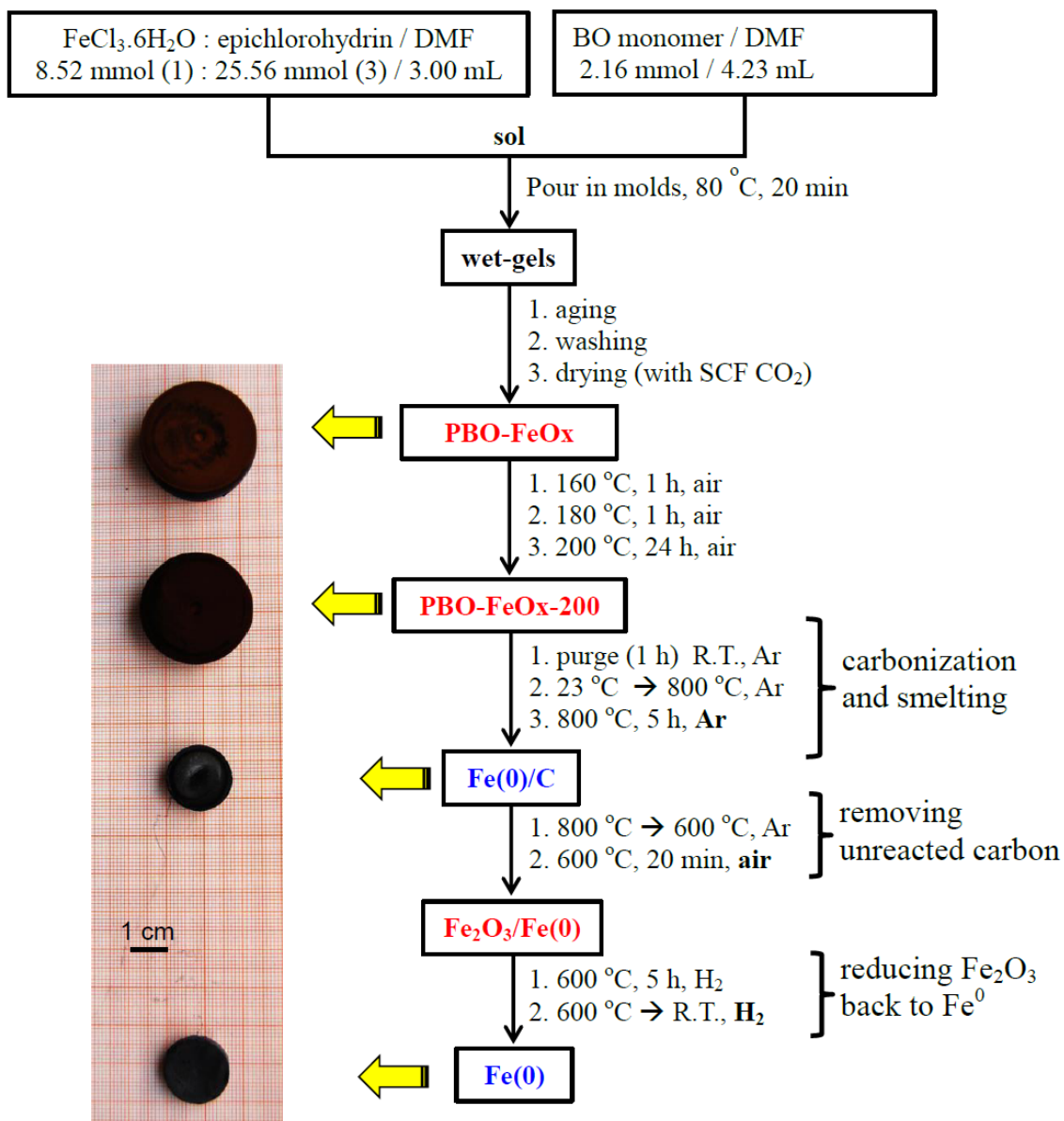
Those issues have been alleviated here by introducing sturdy interpenetrating polybenzoxazine-iron oxide (PBO-FeOx) aerogels. As described in the previous article of this issue, ring-opening polymerization of benzoxazine monomers can be catalyzed with HCl, a strong protic acid. Thus, gelling iron chloride hexahydrate (FeCl<sub>3</sub>·6H<sub>2</sub>O), a fairly strong Brønsted acid itself, catalyzes polymerization of the same benzoxazine monomer at near-ambient temperatures (80 °C), yielding interpenetrating PBO-FeOx networks. The robust PBO network serves the dual purpose of a reducing agent and of a template that holds iron species in place during smelting, and preserves monolithicity into the final iron(0) aerogels. The residual carbon after carbothermal processing (800 °C/Ar) was removed oxidatively (600 °C/air) with no collapse of the iron network. Co-produced  $\alpha$ -Fe<sub>2</sub>O<sub>3</sub> was reduced back to pure iron(0) by switching the flowing gas to H<sub>2</sub>. The evolution of the chemical identity and structural morphology of the network was monitored throughout processing, from gelation to the terminal pure iron(0) aerogels. At the end, the porous iron(0) network was filled with LiClO<sub>4</sub> and was ignited. Thermite behavior is reported from annealed, lower-porosity (~60% v/v) samples, explosive behavior is reported from higher-porosity (>90% v/v) monoliths.

## 2. RESULTS AND DISCUSSION

**2.1 Synthetic Procedures and Material Properties along Processing.** Scheme 1 outlines the overall synthetic protocol from gelation of PBO-FeOx IPNs to pure iron(0) aerogels. (Alternative routes, some of which were abandoned for reasons discussed below, are summarized in Scheme S.1 of the Supporting Information.) Formation of the iron oxide (FeOx) network was carried out via the time-tested method of irreversible deprotonation of hydrated metal salts with epoxides (e.g., epichlorohydrine, see Scheme 2A).<sup>28a,29</sup> FeCl<sub>3</sub>.6H<sub>2</sub>O is a fairly strong Brønsted acid (in ethanol, pK<sub>a,1</sub>=1.19; pK<sub>a,2</sub>=2.49),<sup>26c</sup> and catalyzes ring-opening polymerization of the BO monomer prepared from condensation of bisphenol A, formaldehyde and aniline (Scheme 2B and previous article of this issue).<sup>30</sup> DMF was selected as a common solvent for both chemistries. To increase the chances for a sturdier terminal iron(0) network, it was decided to work close to the solubility limit of FeCl<sub>3</sub>.6H<sub>2</sub>O in the sol. To boost its concentration even higher, the amount of epichlorohydrine was reduced down to the absolutely necessary level for gelation. Thus, while the typical literature epichlorohydrine-to-salt ratio is 10:1 mol:mol,<sup>26,29</sup> it was reasoned that for a continuous three dimensional FeOx network a 3:1 mol:mol ratio would be sufficient. Indeed, “3:1” (epichlorohydrine):(FeCl<sub>3</sub>.6H<sub>2</sub>O) sols gelled, “2:1” sols did not.

Considering: (a) the carbonization yield of PBO (~60% w/w); (b) the stoichiometric need of the smelting process ( $2\text{Fe}_2\text{O}_3 + 3\text{C} \rightarrow 4\text{Fe} + 3\text{CO}_2$ ) for a C:Fe atomic ratio of 3:4; and, (c) the possible leaching of loose BO oligomers out of the wet-gels during solvent exchanges, the (FeCl<sub>3</sub>.6H<sub>2</sub>O):(BO monomer) ratio was set at about 3.9 mol:mol. The expected atomic ratio of C:Fe available for reduction was about 5.9.

Scheme 1. Synthesis of nanoporous iron

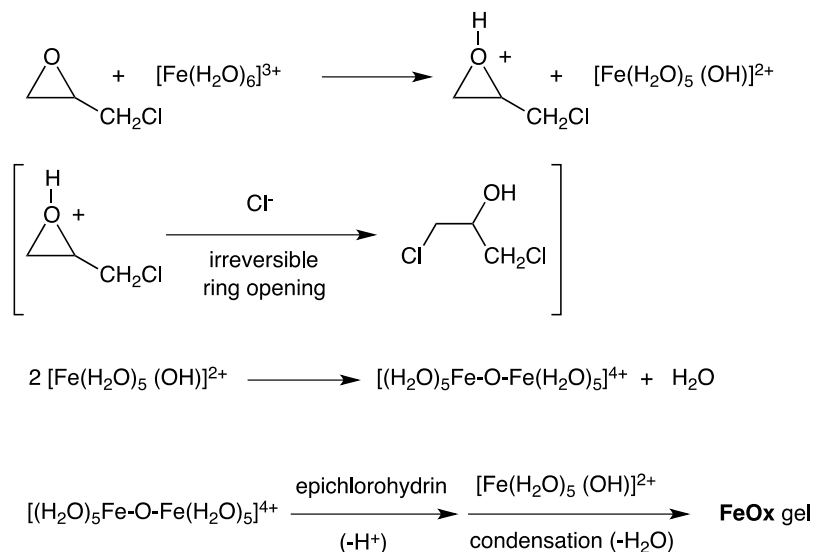


Co-gelation of the  $\text{FeCl}_3 \cdot 6\text{H}_2\text{O}$ /BO-monomer sol was carried out at  $80^\circ\text{C}$ . The resulting gels were aged, solvent-exchanged to acetone, and dried in an autoclave with liquid  $\text{CO}_2$ , taken out at the end as a supercritical fluid (SCF). Leaching of organic matter was indeed observed during solvent-exchanges, and was quantified gravimetrically at

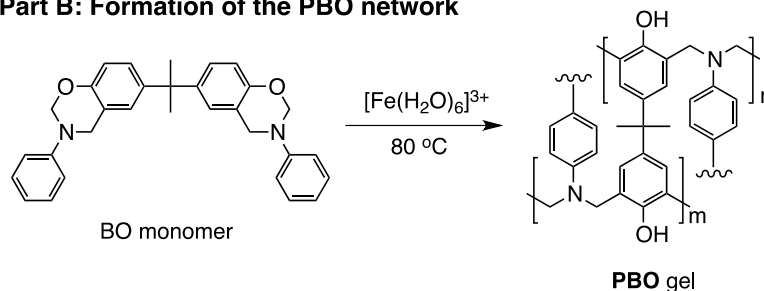
39% w/w of the BO monomer used in the sol. That brought the expected C:Fe atomic ratio to 3.5, hence, necessarily, the carbothermal process was in need of efficient removal of unreacted C (see below). As-prepared interpenetrating networks are referred to as **PBO-FeOx**. Because for isomorphous, high-yield carbonization, PBO networks need to be oxidized (see previous article of this issue), **PBO-FeOx** aerogels were step-cured up to 200 °C in air and are referred to as **PBO-FeOx-200**. For control purposes, pure FeOx aerogels were also prepared via the same route (Scheme 1, minus BO monomer) and are referred to as **FeOx**. For consistency, **FeOx** aerogels were also cured at 200 °C in air, and

Scheme 2. Chemical processes forming the interpenetrating networks

**Part A: Formation of the FeOx network**



**Part B: Formation of the PBO network**



are referred to as **FeOx-200**. Also for control purposes, PBO aerogels were prepared using  $\text{FeCl}_3 \cdot 6\text{H}_2\text{O}$  as a catalyst (Scheme 1, minus epichlorohydrine), and are referred to as **PBO-Fe<sup>3+</sup>**. After curing at 200 °C, those samples are referred to as **PBO-Fe<sup>3+</sup>-200**.

As-prepared as well as cured IPNs and controls were characterized using thermogravimetric analysis in air (TGA – Figure 1), and CHN elemental analysis (Table S.1 in Supporting Information). As-prepared **FeOx** aerogels show a gradual mass loss of 16% w/w up to 300 °C, which has been attributed to “physisorbed and structural water, as well as organic byproducts of the initial synthesis.”<sup>31</sup> Both as-prepared **PBO-FeOx** and cured **PBO-FeOx-200** IPNs loose about the same mass (37% and 35% w/w, respectively), most of which *above* 300 °C. Thermogravimetrically, the **PBO-Fe<sup>3+</sup>-200** control sample behaves similarly to the IPNs, and surprisingly (that is in view of RF-related reports<sup>22-24</sup>) they also show a substantial uptake of iron (25% w/w residual weight, vs. 63-65% from IPNs). (It is noted that HCl-catalyzed **PBO-A-7-200** is burnt off completely, again starting losing weight >300 °C.) Those data together point to strong interactions between  $\text{Fe}^{3+}$  and the PBO network that may have replaced interactions with physisorbed water.

**FeOx-200** controls were pyrolyzed further under flowing  $\text{H}_2$  and was found that they undergo reduction to iron(0) at as low as 400 °C (by XRD, see Figure S.1).<sup>20</sup> However, the resulting samples had shrunk a lot and were no longer monolithic (see Scheme S.1 in the Supporting Information). Thus, our attention was focused on the PBO-FeOx IPNs.

At first, **PBO-FeOx-200** samples were pyrolyzed at 800 °C under flowing  $\text{H}_2$ , followed by: (a) oxidative removal of carbon with air; and, (b) a second  $\text{H}_2$ -treatment to

re-reduce possible  $\text{Fe}_2\text{O}_3$  formed via  $4\text{Fe} + 3\text{O}_2 \rightarrow 2\text{Fe}_2\text{O}_3$ , to iron(0). The rationale of that attempt was to use the sturdy PBO network *only* as a template; the role of the reducing agent was left with  $\text{H}_2$ .<sup>20</sup> Although the terminal samples remained monolithic and showed iron(0) as the only crystalline phase (by XRD - Figure S.1), however, they also underwent significant shrinkage relative to their **PBO-FeOx-200** precursors (see Scheme S.1), compromising several of the material properties, and therefore that route was also abandoned.

In the carbothermal route, the PBO network is used both as a template and as a reducing agent. For that purpose, **PBO-FeOx-200** aerogels were first pyrolyzed at 800 °C under flowing high-purity Ar. (The grade of Ar is emphasized.) Although those samples (designated as **Fe(0)/C**) shrank also significantly relative to their **PBO-FeOx-200** precursors (see Scheme 1 and refer to data in Table 1), it is also noted that they shrank *much less* than their 800 °C/ $\text{H}_2$  counterparts (the relative diameter ratio was >1.5:1 – refer to Scheme S.1). In the optimized process, **Fe(0)/C** samples are not removed from the tube furnace: after the 800 °C/Ar pyrolysis, the furnace is cooled to 600 °C under flowing Ar, and the flowing gas is switched to air. After a short period under those conditions (20 min), the flowing gas is switched to  $\text{H}_2$ , and after a longer pyrolysis period (5 h), the temperature is taken slowly (at 5 °C  $\text{min}^{-1}$ ) back to ambient under continuous flow of  $\text{H}_2$ . The resulting materials are the terminal pure-iron(0) samples of this study, and are designated as **Fe(0)** (see Scheme 1). As inferred from Scheme 1 and confirmed by data in Table 1, the pyrolytic oxidative and re-reduction steps did not affect the size of the samples significantly: the diameters of **Fe(0)/C** and **Fe(0)** are about equal.



By TGA (Figure 1), both **Fe(0)/C** and terminal **Fe(0)** samples gain weight up to 800 °C: 38.6% and 43.5%, respectively. XRD analysis (see Section 2.2b below) shows no other crystalline phase (e.g., oxides) in any of those samples, and CHN analysis gave  $5.45 \pm 0.85\%$  of residual carbon in **Fe(0)/C**, and  $0.07 \pm 0.01\%$  in **Fe(0)** (Table S.1). By assuming no other contaminant in **Fe(0)/C** but carbon, and by employing XRD to confirm that the TGA product was  $\alpha\text{-Fe}_2\text{O}_3$ , the weight gains observed in TGA were used to calculate the percent mass of iron(0) in **Fe(0)/C** and **Fe(0)**. Those values were found equal to  $96.7 \pm 0.5\%$  and  $100.5 \pm 0.1$ , respectively, i.e., in agreement with the results from CHN analysis. Furthermore, the skeletal density of **Fe(0)** ( $7.749 \pm 0.054 \text{ g cm}^{-3}$ ) agrees also well with the bulk density of  $\alpha\text{-Fe}$  ( $7.874 \text{ g cm}^{-3}$ ).

For characterization purposes, in selected runs, the 600 °C/air carbon-removal step was followed by direct cooling to ambient temperature under Ar; those samples are referred to as **Fe<sub>2</sub>O<sub>3</sub>/Fe(0)**. Also, in other runs the 600 °C/air treatment was followed by a H<sub>2</sub>-reduction step at 1200 °C. The purpose of that process was to densify iron aerogels in order to increase their strength for thermite applications (refer to Section 2.3, below). Those samples are referred to as **Fe(0)-1200**.

A comprehensive materials characterization study along processing is summarized in Table 1. Overall, in terms of shrinkage up to 200 °C, **PBO-FeO<sub>x</sub>-200** behaves very similarly ( $21.6 \pm 0.2\%$ ) to the controls (15-22%). Significant shrinkage (53%) is noted after carbothermal reduction, but interestingly manipulations to remove unreacted carbon [i.e., **Fe(0)/C**  $\rightarrow$  **Fe<sub>2</sub>O<sub>3</sub>/Fe(0)**  $\rightarrow$  **Fe(0)**] had little relative effect on the sample size (shrinkage 53  $\rightarrow$  59%). Large differential shrinkage is observed with samples processed at 1200 °C (**Fe(0)-1200**, 76%) versus those at 800 °C (**Fe(0)**, 59%), pointing to

annealing effects. Porosities (as percent of empty space) are uniformly high (>90% v/v), both in the controls and in the IPNs through carbothermal processing, dropping to 66% v/v *only* in the 1200 °C-processed samples (**Fe(0)-1200**). The porosity of **Fe(0)** was 93% v/v. BET surface areas,  $\sigma$ , were generally high in the as-prepared **FeOx** and cured **FeOx-200** controls (in the 300-400 m<sup>2</sup> g<sup>-1</sup> range), pointing to relatively small particles. The surface area of the **PBO-Fe<sup>3+</sup>** controls was low (only 10-20 m<sup>2</sup> g<sup>-1</sup>), yet in accord with the surface area of HCl-catalyzed PBO aerogels (as a result of relatively large skeletal particles - see previous article of this issue). The particle size-based argument for the trends in the surface area is supported by particle size calculations using  $\text{radius} = 3/\rho_s \sigma$  ( $\rho_s$ : skeletal density; results are included in Table 1), however, it is noted also that this calculation is in need of independent evaluation (see next section), because  $\sigma$  and the particle size are not linearly independent. The BET surface area of **PBO-FeOx** and **PBO-FeOx** was also high (270-290 m<sup>2</sup> g<sup>-1</sup>), presumably because of the FeOx network (see next section). The surface area of **Fe(0)/C** was still relatively high (78 m<sup>2</sup> g<sup>-1</sup>), but it dropped precipitously after removal of carbon (to 6.6 m<sup>2</sup> g<sup>-1</sup> in **Fe(0)**), suggesting, qualitatively, that most of the surface area in **Fe(0)/C** was associated with the residual carbon. Similarly, the overall N<sub>2</sub>-sorption isotherms (shown in Figure S.2 in the Supporting Information) indicate mostly macroporous materials, which is confirmed via average pore diameter considerations: values for the latter calculated via the  $4V_{\text{Total}}/\sigma$  method using for the total pore volume,  $V_{\text{Total}}$ , either the single highest amount of N<sub>2</sub> adsorbed on the isotherm, or the value calculated via  $V_{\text{Total}} = (1/\rho_b) - (1/\rho_s)$ , diverge greatly after removal of unreacted carbon (see Table 1).

All material characterization data considered together signify that the PBO network must have played the role of the template holding the developing iron(0) network together into low-density, high-porosity monoliths, as planned. The following section concerns a step-by-setp analysis of the process from gelation to final annealing.

Table 1. Material properties of PBO-FeOx interpenetrating networks and controls

Aerogel	Linear shrinkage [%] <sup>a, b</sup>	Bulk density $\rho_b$ [g cm <sup>-3</sup> ] <sup>a</sup>	Skeletal density $\rho_s$ [g cm <sup>-3</sup> ] <sup>c</sup>	Porosity $\Pi$ [% v/v]	BET Surface area, $\sigma$ [m <sup>2</sup> g <sup>-1</sup> ]	Average pore diameter [nm]		particle radius $r$ [nm] <sup>f</sup>
						via 4V/ <sup>d</sup>	$\sigma$ / <sup>e</sup>	
<i>Control Aerogels</i>								
FeOx	15.2 ± 0.7	0.110 ± 0.032	3.295 ± 0.054	97	407	28.3	86.4	2.2
FeOx-200	22.2 ± 0.8	0.131 ± 0.053	3.916 ± 0.046	97	299	32.4	98.7	2.6
PBO-Fe <sup>3+</sup>	18.4 ± 0.9	0.120 ± 0.006	1.393 ± 0.006	91	12.3	35.6	2480	175
PBO-Fe <sup>3+</sup> -200	21.2 ± 0.5	0.127 ± 0.003	1.471 ± 0.013	91	19.7	9.8	1460	104
<i>Interpenetrating Networks</i>								
PBO-FeOx	15.9 ± 1.1	0.156 ± 0.018	2.607 ± 0.015	94	273	17.3	88.3	4.2
PBO-FeOx-200	21.6 ± 0.2	0.174 ± 0.010	2.579 ± 0.065	93	296	20.0	72.7	3.9
Fe(0)/C	53.4 ± 0.4	0.365 ± 0.040	6.542 ± 0.052	95	78.3	12.9	133	5.9
Fe <sub>2</sub> O <sub>3</sub> /Fe(0)	55.1 ± 0.3	0.552 ± 0.011	5.253 ± 0.016	89	2.26	32.0	2830	250
Fe(0)	59.2 ± 0.6	0.542 ± 0.068	7.749 ± 0.054	93	6.57	13.3	1120	58.9
Fe(0)-1200	76.0 <sub>4</sub> ± 0.9 <sub>9</sub>	2.61 <sub>6</sub> ± 0.11 <sub>1</sub>	7.626 ± 0.178	66	0.37	4.1	2720	1060

<sup>a</sup> Average of three samples. <sup>b</sup> Shrinkage = 100 × (mold diameter - sample diameter)/(mold diameter). <sup>c</sup> Single sample, average of 50 measurements. <sup>d</sup> The specific pore volume (cm<sup>3</sup> g<sup>-1</sup>),  $V$ , was calculated via the single point adsorption method from the N<sub>2</sub>-sorption isotherm. <sup>e</sup>  $V$  was set equal to the total pore volume,  $V_{\text{Total}} = (1/\rho_b) - (1/\rho_s)$ . <sup>f</sup> Calculated via  $r = 3/\rho_s \sigma$ .

## 2.2 Detailed Physicochemical Characterization along Processing

*2.2a The PBO-FeOx interpenetrating network.* By SEM (Figure 2), **PBO-FeOx-200** and the two controls, **FeOx-200** and **PBO-Fe<sup>3+</sup>-200**, all consist of particles. Particles in **PBO-Fe<sup>3+</sup>-200** are much larger than those in **FeOx-200**; Particles in **PBO-FeOx-200**

are about the same size to those in **PBO-Fe<sup>3+</sup>-200**, but are decorated with smaller particles of about the same size as in **FeOx-200**. STEM of **PBO-FeOx-200** shows darker interconnected aggregates, presumably of FeOx embedded in lighter matter (PBO). Neither SEM nor TEM are conclusive about formation of independent PBO and FeOx networks. For identification and assignment of the structural features in microscopy we turned to rheology and dynamic mechanical analysis (DMA) during gelation, followed by small angle x-ray scattering of the resulting aerogels (Section 2.2a.1). Clues about chemical interactions between the two networks come from FTIR and Mössbauer spectroscopy (Section 2.2a.2).

*2.2a.1 The gelation process and nanoscopic characterization.* Reasoning that simple accumulation of matter on a pre-formed gel structure would cause a gradual change of the mechanical properties of the gel, while gelation of a second network inside a first one would cause an abrupt change of the mechanical properties, we used rheology and DMA in tandem in order to follow the gelation of the first network and detect the possible gelation of the second one. Those experiments were conducted with the same sol: a small amount was placed on the rheometer and the remaining was cast in a mold. Shortly after rheology indicated gelation, the gel was removed from the mold and was placed in the dynamic mechanical analyzer (see Experimental). Time for both experiments counted from the moment of mixing the sol.

Rheometry was conducted in the multi-wave oscillation mode.<sup>32</sup> As demonstrated with one frequency (after deconvolution of the data – see Figure 3A), the elastic ( $G'$ ) and viscous ( $G''$ ) moduli of the sol cross one another (near the gel point), as expected. The formal gelation time is identified at the common crossing point of all  $\tan \delta (= G''/G')$ , at

all oscillating frequencies employed.<sup>33</sup> For better accuracy, that common crossing point was identified at the minimum of the statistical function  $\text{Log} [s/\langle \tan \delta \rangle]_t$  as a function of time,  $t$ , (Figure 3B), whereas  $s$  is the standard deviation and  $\langle \tan \delta \rangle$  is the average value of  $\tan \delta$  at each sampling time,  $t$ . Data for the FeOx, PBO-Fe<sup>3+</sup> and PBO-FeOx sols are summarized in Table 2. It is noted that in all cases, the phenomenological and actual gelation times were very close, indicating absence of thixotropic phases. The common  $\tan \delta$  values at the respective gelation points were used to calculate the gel exponents,  $n$ ,<sup>34</sup> which, in turn, were used to calculate the mass fractal dimensions,  $D_f$ , of the particles forming each gel framework.<sup>35</sup> Those fractal dimensions express how matter fills space and are fingerprint-type physical constants of particle aggregates, allowing their tracking and identification as the structure evolves. It is noted that both the gelation time, and the  $D_f$  value of the PBO-FeOx sol closely match the values of the FeOx sols, meaning that the FeOx network is formed first, with minimum interference, from the BO monomer.

Table 2. Rheological and dynamic mechanical analysis data at 80 °C, of sols as indicated.

sols	rheology					DMA			
	$t_{g\text{-phen}}^a$ (min)	$t_{g\text{-rheom}}^b$ (min)	$\tan \delta$ @ $t_{g\text{-rheom}}$	$n^c$	$D_f^d$	$t_{\text{DMA}}^e$ (min)	$\tan \delta$ @ $t_{\text{DMA}}$	$n^c$	$D_f^d$
<b>FeOx</b>	8-10	8	0.13	0.08	2.42	f	f	f	f
<b>PBO-Fe<sup>3+</sup></b>	280-300	275	0.28	0.17	2.35	f	f	f	f
<b>PBO-FeOx</b>	18-20	16	0.16	0.10	2.41	65	0.31	0.19	2.32

<sup>a</sup> Phenomenological gelation time by inverting the molds. <sup>b</sup> Formal gelation times identified at the minima of the statistical functions as shown in Figure 3B <sup>c</sup> Gel exponent,  $n$ , calculated via:  $\tan \delta = \tan (n\pi/2)$ .<sup>34</sup> <sup>d</sup> Calculated via:  $n=D(D+2-2D_f)/2(D+2-D_f)$ ,<sup>35</sup> where  $D(=3)$  is the dimension of non-fractal clusters. <sup>e</sup> Gelation point of the second network obtained with DMA at the minimum of the statistical function as shown in Figure 3D. <sup>f</sup> Not relevant.

Subsequently, in DMA (in the multifrequency compression mode, Figure 3C), the elastic and viscous moduli of the resulting gels did not cross (as also expected), however, the elastic modulus shows an abrupt and rapid increase, at about the same time at all frequencies. Again, all  $\tan \delta$  values cross at a point that was identified accurately from a plot of the statistical function ( $\text{Log} [s/\langle \tan \delta \rangle]_t$ ) as a function of time (Figure 3D). That crossing point matches very well, time-wise, with the stabilization of the pH (at 5.5) inside the PBO-FeOx wet-gels (Figure 3E). In turn, that pH value matches well with the  $\text{pK}_a$  value of *N,N'*-dimethylaniline (5.15, in water),<sup>36</sup> and is attributed to the buffering effect of the (dimethylaniline-like) Mannich bases formed from the ring opening polymerization of the BO monomer (Scheme 2B). Considering those two pieces of evidence together suggests that an independent PBO network is formed inside the pores of the FeOx gel. Additional evidence for the identity of the second network is provided by the  $D_f$  value of the particles that form it, which agrees with the  $D_f$  value of the PBO-Fe<sup>3+</sup> gel, as derived from rheology (Table 2). The difference in the  $t_{g\text{-rheom}}$  (of PBO-Fe<sup>3+</sup>) and  $t_{\text{DMA}}$  (of PBO-FeOx) (275 min versus 65 min, respectively) might be attributed to the different catalytic activity of  $[\text{Fe}(\text{H}_2\text{O})_6]^{3+}$  versus the FeOx sol.

Based on the conclusions from rheology/DMA, the two gel components form two networks successively. As pointed out, however, this is hardly evident from SEM. Thus, a post-gelation quantitative evaluation of the fundamental building blocks of the two networks was obtained with small angle x-ray scattering (SAXS). Primary SAXS data are shown in Figure S.3 of the Supporting Information. Results for **PBO-FeOx-200** along with the control samples are summarized in Table 3. The radii of the smallest particles in **PBO-FeOx-200** match those of the primary particles in the **FeOx-200** controls (7.2 and

6.3 nm, respectively). A second distinguishing feature of those particles is their abrupt interfaces (high- $Q$  slopes = -4.0;  $Q$ : scattering vector), while particles in all acid-catalyzed PBO aerogels have density-gradient (fuzzy) interfaces (high- $Q$  slope = -4.4) and are much larger (with radii around 45 nm).

Analysis of the scattering profiles at lower  $Q$ -values shows that primary particles in the **FeOx-200** control samples form secondary particles of about 27 nm in radius and a mass fractal dimension ( $D_m=2.6\pm0.6$ ). Owing to its large standard deviation (due the narrow  $Q$ -range – Region III in Figure S.3), that  $D_m$  value may be interpreted either as close to the  $D_f$  value of the particles that form the FeOx gel network (Table 2), or as closely-packed primary particles ( $D_m=3.0$ ), or even as surface fractals (slope<-3.0). Probably the situation is somewhere between the two extremes: **FeOx-200** shrink an additional 46% in linear dimensions relative to as-prepared **FeOx** (see Table 1), which is

Table 3. Small angle x-ray scattering (SAXS) data of aerogels as shown

sample	Primary Particles			Secondary Particles		
	high- $Q$ slope <sup>a</sup>	$R_G(1)$ <sup>b</sup> (nm)	$R(1)$ <sup>c</sup> (nm)	$D_m$ <sup>d</sup>	$R_G(2)$ <sup>e</sup> (nm)	$R(2)$ <sup>c</sup> (nm)
<b>FeOx-200</b>	-4.0 <sub>0</sub> ±0.1 <sub>1</sub>	4.8±0.2	6.2±0.3	2.6±0.6	21±3	27±4
<b>PBO-A-7-200</b> <sup>f</sup>	-4.35±0.01	35±1	45±1	<sup>g</sup>	<sup>g</sup>	<sup>g</sup>
<b>PBO-FeOx-200</b>	-4.00±0.05	5.6±0.2	7.3±0.3	2.3±0.5	46±3	60±4

<sup>a</sup> Slopes<-4.0, signifying primary particles with density-gradient boundaries. <sup>b</sup> Radius of gyration of primary particles,  $R_G(1)$ , from first Guinier knee (see Figure S.3). <sup>c</sup> Particle radii =  $R_G/0.77$ . <sup>d</sup> Mass fractal dimension of secondary particles,  $D_m$ , equal to the |slope| of the low- $Q$  power-law along the scattering profile. <sup>e</sup> Radius of gyration of secondary particles,  $R_G(2)$ , from second Guinier knee (see Figure S.3). <sup>f</sup> Values taken from the previous paper of this issue for the approximate density-matched acid-catalyzed PBO network (considering a ~40% BO monomer mass loss during solvent exchange washings). <sup>g</sup> Not accessible within the  $Q$ -range available.

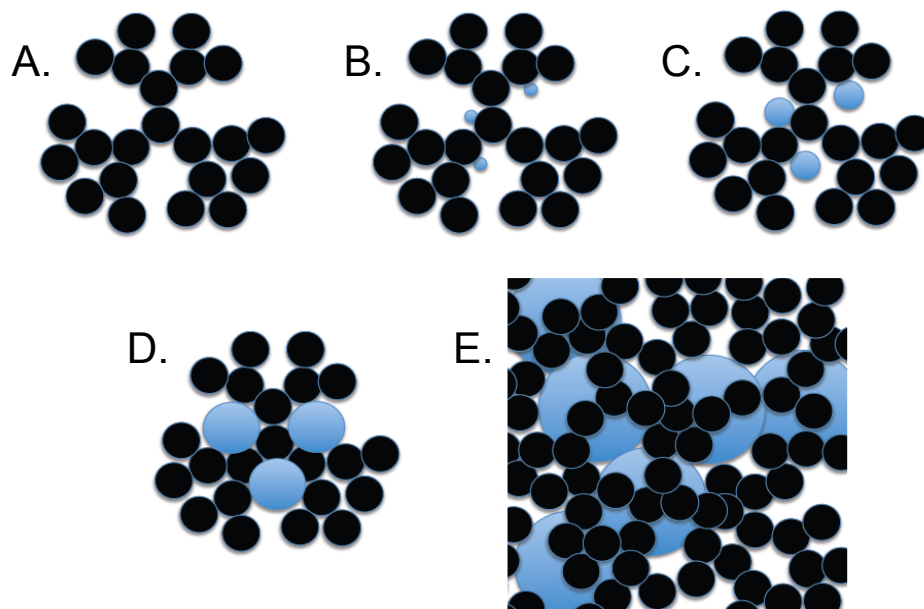
expected to cause a significant rearrangement at the secondary particle level by penetration of primary particles of one secondary particle into the fractal space of another.<sup>37</sup>

Conversely, within the accessible  $Q$ -range, none of the HCl-catalyzed PBO aerogels (e.g., **PBO-A-7-200** – Table 3) shows a second power-law region, or a radius of gyration from higher aggregates. In the same lower- $Q$  range as above, **PBO-FeOx-200** show also a second power-law region (Region III – Figure S.3) with a slope equal to  $-2.3 \pm 0.5$ . That region is followed by a second Guinier knee (Region IV in Figure S.3), corresponding to a second kind of particles with a radius of about 60 nm. The lower- $Q$  power-law slope is not associated with the assembly of PBO particles; those are too large and, as just stated, the power-law region of their assembly is expected beyond the accessible  $Q$ -range. The fractal dimension corresponding to the low- $Q$  slope of **PBO-FeOx-200**,  $D_m = 2.3 \pm 0.5$ , matches (within error) that of the assembly of FeOx primary into secondary particles ( $D_m = 2.6 \pm 0.6$  - see above), but the radius of the next-size moiety (60  $\pm$  4 nm) does not correspond to the radius of the FeOx secondary particles (27  $\pm$  4 nm). Instead, that radius fits better with: (a) the SAXS radius of the PBO particles in **PBO-A-7-200** (45 nm); and, (b) the size of the SEM particles of **PBO-Fe<sup>3+</sup>-200**, or of the larger entities in **PBO-FeOx-200** (Figure 2).

Rheology/DMA/SAXS data together suggest that formation of the second network (PBO) disrupts the FeOx network at the secondary particle level. This is not difficult to reconcile: since the FeOx network is formed first, polymerization of the BO monomer is catalyzed mainly by the acidic surface -Fe-O-H groups, which are mostly located within secondary particles. (It is noted that most of the surface area in



Scheme 3. Proposed growth mechanism of PBO-FeOx interpenetrating networks



A: The fractal network of primary particles (dark circles) within a secondary FeOx nanoparticle. B,C,D: PBO (blue circles) grows out of the surface of primary FeOx nanoparticles, inside secondary FeOx nanoparticles. E. When PBO nanoparticles grow large, they disrupt the FeOx network, and still interconnected FeOx primary particles

hierarchical structures is found within the fractal aggregates.) Thus, as summarized in Scheme 3, growth of PBO particles larger than the FeOx secondary particles inside the latter, turns the FeOx secondary particles ‘inside-out’ and provides a plausible explanation for the SEM structure of the **PBO-FeOx-200** network (Figure 2). To reconcile the slope of the second power-law region with the fractal dimension of the FeOx secondary particles, it is assumed that some of the original geometry is retained within the clusters of FeOx particles decorating the PBO surface. The growth model of Scheme 3, in agreement with conclusions reached from TGA data in Section 2.1, suggests a close chemical interaction between FeOx and PBO, which is discussed in the next section.

2.2a.2 *Cross-particle chemical interactions.* Those were probed with FTIR and Mössbauer spectroscopy.

In FTIR (Figure 4), as-prepared **PBO-Fe<sup>3+</sup>** controls show the characteristic out-of-plane C-H bending absorption of *para*-substituted aniline at 825 cm<sup>-1</sup> (compare with the spectrum of the HCl-catalyzed **PBO-A-7-RT**),<sup>38</sup> confirming that the polymerization mechanism is acid-catalyzed, as designed. (For assignment of other absorptions above 1000 cm<sup>-1</sup> see previous paper of this issue.) That 825 cm<sup>-1</sup> absorption becomes weaker in the **PBO-Fe<sup>3+</sup>-200** samples, consistent with oxidation processes that involve ring-closure along the polymeric backbone, between *para*-substituted aniline and phenol (refer to Scheme 4 of the previous article of this issue). Taking into consideration the lower absorption intensities (due to the “dilution” effect of FeOx), the same observations extend to **PBO-FeOx** and its cured counterpart, **PBO-FeOx-200**.

Moreover, all iron-related samples show strong absorptions below 600 cm<sup>-1</sup>. Absorptions in the 450-480 cm<sup>-1</sup> range are attributed to Fe-O stretches in octahedral coordination [FeO<sub>6</sub>], and those at 560-580 cm<sup>-1</sup> to Fe-O stretches in tetrahedral coordination [FeO<sub>4</sub>].<sup>39</sup> In that regard, the spectra of **FeOx** (not shown) and **FeOx-200** (Figure 4) are similar, showing both of those absorptions, albeit in inverse relative intensity. As-prepared **PBO-Fe<sup>3+</sup>** controls show also a strong absorption in the 560-580 cm<sup>-1</sup> range indicating that iron, which, according to TGA (Figure 1), is retained within the PBO network, is found mainly in tetrahedral coordination sites, in accord also with reports on preferred tetrahedral coordination of polybenzoxazines with other metal ions (e.g., Cu<sup>2+</sup>).<sup>40</sup> Upon curing at 200 °C/air, **PBO-Fe<sup>3+</sup>-200** shows an increase of the [FeO<sub>6</sub>] absorption in the 450-480 cm<sup>-1</sup> range. On the other hand, the FTIR spectrum of as-

prepared **PBO-FeOx** is identical to that of **PBO-200** (Figure 4), but after curing, **PBO-FeOx-200** shows a distinctly different pattern with a single maximum absorption at  $585\text{ cm}^{-1}$  (pointed with an arrow) that is assigned to the Fe-O lattice mode in  $\text{Fe}_3\text{O}_4$ .<sup>41</sup> Presence of  $\text{Fe}_3\text{O}_4$  after curing at  $200\text{ }^\circ\text{C}$ , means that the **FeOx** network is involved in the oxidation of PBO, itself getting reduced. This view is important for the subsequent carbothermal processing, and was investigated by looking in detail into the chemical state of iron with Mössbauer spectroscopy (Figure 5).

As summarized in Table 4, the Mössbauer spectrum of **FeOx-200** can be fitted, based on the chemical isomer shift ( $\delta$ ) and quadrupole splitting ( $\Delta$ ), into either (a) two quadrupole doublets, corresponding to  $\text{Fe}^{3+}$  in tetrahedral and octahedral co-ordination sites,<sup>42</sup> as for example in akaganèite ( $\beta\text{-FeOOH}$ ), one of the hydrolysis products of ferric chloride);<sup>43</sup> or, (b) a single quadrupole doublet with mean quadrupole splitting  $\Delta=0.68\text{ mm s}^{-1}$ , whereas broadness (full width at half maxima  $F=0.61\text{ mm s}^{-1}$ ) can be attributed to more than one type of octahedral sites (e.g.,  $\alpha\text{-}$  and  $\beta\text{-FeOOH}$ , i.e., a mixture of oxide hydroxides).<sup>42a,44</sup> FTIR data above support  $\text{Fe}^{3+}$  in both tetrahedral and octahedral sites. As-prepared **PBO-FeOx** aerogels demonstrate very similar structures to those of **FeOx-200**, again in agreement with FTIR, with the only difference being in the distribution of  $\text{Fe}^{3+}$  between tetrahedral versus octahedral sites; the 4-hedral:8-hedral ratio is increased from 1.1 (in **FeOx-200**) to 1.2 (in **PBO-FeOx**), i.e., in favor of the tetrahedral sites as discussed above.<sup>40</sup> After curing in air, **PBO-FeOx-200\_(Air)** aerogels show a dramatic decrease of  $\text{Fe}^{3+}$  in 8-hedral co-ordination accompanied by a small further increase of  $\text{Fe}^{3+}$  in 4-hedral sites, but most importantly by a new component (sextet) with a magnetic hyperfine field,  $H_{\text{hf}}=454\text{ kOe}$ . That hyperfine splitting fits *only* to the B-sites (octahedral

Table 4. Mössbauer spectroscopy data for samples as shown

Sample		$\delta^a$ (mm s <sup>-1</sup> )	$\Delta$ or $\varepsilon^*$ <sup>b</sup> (mm s <sup>-1</sup> )	$\Gamma^c$ (mm s <sup>-1</sup> )	$H_{hf}^d$ (kOe)	State of iron	Type of site <sup>g</sup>	Site %
<b>FeOx-200</b>	Doublet 1	0.343	1.005	0.538	<sup>e</sup>	Fe <sup>3+</sup>	8-hedral	48.0
	Doublet 2	0.346	0.497	0.461	<sup>e</sup>	Fe <sup>3+</sup>	4-hedral	52.0
<b>PBO-FeOx</b>	Doublet 1	0.346	0.955	0.513	<sup>e</sup>	Fe <sup>3+</sup>	8-hedral	46.0
	Doublet 2	0.349	0.492	0.496	<sup>e</sup>	Fe <sup>3+</sup>	4-hedral	54.0
<b>PBO-FeOx-200 (Air)</b>	Doublet 1	0.380	1.150	0.590	<sup>e</sup>	Fe <sup>3+</sup>	8-hedral	13.0
	Doublet 2	0.363	0.610	0.594	<sup>e</sup>	Fe <sup>3+</sup>	4-hedral	58.8
	Sextet	0.613	0.062	1.454	454.0	Fe <sub>3</sub> O <sub>4</sub>	<sup>h</sup>	28.7
<b>PBO-FeOx-200 (Ar)</b>	Doublet 1 (d1)	0.351	0.995	0.448	<sup>e</sup>	Fe <sup>3+</sup>	8-hedral	17.0
	Doublet 2 (d2)	0.349	0.563	0.506	<sup>e</sup>	Fe <sup>3+</sup>	4-hedral	58.0
	Doublet 3 (d3)	0.780	1.070	0.654	<sup>e</sup>	Fe <sup>3+</sup> / Fe <sup>2+</sup> <sup>f</sup>	<sup>f</sup>	17.3
	Double 4 (d4)	1.170	1.800	0.780	<sup>e</sup>	Fe <sup>2+</sup>	4-hedral	7.7
<b>Fe(0)</b>	Doublet	0.402	0.814	0.395		Fe <sup>3+</sup>	4-hedral	4.2
	Sextet	-0.000 <sub>1</sub>	0.000 <sub>0</sub>	0.353	329.8	Fe <sup>0</sup>	<sup>h</sup>	95.8

<sup>a</sup>  $\delta$ : Chemical isomer shift versus an iron foil standard ( $\alpha$ -Fe). <sup>b</sup>  $\Delta$ : quadrupole splitting vs. Fe<sup>0</sup>;  $\varepsilon^*$ : quadrupole isomer shift (for magnetically ordered materials) versus  $\alpha$ -Fe. <sup>c</sup>  $\Gamma$ : full width at half maxima. <sup>d</sup> Magnetic hyperfine field. <sup>e</sup> Not detected. <sup>f</sup> See text. <sup>g</sup> Tetrahedral (4-hedral): coordination number=4; Octahedral (8-hedral): coordination number=6. <sup>h</sup> Not relevant.

Fe<sup>2+</sup> + Fe<sup>3+</sup>) of Fe<sub>3</sub>O<sub>4</sub>, however, the associated hyperfine splitting expected simultaneously from Fe<sup>3+</sup> in the A- (tetrahedral) sites of Fe<sub>3</sub>O<sub>4</sub> could not be detected.<sup>45</sup> That could be attributed to the difficulty to fit the new low-intensity sextet accurately, or, alternatively, it could be claimed that the sextet belongs to  $\gamma$ -Fe<sub>2</sub>O<sub>3</sub>, which is known to be produced by heating FeOx aerogels at 260 °C in air.<sup>31,46</sup> The latter explanation, however, is rather unlikely in our case, first because the hyperfine splittings of  $\gamma$ -Fe<sub>2</sub>O<sub>3</sub> are larger (488 kOe and 499 kOe for the A- and B-sites, respectively,<sup>47a</sup>) than the  $H_{hf}$  value observed here, second because its isomer shifts ( $\delta = 0.27$  and  $0.41$  mm s<sup>-1</sup>) are also very different from the isomer shift of the new sextet ( $\delta = 0.613$  mm s<sup>-1</sup>), and third because the **FeOx-200** control, as discussed above, did not show any indication for hyperfine

splitting, thus excluding formation of  $\gamma\text{-Fe}_2\text{O}_3$  at 200 °C. In summary, Mössbauer data so far suggest that the new sextet belongs to the reduction product of FeOx with PBO.

That view was investigated further by heating as-prepared **PBO-FeOx** aerogels at 200 °C under Ar. The Mössbauer spectra of those **PBO-FeOx-200\_(Ar)** samples show a similar percentage of 4-hedrally coordinated  $\text{Fe}^{3+}$  as in **PBO-FeOx-200\_(Air)** (58% vs. 59%, respectively), and a similar reduction in the 8-hedral site population of  $\text{Fe}^{3+}$  (17% vs. 13%, respectively, relative to 46% in **PBO-FeOx** - refer to Table 4). However, unlike **PBO-FeOx-200\_(Air)**, no hyperfine splitting is observed in **PBO-FeOx-200\_(Ar)**, and the reduced number of 8-hedral sites for  $\text{Fe}^{3+}$  is accompanied by the appearance of two new doublets (d3 and d4) with  $\delta_{d3}=0.780 \text{ mm s}^{-1}$  ( $\Delta=1.070 \text{ mm s}^{-1}$ ) and  $\delta_{d4}=1.170 \text{ mm s}^{-1}$  ( $\Delta=1.800 \text{ mm s}^{-1}$ ). Doublet d4 (relative atomic contribution: 7.7%) is attributed to 4-hedrally coordinated  $\text{Fe}^{2+}$  (expected  $\delta=0.989\text{-}1.208 \text{ mm s}^{-1}$  with  $\Delta=1.780\text{-}2.490 \text{ mm s}^{-1}$ ).<sup>42a,48</sup> The origin of doublet d3 (relative contribution: 17.3%) is ambiguous as its chemical isomer shift value  $\delta=0.780 \text{ mm s}^{-1}$  lies in between the  $\text{Fe}^{2+}$  and  $\text{Fe}^{3+}$  oxidation states.<sup>42a,48</sup> Overall, since iron in **FeOx-200** remains in the +3 oxidation state, it is clear from **PBO-FeOx-200\_(Air)** and **PBO-FeOx-200\_(Ar)** that the +2 oxidation state is due to the presence of PBO. Hence, in conclusion FeOx is involved directly in the oxidation of the PBO network, which, as demonstrated in the previous article of this issue, is essential for its ability to carbonize. That reaction is definitely not quantitative up to 200 °C, and  $\text{Fe}_3\text{O}_4$  has been the only identifiable product from the reduction of FeOx. One of the issues addressed in the next section is whether FeOx is enough for complete oxidation of the PBO network (perhaps at some higher temperature), in which case the curing step at 200 °C/air could be by-passed, thus simplifying the process.

2.2b *The carbothermal conversion of PBO-FeOx to Fe(0)*. X-Ray diffraction (XRD) analysis along pyrolysis of **PBO-FeOx-200** and controls, is shown in Figure 6. Corresponding SEM images are shown in Figure 7.

Cured **PBO-FeOx-200** aerogels appear amorphous with only weak bumps over the baseline (marked with asterisks) corresponding to diffractions from the (311) and (440) planes of  $\text{Fe}_3\text{O}_4$ . Upon heating at 600 °C under Ar [sample denoted as **PBO-FeOx-200 @ 600 °C (Ar)**], the XRD spectrum is identified with  $\text{Fe}_3\text{O}_4$ . In SEM, the oxide appears as large, randomly oriented and apparently interconnected crystals, embedded in amorphous material (carbon). To form micron-size crystals,  $\text{Fe}_3\text{O}_4$  needs to melt, but that should occur at a more-than-800 °C lower temperature than the melting point of the bulk material (m.p. = 1,597 °C). For control purposes, **FeOx-200** (an amorphous material as well) was also heated under Ar at 800 °C; the only crystalline phase there was  $\alpha\text{-Fe}_2\text{O}_3$  (Figure 6), and again SEM shows evidence of annealing (larger particles with wider necks - compare Figures 7 with Figure 2). (It is noted that the m.p. of  $\alpha\text{-Fe}_2\text{O}_3$  is 1,566 °C.) Low-temperature annealing of iron oxide ribbons (250-400 °C)<sup>49</sup> and films (400-700 °C)<sup>50</sup> has been observed before. Annealing is attributed to surface melting phenomena, whose effectiveness depends on particle size (actually on the surface-to-volume ratio) and have lead to the advancement of the melt-dispersion reaction mechanism.<sup>51</sup>

By heating **PBO-FeOx-200** to 800 °C under the flowing Ar, the XRD spectrum shows  $\alpha\text{-Fe}$  as the only crystalline phase. As discussed in Section 2.1 above, those samples contain 4-5.5% carbon and are denoted as **F(0)/C**. According to SEM (Figure 7), iron(0) forms a continuous network, which, under high magnification, shows crystallites fused together, as from partial melting. Analysis of the (110) diffraction peak using the

Scherrer equation is inherently inaccurate due to the large size of the crystallites, but in the broad sense results agree with SEM (sizes >250 nm). Residual carbon appears as minor debris segregated and localized randomly at various spots of the network.

To address the question whether the 200 °C/air curing step is even necessary on the way to carbothermal reduction, as-prepared PBO-FeOx samples were pyrolyzed directly at 800 °C under Ar. XRD analysis (Figure S.1) shows that the product consists mostly of  $\alpha$ -Fe together with a very small amount of Fe<sub>3</sub>O<sub>4</sub>. Since the data above show that PBO-FeOx-200 is first converted to Fe<sub>3</sub>O<sub>4</sub> and then to  $\alpha$ -Fe, we conclude that the original PBO-FeOx samples contained enough PBO to reduce the entire amount of FeOx to Fe<sub>3</sub>O<sub>4</sub>, however, for converting all of that Fe<sub>3</sub>O<sub>4</sub> to  $\alpha$ -Fe, slightly more carbon than that produced from the equivalent amount of oxidized PBO was needed. Therefore, it is concluded that the air-oxidation step is necessary in order to ensure complete conversion of all PBO in PBO-FeOx to its carbonizable oxidized form.

The residual carbon in **Fe(0)/C** was removed at 600 °C under flowing air. By XRD, those samples (denoted as **Fe<sub>2</sub>O<sub>3</sub>/Fe(0)**) consisted of  $\alpha$ -Fe<sub>2</sub>O<sub>3</sub> and  $\alpha$ -Fe(0), in 89:11 w/w ratio (by quantitative phase analysis of the XRD spectrum of Figure 6). In SEM, the network appears similar to that of **Fe(0)/C**, although the thickness of the network walls is somewhat larger. No crystallites are visible under higher magnification.

$\alpha$ -Fe<sub>2</sub>O<sub>3</sub> was reduced back to iron(0) by switching the flowing gas to H<sub>2</sub>. XRD of the **Fe(0)** terminal samples shows only one crystalline phase ( $\alpha$ -Fe), and the lattice appears defect-free: the distance between (110) planes (via HRTEM - included in Figure 7) is equal to 0.21 nm throughout the sample.<sup>52</sup> In SEM, **Fe(0)** retain the general porous structure of their immediate precursor (**Fe<sub>2</sub>O<sub>3</sub>/Fe(0)**). Under higher resolution, **Fe(0)**

show some crystalline protrusions out of their smooth surfaces, which, however, are larger and fewer than those in as-prepared **Fe(0)/C**.

Although TGA, CHN analysis and skeletal density considerations of **Fe(0)** (see Section 2.1 above) point to pure iron, the Mössbauer spectrum (Figure 5) shows a superposition of the metallic iron sextet with a magnetic hyperfine field of 329.8 kG,<sup>47b</sup> and a quadrupole doublet assigned to Fe<sup>3+</sup> in octahedral coordination. The relative Fe(0):Fe<sup>3+</sup> site population was 96:4 (see Table 4). Since XRD of **Fe(0)** shows no other crystalline phase than  $\alpha$ -Fe, and since there is no other indication for impurities, the presence of Fe<sup>3+</sup> is attributed to amorphous surface oxide formed during the long exposure of the sample to the air during Mössbauer spectroscopy.

Industrial iron-making involves reduction of iron ore (oxides) with carbon in blast furnaces.<sup>53</sup> Both in the so-called direct reduction process, and in the pre-reduction stage of the smelting process the reducing agent is CO, which is produced by oxidation of carbon with air. Reduction by CO takes place stepwise from Fe<sub>2</sub>O<sub>3</sub> (hematite) to Fe<sub>3</sub>O<sub>4</sub> (magnetite), to FeO, to Fe(0). In the smelting process the bulk of the reduction takes place in molten iron that dissolves carbon. Hence, smelting is inherently a high-temperature process. Here, taking into consideration that: (a) reduction of **FeO<sub>x</sub>** aerogels at 800 °C under flowing CO gave only iron carbide (Fe<sub>3</sub>C) and graphite (see Figure S.1 in Supporting Information); (b) the gradual decrease of the amount of the remaining carbon with increasing pyrolysis temperature from 200 °C to 700 °C (via CHN analysis, see Table S.1); (c) the concomitant dominance of Fe<sub>3</sub>O<sub>4</sub> as the only crystalline phase below 800 °C and the associate annealing phenomena discussed above; and, (d) literature reports on mechanochemical studies with, for example, Al and C, showing a 800 °C



decrease of the synthesis temperature of  $\text{Al}_4\text{C}_3$  and suggesting a mechanism change from liquid-solid (case of high temperature reaction of bulk Al and C) to solid-solid,<sup>54</sup> we postulate a pre-reduction-like process between PBO (or its decomposition products) and  $\text{FeO}_x$  below 800 °C whereas the oxide is transformed gradually into  $\text{Fe}_3\text{O}_4$ , followed by a solid(C)- liquid( $\text{Fe}_3\text{O}_4$ ) reaction at the interface of the two materials. In that scheme, the role of the product, iron(0), should not be underestimated either: iron(0) (m.p.: 1,538 °C), is expected to undergo surface-melting as well, solubilizing the remaining carbon thus facilitating smelting in the classical sense.<sup>55</sup> Annealing of iron(0) is already observed in **Fe(0)** (Figure 7), but if the final reduction of  $\text{Fe}_2\text{O}_3/\text{Fe(0)}$  is carried out at 1,200 °C (instead of 600 °C - all other conditions kept the same:  $\text{H}_2/5\text{h}$ ), annealing phenomena are enhanced and the solid framework of the resulting **Fe(0)-1200** samples consists of thicker, completely structureless filaments with larger pores (Figure 7). Those annealing-related structural changes are responsible for the excessive shrinkage observed in **Fe(0)-1200** (76% – see Table 1 and photograph in Figure 8 below). However, it is also reminded that the porosity in annealed **Fe(0)-1200** still remains relatively high (66% v/v), hence **Fe(0)-1200** can be infiltrated easily with oxidizers (see next section).

**2.3 From Explosives to Thermites by Tuning the Porosity of Iron(0) Aerogels.** The immediate goal for the **Fe(0)** and **Fe(0)-1200** aerogels was their evaluation as energetic materials. For this, using capillary action, samples were infiltrated with acetone solutions of anhydrous  $\text{LiClO}_4$  and were dried exhaustively at 80 °C under vacuum for 24 h. **Fe(0)** are strong enough to tolerate the capillary forces of the evaporating solvent and remained monolithic. The amount of the salt retained within the pores was determined gravimetrically.  $\text{LiClO}_4$  was chosen over alternatives (e.g.,  $\text{NaClO}_4$

and  $\text{KClO}_4$ ) because of its higher solubility in acetone (0.427 mol:mol, versus 0.197 mol:mol for  $\text{NaClO}_4$ ),<sup>55</sup> and its relatively low melting point (236 °C) that promotes better contact of the two reactants once the ignition process is started. For that, dry small **Fe(0)**/ $\text{LiClO}_4$  samples (typically ~0.1 g) were placed in open vials and were ignited with a burner, or with a hot wire. Alternatively, samples were ignited in a bomb calorimeter (see Experimental) for determination of the heat released by the reaction, as a means of process identification and future applications design.

As shown in Figure 8A (picture captured from Movie S.1 in the Supporting Information), **Fe(0)**/ $\text{LiClO}_4$  samples explode violently. (**CAUTION:** the experiment was conducted in a 5-foot fume hood, all other items removed, behind: (a) a 0.25'' thick protective Plexiglass shield; and, (b) the hood sash closed.) Because the reaction of iron(0) with  $\text{LiClO}_4$  should not evolve gases, explosive behavior was not expected. (It is noted that heating  $\text{LiClO}_4$  by itself under the same conditions leads only to melting.) Since **Fe(0)** aerogels are 93% porous (Table 1), it was reasoned that the explosion was caused by rapid heating and expansion of the pore-filling air. Indeed, repeating that experiment with much less porous **Fe(0)-1200**/ $\text{LiClO}_4$  (Figure 8B from Movie S.2 in the Supporting Information) yielded a totally different behavior: **Fe(0)-1200**/ $\text{LiClO}_4$  samples do not explode, instead glow for a few seconds and remain monolithic. The process was repeated 3 times in a bomb calorimeter. Residues were collected and analyzed with XRD for residual iron(0) and products. The heat released was quantified at  $59 \pm 9 \text{ Kcal mol}^{-1}$  of iron reacted, in agreement with: (a)  $4\text{Fe} + \text{LiClO}_4 \rightarrow 4\text{FeO} + \text{LiCl}$  ( $66.64 \text{ Kcal mol}^{-1}$ ),<sup>56</sup> thus confirming independently the XRD results showing FeO as the only iron-related product in the bomb calorimeter experiment (see Figure S.1); and, (b) literature reports

on the reaction of iron with  $\text{KClO}_4$  showing formation of only  $\text{FeO}$ .<sup>57</sup> Notably, XRD analysis of the products from ignition of  $\text{Fe(0)}/\text{LiClO}_4$  in air (Figure 8A or 8B) shows a mixture of both  $\text{Fe}_3\text{O}_4$  and  $\text{FeO}$ , hence pointing to a pyrotechnics-like participation of air in the combustion process,<sup>26b</sup> namely via  $3\text{Fe} + 2\text{O}_2 \rightarrow \text{Fe}_3\text{O}_4$ , or  $3\text{FeO} + (\frac{1}{2})\text{O}_2 \rightarrow \text{Fe}_3\text{O}_4$ . Since overall oxidation of iron to  $\text{Fe}_3\text{O}_4$  is a more exothermic process (91.3 Kcal  $\text{mol}^{-1}$  of iron reacted),<sup>56</sup> those reactions intensify the violent explosion in Figure 8A, and can be desirable, depending on the application.

### 3. CONCLUSION

Polybenzoxazine (PBO) aerogels are mechanically and thermally robust, and yield carbon aerogels in high yield, hence, can play the role of sacrificial templates for the carbothermal synthesis of nanoporous pyrophoric metals as demonstrated herewith with iron(0) aerogels. For this, it is necessary to form IPNs of PBO with iron oxide, which is conveniently carried out via the newly discovered Brønsted-acid catalysis of the ring opening polymerization of benzoxazine monomers. Evidence shows that the process follows age-old smelting principles, however, owing to the large surface-to-volume ratio of the reacting nanoparticles, all processes have been carried out at over 800 °C lower temperatures than those in the classical process. A first application for the new iron(0) monolithic aerogels has been in energetic materials, demonstrating both explosive and thermite behavior by infiltrating the porous structure with an oxidant ( $\text{LiClO}_4$ ). We see no reason why this method could not be extended to alloys via multiple IPNs of various metal oxides.

## 4. EXPERIMENTAL SECTION

**4.1 Materials.** All reagents and solvents were used as received unless otherwise noted. Iron chloride hexahydrate ( $\text{FeCl}_3 \cdot 6\text{H}_2\text{O}$ ), paraformaldehyde (96%), aniline, and 4,4'-isopropylidenediphenol (bisphenol A) were obtained from Acros Organics. Dimethylformamide (DMF) and epichlorohydrin were obtained from Sigma-Aldrich. All reagents and solvents were used as received unless noted otherwise. Ultra-high purity argon (99.99999%), hydrogen (99.9999%) and compressed air were purchased from either Airgas (Rolla, MO) or Ozark Gas (Rolla, MO). Benzoxazine monomer (BO monomer) was synthesized as described in the previous article of this issue.

**4.2 Preparation of Polybenzoxazine-iron Oxide Interpenetrating Networks (PBO-FeOx Aerogels).** Solution A was prepared by dissolving 1 g (2.16 mmol) of purified BO monomer in 4.23 mL (4 g) DMF. Solution B was prepared by first dissolving (with ultra-sonication) 2.30 g (8.52 mmol) of iron chloride hexahydrate in 3 mL (2.8 g) DMF, and then adding 2.06 mL (25.56 mmol) of epichlorohydrin. Upon addition of epichlorohydrine, Solution B was immediately added to Solution A in a round bottom flask, the resulting sol was stirred magnetically for 5 min at room temperature and was poured into polypropylene jars (Fisherbrand, part no. 02-912-025, 1.5 inch in diameter), which were screw-capped and placed in an oven at 80 °C. Gelation took place in 15-20 min. Wet-gels were aged in their molds at 80 °C for 2 days, subsequently were removed from the molds and washed with DMF (2×12 h), followed with DMF:acetone (50:50 v/v, 2×12 h) and pure acetone (4×12 h). Acetone-filled wet-gels were dried in an autoclave with  $\text{CO}_2$  that was removed at the end as a supercritical fluid (SCF). The resulting PBO-

FeOx aerogels were step-cured in air at 160 °C for 1 h, at 180 °C for 1 h, and at 200 °C for 24 h. The final materials are referred to as **PBO-FeOx-200**.

For control purposes, iron oxide aerogels (**FeOx**) were prepared with iron chloride hexahydrate (2.30 g, 8.51 mmol), DMF (7.23 mL, 6.82 g) and epichlorohydrin (2.06 mL, 2.43 g, 26.26 mmol).  $[\text{Fe}(\text{H}_2\text{O})_6]^{3+}$ -catalyzed polybenzoxazine aerogels (**PBO-Fe<sup>3+</sup>**) were obtained with BO monomer (1 g, 2.11 mmol), iron chloride hexahydrate (2.30 g, 24.86 mmol) and DMF (7.23 mL, 6.82 g). Control sols and the resulting wet-gels were processed in the same way like the PBO-FeOx wet-gels. As-prepared aerogels from both controls were also step-cured at 200 °C and the resulting materials are referred to as **FeOx-200** and **PBO-Fe<sup>3+</sup>-200**, respectively.

#### 4.3 Conversion of PBO-FeOx Aerogels into Nanoporous Iron(0) Aerogels.

**PBO-FeOx-200** aerogels were transferred to a MTI GSL1600X-80 tube furnace (alumina 99.8%, 72 mm and 80 mm inner and outer diameters, respectively, with a 457 mm heating zone), which was flushed with ultra-high purity Ar for 1 h (300 mL min<sup>-1</sup>). Subsequently, the temperature of the furnace was raised to 800 °C at 5 °C min<sup>-1</sup> and was maintained there for 5 h under a 150 mL min<sup>-1</sup> flow of ultra-high purity Ar. At the end of the period, the temperature was first lowered to 600 °C at 5 °C min<sup>-1</sup>, the flowing gas was switched to air (at 150 mL min<sup>-1</sup>) and the new conditions were maintained for 20 min. Subsequently, while at 600 °C, the flowing gas was switched to H<sub>2</sub> and the flow (at 150 mL min<sup>-1</sup>) was maintained for 5 h. At the end, the tube furnace was cool down to room temperature at 5 °C min<sup>-1</sup> under flowing H<sub>2</sub>. Those samples are referred to as **Fe(0)**. For process identification purposes, samples were also removed from the furnace (with proper cooling at 5 °C min<sup>-1</sup>) after the 800 °C/Ar step (referred to as **Fe(0)/C**), and after

the 600 °C/air step (referred to as **Fe<sub>2</sub>O<sub>3</sub>/Fe(0)**). Alternatively, the final heating step under flowing H<sub>2</sub> was conducted at 1200 °C for 5 h (**Fe(0)-1200**).

**4.4 Methods and Procedures.** SCF drying was conducted in an autoclave (SPI-DRY Jumbo Supercritical Point Dryer, SPI Supplies, Inc. West Chester, PA). Bulk densities ( $\rho_b$ ) were calculated from the weight and the physical dimensions of the samples. Skeletal densities ( $\rho_s$ ) were determined with helium pycnometry using a Micromeritics AccuPyc II 1340 instrument. Porosities ( $IT$ ) as percent of empty space were determined from the  $\rho_b$  and  $\rho_s$  values via  $IT=100\times[(\rho_s-\rho_b)/\rho_s]$ .

*Characterization of the gelation process.* The rheological behavior of PBO-FeOx sols and controls was recorded with a TA Instruments AR 2000ex rheometer using an aluminum cone (60 mm diameter, 2° angle), a Peltier plate and a 1 mm gap between those. The instrument was operated in the continuous oscillation mode, and time-sweep experiments were performed with a fixed strain amplitude from mixing to gelation. The Peltier plate was set at 80 °C. The gel point was determined using a dynamic multiwave method with four superimposed harmonics with frequencies 1, 4, and 8 and 16 rad s<sup>-1</sup>. The strain of the fundamental oscillation (1 rad s<sup>-1</sup>) was set at 5%. The viscoelastic properties of newly formed PBO-FeOx wet-gels (i.e., right after gelation) were determined with a TA Instruments Model Q800 Dynamic Mechanical Analyzer in a multi frequency mode (superimposed harmonics: 1.0, 2.7, 4.5, 6.2, 8.0 Hz) using a submersion compression clamp (TA Instruments Part Number: 985067.901 - those clamps are useful for testing low to medium modulus samples while they are submerged in solvent). The experiment was conducted at 80 °C in DMF and was amplitude-controlled with 15 μm strain, and a ratio of static to dynamic force of 1.25 (preload force = 0.01N). The PBO-

FeO<sub>x</sub> wet-gels that were tested were ~1'' in diameter, 10 cm thick. The pH was also monitored during gelation with a pH electrode dipped in the sol. The electrode remained embedded in the gel, and monitoring continued past the phenomenological gelation point.

*Thermogravimetric analysis.* (TGA) was conducted in air with a TA Instruments Model TGA Q50 Thermogravimetric Analyzer, using a heating rate of 10 °C min<sup>-1</sup>.

*Chemical Characterization.* CHN elemental analysis was conducted with Perkin-Elmer Model 2400 CHN Elemental Analyzer, calibrated with acetanilide purchased from the National Bureau of Standards. Infrared (IR) spectra were obtained in KBr pellets using a Nicolet-FTIR Model 750 spectrometer. X-ray diffraction (XRD) was performed with powders from the corresponding materials using a PANalytical X'Pert Pro multipurpose diffractometer with Cu K $\alpha$  radiation ( $\lambda = 1.54 \text{ \AA}$ ) and a proportional counter detector equipped with a flat graphite monochromator. <sup>57</sup>Fe Mössbauer experiments were performed in the transmission geometry at room temperature using a conventional constant acceleration spectrometer and a gamma-ray source of <sup>57</sup>Co in a Rh matrix. Velocity calibration and isomer shifts are given with respect to alpha-Fe foil at room temperature. Mössbauer data were analyzed using Lorentzian line fitting with the RECOIL software package.<sup>58</sup>

*Skeletal framework analysis.* Scanning electron microscopy (SEM) was conducted with Au-coated samples on a Hitachi Model S-4700 field-emission microscope. SAXS was conducted with a PANalytical X'Pert Pro multipurpose diffractometer (MPD), configured for SAXS using Cu K $\alpha$  radiation ( $\lambda = 1.54 \text{ \AA}$ ) and a 1/32° SAXS slit and a 1/16° anti-scatter slit on the incident beam side, and 0.1 mm anti-scatter slit and Ni 0.125 mm automatic beam attenuator on the diffracted beam side.

Samples were placed in circular holders between thin Mylar<sup>TM</sup> sheets and scattering intensities were measured with a point detector in transmission geometry by 2 Theta scans ranging from -0.1 up to 5°. All scattering data were reported in arbitrary units as a function of  $Q$ , the momentum transferred during a scattering event. Data analysis was conducted using the Beaucage Unified Model<sup>59</sup> applied with the *Irena SAS* tool for modeling and analysis of small angle scattering within the commercial *Igor Pro* application (scientific graphing, image processing, and data analysis software from Wave Metrics, Portland, OR). Transmission Electron Microscopy (TEM) of **Fe(0)** was conducted with an FEI Tecnai F20 instrument employing a Schottky field emission filament operating at a 200 kV accelerating voltage. Scanning Transmission Electron Microscopy (STEM) of **PBO-FeOx-200** was conducted with the same instrument in the STEM mode, whereas the accelerating voltage of the Schotky field emission source was set at 120 kV. For both methods, aerogel samples were ground by hand in a mortar with a pestle. Small particles were dry-dusted onto a Quantifoil R1.2/1.3 holey carbon 200 mesh copper grid. Particles were sprinkled on the carbon film side three times, with light puffs of air across the sample between loadings, to remove loose particles. At least different 6 areas/particles were examined on each sample to insure that the results were uniform over the whole sample. Images were processed with Image J, a freely available software package that allows measurements of the spacing between the lattice fringes.

*Porosimetry.* Surface area, and pore size distributions were determined using N<sub>2</sub> sorption porosimetry with a Micromeritics ASAP 2020 surface area and porosity analyzer. Samples for porosimetry, pore size, and skeletal density determination were outgassed under vacuum for 24 h at 80 °C. Average pore diameters were determined with



the  $4 \times V_{\text{Total}}/\sigma$  method, where  $V_{\text{Total}}$  is the total pore volume per gram of sample and  $\sigma$ , the surface area determined with the Brunauer-Emmett-Teller (BET) method.  $V_{\text{Total}}$  can be calculated from either the single highest volume of  $\text{N}_2$  adsorbed along the adsorption isotherm, or from the relationship  $V_{\text{Total}} = (1/\rho_b) - (1/\rho_s)$ . Material lacks macroporosity when the two average pore diameters coincide.

*Calorimetry.* The enthalpy of the reaction taking place in  $\text{LiClO}_4$ -impregnated **Fe(0)** was measured in a 400 mL bomb calorimeter (Parr Instrument Company, Model 1672 Thermometer). The heat capacity of the calorimeter was measured using benzoic acid as standard. The sample was ignited with a nichrome fuse wire connected to the terminal socket on the apparatus head, which in turn was connected to the ignition unit. The heat released by the fuse was also taken into consideration in the calculations. After each experiment, the residue was collected and analyzed with XRD for the fraction of iron reacted and the iron products produced.

**SUPPORTING INFORMATION.** Alternative processes and controls including pictures of the resulting materials (Scheme S.1). CHN analysis data (Table S.1). XRD data of samples from control processes (Figure S.1).  $\text{N}_2$ -sorption data (Figure S.2). SAXS data (Figure S.3). Movies S.1 and S.2 of  $\text{LiClO}_4$ -loaded iron(0) samples upon ignition. This information is available free of charge via the Internet at <http://pubs.acs.org>.

**ACKNOWLEDGEMENTS.** We thank the Army Research Office for financial support under Award Number W911NF-12-2-0029, and Program Manager Dr. Michael Ding for his contagious enthusiasm and insightful comments. We also thank Dr. Amitava Choudhury for his assistance with Mössbauer spectroscopy and the Materials Research Center of MS&T for support with materials characterization.

## REFERENCES

1. (a) Yeh, F. -H.; Tai, C. -C. Huang, J. -F.; Sun, I. -W. *J. Phys. Chem. B* **2006**, *110*, 5215-5222. (b) Biener, J.; Hodge, A. M.; Hamza, A. M.; Hsiung, L. M.; Satcher, J. H. Jr. *J. Appl. Phys.* **2005**, *97*, 024301.
2. Hieda, M.; Garcia, R.; Dixon, M.; Daniel, T.; Allara, D.; Chan, M. H. W. *Appl. Phys. Lett.* **2004**, *84*, 628-630.
3. (a) Steele, B. C. H.; Heinzl, A. *Nature* **2001**, *414*, 345-352. (b) Ding, Y.; Chen, M.; Erlebacher, J.; *J. Am. Chem. Soc.* **2004**, *126*, 6876-6877.
4. (a) Bonroy, K.; Friedt, J. M.; Frederix, F.; Laureyn, W.; Langerock, S.; Campitelli, A.; Sára M.; Borghs, G.; Goddeeris, B.; Declerck, P. *Anal. Chem.* **2004**, *76*, 4299-4306. (b) Song, Y. Y.; Zhang, D.; Gao, W.; Xia, X. H.; *Chem. -Eur. J.* **2005**, *11*, 2177-2182.
5. Biener, J.; Wittstock, A.; Zepeda-Ruiz, L. A.; Biener, M. M.; Zielasek, V.; Krammer, D.; Viswanath, R. N.; Weissmüller, J.; Bäumer, M.; Hamza, A. V. *Nat. Mater.* **2009**, *8*, 47-51.
6. (a) Krishna, K. S.; Sandeep, S. S.; Philip, R.; Eswaramoorthy, M. *ACS Nano* **2010**, *4*, 2681-2688. (b) Wang, Y.; Shi, Y. -F.; Chen, Y. -B.; Wu, L. -M. *J. Solid State Chem.* **2012**, *191*, 19-26.
7. (a) Kulinowski, K. M.; Jiang, P.; Vaswani, H.; Colvin, V. *Adv. Mater.* **2000**, *12*, 833-838. (b) Velev, O. D.; Kaler, E. W. *Adv. Mater.* **2000**, *12*, 531-534.
8. Schimpf, S.; Lucas, M.; Mohr, C.; Rodemerck, U.; Bruckner, A.; Radnik, J.; Hofmeister, H.; Claus, P. *Catal. Today* **2002**, *72*, 63-78.
9. (a) Yeh, F. -H.; Tai, C. -C. Huang, J. -F.; Sun, I. -W. *J. Phys. Chem. B* **2006**, *110*, 5215-5222. (b) Biener, J.; Hodge, A. M.; Hamza, A. M.; Hsiung, L. M.; Satcher, J. H. Jr. *J. Appl. Phys.* **2005**, *97*, 024301. (c) Toberer, E. S.; Seshadri, R. *Chem. Commun.* **2006**, *30*, 3159-3165.
10. (a) Krishna, K. S.; Sandeep, S. S.; Philip, R.; Eswaramoorthy, M. *ACS Nano* **2010**, *4*, 2681-2688. (b) Wang, Y.; Shi, Y. -F.; Chen, Y. -B.; Wu, L. -M. *J. Solid State Chem.* **2012**, *191*, 19-26.
11. (a) Walsh, D.; Arcelli, L.; Ikoma, T.; Tanaka, J.; Mann, S. *Nat Mater.* **2003**, *2*, 386-390. (b) Tappan, B. C.; Huynh, M. H.; Hiskey, M. A.; Chavez, D. E.; Luther, E. P.; Mang, J. T.; Son, S. F. *J. Am. Chem. Soc.* **2006**, *128*, 6589-6594. (c) Hua, Z.; Deng, Y.; Li, K.; Yang, S. *Nanoscale Res. Lett.* **2012**, *7*, 1-7.
12. Gash, A. E.; Simpson, R. L.; Satcher, Jr.; J. H. Aerogels and Sol-Gel composite as Nanostructured Energetic Materials. In *Aerogels Handbook*; Agerter, M. A., Leventis, N., Koebel, M. M., Eds.; Springer: New York, 2011, pp 3-18.

13. See for example: (a) Henz, B. J.; Hawa, T.; Zachariah, M. *J. Appl. Phys.* **2009**, *105*, 124310. (b) Streletskii, A. N.; Povstugar, I. V.; Borunova, A. B.; Lomaeva, S. F.; Yu, P. *Butyagin, Colloid J.* **2006**, *68*, 470–480.
14. (a) Prentice, D.; Pantoya, M. L.; Gash, A. E. *Energy & Fuels* **2006**, *20*, 2370–2376. (b) Kim, S.; Zachariah, M. R. *Adv. Mater.* **2004**, *16*, 1821–1825.
15. Morris, C. A.; Anderson, M. L.; Stroud, R. M.; Merzbacher, C. I.; Rolison, D. R. *Science* **1999**, *284*, 622–624.
16. Tillotson, T. M.; Gash, A. E.; Simpson, R. L.; Hrubesh, L. W.; Satcher, J. H.; Poco, L. F.; *J. Non-Cryst. Solids* **2001**, *285*, 338–345.
17. Bigall, N. C.; Herrmann, A.-K.; Vogel, M.; Rose, M.; Simon, P.; Carrillo-Cabrera, W.; Dorfs, D.; Kaskel, S.; Gaponik, N.; Eychmuller, A. *Angew. Chem. Int. Ed.* **2009**, *48*, 9731–9734.
18. Armor, J. N.; Carlson, E. J.; Carrasquillo, G. *Mater. Lett.* **1986**, *4*, 373–376.
19. Tang, Y.; Yeo, K. L.; Chen, Y.; Yap, L. W.; Xiong, W.; Cheng, W. *J. Mater. Chem. A.* **2013**, *1*, 6723–6726.
20. Gash, A. E.; Satcher, J. H.; Simpson, R. L. Preparation of Porous Pyrophoric Iron using Sol-gel Methods U.S. Patent Application No. 20060042417A1, March 2, 2006.
21. Merzbacher, C.; Limparis, K.; Bernstein, T. F.; Rolison, D.; Homrighaus, Z. J.; Berry, A. D., U.S. Patent No. 6,296,678, (2001).
22. (a) Baumann, T. F.; Fox, G. A.; Satcher, J. H.; Yoshizawa, N.; Fu, R.; Dresselhaus, M. S. *Langmuir* **2002**, *18*, 7073–7076. (b) Baumann, T. F.; Satcher, J. H. *Chem. Mater.* **2003**, *15*, 3745–3747.
23. Job, N.; Picard, R.; Vertruyen, B.; Colomer, J.-F.; Marien, J.; Picard, J.-P. *J. Non-Cryst. Solids* **2007**, *353*, 2333–2345.
24. (a) Fu, R.; Baumann, T. F.; Cronin, S.; Dresselhaus, G.; Dresselhaus, M. S.; Satcher, J. H. *Langmuir* **2005**, *21*, 2647–2651. (b) Maldonado-Hódar, F. J.; Moreno-Castilla, C.; Rivera-Utrilla, J.; Hanzawa, Y.; Yamada, Y. *Langmuir* **2000**, *16*, 4367–4373. (c) Yoshizawa, N.; Hatori, H.; Soneda, Y.; Hanzawa, Y.; Kaneko, K.; Dresselhaus, M. S. *J. Non-Cryst. Solids* **2003**, *330*, 99–105. (d) Maldonado-Hódar, F. J.; Moreno-Castilla, C.; and A. F. Pérez-Cadenas, A. F. *Microporous Mesoporous Mater.* **2004**, *69*, 119–125. (e) Steiner, S. A.; Baumann, T. F.; Kong, J.; Satcher, J. H.; Dresselhaus, M. S. *Langmuir* **2007**, *23*, 5161–5166.
25. (a) Pleiner, R. *Iron in Archaeology: The European Bloomery Smelters*; Archeologicky ustav AV CR: Praha, 2000, pp 400 (ISBN: 978-80-86124-26-1). (b) Shrivastava, R. *Mining and Metallurgy in Ancient India*; Munshiram Manoharlal Publishers: New Delhi, 2006 (ISBN: 8121510090).

26. (a) Leventis, N.; Chandrasekaran, N.; Sotiriou-Leventis, C.; Mumtaz, A. *J. Mater. Chem.* **2009**, *19*, 63-65. (b) Leventis, N.; Chandrasekaran, N.; Sadekar, A. G.; Sotiriou-Leventis, C.; Lu, H. *J. Am. Chem. Soc.* **2009**, *131*, 4576-4577. (c) Leventis, N.; Chandrasekaran, N.; Sadekar, A. G.; Mulik, S.; Sotiriou-Leventis, C. *J. Mater. Chem.* **2010**, *20*, 7456–7471.
27. (a) Leventis, N. *Acc. Chem. Res.* **2007**, *40*, 874-884. (b) Leventis, N.; Sotiriou-Leventis, C.; Zhang, G.; Rawashdeh, A.-M. *NanoLetters* **2002**, *2*, 957-960.
28. (a) Gash, A. E.; Simpson, R. L.; Satcher, Jr.; J. H. Aerogels and Sol-Gel composite as Nanostructured Energetic Materials. In *Aerogels Handbook*; Agerter, M. A., Leventis, N., Koebel, M. M., Eds.; Springer: New York, 2011, pp 3-18. (b) Cooper, P. W. *Explosives Engineering* EDs; Wiley-VCH: New York, 1996.
29. (a) Ziese, W. *Ber.* **1933**, *66*, 1965–1972. (b) Kearby, K.; Kistler, S. S.; Swann, S. Jr. *Ind. Eng. Chem.* **1938**, *30*, 1082–1086. (c) Sydney, L. E. “Preparation of sols and gels,” British Patent No.: 2,111,966 (1983). (d) Jones, R. W. “Fundamental principles of sol-gel technology,” The Institute of Metals, 1989, London: UK. (e) Gash, A. E.; Tillotson, T. M.; Satcher, J. H.; Hrubesh, L. W.; Simpson, R. L. *J. Non-Cryst. Solids* **2001**, *285*, 22–28. (f) Gash, A. E.; Tillotson, T. M.; Satcher, J. H.; Poco, J. F.; Hrubesh, L. W.; Simpson, R. L. *Chem. Mater.* **2001**, *13*, 999–1007. (g) Leventis, N.; Vassilaras, P.; Fabrizio, E. F.; Dass, A. *J. Mater. Chem.* **2007**, *17*, 1502-1508. (h) Sisk, C. N.; Hope-Weeks, J. *J. Mater. Chem.* **2008**, *18*, 2607–2610.
30. Ishida H. U.S. Patent 5,543,516 (1996).
31. Long, J. W., Logan, M. S.; Rhodes, C. P.; Carpenter, E. E.; Stroud, R. M.; Rolison, D. R. *J. Am. Chem. Soc.* **2004**, *126*, 16879-16889.
32. Kim, S.-Y.; Choi, D.-G.; Yang, S.-M. *Korean J. Chem. Eng.* **2002**, *19*, 190–196.
33. Winter, H. H. *Polym. Eng. Sci.* **1987**, *27*, 1698–1702.
34. Raghavan, S. R.; Chen, L. A.; McDowell, C.; Khan, S. A.; Hwang, R.; White, S. *Polymer* **1996**, *37*, 5869–5875.
35. Muthukumar, M. *Macromolecules* **1989**, *22*, 4656–4658.
36. Serjeant, E. P.; Dempsey, B. *Ionization Constants of Organic Acids in Aqueous Solution*, Pergamon Press: Oxford, 1979.
37. (a) Mohite, D. P.; Mahadik-Khanolkar, S.; Luo, H.; Lu, H.; Sotiriou-Leventis, C.; Leventis, N. *Soft Matter* **2013**, *9*, 1531-1539. (b) Mohite, D. P.; Larimore, Z. J.; Lu, H.; Mang, J. T.; Sotiriou-Leventis, C.; Leventis, N. *Chem. Mater.* **2012**, *24*, 3434-3448.
38. Ran, Q.-C.; Zhang, D.-X.; Zhu, E.-Q.; Gu, Y. *Polymer* **2012**, *53*, 4119-4127.
39. Rada, S.; Dehelean, A.; Culea, E. *J Mol. Model.* **2010**, *17*, 2103-2111.

40. Chirachanchai, S.; Suttinum, P.; Laobuthee, A.; Tashiro, K. "Mono-Substituted Phenol-Based Benzoxazines: Inevitable Dimerization via Self-Termination and Its Metal Complexation," In *Handbook of Benzoxazine Resins*; Ishida, H.; Agag, T.; Eds.; Elsevier: Oxford, 2011, pp 111-126.
41. (a) Fan, T.; Pan, D.; Zhang, H. *Ind. Eng. Chem. Res.* **2011**, *50*, 9009-9018. (b) Jubb, A. M.; Allen, H. C. *ACS Appl. Mater. Interfaces* **2010**, *10*, 2804-2812.
42. (a) Bancroft, G. M.; 1973. *Mössbauer spectroscopy: an introduction for inorganic chemists and geochemists* 1<sup>st</sup> ed.; Wiley and Sons, New York, pp 251. (b) Kuzmann, E.; Nagy, S.; Vértes A. *Pure Appl. Chem.* **2003**, *75*, 801-858.
43. Murad E. *Clay Miner.* **1979**, *14*, 273-283.
44. Kuzmann, E.; Nagy, S.; Vértes A. *Pure Appl. Chem.* **2003**, *75*, 801-858.
45. Lyubutin, I. S.; Lin, C. R.; Korxhetskiy, Y. V.; Dmitriev, T. V.; Chian, R. K. *J. Appl. Phys.* **2009**, *106*, 034311-1-5.
46. Carpenter, E. E.; Long, J. W.; Rolison, D. R.; Logan M. S.; Pettigrew, K.; Stroud, R. M.; Kuhn, L. T.; Hansen, B. R.; Mørup, S. *J. Appl. Phys.* **2006**, *99*, 08711.
47. Greenwood, N. N. Gibb, T. C. *Mössbauer Spectroscopy* 1<sup>st</sup> ed.; Chapman and Hall Ltd: London, 1971: (a) pp 241; (b) pp 305.
48. Kuzmann, E.; Nagy, S.; Vértes A. *Pure Appl. Chem.* **2003**, *75*, 801-858.
49. Yang, S.; Sun, Y.; Chen, L.; Hernandez, Y.; Feng, X.; Müllen, K. *Sci. Rep.* **2012**, *2*, 427; DOI:10.1038/srep00427.
50. Navale, S. T.; Bandgar, D. K.; Nalge, S. R.; Milik, R. N.; Pawar, S. A.; Chougule, M. A.; Patil, V. B. *J. Mater. Sci.: Mater. Electron* **2013**, *24*, 1422-1430.
51. (a) Levitas, V. I. *Combust. Flame* **2009**, *156*, 543-546. (b) Cao, B.; Starace, A. K.; Judd, O. H.; Jarrold, M. F. *J. Am. Chem. Soc.* **2009**, *131*, 2446-2447.
52. Li, Y.; Hu, Y.; Huang, G.; Li, C. *Particuology* **2013**, *11*, 460-467.
53. Chatterjee, A. *Beyond the Blast Furnace*, CRC Press: Boca Raton, FL, 1994.
54. Streletskii, A. N.; Povstugar, I. V.; Borunova, A. B.; Lomaeva, S. F.; Butyagin, P. Yu. *Colloid J.* **2006**, *68*, 470-480.
55. Pullin, A. D. E.; Pollock, J. McC. *Trans. Faraday Soc.* **1958**, *54*, 11-18.
56. Cox, J. D., Wagman, D. D., Medvedev, V. A. *CODATA Key Values for Thermodynamics*, Hemisphere Publishing Corp., New York, 1989.
57. Guidotti, R. A.; Odinek, J.; Reinhardt, F. W. *J. Energ. Mater.* **2006**, *24*, 271-305.

58. Lagarec, K.; Rancourt, D. G. *Nucl. Instrum. Meth. Phys. Res. B* 1997, 129, 266-280.
59. (a) Beaucage, G. *J. Appl. Cryst.* **1995**, 28, 717-728. (b) Beaucage, G. *J. Appl. Cryst.* **1996**, 29, 134-146.

## FIGURES

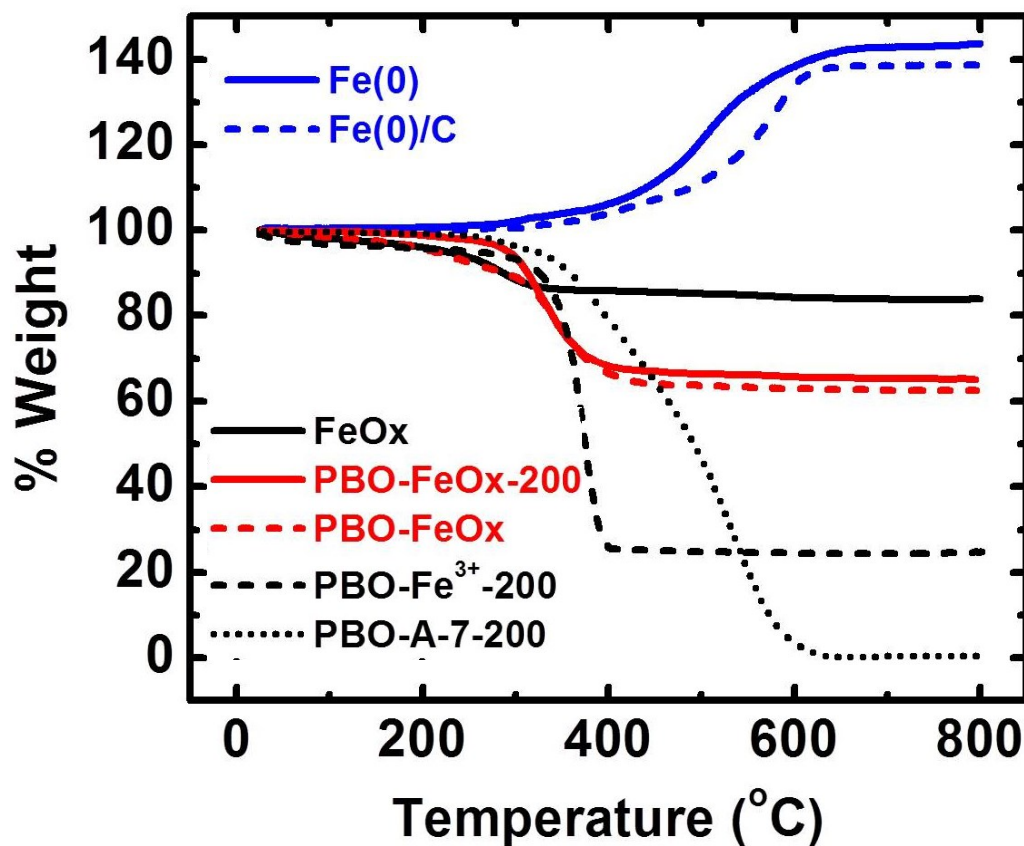


Figure 1 Thermogravimetric analysis of samples as shown in air. (Heating rate: 10 °C min<sup>-1</sup>.) Percent residual weights at 800 °C (% w/w): FeOx: 83.8; PBO-FeOx-200: 65.2; PBO-FeOx: 62.5; PBO-Fe<sup>3+</sup>-200: 24.8; PBO-A-7-200 (previous article): 0.0; Fe(0)/C: 138.6; Fe(0): 143.5.

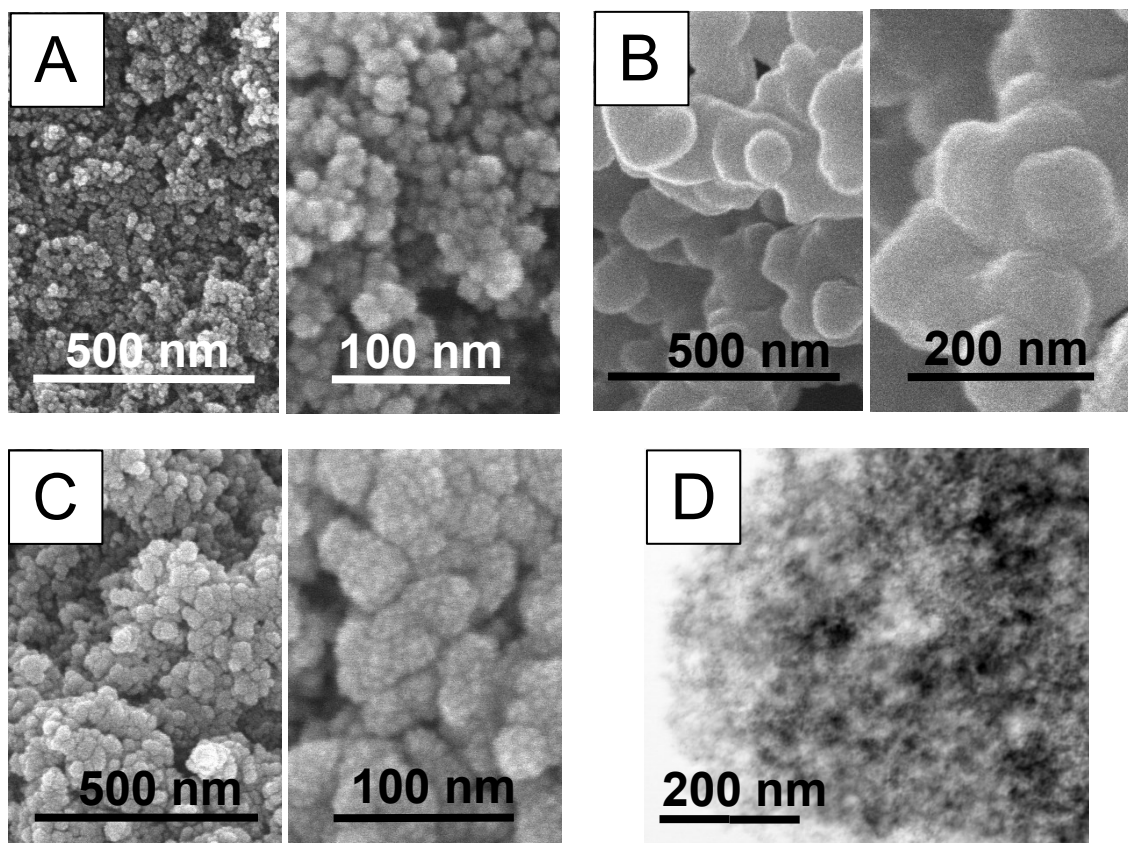


Figure 2 A-C: Scanning electron microscopy (SEM) at two different magnifications of FeOx-200 (A); PBO-Fe<sup>3+</sup>-200 (B); PBO-FeOx-200 (C). Scanning transmission electron microscopy (STEM- bright field) of PBO-FeOx-200.



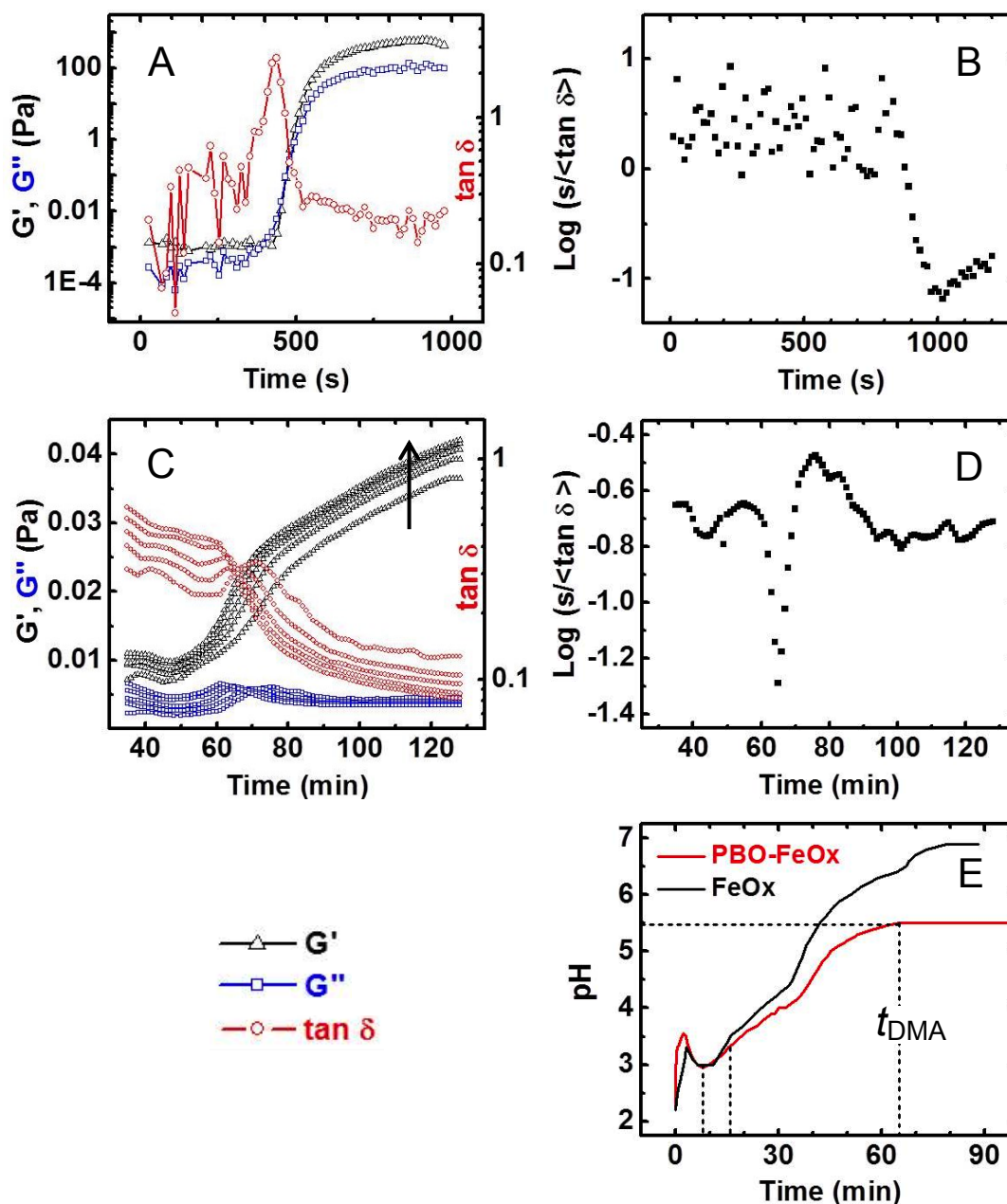


Figure 3 (A) Rheology of a PBO-FeOx sol at 80 °C (multifrequency oscillation mode; for clarity, only one frequency ( $1 \text{ rad s}^{-1}$ ) is shown). (B) Referring to (A), plot of the statistical function as a function of time at all four frequencies employed. (C) DMA at 80 °C (multifrequency oscillation mode) of the same PBO-FeOx sample, right after gelation. Data shown at all frequencies employed (see Experimental). Arrow shows the effect of increasing frequency on the elastic modulus ( $G'$ ). (D) Referring to (C), plot of the statistical function as a function of time at all five frequencies employed. (E) Variation of the pH during gelation (80 °C) of the two sols as shown. The first two dashed vertical lines mark the rheological gelation points ( $t_{g-rheom}$ ) of the two sols; the third one marks  $t_{DMA}$  of the PBO-FeOx gel (see Table 2).

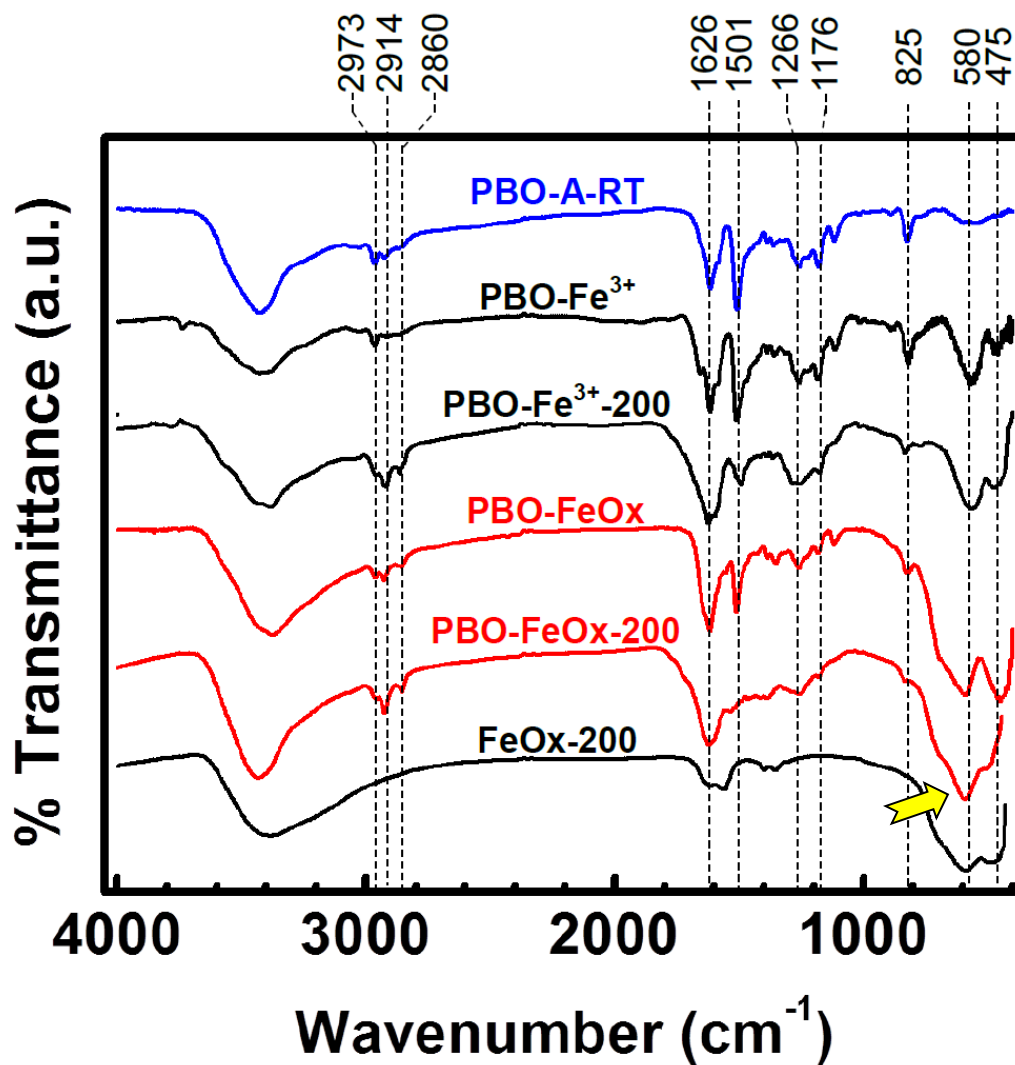


Figure 4 Infrared (FTIR) spectra of PBO-FeOx aerogels and controls as-prepared and after curing at 200 °C in air. The spectrum of an as-prepared HCl-catalyzed PBO aerogel (PBO-A-RT) is included for comparison. Arrow points to the lattice vibration of Fe<sub>3</sub>O<sub>4</sub>.

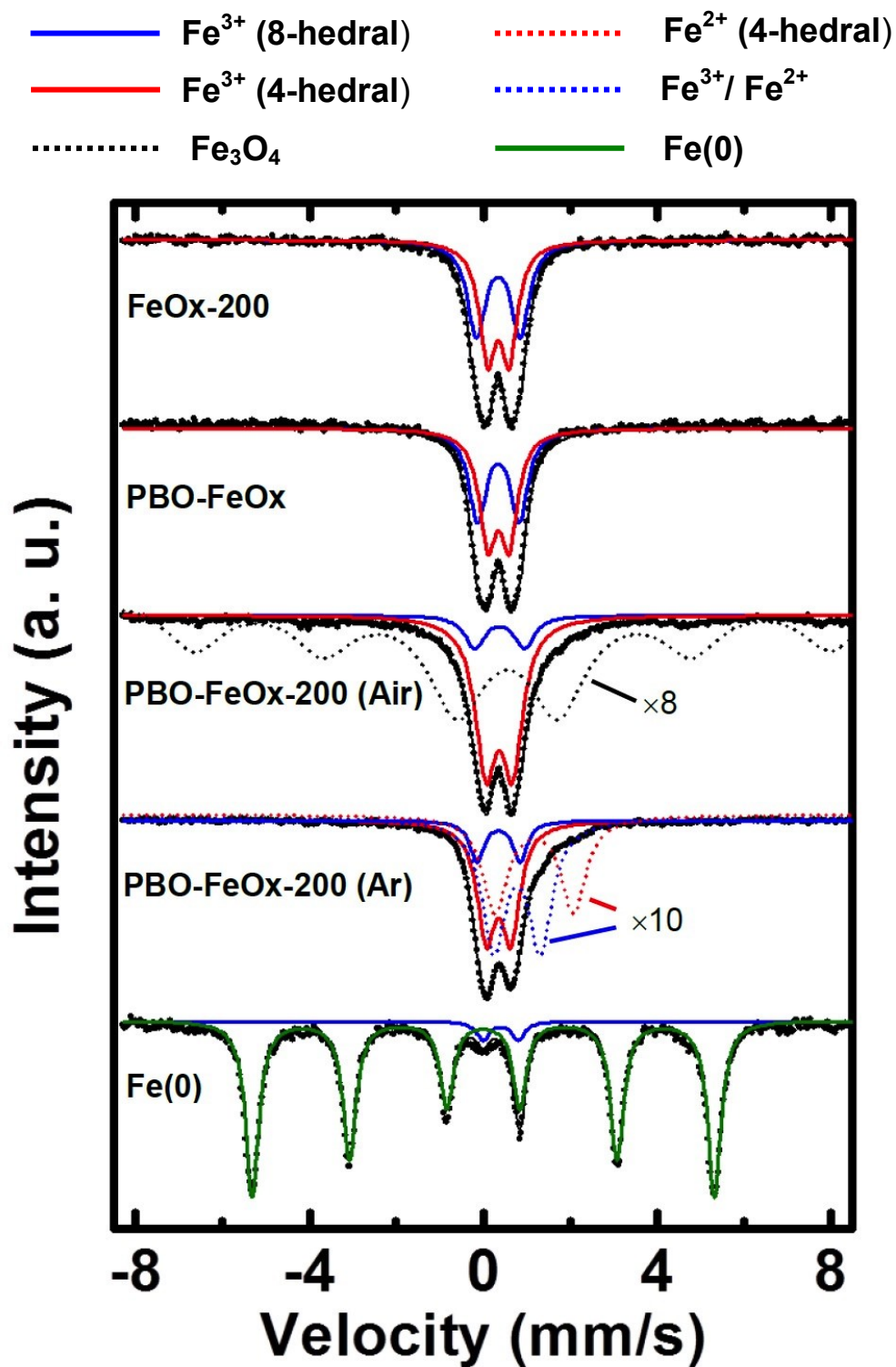


Figure 5 Mössbauer spectra (black solid lines) of the samples as shown. Spectra include the fitting spectra at scale (see Table 4) according to the index shown on top.

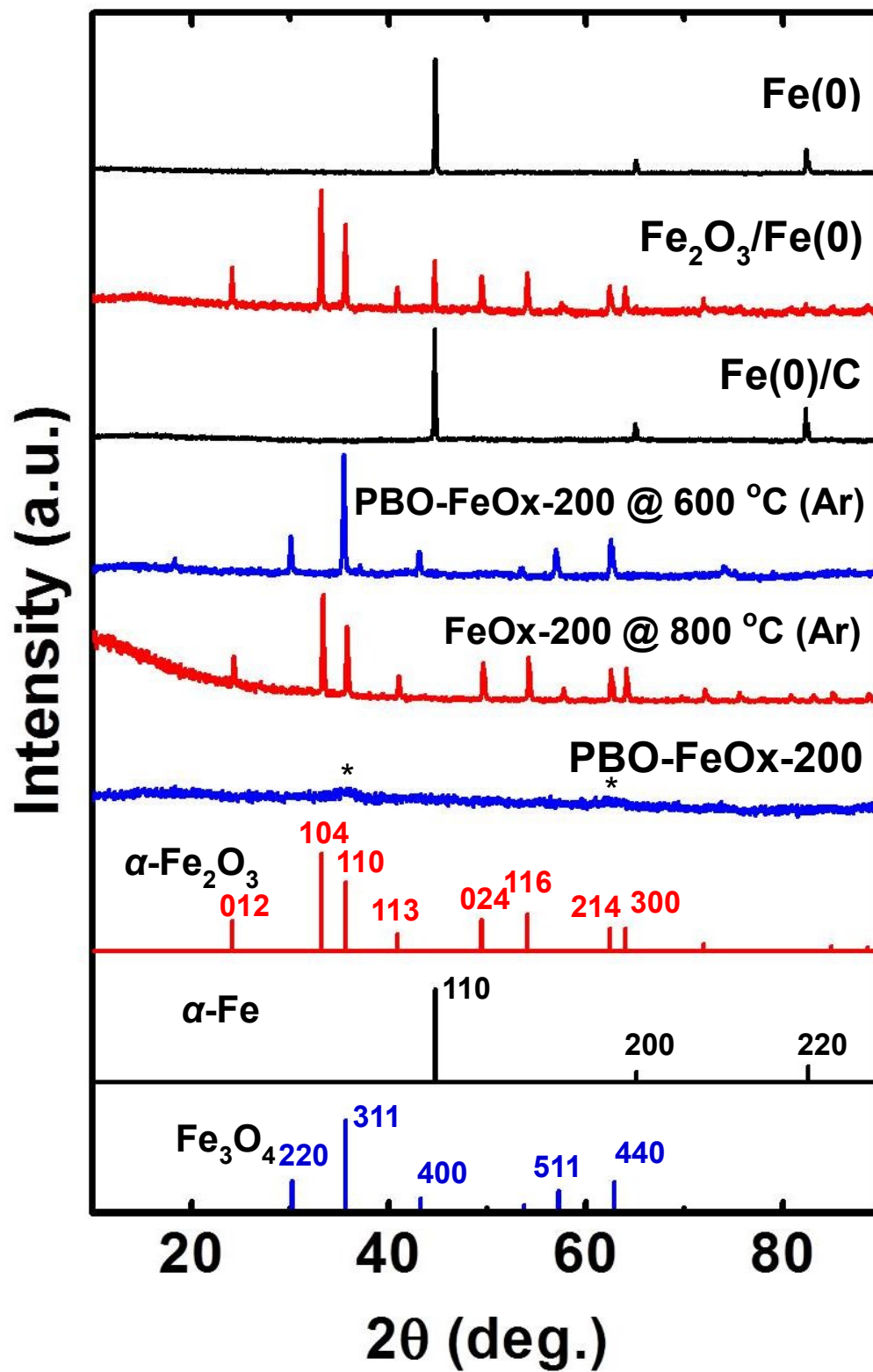


Figure 6 X-ray diffraction (XRD) data for interpenetrating networks and controls along processing as shown. Relevant line spectra are shown at the bottom.

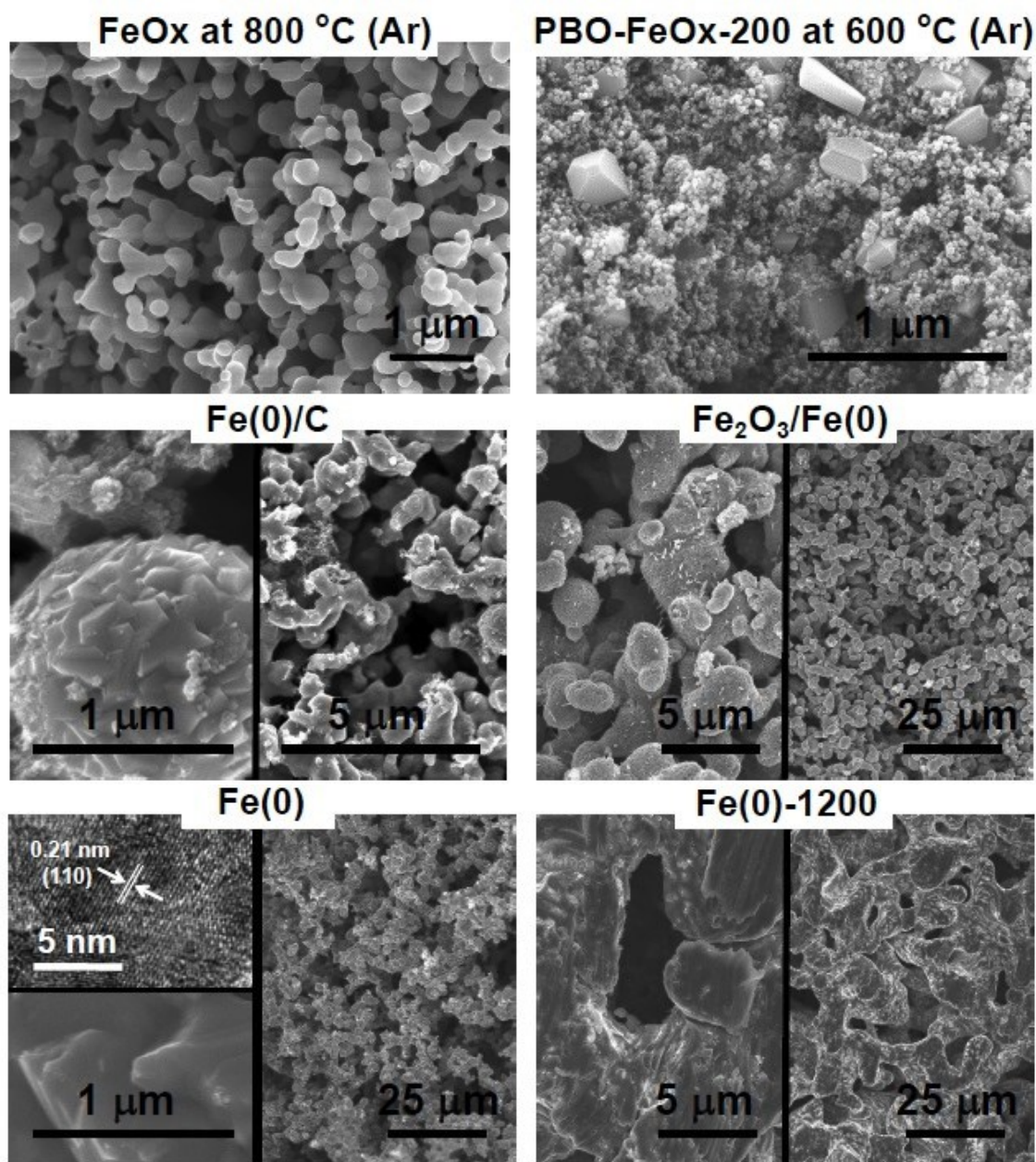


Figure 7 SEM data, some at two different magnifications along processing of samples as shown. A TEM image of Fe(0) is also included.

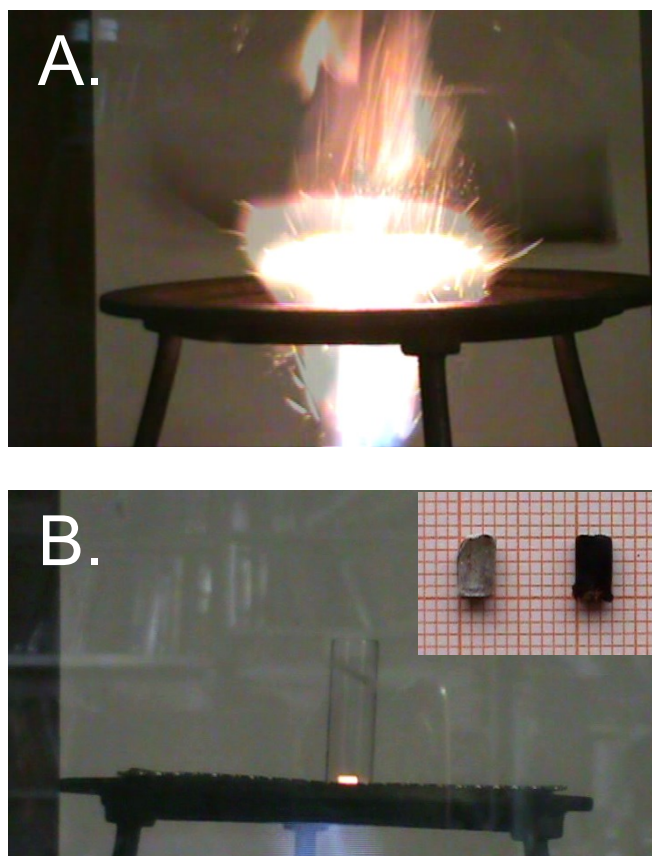


Figure 8 (A) An exploding  $\text{Fe}(0)/\text{LiClO}_4$  sample ( $\text{iron}(0):\text{LiClO}_4=1:0.395$  mol/mol) ignited with a burner (see also Movie S.1 in Supporting Information). (B) A  $\text{Fe}(0)\text{-}1200/\text{LiClO}_4$  sample behaving as a thermite (see Movie S.2). Inset: Photograph on a millimeter paper of a  $\text{Fe}(0)\text{-}1200/\text{LiClO}_4$  sample before ignition (left) and another one after testing (right). As shown, the latter remained monolithic.

**SUPPORTING INFORMATION****Index**

<b>Scheme S.1</b>	Alternative processes and controls
<b>Table S.1</b>	CHN analysis data
<b>Figure S.1</b>	XRD data of samples from control processes
<b>Figure S.2</b>	N <sub>2</sub> -sorption data for all samples
<b>Figure S.3</b>	SAXS data
<b>Movies S.1</b>	Ignition of a low-density <b>Fe(0)</b> sample loaded with LiClO <sub>4</sub> (separate file)
<b>Movies S.2</b>	Ignition of a high-density <b>Fe(0)-1200</b> sample loaded with LiClO <sub>4</sub> (separate file)

Scheme S.1 Alternative processes and controls.

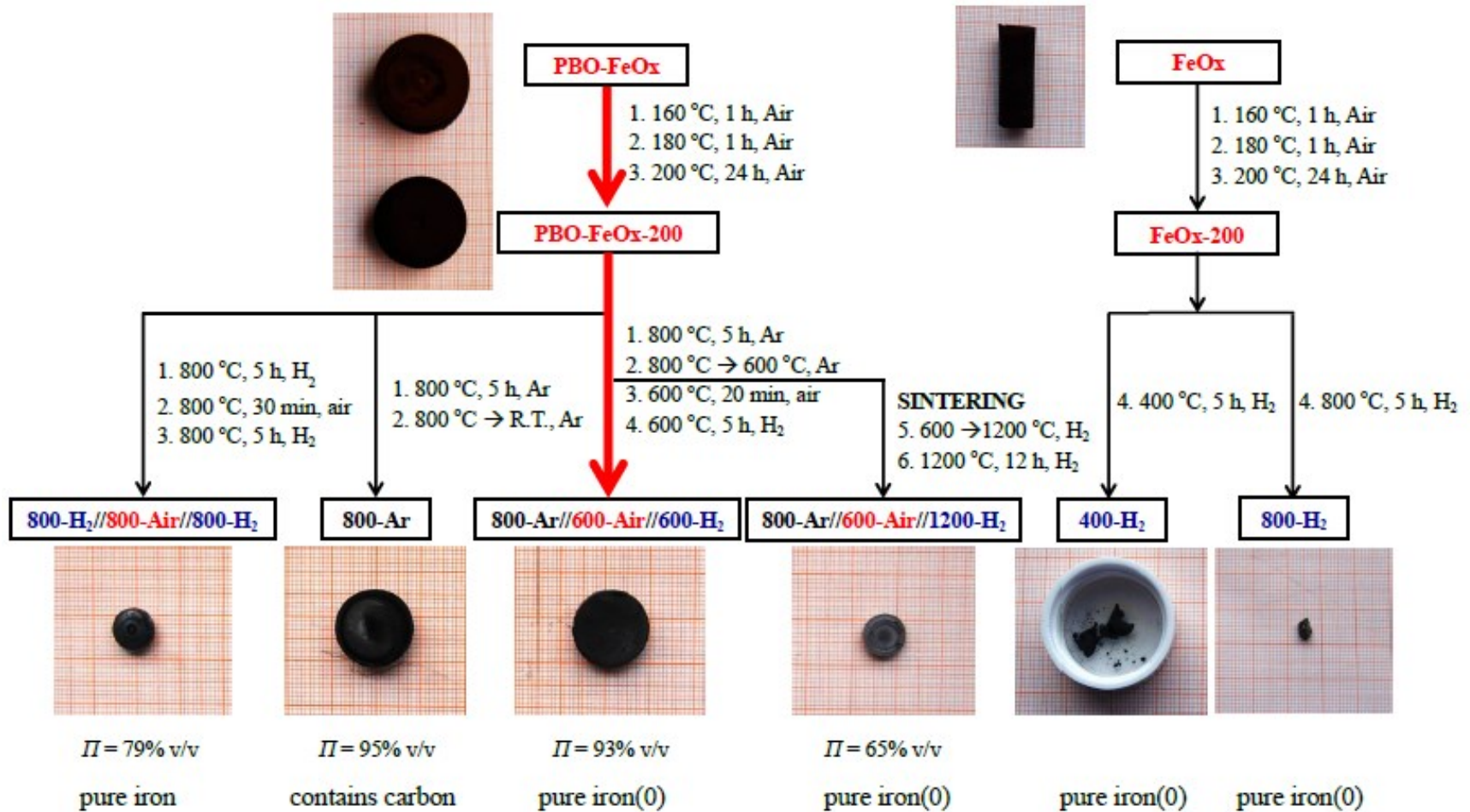




Table S.1 CHN elemental analysis data for all samples.

Sample ID	% C (w/w)	% H (w/w)	% N (w/w)	% O (w/w)
<b>Standard-acetanilide</b>	71.12 ± 0.02	6.85 ± 0.00	10.31 ± 0.04	11.73 ± 0.01
<b>acetanilide (theoretical)</b>	71.09	6.71	10.36	11.84
BO monomer	81.46 ± 0.38	6.44 ± 0.05	5.73 ± 0.05	6.38 ± 0.38
BO monomer (expected)	80.49	6.54	6.06	6.92
<b>FeOx</b>	3.68 ± 0.07	1.43 ± 0.10	0.42 ± 0.03	
<b>FeOx-200</b>	1.25 ± 0.01	0.74 ± 0.04	0.23 ± 0.02	
<b>PBO-Fe<sup>3+</sup></b>	58.16 ± 0.15	4.57 ± 0.17	4.47 ± 0.02	
<b>PBO-Fe<sup>3+</sup>-200</b>	53.61 ± 0.50	2.94 ± 0.18	4.40 ± 0.04	
<b>PBO-FeOx</b>	22.86 ± 0.73	2.44 ± 0.03	1.84 ± 0.08	
<b>PBO-FeOx-200</b>	18.1 ± 0.24	1.51 ± 0.04	1.44 ± 0.07	
<b>PBO-FeOx-200 → 600 °C (Ar)</b>	16.32 ± 0.12	0.20 ± 0.05	1.06 ± 0.09	
<b>PBO-FeOx-200 → 700 °C (Ar)</b>	10.10 ± 0.15	0.12 ± 0.01	0.55 ± 0.02	
<b>PBO-FeOx-200 → 800 °C (Ar)</b> referred to as: <b>Fe(0)/C</b>	5.45 ± 0.85	0.00 ± 0.00	0.20 ± 0.06	
<b>Fe(0)</b>	0.07 ± 0.01	0.00 ± 0.00	0.03 ± 0.02	

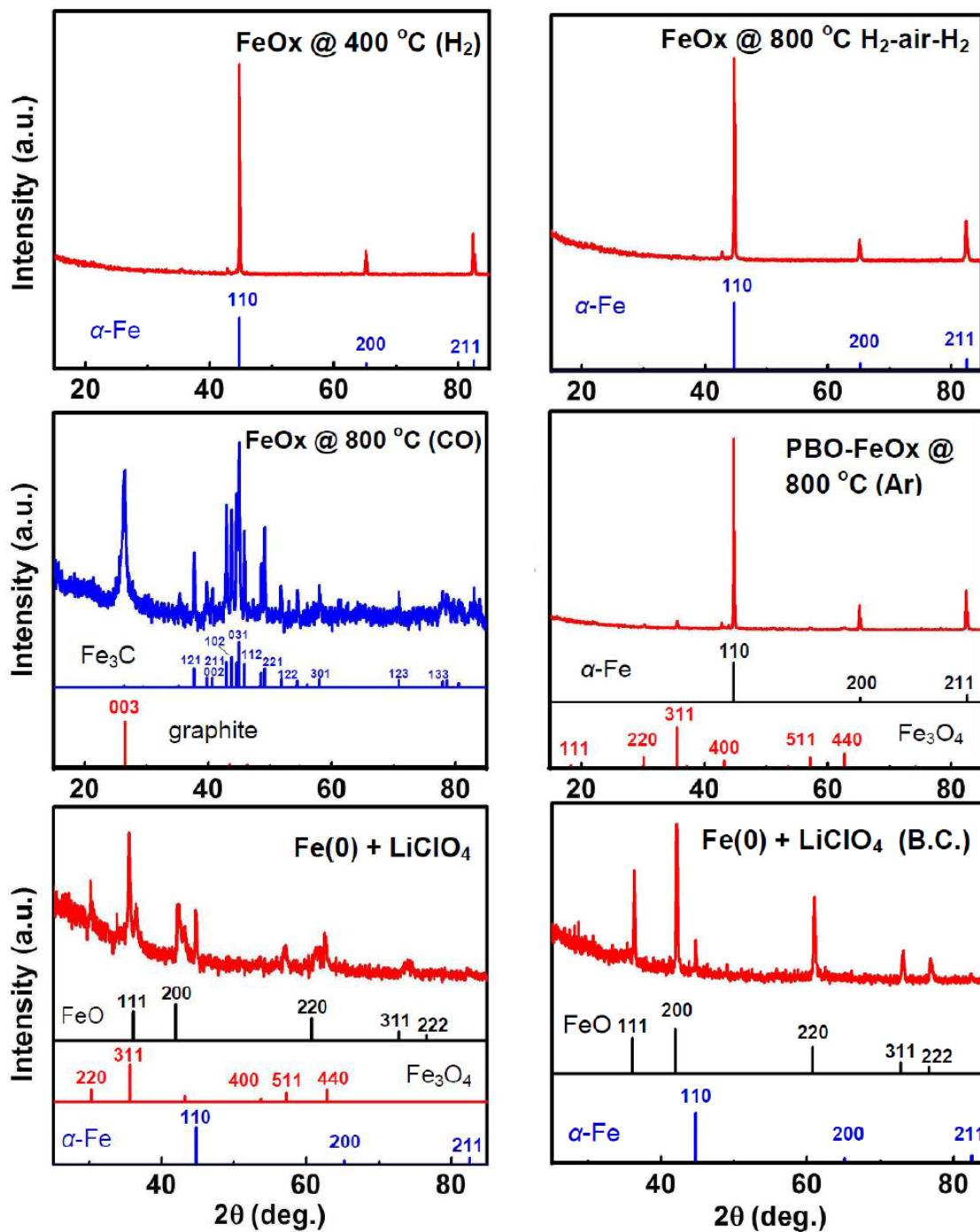
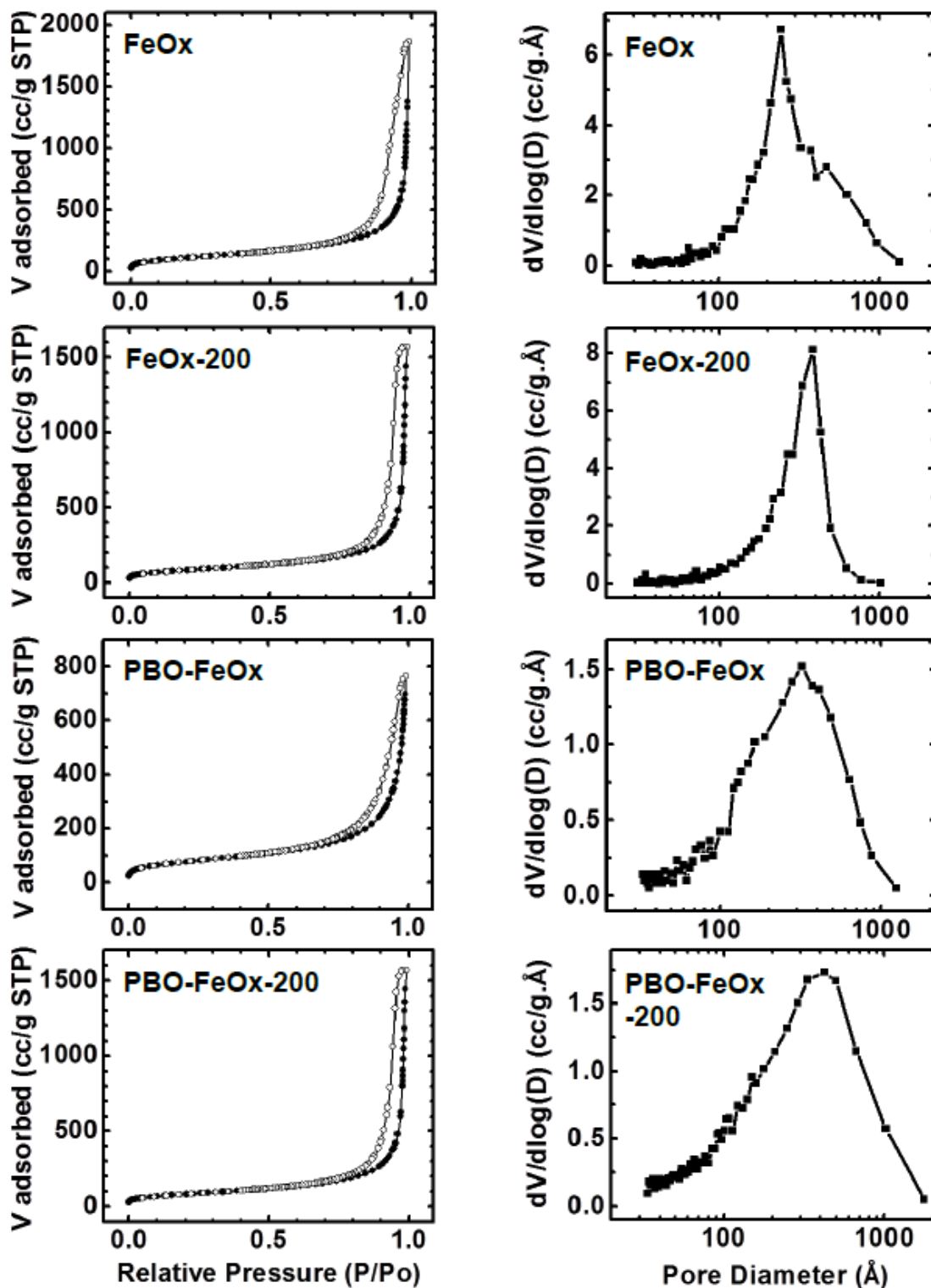


Figure S.1 XRD data of samples from control processes as shown, including the residues from ignition experiments (bottom two spectra). B.C.: ignition in a bomb calorimeter.

Figure S.2  $N_2$ -sorption data for all samples (continued on next page).

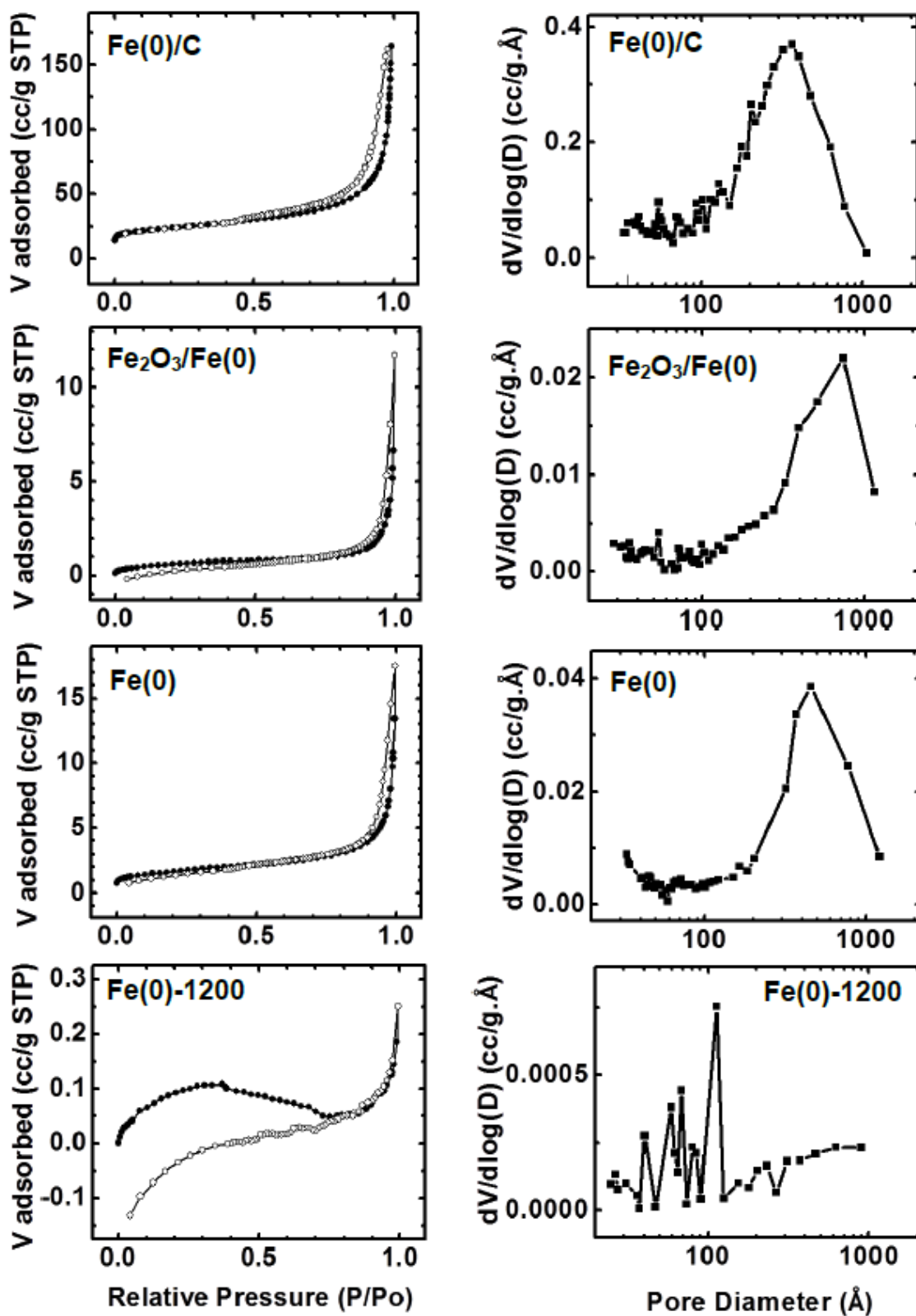


Figure S.2 (Continued from last page) N<sub>2</sub>-sorption data for all samples (continued on next page).

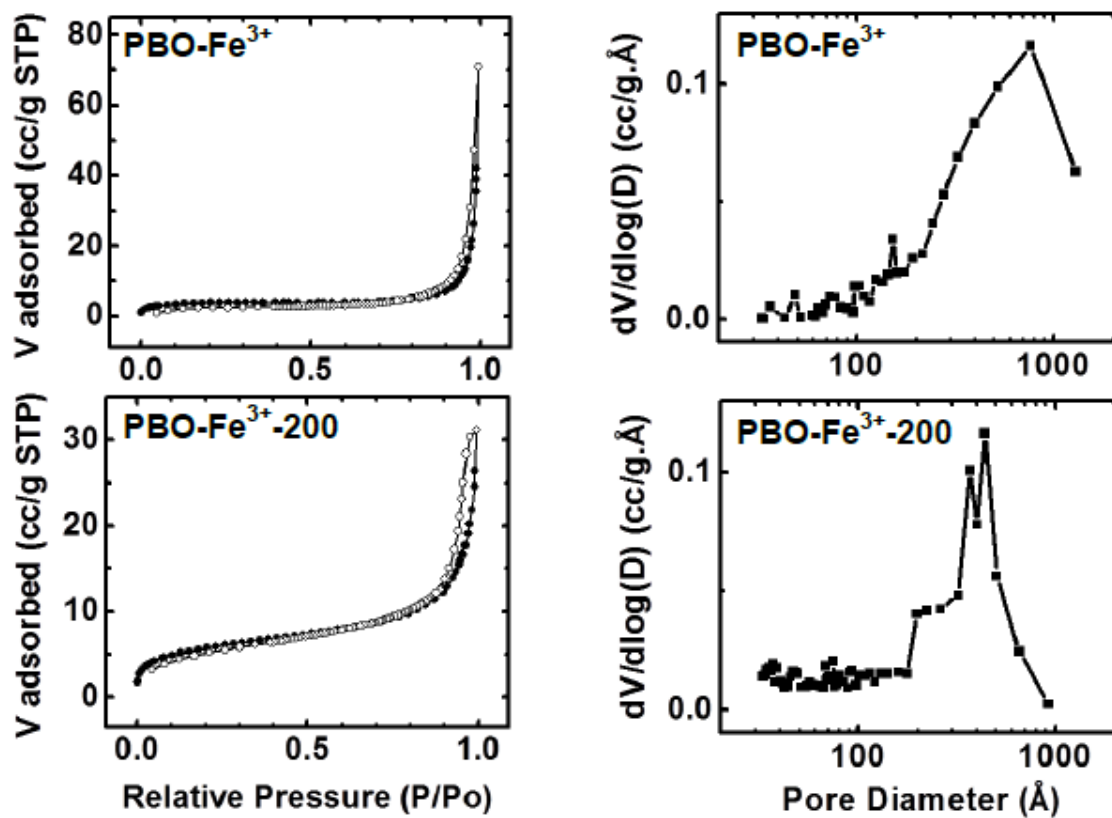
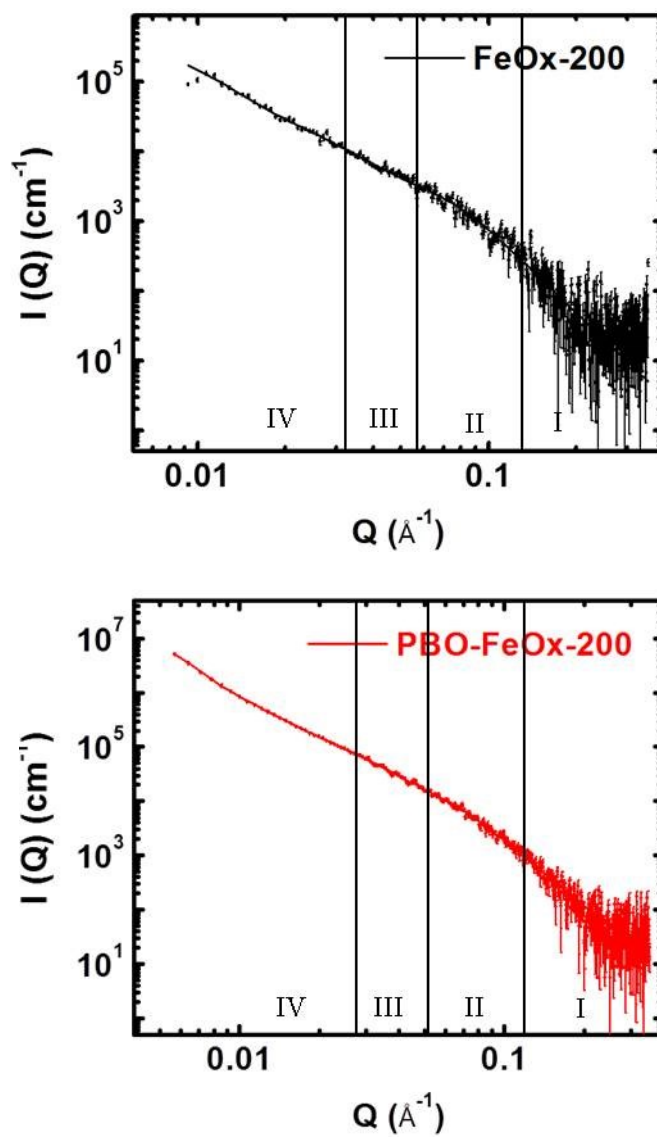


Figure S.2 (Continued from last page)  $N_2$ -sorption data for all samples.



**Figure S.3** Small angle x-ray scattering (SAXS) data. Scattering intensity versus scattering vector  $Q$ . Data fitted using the Beaucage Unified Model (see Experimental in the main article). Vertical lines are guides to the eye for:

Region I: High- $Q$  power law region.

Region II: Guinier knee with radius of gyration  $R_G(1)$ . Radius of primary particles:

$$R(1)=R_G(1)/0.77.$$

Region III: Power law region. Mass fractal dimension of secondary particles,  $D_m=|\text{slope}|$ .

Region IV: Second Guinier knee, yielding the radius of the secondary particles via

$$R(2)=R_G(2)/0.77.$$

## SECTION

### 2. CONCLUSIONS

Mechanically strong and energy-efficient polybenzoxazine (PBO) aerogels were successfully synthesized using acid catalyzed polymerization. Resultant aerogels were found equivalent or slightly better than the conventional heat induced counterparts in terms of surface area and thermal insulation properties. Detailed chemical characterizations confirmed aromatization process upon oxidative curing of aerogels, which in turn was a necessary step to yield nanoparticulate carbon aerogels. Carbon aerogels obtained via conventional as well as new acid catalyzed route possess multiscale porosity ranging from micro to meso to macro, originated from rigid molecular structure imposed via oxidative curing. Robust nature, cost-effective raw materials and enhanced surface area with multiscale porosity in carbon aerogels makes polybenzoxazine as an ideal replacement of RF aerogels in commercial production of porous carbons.

Acid catalyzed gelation was further utilized to develop interpenetrating networks of PBO and iron oxide nanoparticles (PBO-FeOx). PBO network upon heating causes reduction of iron oxide nanoparticles to magnetite ( $\text{Fe}_3\text{O}_4$ ), which undergo smelting (liquid-solid) reaction at low temperature (800 °C) generating monolithic iron(0) aerogels. PBO network act as a sacrificial template for reduction of magnetite and retains the 3D structure of iron(0). Oxidative removal of excess carbon followed by reduction with  $\text{H}_2$  yielded pure iron(0) aerogels. Porosity of the iron framework facilitates production of energetic composite by simple impregnation with oxidizers (e.g.;  $\text{LiClO}_4$ ,  $\text{NaClO}_4$ ). Energetic composite thus obtained demonstrated equivalent performance to commercially utilized thermal batteries in terms of energy release.

**BIBLIOGRAPHY**

1. Cao, G.; Wang, Y. *Nanostructures and Nanomaterials: Synthesis, Properties and Applications* Eds.; World Scientific Publishing Co. Pte. Ltd: Danvers, MA, 2011, 1-15
2. Ashby, M. F.; Ferreira, P.; Schodek, D. L. *Nanomaterials, Nanotechnologies and Design* Eds.; Elsevier Ltd: Burlington, MA, 2009, 317-328.
3. Tillotson, T. M.; Hrubesh, L. W. "Transparent Ultralow-density Silica Aerogels Prepared by a Two-step Sol-gel Process," *J. Non-Cryst. Solids* **1992**, *145*, 44-50.
4. (a) Rolison, D. R.; Dunn, B. "Electrically Conductive Oxide Aerogels: New Materials in Electrochemistry," *J. Mater. Chem.* **2001**, *11*, 963-980. (b) Al-Muhtaseb, S. A.; Ritter, J. A. "Preparation and Properties of Resorcinol-Formaldehyde Organic and Carbon Gels," *Adv. Mater.* **2003**, *15*, 101-114.
5. (a) Kistler, S. S. "Coherent Expanded Aerogels and Jellies," *Nature* **1931**, *127*, 741. (b) Kistler, S. S. "The Relation between Heat Conductivity and Structure in Silica Aerogel," *J. Phys. Chem.* **1934**, *39*, 79-86. (c) Lu, X.; Caps, R.; Fricke, J.; Pekala, R. W. "Correlation between Structure and Thermal Conductivity of Organic Aerogels," *J. Non-Cryst. Solids* **1995**, *188*, 226-234.
6. (a) Kistler, S. S. "Coherent Expanded-Aerogels," *J. Phys. Chem.* **1931**, *36*, 52-64. (b) Kistler, S. S.; Sherlock, S.; Appel, E. G. "Aerogel Catalysts - Thoria: Preparation of Catalyst and Conversions of Organic Acids to Ketones," *Ind. Eng. Chem.* **1934**, *26*, 388-391.
7. Hunt, A.; Ayers, M. History of Silica Aerogels. <http://energy.lbl.gov/ECS/aerogels/> (accessed on 06/01/2013), part of Microstructured Materials Group at Lawrence Berkeley National Laboratory <http://energy.lbl.gov/ECS/aerogels/mmg.html> (accessed on 06/01/2013).
8. Pierre A.; Pajonk, G. "Chemistry of Aerogels and Their Applications," *Chem. Rev.* **2002**, *102*, 4243-4265.
9. Kanamori, K.; Nakanishi, K. "Controlled Pore Formation in Organotrialkoxysilane-derived Hybrids: from Aerogels to Hierarchically Porous Monoliths," *Chem. Soc. Rev.* **2011**, *40*, 754-770.
10. Aerogel Quick Facts <http://stardust.jpl.nasa.gov/images/technology-aerogelhand.jpg> (accessed on 06/02/2013), part of Stardust Program of Jet Propulsion Laboratory, NASA <http://stardust.jpl.nasa.gov/tech/aerogel.html> (accessed on 06/02/2013)
11. Livage, J.; Sanchez, C. "Sol-gel Chemistry," *J. Non-Cryst. Solids* **1992**, *145*, 11-19.



12. (a) Zarzycki, J.; Prassas, M.; Phalippou, J. "Synthesis of Glasses from Gels: The Problem of Monolithic Gels," *J. Mat. Sci.* **1982**, *17*, 3371-3379. (b) Tewari, P. H.; Hunt, A. J.; Lofftus, K. D. "Ambient-temperature Supercritical Drying of Transparent Silica Aerogels," *Mater. Lett.* **1985**, *3*, 363-367
13. (a) Wittwer, V. "Development of Aerogel Windows," *J. Non-Cryst. Solids* **1992**, *145*, 233-236. (b) Gerlach, R.; Kraus, O.; Fricke, J.; Eccardt, P. C.; Kroemer, N.; Magori, V. "Modified SiO<sub>2</sub> Aerogels as Acoustic Impedance Matching Layers in Ultrasonic Devices," *J. Non-Cryst. Solids* **1992**, *145*, 227-232.
14. Jo, M. H.; Park, H. H. "Leakage Current and Dielectric Breakdown Behavior in Annealed SiO<sub>2</sub> Aerogel Films," *Appl. Phys. Lett.* **1998**, *72*, 1391-1393.
15. Pajonk, G. M. "Aerogel Catalysts," *Appl. Catal.* **1991**, *72*, 217-266.
16. Morris, C. A.; Anderson, M. L.; Stroud, R. M.; Merzbacher, C. I.; Rolison, D. R. "Silica Sol as a Nanoglue: Flexible Synthesis of Composite Aerogels," *Science* **1999**, *284*, 622-624.
17. daCunha, J. P.; Neves, P.; Lopes, M. "On the Reconstruction of Cherenkov Rings from Aerogel Radiators," *Nucl. Instrum. Methods Phys. Res., Sect. A* **2000**, *452*, 401-421.
18. Woignier, T.; Phalippou, J. "Scaling Law Variations of The Mechanical Properties of Silica Aerogels," *J. Phys. Colloques* **1989**, *50*, C4-179-184.
19. (a) Katti, A.; Shimpi, N.; Roy, S.; Lu, H.; Fabrizio, E. F.; Dass, A.; Capadona, L. A.; Leventis, N. "Chemical, Physical, and Mechanical Characterization of Isocyanate Cross-linked Amine-Modified Silica Aerogels," *Chem. Mater.* **2006**, *18*, 285-296. (b) Meador, M. A.; Capadona, L. A.; McCorkle, L.; Papadopoulos, D. S.; Leventis, N. "Structure-Property Relationships in Porous 3D Nanostructures as a Function of Preparation Conditions: Isocyanate Cross-Linked Silica Aerogels," *Chem. Mater.* **2007**, *19*, 2247-2260. (c) Ilhan, U. F.; Fabrizio, E. F.; McCorkle, L.; Scheiman, D. A.; Dass, A.; Palczer, A.; Meador, M. A. B.; Johnston, J. C.; Leventis, N. "Hydrophobic Monolithic Aerogels by Nanocasting Polystyrene on Amine-modified Silica," *J. Mater. Chem.* **2006**, *16*, 3046-3054.
20. (a) Leventis, N. *Acc. Chem. Res.* **2007**, *40*, 874-884. (b) Leventis, N.; Mulik, S.; Wang, X.; Dass, A.; Sotiriou-Leventis, C.; Lu, H. "Stresses at the Interface of Micro with Nano," *J. Am. Chem. Soc.* **2007**, *129*, 10660-10661. (c) Leventis, N.; Sotiriou-Leventis, C.; Zhang, G.; Rawashdeh, A.-M. M. "Nano Engineering Strong Silica Aerogels," *NanoLetters* **2002**, *2*, 957-960.
21. Husing, N.; Schubert, U.; Mezer, R.; Fratzl, P.; Riegel, B.; Kiefer, W.; Kohler, D.; Mader, W. "Formation and Structure of Gel Networks from Si(OEt)<sub>4</sub>/(MeO)<sub>3</sub>Si(CH<sub>2</sub>)<sub>3</sub>NR'<sub>2</sub> Mixtures (NR'<sub>2</sub> = NH<sub>2</sub> or NHCH<sub>2</sub>CH<sub>2</sub>NH<sub>2</sub>)" *Chem. Mater.* **1999**, *11*, 451-457.

22. Meador, M. A. B.; Fabrizio, E. F.; Ilhan, F.; Dass, A.; Zhang, G.; Vassilaras, P.; Johnston, J. C.; Leventis, N. "Cross-linking Amine-Modified Silica Aerogels with Epoxies: Mechanically Strong Lightweight Porous Materials," *Chem. Mater.* **2005**, *17*, 1085–1098.
23. (a) Pekala, R. "Organic Aerogels from The Polycondensation of Resorcinol with Formaldehyde," *J. Mater. Sci.* **1989**, *24*, 3221-3227. (b) Mayer, S. T.; Pekala R. W.; Kaschmitter, J. L. "The Aerocapacitor: An Electrochemical Double-Layer Energy-Storage Device," *J. Electrochem. Soc.*, **1993**, *140*, 446–451.
24. (a) Ruben, G. C.; Pekala, R. W. "High-resolution Transmission Electron Microscopy of The Nanostructure of Melamine-formaldehyde Aerogels," *J. Non-Cryst. Solids* **1995**, *186*, 219-231. (b) Li, W.; Guo, S. "Preparation of Low-density Carbon Aerogels from a Cresol/formaldehyde mixture," *Carbon* **2000**, *38*, 1520-1523. (c) Pekala, R. W.; Alviso, C. T.; Lu, X.; Gross, J.; Fricke, J. "New Organic Aerogels Based Upon a Phenolic-furfural Reaction," *J. Non-Cryst. Solids* **1995**, *188*, 34-40.
25. Al-Muhtaseb, S.; Ritter, J. "Preparation and Properties of Resorcinol–Formaldehyde Organic and Carbon Gels," *Adv. Mater* **2003**, *15*, 101-114.
26. (a) Durairaj, R. *Resorcinol: Chemistry, Technology and Applications* Eds.; Springer: Germany, 2005, 186-187. (b) Mulik, S.; Sotiriou-Leventis, C.; Leventis, N. "Time-Efficient Acid-Catalyzed Synthesis of Resorcinol–Formaldehyde Aerogels," *Chem. Mater.* **2007**, *19*, 6138-6144
27. Mulik, S.; Sotiriou-Leventis, C. Resorcinol-Formaldehyde Aerogels. In *Aerogels Handbook*; Agerter, M. A., Leventis, N., Koebel, M. M., Eds.; Springer: New York, 2011, pp 3-18.
28. (a) Barbieri O.; Ehrburger-olle F.; Rieker T.; Pajonk, G.; Pinto, N.; Venkateswara Rao, A. "Small-angle X-ray Scattering of a New Series of Organic Aerogels," *J. Non-Cryst. Solids* **2001**, *285*, 109-115. (b) Brandt, R.; Fricke, J. *J Non-Cryst. Solids* **2004**, *350*, 131-135. Fairen-Jimenez, D.; Carrasco-Martin, F.; Moreno-Castilla, C. Porosity and Surface Area of Monolithic Carbon Aerogels Prepared Using Alkaline Carbonates and Organic Acids as Polymerization Catalysts," *Carbon* **2006**, *44*, 2301-2307. (c) Berthon, S.; Barbieri, O.; Ehrburger-Dolle, F.; Geissler, E.; Achard, P.; Bley, F.; Hecht, A. –M.; Livet, F.; Pajonk, G.; Pinto, N.; Riggaci, A.; Rochas, C. "DLS and SAXS Investigations of Organic Gels and Aerogels," *J. Non-Cryst. Solids* **2001**, *285*, 154-161. (d) Brandt, R.; Petricevic, R.; Proebstle, H.; Fricke, J. "Acetic Acid Catalyzed Carbon Aerogels," *J Porous Mater.* **2003**, *10*, 171-178. (e) Reuß, M.; Ratke, L. "Subcritically Dried RF-aerogels Catalysed by Hydrochloric Acid," *J Sol-Gel Sci. Technol.* **2008**, *47*, 74-80.

29. Peikolainen, A. -L.; Volobujeva, O.; Aav, R.; Uibu, M.; Koel, M. "Organic Acid Catalyzed Synthesis of 5-methylresorcinol Based Organic Aerogels in Acetonitrile," *J Porous Mater.* **2012**, *19*, 189-194.
30. (a) Horikawa, T.; Hayashi, J.; Muroyama, K. "Controllability of Pore Characteristics of Resorcinol-Formaldehyde Carbon Aerogel," *Carbon* **2004**, *42*, 1625-1633. (b) Horikawa, T.; Hayashi, J.; Muroyama, K. "Size Control and Characterization of Spherical Carbon Aerogel Particles from Resorcinol-Formaldehyde Resin," *Carbon* **2004**, *42*, 169-175.
31. Mirzaeian M.; Hall, P. The Control of Porosity at Nanoscale in Resorcinol Formaldehyde Carbon Aerogels," *J. Mater. Sci.* **2009**, *44*, 2705-2713.
32. (a) Gebert M.; Pekala, R. "Fluorescence and Light-Scattering Studies of Sol-Gel Reactions," *Chem. Mater.* **1994**, *6*, 220-226. (b) Tamon, H.; Ishizaka, H.; Mikami, M.; Okazaki, M. "Porous Structure of Organic and Carbon Aerogels Synthesized by Sol-Gel Polycondensation of Resorcinol with Formaldehyde," *Carbon* **1997**, *35*, 791-796.
33. Holly, F. W.; Cope, A.C. "Condensation Products of Aldehydes and Ketones with o-Aminobenzyl Alcohol and o-Hydroxybenzylamine," *J. Am. Chem. Soc.* **1944**, *66*, 1875-1879.
34. Burke, W. J.; Glennie, E. L. M.; Weatherbee, C. "Condensation of Halophenols with Formaldehyde and Primary Amines," *J. Org. Chem.* **1964**, *29*, 909-912.
35. (a) Schreiber, H. German Offen, 2,323,936, 1973. (b) Higginbottom, H. P. Polymerizable Compositions Comprising Polyamines and Poly(dihydrobenzoxazines) U.S. Pat. 4,501,864 (1985).
36. Ning, X.; Ishida, H. "Phenolic Materials via Ring-Opening Polymerization: Synthesis and Characterization of Bisphenol-A based Benzoxazines and Their Polymers," *J. Polym. Sci. Part A Polym. Chem.* **1994**, *32*, 1121-1129.
37. Dunkers, J. P. Vibrational, Crystallographic, and Mechanistic Studies of Benzoxazine Monomers and Their Resulting Polybenzoxazine as Novel Resins. Ph.D. dissertation Case Western Reserve University, Cleveland, OH, January 1994.
38. Wang, Y. X.; Ishida, H. "Cationic Ring-Opening Polymerization of Benzoxazines," *Polymer* **1999**, *40*, 4563-4570.
39. Reiss, G.; Schwob, J. M.; Guth, G.; Roche, M.; Lande, B. *Advances in Polymer Synthesis*; Culbertson, B. M., McGrath, J. E., Eds., Plenum: New York, 1986.

40. Ishida H. Process for Preparation of Benzoxazine Compounds in Solventless Systems US patent 5,543,516 August 6, 1996
41. (a) Ishida, H.; Rodriguez, Y. "Catalyzing the Curing Reaction of a New Benzoxazine-based Phenolic Resin," *J. Appl. Polym. Sci.* **1995**, *58*, 1751-1760. (b) Dunkers, J.; Ishida, H. "Reaction of Benzoxazine-based Phenolic Resins with Strong and Weak Carboxylic Acids and Phenols as Catalysts," *J. Polym. Sci., Polym. Chem. Ed.* **1999**, *37*, 1913-1921.
42. (a) Wang, Y. -X.; Ishida, H. "Synthesis and Properties of New Thermoplastic Polymers from Substituted 3,4-Dihydro-2H-1,3-benzoxazines," *Macromolecules*, **2000**, *33*, 2839-2847. (b) Liu, C.; Shen, D.; Sebastián, R. M.; Marquet, J.; Schönfeld, R. "Mechanistic Studies on Ring-Opening Polymerization of Benzoxazines: A Mechanistically Based Catalyst Design," *Macromolecules* **2011**, *44*, 4616-4622. (c) Liu, C.; Shen, D.; Sebastián, R. M.; Marquet, J.; Schönfeld, R. "Catalyst Effects on the Ring-Opening Polymerization of 1,3-benzoxazine and On The Polymer Structure," *Polymer* **2013**, *54*, 2873-2878. (d) Sudo, A.; Kudoh, R.; Nakayama, H.; Arima, K.; Endo, T. "Selective Formation of Poly(N,O-acetal) by Polymerization of 1,3-Benzoxazine and Its Main Chain Rearrangement," *Macromolecules* **2008**, *41*, 9030-9034.
43. (a) Santhosh Kumar, K.S.; Raghunadhan Nair, C. P.; Ninan, K. N. "Silica Fiber-Polybenzoxazine-Syntactic Foams; Processing and Properties," *J. Appl. Polym. Sci.* **2008**, *107*, 1091-1099. (b) Santhosh Kumar, K.S.; Raghunadhan Nair, C. P.; Ninan, K. N. "Mechanical Properties of Polybenzoxazine Syntactic Foams," *J. Appl. Polym. Sci.* **2008**, *108*, 1021-1028. (c) Lorjai, P.; Wongkasemjit, S.; Chaisuwan, T. "Preparation of Polybenzoxazine Foam and Its Transformation to Carbon Foam," *Mater. Sci. Eng. A.* **2009**, *527*, 77-84. (d) Su, Y. -C.; Chen, W. -C.; Ou, K. -L.; Chang, F. -C. "Study of The Morphologies and Dielectric Constants of Nanoporous Materials Derived from Benzoxazine-Terminated Poly( $\epsilon$ -caprolactone)/Polybenzoxazine Co-polymers," *Polymer* **2005**, *46*, 3758-3766. (e) Hu, D.; Zheng, S. "Reaction-Induced Microphase Separation in Polybenzoxazine Thermosets Containing Poly(*N*-vinyl pyrrolidone)-block-Polystyrene Diblock Copolymer," *Polymer* **2010**, *51*, 6346- 6354. (f) Chu, W. -C.; Li, J. -G.; Kuo, S. -W. "From Flexible to Mesoporous Polybenzoxazine Resins Templated by Poly(ethylene oxide-*b*- $\epsilon$ -caprolactone) Copolymer Through Reaction Induced Microphase Separation Mechanism," *RSC Advances* **2013**, *3*, 6485-6498. (g) Job, N., Marie, J.; Lambert, S.; Berthon-Fabry, S.; Achard, P. "Carbon Xerogels as Catalyst Supports for PEM Fuel Cell Cathode," *Energy Convers. Manage.* **2008**, *49*, 2461-2470. (h) Lorjai, P.; Chaisuwan, T.; Wongkasemjit, S. "Porous Structure of Polybenzoxazine-Based Organic Aerogel Prepared by Sol-Gel Process and Their Carbon Aerogels," *J. Sol-Gel Sci. Technol.* **2009**, *52*, 56-64.

44. Ishida, H. Overview and Historical Background of Polybenzoxazine Research. In *Handbook of Benzoxazine Resins*; Ishida, H.; Agag, T.; Eds.; Elsevier: Oxford, 2011, pp 3- 69.
45. Lorjai, P.; Wongkasemjit, S.; Chaisuwan, T.; Jamieson, A. M. "Significant Enhancement of Thermal Stability in The Non-oxidative Thermal Degradation of Bisphenol-A/Aniline Based Polybenzoxazine Aerogel," *Polym. Degrad. Stab.* **2011**, *96*, 708-718.
46. Rubenstein, D. A.; Lu, H.; Mahadik, S. S.; Leventis, N.; Yin, W. "Characterization of the Physical Properties and Biocompatibility of Polybenzoxazine-Based Aerogels for Use as a Novel Hard-Tissue Scaffold," *J. Biomat. Sci.-Polym.Ed.* **2012**, *23*, 1171-1184.
47. Lee, J.; Kim, J.; Hyeon, T. "Recent Progress in the Synthesis of Porous Carbon Materials," *Adv. Mater.* **2006**, *18*, 2073-2094.
48. (a) Liang, C.; Li, Z.; Dai, S. "Mesoporous Carbon Materials: Synthesis and Modification," *Angew. Chem., Int. Ed.* **2008**, *47*, 3696-3717. (b) White, R. J.; Budarin, V.; Luque, R.; Clark, J. H.; Macquarriea, D. J. "Tuneable Porous Carbonaceous Materials from Renewable Resources," *Chem. Soc. Rev.* **2009**, *38*, 3401-3418. (c) Hanai, T. "Separation of Polar Compounds Using Carbon Columns," *J. Chromatogr. A* **2003**, *989*, 183-196.
49. Kabbour, H.; Baumann, T. F.; Satcher, J. H.; Saulnier, A.; Ahn, C. C. "Toward New Candidates for Hydrogen Storage: High-Surface-Area Carbon Aerogels," *Chem. Mater.* **2006**, *18*, 6085-6087.
50. Marques, L. M.; Carrott, P. J. M.; Ribeiro Carrott, M. M. L. "Amine-modified Carbon Aerogels for CO<sub>2</sub> Capture," *Adsorpt. Sci. Technol.* **2013** *31*, 223-232.
51. (a) Antolini, E. "Carbon Supports for Low-Temperature Fuel Cell Catalysts," *Appl. Catal. B* **2009**, *88*, 1-24. (b) Stüber, F.; Font, J.; Fortuny, A.; Bengoa, C.; Eftaxias, A.; Fabregat, A. "Carbon Materials and Catalytic Wet Air Oxidation of Organic Pollutants in Wastewater," *Top. Catal.* **2005**, *33*, 3-50
52. (a) Katanyoota, P.; Chaisuwan, T.; Wongchaisuwat, A.; Wongkasemjit, S. "Novel Polybenzoxazine-based Carbon Aerogel Electrode for Supercapacitors," *Mater. Sci., Eng. B.* **2010**, *167*, 36-42. (b) Xing, W.; Bai, P.; Li, Z. F.; Yu, R. J.; Yan, Z. F.; Lu, G. Q.; Lu, L. M. "Synthesis of Ordered Nanoporous Carbon and Its Application in Li-ion Battery," *Electrochim. Acta* **2006**, *51*, 4626- 4633.
53. Knox, J. H.; Kaur, B.; Millward, G. R. "Structure and Performance of Porous Graphitic Carbon in Liquid Chromatography," *J. Chromatogr.* **1986**, *352*, 3-25.

54. (a) Beck, J. S.; Vartuli, J. C.; Roth, W. J.; Leonowisc, M. E.; Kresge, C. T.; Schmitt, K. D.; Chu, C. T.-W.; Olson, D. H.; Sheppard, E. W.; McCullen, S. B.; Higgins, J. B.; Schlenker, J. L. "A New Family of Mesoporous Molecular Sieves Prepared with Liquid Crystal Templates," *J. Am. Chem. Soc.* **1992**, *114*, 10834-10843. (b) Yang, Z.; Xia, Y.; Sun, X.; Mokaya, R. "Preparation and Hydrogen Storage Properties of Zeolite-Templated Carbon Materials Nanocast Via Chemical Vapor Deposition: Effect of The Zeolite Template and Nitrogen Doping," *J. Phys. Chem. B* **2006**, *110*, 18424-18431. (c) Liu, B.; Shioyama, H.; Akita, T.; Xu, Q. "Metal-Organic Framework as a Template for Porous Carbon Synthesis," *J. Am. Chem. Soc.* **2008**, *130*, 5390-5391.
55. Rolison, D. "Catalytic Nanoarchitectures-the Importance of Nothing and the Unimportance of Periodicity," *Science* **2003**, *299*, 1698-1701.
56. Merzbacher, C.; Meier, S.; Piercer J.; Korwin, M. "Carbon Aerogels as Broadband Non-Reflective Materials," *J. Non-Cryst. Solids* **2001**, *285*, 210-215.
57. Li, W.; Guo, S. "Preparation of Low-density Carbon Aerogels from a Cresol/Formaldehyde Mixture," *Carbon* **2000**, *38*, 1520-1523.
58. Zhang, R.; Lu, Y.; Zhan, L.; Liang, X.; Wu, G.; Ling, L. "Monolithic Carbon Aerogels from Sol-Gel Polymerization of Phenolic Resoles and Methylolated Melamine," *Carbon* **2003**, *41*, 1660-1663.
59. (a) Wu, D.; Fu, R.; Yu, Z. "Organic and Carbon Aerogels from the NaOH-Catalyzed Polycondensation of Resorcinol-Furfural and Supercritical Drying in Ethanol," *J. Appl. Polym. Sci.* **2005**, *96*, 1429-1435. (b) Wu, D.; Fu, R.; Zhang, S.; Dresselhaus, M.; Dresselhaus, G. "The Preparation of Carbon Aerogels Based Upon the Gelation of Resorcinol-Furfural in Isopropanol with Organic Base Catalyst," *J. Non-Cryst. Solids* **2004**, *336*, 26-31. (c) Fu, R.; Zheng, B.; Liu, J.; Dresselhaus, M. S.; Dresselhaus, G.; Satcher, Jr.; Baumann, T. "The Fabrication and Characterization of Carbon Aerogels by Gelation and Supercritical Drying in Isopropanol," *Adv. Funct. Mater.* **2003**, *13*, 558-562.
60. Wu, d.; Fu, R. "Synthesis of Organic and Carbon Aerogels from Phenol-Furfural by Two-Step Polymerization," *Microporous Mesoporous Mater.* **2006**, *96*, 115-120
61. (a) Grishchko, L. I.; Amaral-Labat, G.; Szczurek, A.; Fierro, V.; Kuznetsov, B. N.; Celzard, A. "Lignin-Phenol-Formaldehyde Aerogels and Cryogels," *Microporous Mesoporous Mater.* **2013**, *168*, 19-29. (b) Szczurek, A.; Amaral-Labat, G.; Fierro, V.; Pizzi, A.; Masson, E.; Celzard, A. "The Use of Tannin to Prepare Carbon Gels. Part I: Carbon aerogels," *Carbon*, **2011**, *49*, 2773-2784.

62. Biesmans, G.; Mertens, A.; Duffours, L.; Woignier, T.; Phalippou, J. "Polyurethane Based Organic Aerogels and Their Transformation into Carbon Aerogels," *J. Non-Cryst. Solids* **1998**, *225*, 64-68.
63. Leventis, N.; Sotiriou-Leventis, C.; Chandrasekaran, N.; Mulik, S.; Larimore, Z. J.; Lu, H.; Churu, G.; Mang, J. T. "Multifunctional Polyurea Aerogels from Isocyanates and Water. A Structure-Property Case Study," *Chem. Mater.* **2010**, *22*, 6692–6710
64. (a) Talbi, H.; Just, P. -E.; Dao, L. H. "Electropolymerization of Aniline on Carbonized Polyacrylonitrile Aerogel Electrodes: Applications for Supercapacitors," *J. Appl. Electrochem.* **2003**, *33*, 465-473. (b) Sadekar, A. G.; Mahadik, S. S.; Bang, A. N.; Larimore, Z. J.; Wisner, C. W.; Bertino, M. F.; Kaan Kalkan, A.; Mang, J. T.; Sotiriou-Leventis, C.; Leventis, N. "From 'Green' Aerogels to Porous Graphite by Emulsion Gelation of Acrylonitrile," *Chem. Mater.* **2012**, *24*, 26-47. (c) Feng, J.; Zhang, C.; Feng, J. "Carbon Fiber Reinforced Carbon Aerogel Composites for Thermal Insulation Prepared by Soft Reinforcement," *Mater. Lett.* **2012**, *67*, 266-268.
65. (a) Rhine, W.; Wang, J.; Begag, R. Polyimide aerogels, carbon aerogels, and metal carbide aerogels and methods of making same, U.S. Patent No. 7,074,880 (2006). (b) Chidambareswarapattar, C.; Larimore, Z.; Sotiriou-Leventis, C.; Mang, J. T.; Leventis, N. "One-Step Room-Temperature Synthesis of Fibrous Polyimide Aerogels from Anhydrides and Isocyanates and Conversion to Isomorphic Carbons," *J. Mater. Chem.* **2010**, *20*, 9666–9678.
66. (a) Wang, S.; Li, W. -C.; Hao, G. -P.; Hao, Y.; Sun, Q.; Zhang, Q. -Z.; Lu, A. -H. "Temperature-Programmed Precise Control over the Sizes of Carbon Nanospheres Based on Benzoxazine Chemistry," *J. Am. Chem. Soc.* **2011**, *133*, 15304–15307. (b) Hao, G. -P.; Li, W. -C.; Qian, D.; Wang, G. -H.; Zhang, W.; -P.; Zhang, T.; Wang, A. -Q.; Schüth, F.; Bongard, H.; -J.; Lu, A. -H. "Structurally Designed Synthesis of Mechanically Stable Poly(benzoxazine-co-resol)-Based Porous Carbon Monoliths and Their Application as High-Performance CO<sub>2</sub> Capture Sorbents," *J. Am. Chem. Soc.* **2011**, *133*, 11378–11388.
67. (a) Kulinowski, K. M.; Jiang, P.; Vaswani, H.; Colvin, V. "Porous Metals from Colloidal Templates," *Adv. Mater.* **2000**, *12*, 833-838. (b) Velev, O. D.; Kaler, E. W. "Structured Porous Materials via Colloidal Crystal Templating: From Inorganic Oxides to Metals," *Adv. Mater.* **2000**, *12*, 531-534.
68. Schimpf, S.; Lucas, M.; Mohr, C.; Rodemerck, U.; Bruckner, A.; Radnik, J.; Hofmeister, H.; Claus, P. "Supported Gold Nanoparticles: In-depth Catalyst Characterization and Application in Hydrogenation and Oxidation Reactions," *Catal. Today* **2002**, *72*, 63–78.

69. (a) Yeh, F. -H.; Tai, C. -C. Huang, J. -F.; Sun, I. -W. "Formation of Porous Silver by Electrochemical Alloying/Dealloying in a Water-Insensitive Zinc Chloride-1-ethyl-3-methyl Imidazolium Chloride Ionic Liquid," *J. Phys. Chem. B* **2006**, *110*, 5215-5222. (b) Biener, J.; Hodge, A. M.; Hamza, A. M.; Hsiung, L. M.; Satcher, J. H. Jr. "Nanoporous Au: A High Yield Strength Material," *J. Appl. Phys.* **2005**, *97*, 024301.
70. Walsh, D.; Arcelli, L.; Ikoma, T.; Tanaka, J.; Mann, S. "Dextran Templating for the Synthesis of Metallic and Metal Oxide Sponges," *Nat Mater.* **2003**, *2*, 386-390.
71. (a) Menon, V. P.; Martin, C. R. "Fabrication and Evaluation of Nanoelectrode Ensembles," *Anal. Chem.* **1995**, *67*, 1920-1928. (b) Xia, Y.; Venkateswaran, N.; Qin, D.; Tien, J.; Whitesides, G. M. "Use of Electroless Silver as the Substrate in Microcontact Printing of Alkanethiols and Its Application in Microfabrication," *Langmuir* **1998**, *14*, 363-371.
72. (a) Toberer, E. S.; Seshadri, R. *Chem. Commun.* "Template-Free Routes to Porous Inorganic Materials," **2006**, *30*, 3159-3165. (b) Rajamathi, M.; Thimmaiah, S.; Morgan, P. E. D.; Seshadri, R. "Macroporous Materials from Crystalline Single-Source Precursors Through Decomposition Followed by Selective Leaching," *J. Mater. Chem.* **2001**, *11*, 2489-2492 (c) Toberer, E. S.; Joshi, A.; Seshadri, R. "Template-Free Routes to Macroporous Monoliths of Nickel and Iron Oxides: Toward Porous Metals and Conformally Coated Pore Walls," *Chem. Mater.* **2005**, *17*, 2142-2147 (d) Panda, M.; Rajamathi, M.; Seshadri, R. "A Template-Free, Combustion-Chemical Route to Macroporous Nickel Monoliths Displaying a Hierarchy of Pore Sizes," *Chem. Mater.* **2002**, *14*, 4762-4767.
73. (a) Krishna, K. S.; Sandeep, S. S.; Philip, R.; Eswaramoorthy, M. "Mixing Does the Magic: A Rapid Synthesis of High Surface Area Noble Metal Nanosponges Showing Broadband Nonlinear Optical Response," *ACS Nano* **2010**, *4*, 2681-2688. (b) Wang, Y.; Shi, Y. -F.; Chen, Y. -B.; Wu, L. -M. "Hydrazine reduction of metal ions to porous submicro-structures of Ag, Pd, Cu, Ni, and Bi," *J. Solid State Chem.* **2012**, *191*, 19-26.
74. Tappan, B. C.; Huynh, M. H.; Hiskey, M. A.; Chavez, D. E.; Luther, E. P.; Mang, J. T.; Son, S. F. "Ultralow-Density Nanostructured Metal Foams: Combustion Synthesis, Morphology, and Composition," *J. Am. Chem. Soc.* **2006**, *128*, 6589-6594.
75. Hua, Z.; Deng, Y.; Li, K.; Yang, S. "Low-density Nanoporous Iron Foams Synthesized by Sol-Gel Autocombustion," *Nanoscale Res. Lett.* **2012**, *7*, 1-7.
76. Armor, J. N.; Carlson, E. J.; Carrasquillo, G. "Metallic Aerogels: A Novel Synthesis of Very Fine Copper Powder," *Mater. Lett.* **1986**, *4*, 373-376.



77. Bigall, N. C.; Herrmann, A. -K.; Vogel, M.; Rose, M.; Simon, P.; Carrillo-Cabrera, W.; Dorfs, D.; Kaskel, S.; Gaponik, N.; Eychmuller, A. "Hydrogels and Aerogels from Noble Metal Nanoparticles," *Angew. Chem. Int. Ed.* **2009**, *48*, 9731-9734.
78. Tang, Y.; Yeo, K. L.; Chen, Y.; Yap, L. W.; Xiong, W.; Cheng, W. "Ultralow-Density Copper Nanowire Aerogel Monoliths with Tunable Mechanical and Electrical Properties," *J. Mater. Chem. A.* **2013**, *1*, 6723-6726.
79. (a) Steele, B. C. H.; Heinzl, A. "Materials for Fuel-Cell Technologies," *Nature* **2001**, *414*, 345-352. (b) Ding, Y.; Chen, M.; Erlebacher, J. "Metallic Mesoporous Nanocomposites for Electrocatalysis," *J. Am. Chem. Soc.* **2004**, *126*, 6876-6877.
80. Hieda, M.; Garcia, R.; Dixon, M.; Daniel, T.; Allara, D.; Chan, M. H. W. "Ultrasensitive Quartz Crystal Microbalance with Porous Gold Electrodes," *Appl. Phys. Lett.* **2004**, *84*, 628-630.
81. (a) Bonroy, K.; Friedt, J. M.; Frederix, F.; Laureyn, W.; Langerock, S.; Campitelli, A.; Sára M.; Borghs, G.; Goddeeris, B.; Declerck, P. "Realization and Characterization of Porous Gold for Increased Protein Coverage on Acoustic Sensors," *Anal. Chem.* **2004**, *76*, 4299-4306. (b) Song, Y. Y.; Zhang, D.; Gao, W.; Xia, X. H. "Nonenzymatic Glucose Detection by Using a Three-Dimensionally Ordered, Macroporous Platinum Template," *Chem. -Eur. J.* **2005**, *11*, 2177-2182.
82. Biener, J.; Wittstock, A.; Zepeda-Ruiz, L. A.; Biener, M. M.; Zielasek, V.; Krammer, D.; Viswanath, R. N.; Weissmüller, J.; Bäumer, M.; Hamza, A. V. "Surface-Chemistry-Driven Actuation in Nanoporous Gold," *Nat. Mater.* **2009**, *8*, 47-51.
83. Gash, A. E.; Simpson, R. L.; Satcher, Jr.; J. H. Aerogels and Sol-Gel composite as Nanostructured Energetic Materials. In *Aerogels Handbook*; Agerter, M. A., Leventis, N., Koebel, M. M., Eds.; Springer: New York, 2011, pp 3-18.
84. Tillotson, T. M.; Gash, A. E.; Simpson, R. L.; Hrubesh, L. W.; Satcher, J. H.; Poco, L. F. "Nanostructured Energetic Materials using Sol-Gel Methodologies," *J. Non-Cryst. Solids* **2001**, *285*, 338-345.
85. Kim, S.; Zachariah, M. R. "Enhancing the Rate of Energy Release from NanoEnergetic Materials by Electrostatically Enhanced Assembly," *Adv. Mater.* **2004**, *16*, 1821-1825.
86. Prentice, D.; Pantoya, M. L.; Gash, A. E. "Combustion Wave Speeds of Sol-Gel-Synthesized Tungsten Trioxide and Nano-Aluminum: The Effect of Impurities on Flame Propagation," *Energy & Fuels* **2006**, *20*, 2370-2376.

87. Merzbacher, C.; Limparis, K.; Bernstein, T. F.; Rolison, D.; Homrighaus, Z. J.; Berry, A. D. 2001, US patent 6,296,678B1.
88. Gash, A. E.; Satcher, J. H.; Simpson, R. L.; Baumann, T. F.; Worsley, M. A. 2009, US patent pending
89. Gash, A. E.; Satcher, J. H.; Simpson, R. L. Preparation of Porous Pyrophoric Iron using Sol-gel Methods U.S. Patent 20060042417A1, March 2, 2006.
90. Leventis, N.; Chandrasekaran, N.; Sadekar, A. G.; Sotiriou-Leventis, C.; Lu, H. "One-Pot Synthesis of Interpenetrating Inorganic/Organic Networks of CuO/Resorcinol-Formaldehyde Aerogels: Nanostructured Energetic Materials," *J. Am. Chem. Soc.* **2009**, 131, 4576-4577.
91. (a) Leventis, N.; Chandrasekaran, N.; Sotiriou-Leventis, C.; Mumtaz, A. "Smelting in the Age of Nano: Iron Aerogels," *J. Mater. Chem.* **2009**, 19, 63-65. (b) Leventis, N.; Chandrasekaran, N.; Sadekar, A. G.; Mulik, S.; Sotiriou-Leventis, C. "The effect of compactness on the carbothermal conversion of interpenetrating metal oxide/resorcinol-formaldehyde nanoparticle networks to porous metals and carbides," *J. Mater. Chem.* **2010**, 20, 7456 –7471.
92. (a) Tappan, B. C.; Brill, T. B. "Thermal Decomposition of Energetic Materials 85: Cryogels of Nanoscale Hydrazinium Diperchlorate in Resorcinol-Formaldehyde," *Propell. Explos. Pyrot.* **2003**, 28, 72-76. (b) Cuzilo, S.; Kicinski, W. "Preparation and Characterization of Energetic Nanocomposites of Organic Gel – Inorganic Oxidizers," *Propell. Explos. Pyrot.* **2009**, 34, 155-160.

## VITA

Shruti Mahadik-Khanolkar was born in 1987 in Kalyan, Thane, Maharashtra, India. She received her Bachelors degree in 2008 in Surface Coating Technology from the University Institute of Chemical Technology (UICT) at Mumbai, India. She came to the U.S. in August 2008 and joined the Chemistry Department of the Missouri University of Science and Technology to pursue her Ph.D. degree in Chemistry. During the course of her dissertation work, she co-authored eight journal articles and presented her results in two National ACS Meetings. In December, 2013, she received her PhD in Chemistry from Missouri University of Science and Technology.

